Balliou Angelika-Maria

# Hybrid molecular solid state memories & electronic nanodevices based on Polyoxometalates & other molecules of reversible redox activity

ATHENS, 2016

institute of nanoscience & nanotechnology, ncsr demokritos

school of chemical engineering, ntua

# Συμβουλευτικη Επιτροπη

Μπουρουσιάν Μιρτάτ, Αναπληρωτης Καθηγητης ΕΜΠ

Γλέζος Νικόλαος, Ερευνητης Α', ΕΚΕΦΕ "Δημοκριτος"

Λοΐζος Ζαφείρης, Καθηγητης ΕΜΠ

# Εξεταστικη Επιτροπη

Μπουρουσιάν Μιρτάτ, Αναπληρωτης Καθηγητης ΕΜΠ

Cronin (Lee) Leroy, Καθηγητης Πανεπιστημιου Γλασκωβης

Γλέζος Νικόλαος, Ερευνητης Α', ΕΚΕΦΕ "Δημοκριτος"

Κέννου Στέλλα, Καθηγητρια Πανεπιστημιου Πατρων

Λοΐζος Ζαφείρης, Καθηγητης ΕΜΠ

Pfleger Jirí, Καθηγητης Ακαδημιας Επιστημων Τσεχικης Δημοκρατιας

Τσουκαλάς Δημήτριος, Καθηγητης ΕΜΠ

* Η έγκριση της διδακτορικής διατριβής από την Ανωτάτη Σχολή Χημικών Μηχανικών του Ε.Μ.Πολυτεχνείου δεν υποδηλώνει αποδοχή των γνωμών του συγγραφέα. (Ν. 5343/1932, Άρθρο 202)

# Advisory Committee

Bouroushian Mirtat, Associate Professor, NTUA

Glezos Nikolaos, Director of Research, NCSR "Demokritos"

Loizos Zafeiris, Professor, NTUA

# Examining Committee

Bouroushian Mirtat, Associate Professor, National Technical University of Athens

Cronin (Lee) Leroy, Professor, University of Glasgow

Glezos Nikolaos, Director of Research, Nat. Cent. for Scientific Research "Demokritos"

Kennou Stella, Professor, University of Patras

Loizos Zafeiris, Professor, National Technical University of Athens

Pfleger Jirí, Professor, Academy of Sciences of the Czech Republic

Tsoukalas Dimitrios, Professor, National Technical University of Athens

* Approval of the present dissertation by the School of Chemical Engineering of National Technical University of Athens does not imply acceptance of the writer's personal opinions. (L. 5343/1932, A. 202).

*Create yourself freedom for new creating*

# Abstract

According to ITRS 2.0 2015, memory technologies will continue to drive pitch scaling and highest transistor count. As DRAM products are expected to reach their scaling limits by 2024, and unless some major breakthrough occurs, flash memory is expected to lead the semiconductor industry towards the next revolution in transistor density.

Inspired from this fact, this work focuses on molecular flash memories and logic switching molecular networks which, among all emerging technology candidates, are considered particularly promising due to their ability for reduction of size per cell and solution processing (low cost, injection-printing friendly), conceptual compatibility with photonic addressing due to molecular photosensitivity, multilevel storage, high information density, quick write-read operations, low power consumption, mechanical flexibility, bottom-up fabrication logic (overcoming the lithographic patterning constrains), conceptual non-binary data representation and properties' tunability through chemical tailoring.

Molecular electronic devices are fabricated via a combination of bottom-up layer-by-layer nanofabrication and self-assembly with CMOS platform lithography in order to provide a low cost large-scale route towards extension of the functional value of Si-based platforms.

Tungsten Polyoxometalates (POM, $[PW_{12}O_{40}]^{3-}$) of the Keggin class are being self-arranged both on nanocrystal and hyperstructure level in a rational way resulting in layers of tunable spatial correlation length. The hyperstructures exhibit tunable valence and conduction bands and, hence, adjustable electronic properties directly related to the extent of crystallization of their building blocks.

Dimensional crossover-driven insulator-to-semimetal transitions can be enforced in these hyperstructures via tuning the extent of crystallization in solution. Being able to transport or confine charge at will, these hyperstructures constitute ideal candidates for alternative molecule-based solution-printed circuitry components and transistor channels.

Hybrid CMOS/molecular memory devices based on the parallel plate architecture are fabricated, characterized and tested. Each memory element contains a planar hyperstructure of molecules (typically several

millions) that can store charge having multiple times the charge density of a typical DRAM capacitor.

Transition-metal-oxide hybrids composed of high surface-to-volume ratio $Ta_2O_5$ matrices and tungsten POMs are investigated as a charge storage composite in molecular nonvolatile capacitive memory cells. Enhanced internal scattering of carriers results in a memory window of 4.0 V for the write state and a retention time around $10^4$ s without blocking medium.

Differential distance of molecular trapping centers from the cells gate and electronic coupling to the space charge region of the underlying Si substrate are being identified as critical parameters for enhanced electron trapping for the first time in such devices.

The incorporation of a molecular-friendly blocking oxide that facilitates long term retention while suppressing cross-talking, is performed through realization of a multi-functional oxide stack ($SiO_2$/hybrid $Ta_2O_5$-POM transition metal oxide/$Al_2O_3$) that takes parallel advantage of photonically-addressed phononic modes to boost information storage and reach molecular states that were previously non-available. A 37 % information density increase is attained via phononic pumping, while the memory window reaches 7.0 V, corresponding to $\sim 4 \times 10^{14} cm^2$ charging nodes able to carry 65-195 $\mu$Cb/$cm^2$. Ability of multi-state addressing and write speed of 10 ns are being documented for the packed cell.

The fabricated high performance non-volatile memories are the first documented CMOS-compatible long term (10 years criterion satisfaction) retention molecular capacitive cell of its kind.

Following a different approach, brain-inspired, neural systems performing in networks and data-centric non-Von Neumann processing are among the latest trends for non-conventional approaches in the semiconductor industry. We focus on hybrid molecular-nanoparticle networks that exploit the massive parallelism of designless interconnected networks of locally active components, obviating the need for expensive lithographic steps.

Molecular multi-junction networks comprising of gold nanoparticles (AuNPs) of diam.~1.4 nm, electronically linked by means of copper 3-diethylamino-1-propylsulphonamide sulfonic acid substituted phthalocyanine (CuPcSu) molecules are fabricated and studied.

When electrons flow through the non-linked nanoparticle arrays, they experience on-site Coulomb repulsion and are strongly localized, with localization length ($\xi$=0.7 nm). Under dynamic excitation the system undergoes Coulomb oscillations, while the introduction of CuPcSu molecules results in the formation of a network of multiple molecular/Au nanojunctions and conductance increases by 5 orders of magnitude.

This switching behavior functions on reversible red-ox reactions and pushes carriers in a weak localization state. In this state electrons spread over several junctions and all temperature scaled current vs voltage curves, $J/T^{1+\alpha}$ vs eV/kT, collapse in one universal curve, characterizing the network and the extent of its disorder.

On the other hand, the strongly non-linear I-V response and negative differential resistance of drop-cast nanojunction 3-d arrays makes them suitable platforms for logic function exhibition. Common miniaturization bottlenecks such as capacitive crosstalk, are embraced as exploitable physical processes, that can lead to robust computational functionality. The networks can be configured on-flight with pulses as quick as 10 ns to modify their resistance between two discrete levels. Both levels can be addressed real time utilizing patterned nano-electrode pairs and reading voltage of the order of 500 mV. The networks are able to perform as a two-input "then-if" logic gates.

# Acknowledgments

This research was conducted at the Institute of Nanoscience & Nanotechnology of National Center for Scientific Research (NCSR) Demokritos in collaboration with the School of Chemical Engineering of National Technical University of Athens (NTUA).

It was primarily funded by NCSR Demokritos & the Hellenic Ministry of Development–Greek Research and Technology Network under the form of exam-granted Postgraduate Scholarship and by the "NANOMOL"-Nanoelectronic Devices based on Molecular Materials program (E-11634) for "Development of Hybrid Nanodevices based on Polyoxometalate anions". Partial support from the "NANOTRAP" Greek–Czech bilateral scientific cooperation program of the European Community (B4959-E9K/-MOBILITY No.7AMB12GR022) is also gratefully acknowledged.

Foremost, I would like to express my sincere gratitude to my advisor in NCSR Demokritos Dr. Nikos Glezos who provided me the opportunity to join the team of Nanoscience & Nanotechnology Institute as a Ph.D. candidate. I thank him for the continuous support of my Ph.D. study and, during the difficult times when writing this thesis, for his providing the moral support and freedom I needed to move on. Mr. Glezos thank you a lot.

I am deeply grateful to my advisor in NTUA Assoc. Prof. Mirtat Bouroushian who provided me the opportunity to conduct this research as a Ph.D. candidate of the school of Chemical Engineering. I have had the luck to be in his classes both as an undergraduate and masters' student. His spirit of enthusiasm and motivating teaching have been a true inspiration to me all these years. I thank him for his precious support and immense availability.

Besides my advisors, I would like to thank the rest of my thesis committee; Prof. Zafeiris Loizos who kindly accepted the invitation for becoming a co-advisor. I thank him for his availability and cooperative spirit.

I thank Dr. Antonios Douvas for the sleepless nights we have been working together in the lab. For his invaluable guidance in the world of chemical protocols and layer-by-layer self-assembly of POMs and for all the fun we have had in the last years.

My sincere thanks also goes to Dr. Panagiotis Argitis, Dr.Pascal Normand, and Dr. Panagiotis Dimitrakis , who gave access to their laboratories and/or research facilities but also for their invaluable to-the-point comments now and then. Their scientific drive, and immense knowledge inspired me to go on and widen my research from various perspectives.

I would like to thank Dr. Jiri Pfleger for providing access to his well-organized laboratory and the facilities of the Institute of Macromolecular Chemistry in Prague, as well as his professional cooperation and support during my stay there. Many thanks to Samrana Kazim and David Rais, former postdoc researchers of the Institute, with whom I more than pleasantly worked together most of my lab time there. It has been a pleasure meeting you both!

In regards to the $Ta_2O_5$ oxides, I thank Dr. George Papadimitropoulos for growing the oxides (from brand new filament!!!:-)) in their home-made CVD chamber and for being always a positive energy and a great person.

As for the $Al_2O_3$ oxides these have been grown by Dr. Dimitrios Skarlatos, whom I deeply thank not only for his scientific contribution but also for his being a source of humor, kindness and energy.

Dr. Stella Kennou and her team is responsible for the acquisition of UPS and XPS spectra of this work. Her insightful comments and great interest for my work helped and motivated me at all stages of my research. I thank her for accepting our invitation to take part in this work's evaluation committee and for being a role model for me as well as the source of my interest for UPS and XPS methods and analysis.

I will grab the opportunity to thank Dr. Nikos Boukos, researcher at the Institute of Materials Science in NCSR Demokritos. I thank him for the nice TEM images of my self-assembled molecular layers on nanostructured $Ta_2O_5$. And I thank him for being a true inspiration to me all these years. He was the first person to guide me during my first internship back in 2004, the reason why I stack with physics and a truly

amazing teacher and scientist.

I thank Dr. Kostantinos Giannakopoulos for the nice TEM cross sections he has kindly offered to do.

I could not skip mentioning my gratitude to all staff of NCSR Demokritos whose work assisted my efforts all these years.

I will end this part by thanking the family of closest companions and friends, my best friend and brothers who need not be named but are always there. Their presence and sharp spirit always supports me throughout everything. Be this the writing of this thesis or my life in general.

A million thanks to all my speleology, climbing and hiking companions (occasional & permanent) who were fortunately (!!!) there when I really needed to let off steam. Thanks a lot guys!

Special thanks to the almost legendary fisherman Miltos Karamanlis and his amazing family that have welcomed and embraced me at their home at all occasions, a tradition that I hope will continue for decades to come! I cannot forget Miss Billio who has and will always be inspiring me...

*Athens, Greece,*
*December 2016*

In case of feedback please contact :
Angelika-Maria Balliou @ mpallidio@gmail.com

# Περίληψη


## ΓΕΝΙΚΟ ΠΕΡΙΕΧΟΜΕΝΟ ΔΙΑΤΡΙΒΗΣ
## ΚΙΝΗΤΡΑ - ΠΡΟΟΠΤΙΚΕΣ

Στα πλαίσια αυτής της διατριβής κατασκευάστηκαν και μελετήθηκαν υβριδικές μοριακές/ημιαγώγιμες ηλεκτρονικές διατάξεις ως μια βιώσιμη εναλλακτική στις διαρκώς αυξανόμενες απαιτήσεις για σμίκρυνση των ολοκληρωμένων κυκλωμάτων, αύξηση της πυκνότητας της αποθηκευόμενης πληροφορίας, περαιτέρω βελτίωση της ταχύτητας εγγραφής/ανάγνωσης και ελαχιστοποίηση της κατανάλωσης ενέργειας.

Σύμφωνα με το Διεθνή Τεχνολογικό Χάρτη για την Τεχνολογία Ημιαγωγών και Ημιαγώγιμων Διατάξεων (ITRS 2.0, 2015), οι τεχνολογίες μνήμης θα συνεχίσουν να είναι αυτές που θα επιβάλλουν όχι μόνο το ρυθμό σμίκρυνσης αλλά και την τελική ταχύτητα του τρανζίστορ.

Και, καθώς οι μνήμες τυχαίας προσπέλασης (DRAM) αναμένεται να αγγίξουν τα τεχνολογικά όρια σμίκρυνσής τους μέχρι το 2024, καθίσταται σαφές ότι, εκτός και αν βιώσουμε κάποιο νέο τεχνολογικό επίτευγμα, οι μνήμες flash θα γίνουν πλέον ο οδηγός του επόμενου επιτεύγματος της βιομηχανίας ημιαγωγών προς την αύξηση της πυκνότητας ολοκλήρωσης των τρανζίστορ.

Ορμώμενοι από αυτό το γεγονός, εστιάσαμε την παρούσα δουλειά στην επίλυση του προβλήματος κατασκευής και βελτιστοποίησης μιας μοριακής μνήμης flash με επιπρόσθετη φωτονική λειτουργία καθώς και στην διερεύνηση εναλλακτικών αρχιτεκτονικών διαχείρισης πληροφορίας, όπως υβριδικά μοριακά δίκτυα με λειτουργία λογικών πυλών.

Ο λόγος που, ανάμεσα στην πληθώρα νεοαναδυόμενων τεχνολογιών, επιλέχθηκε η χρήση μορίων είναι το γεγονός ότι υπόσχονται ταυτόχρονα ένα πλήθος πολύ ελκυστικών χαρακτηριστικών αλλά και τελείως νέων ιδιοτήτων. Το υπονανομετρικό τους μέγεθος, η ικανότητα επεξεργασίας/επίστρωσης από διάλυμα (χαμηλό κόστος, injection-printing friendly), η δυνατότητα εύκολης χημικής τροποποίησής τους προς πρόσδοση νέων επιθυμητών ιδιοτήτων, η συμβατότητα με φωτονικές λειτουργίες λόγω φωτοευαισθησίας, η ικανότητα αξιοποίησης πολ-

λαπλών μοριακών σταθμών για αποθήκευση πληροφορίας, οι μικροί χρόνοι εγγραφής/ανάγνωσης πληροφορίας (μικροί χρόνοι διέγερσης), η χαμηλή κατανάλωση ενέργειας, η μηχανική ευκαμψία και δυνατότητα βιοσυμβατότητας. Τέλος η δυνατότητα μιας εναλλακτικής κατασκευαστικής λογικής αυτοοργάνωσης από κάτω προς τα πάνω η οποία παρακάμπτει (τουλάχιστον εν μέρει) το υψηλό κόστος των λιθογραφικών τεχνικών διαμόρφωσης και δίνει προοπτικές για non-binary αναπαράσταση δεδομένων και non-Boolean λογικές διεργασίες.

## ΜΟΡΙΑΚΕΣ ΜΝΗΜΕΣ FLASH

Στην περίπτωση των μοριακών μνημών flash οι μελετούμενες ηλεκτρονικές διατάξεις στερεάς κατάστασης κατασκευάζονται με ένα συνδιασμό συμβατικής οπτικής λιθογραφίας (παραδοσιακής λογικής διαμόρφωσης από πάνω προς τα κάτω) CMOS και μοριακής αυτοοργάνωσης από διάλυμα (λογικής χτισίματος υπερδομής από κάτω προς τα πάνω). Αυτή η προσέγγιση συνάδει με μια ακόμη πρόκληση που έχει τεθεί από το ITRS 2.0, 2015 για την ανάπτυξη μιας νέας τεχνολογίας η οποία να είναι συμβατή με τις διαδικασίες της γραμμής παραγωγής CMOS συνδυάζοντας τα καλύτερα χαρακτηριστικά των υπαρχουσών τεχνολογιών με τη δυνατότητα για περαιτέρω σμίκρυνση.

Θα δειχθεί ότι η προσεκτική επιλογή των μορίων και η κατάλληλη διαχείριση και οργάνωσή τους στη στερεά κατάσταση είναι στοιχεία αρκετά για να ξεπεραστούν τα προβλήματα μειωμένης απόδοσης και μεταβλητότητας των ιδιοτήτων που τυπικά εμφανίζονται σε δομές που προκύπτουν από διάλυμα λόγω άτακτης οργάνωσης και ατελειών.

Στην παρούσα διατριβή γίνεται χρήση οξειδοαναγωγικών μορίων σταθερής δομής τύπου κλωβού και υψηλής συμμετρίας (τετραεδρική) με διάμετρο 1 nm αποτελούμενα από οξείδια μετάλλων μετάπτωσης. Τα μόρια αυτά (Βολφραμο-φωσφορικό οξύ, POM, $PW_{12}O_{40}^{3-}$ δομής Keggin) χρησιμοποιούνται ως ενεργό στοιχείο αποθήκευσης στις υβριδικές διατάξεις.

Τόσο τα ίδια τα μόρια POM όσο και υπερδομές βασιζόμενες σε αυτά επιδεικνύουν εξαιρετικές ηλεκτρονικές και ηλεκτρικές ιδιότητες, καθώς και ευκολία διαχείρισης και οργάνωσης. Εμφανίζουν μεταβλητές κατά βούληση ζώνες σθένους και ζώνες αγωγιμότητας και, συνεπώς ρυθμιζόμενες ηλεκτρονικές ιδιότητες.

Η οργάνωσή τους πραγματοποιείται εδώ σε δύο διακριτά στάδια, προκειμένου να ελεγχθούν ανεξάρτητα οι διαμοριακές δυνάμεις POM-POM και οι δυνάμεις μορίων-υποστρώματος. Η διαδικασία καταλήγει στη δημιουργία μοριακών υπερδομών από διάλυμα με μεταβαλλόμενο (κατά βούληση) μέγεθος δομικής μονάδας και συνολικών αλλά και το-

πικών ηλεκτρονικών ιδιοτήτων.

Μεταβάσεις μονωτή-ημιμετάλλου (Insulator-to-semimetal transitions, SMIT) μπορούν να προκληθούν στις παραγόμενες υπερδομές POM μέσω ρύθμισης/ελέγχου του βαθμού κρυστάλλωσης των δομικών τους στοιχείων (νανοκρυστάλλων POM) στο διάλυμα. Καθώς προχωράει η κρυστάλλωση οι ενδοκρυσταλλικές αλληλεπιδράσεις ηλεκτρονίου-ηλεκτρονίου εντός των νανοκρυστάλλων ενισχύονται στο βαθμό που δημιουργούνται απεντοπισμένα συσχετιζόμενα ηλεκτρόνια εκεί που πριν υπήρχαν ισχυρά εντοπισμένες ηλεκτρονικές καταστάσεις. Αυτό έχει ως αποτέλεσμα να εμφανίζεται μία διαστατικά υποκινούμενη μετάβαση μονωτή-ημιμετάλλου σε κάθετη αγωγή (η οποία ανιχνεύεται με χρήση STM).

Από την άλλη πλευρά, στο επίπεδο (εδώ η αγωγιμότητα εξετάζεται με χρήση επίπεδων νανοηλεκτροδίων κατασκευασμένων με λιθογραφία e-beam), οι ηλεκτρονικές καταστάσεις συνεχίζουν να παραμένουν ισχυρά εντοπισμένες, όπως και στην μη εκτεταμένη νανοκρυστάλλωση, λόγω της πολύ ασθενούς σύζευξης μεταξύ των νανοκρυστάλλων στην υπερδομή.

Οι παραγόμενες υπερδομές διατηρούν σε μεγάλο βαθμό τις ιδιότητες των μεμονωμένων νανοκρυστάλλων στο επίπεδο, τροποποιημένες μόνο μέσω αλληλεπιδράσεων Coulomb ευρείας κλίμακας μεταξύ γειτονικών νανοκρυστάλλων.

Με κατάλληλη επιλογή των ηλεκτροδίων αναφοράς (τα επίπεδα νανοηλεκτρόδια λιθογραφίας e-beam που αναφέρθηκαν παραπάνω τα οποία μπορεί να είναι είτε αντιτιθέμενα είται αλληλοεπικαλυπτόμενα) μπορεί να γίνει επιλογή μεταξύ αγωγής σε 1 ή 2 διαστάσεις.

Γίνεται λοιπόν φανερό από τα παραπάνω ότι η εφαρμογή ενός τέτοιου ηλεκτρονικά ευέλικτου υλικού ως κανάλι τρανζίστορ ή ενεργού υλικού μνήμης υπόσχεται σημαντική διαμόρφωση του ρεύματος ή του φραγμού έγχυσης ηλεκτρονίων αντίστοιχα, χαράσσοντας έτσι το δρόμο για φτηνές εκτυπωνόμενες διατάξεις από διάλυμα με ρυθμιζόμενα χαρακτηριστικά απόδοσης.

Εν συνεχεία υβριδικές CMOS/μοριακές διατάξεις μνήμης βασισμένες σε αρχιτεκτονική παραλλήλων πλακών (πυκνωτικό κελίο) μελετώνται, κατασκευάζο-νται και ελέγχονται ηλεκτρικά. Τα μόρια POM ενσωματώνονται με την τεχνική δύο σταδίων που αναφέρθηκε προηγουμένως, η οποία εισάγει ελάχιστες τροποποιήσεις στο κατασκευαστικό πρωτόκολλο CMOS.

Κάθε στοιχείο μνήμης περιέχει τελικά μια επίπεδη υπερδομή μορίων POM (τυπικά αρκετά εκατομμύρια μόρια) τα οποία μπορούν να

αποθηκεύσουν φορτίο και έχουν πολλαπλάσια πυκνότητα αποθήκευσης σε σχέση με έναν τυπικό πυκνωτή DRAM.

Η ικανότητα αποθήκευσης φορτίου καθώς και η ηλεκτρονική δομή των μοριακών στρωμάτων ελέγχεται μέσω τεχνικών ηλεκτρικού χαρακτηρισμού όπως χαρακτηριστικών χωρητικότητας-τάσης (C-V), ρεύματος-τάσης (I-V), αγωγιμότητας-συχνότητας εναλλασσόμενης τάσης (G-f), καθώς και με μετρήσεις χρονικής εξέλιξης της χωρητικότητας μετά από αρχική διέγερση/πόλωση της διάταξης σε παλμό ή βήμα τάσης (C(t)).

Διατυπώνεται η άποψη ότι οι κορυφές που απαντώνται στις εκτός ισορροπίας χαρακτηριστικές ρεύματος-τάσης (transient current peaks) είναι αποτέλεσμα της δυναμικής ανταλλαγής φορέων μεταξύ ηλεκτροδίου πύλης και των διακριτών μοριακών σταθμών POM, ενώ οι χρονικά εξελισσόμενη χωρητικότητα (C(t)) κάτω από συνθήκες μοριακής φόρτισης μπορεί να δώσει πληροφορία για το ρυθμό μεταβολής του φορτίου που δεσμεύεται και αποδεσμεύεται από και εντός του μοριακού στρώματος.

Δομικός χαρακτηρισμός στην στερεά κατάσταση μέσω ηλεκτρονικής μικροσκοπίας σάρωσης (FE-SEM) σε επίπεδη θέαση αλλά και σε τομή, μικροσκοπία ατομικής δύναμης (AFM), μικροσκοπία σάρωσης φαινομένου σήραγγος (STM), φασματοσκοπική ελλειψομετρία (SE), φασματοσκοπία απορρόφησης UV-ορατού (UV-vis), φασματοσκοπία ανάκλασης υπεριώδους μετασχηματισμού Fourier (FTIR), φασματοσκοπίες φωτοηλεκτρονίων υπεριώδους και ακτίνων X, (UPS, XPS) αλλά και στο διάλυμα μέσω φασματοσκοπίας UV-vis και κυκλικής βολταμετρίας, συμβάλλουν στην διεξαγωγή των χαρακτηριστικών της ηλεκτρονικής δομής των παραγόμενων μοριακών υμενίων καθώς και των δομικών λίθων τους.

Εφόσον οι χαρακτηριστικοί χρόνοι ηλεκτρικής απόκρισης (διέγερσης-από-διέγερσης) των μορίων POM στο πυκνωτικό κελίο έχουν προσδιοριστεί και, προκειμένου να επιτευχθεί διατήρηση της αποθηκευόμενης πληροφορίας για ικανοποιητικό βάθος χρόνου, αναπτύσσονται υβριδικά (μορίων και χαμηλοδιάστατης μήτρας στερεάς κατάστασης) στρώματα οξειδίων μετάλλων μετάπτωσης.

Τα στρώματα αυτά αποτελούνται από στοιχειομετρικό (όπως καταδεικνύεται από μετρήσεις XPS) $Ta_2O_5$ υψηλού λόγου επιφάνειας προς όγκο (το οποίο ουσιαστικά είναι ένα πολύ-νανοκρυσταλλικό (effectively άμορφο) υλικό φράκταλ δομής το οποίο χρησιμεύει ως αποστάτης παρεμποδισμού διαρροής του εγχυνόμενου στα μόρια φορτίου προς την πύλη) και μορίων POM ως ενεργών κόμβων αποθήκευσης φορτίου.

Τα μόρια POM αυτοοργανώνονται ηλεκτροστατικά πάνω στη μεγάλη ενεργό επιφάνεια της χαμηλοδιάστατης μήτρας $Ta_2O_5$ η οποία έχει προηγουμένως διαμορφωθεί με ένα μονομοριακό στρώμα μορίων αμινοσιλάνης (APTES) με πρωτογενείς αμίνες ως την ομάδα επιφανειακής «ηλεκτροστατικής αγκύρωσης» των μορίων POM. Οι περιοχές συγκράτησης φορτίου σε αυτό το σύνθετο υλικό είναι τα τροχιακά του μεταλλικού πλαισίου των μοριακών κλωβών POM καθώς και οι πολλαπλές (λόγω fractality) διεπιφάνειες μορίων-$Ta_2O_5$, οι οποίες έχουν την ικανότητα να ακινητοποιούν αρνητικά φορτισμένα ευκίνητα πλεγματικά κενά οξυγόνου (όπως προκύπτει από ηλεκτρικές μετρήσεις).

Η επίδοση του νανοσύνθετου ως διάταξη μνήμης εξετάζεται αρχικά χωρίς τη χρήση οξειδίου πύλης (οξειδίου φραγμού) προκειμένου να διεξαχθούν χρήσιμα μεγέθη χαρακτηριστικά της δομής που μπορούν να βοηθήσουν στην βελτιστοποίηση και τον επανασχεδιασμό του υλικού. Με αυτόν τον τρόπο συστηματοποιείται η διαδικασία βελτιστοποίησης προς μεγιστοποίηση της απόδοσης του υλικού σε λειτουργία μη πτητικής αποθήκευσης πληροφορίας.

Το νανοσύνθετο αναπτύσσεται πάνω σε ένα οξείδιο σήραγγος $SiO_2$ σε n-Si (001) πάχους 3.1 nm. Ο ηλεκτρικός χαρακτηρισμός του υλικού καταδεικνύει ότι έχει τον διπλό ρόλο α/ βελτιωτικού της υποκείμενης διεπιφάνειας $SiO_2$/Si, μειώνοντας την επίδραση των αρχικών διεπιφανειακών καταστάσεων στις χαρακτηριστικές C-V και β/ μέσου αποθήκευσης ηλεκτρονίων υψηλής πυκνότητας.

Μετά από συγκριτική μελέτη διαφόρων τοπολογιών, καταδεικνύεται ότι η διευθέτηση κατά την οποία τα μόρια POM είναι εγκλωβισμένα μεταξύ δύο στρωμάτων $Ta_2O_5$ επιτρέπει την ενίσχυση του φαινομένου εσωτερικών πολλαπλών σκεδάσεων των αποθηκευόμενων ηλεκτρονίων με αποτέλεσμα να συγκρατείται περισσότερο short term φορτίο μετά την εφαρμογή παλμού εγγραφής και συνακόλουθα να διευρύνεται και το μετρούμενο παράθυρο μνήμης.

Ενδεικτικά, ανιχνεύεται για τη δομή ένα παράθυρο μνήμης 4.0 V στην κατάσταση εγγραφής και ένας χρόνος εγγενούς διατήρησης της πληροφορίας από τη δομή (retention) την τάξεως των $10^4$ s χωρίς τη χρήση οξειδίου φραγμού.

Η διαφορική απόσταση των μοριακών κέντρων από την μεταλλική πύλη (gate) του πυκνωτή και η ηλεκτρονική σύζευξη των μορίων αυτών με την περιοχή φορτίου-χώρου του υποκείμενου υποστρώματος Si αναγνωρίζονται για πρώτη φορά (μέσω κατάλληλων ηλεκτρικών μετρήσεων και εφαρμογής ενός επαναληπτικού αριθμητικού ηλεκτροστατικού μοντέλου βασισμένου στη μέθοδο πεπερασμένων στοιχείων για τη δομή) ως κρίσιμες παράμετροι τόσο για την ενίσχυση του φαινομένου παγίδευσης ηλεκτρονίων όσο και την ενίσχυση της επίδρασης

που αυτό έχει στο μετρούμενο παράθυρο μνήμης.

Το αναπτυχθέν μοντέλο έχει την επιπλέον πρακτική αξία ότι τροφοδοτείται με ρεαλιστικές παραμέτρους για τη δομή, όπως αυτές προκύπτουν από μετρήσεις AFM, STM, XPS, UPS, φασματοσκοπία UV-vis και SE. Έτσι μπορεί να γίνει μια κατά το δυνατόν αξιόπιστη ερμηνεία της ηλεκτρικής συμπεριφοράς του νανοσύνθετου ενώ αποκτάται μία εικόνα για την ηλεκτροστατική απόκριση/αλληλεπίδραση των συστατικών μερών ενός τέτοιου υλικού μεταξύ τους χρήσιμη για περαιτέρω βελτιστοποίηση σε επίπεδο σχεδιασμού.

Παρά το σχετικά μεγάλο παράθυρο μνήμης και την επιτυχημένη συγκράτηση του φορτίου για κάποιες ώρες η διάταξη που κατασκευάστηκε χρήζει περαιτέρω βελτίωσης προκειμένου να μπορεί να χαρακτηριστεί ως ανταγωνιστική μη πτητική μνήμη εμπορικού ενδιαφέροντος. Σε σχέση με τη διατήρηση πληροφορίας ελάχιστος στόχος είναι η ικανοποίηση του κριτηρίου των 10 ετών για εμπορικά αξιοποιήσιμες μη πτητικές μνήμες. Ο τρόπος επίτευξης αυτού του στόχου στην περίπτωσή μας είναι η ανάπτυξη ενός επιπλέον φιλμ οξειδίου παρεμβαλλόμενου μεταξύ πύλης και ενεργού υλικού αποθήκευσης. Αυτό είναι το λεγόμενο οξείδιο φραγμού που αναφέρεται παραπάνω.

Ωστόσο, η επιτυχημένη κατασκευή ενός καλής ποιότητας τέτοιου οξειδίου (κάτι το οποίο συνήθως απαιτεί υψηλές θερμοκρασίες ανάπτυξης ή μετέπειτα ανόπτησης) το οποίο να παραμένει μοριακά φιλικό δεν είναι μέχρι σήμερα ένα τετριμμένο εγχείρημα. Επιπρόσθετα, παρόλο που η αποθήκευση σε πολλαπλές στάθμες τονίζεται ως ένα από τα βασικά πλεονεκτήματα των μοριακών μνημών, η πειραματική επαλήθευση της υπόθεσης αυτής στην περίπτωση των χωρητικών μνημών παραμένει ένα θεωρητικό σενάριο.

Σε αυτή τη δουλειά επιχειρούμε να αντιμετωπίσουμε ταυτόχρονα και τις δύο αυτές προκλήσεις με έναν κατά το δυνατό κομψό τρόπο. Η λύση συνίσταται στο σχεδιασμό και την υλοποίηση ενός «έξυπνου» πολυλειτουργικού νανοδομημένου οξειδίου, ικανού να αναφερθεί σε όλες τις πτυχές του προβλήματος. Πρόκειται για μια αλληλουχία ετεροδομών αποτελούμενη από διαδοχικά λειτουργικά στρώματα τα οποία δρουν συνεργικά προς μεγιστοποίηση της ικανότητας αποθήκευσης και συγκράτησης φορέων.

Πιο συγκεκριμένα, μελετήθηκε και υλοποιήθηκε μια η αλληλουχία $SiO_2$/υβριδικό οξείδιο μετάλλων μετάπτωσης ($Ta_2O_5$-POM)/$Al_2O_3$ η οποία ενσωματώνει τόσο νανοδομημένα όσο και μοριακά οξείδια. Το υλικό αναπτύσσεται με ένα συνδυασμό εναποθέσεων από στερεό-υγρό-αέριο προκειμένου να αντιμετωπιστούν τα προβλήματα κατα-

σκευαστικής συμβατότητας των εμπλεκόμενων υλικών και με μόνο μικρές τροποποιήσεις στο standard CMOS-line πρωτόκολλο.

Κάθε ένα από τα συστατικά φιλμ επιτελεί μια αυστηρά καθορισμένη λειτουργία. Το $SiO_2$ (οξείδιο σήραγγος) δρα αφενός ως στρώμα παθητικοποίησης των επιφανειακών ατελειών του υποκείμενου τερματιζόμενου στρώματος πυριτίου και αφετέρου ως φραγμός έγχυσης φορέων. Τα ηλεκτρόνια εγχέονται στο νανοσύνθετο ($Ta_2O_5$-POM) και δεσμεύονται στα τροχιακά των οξειδοαναγωγικών μοριακών κόμβων. Στη λογική που αναφέρθηκε παραπάνω η διαφορική απόσταση των μορίων από την πύλη στο υβριδικό στρώμα και οι πολλαπλές διεπιφάνειες στον όγκο του ενισχύουν την αποθήκευση.

Ωστόσο, οι ηλεκτρονικές μεταβάσεις προς διεγερμένες καταστάσεις εντός των μοριακών νανοκρυστάλλων απέχουν πολύ από το να είναι αποδοτικές καθώς είναι έμμεσου τύπου και συχνά συμβαίνουν μεταξύ χωρικά διακριτών μορίων. Θα επιθυμούσε κανείς λοιπόν να ενισχύσει το ρόλο των φωνονικών ρυθμών στην εγγύς περιοχή των μοριακών κέντρων. Αυτό τον ρόλο αναλαμβάνει εδώ το επιφανειακό στρώμα $Al_2O_3$.

Στην πραγματικότητα δρα παράλληλα ως οξείδιο φραγμού, εμποδίζοντας την διαφυγή ηλεκτρονίων προς τη μεταλλική πύλη και σαν φωτονικά ενεργοποιούμενος φωνονικός κυματοδηγός, παρέχοντας τους απαραίτητους φωνονικούς ρυθμούς για ενίσχυση των έμμεσων διεγέρσεων των μορίων POM στη διεπιφάνεια $Al_2O_3$/(POM-$Ta_2O_5$).

Με τον τρόπο αυτό πολλαπλασιάζεται το μέγεθος της αποθηκευόμενης πληροφορίας (~37% αύξηση της πυκνότητας αποθηκευόμενης πληροφορίας μέσω φωνονικής άντλησης), καθώς γίνονται πλέον προσβάσιμες μοριακές καταστάσεις στις οποίες δεν μπορούσαμε προηγουμένως να αναφερθούμε.

Κατά το Διεθνή Τεχνολογικό Χάρτη ITRS 2.0 2015, το επόμενο βήμα στην 3d ολοκλήρωση λογικών στοιχείων και μνημών είναι η ενσωσμάτωση φωτονικών λειτουργιών προς μείωση της ισχύος και ενίσχυσης της φυσικής πυκνότητας του εύρους συχνοτήτων λειτουργίας (bandwidth). Η ανάπτυξη και ενσωμάτωση στοιχείων που επιτρέπουν την εκμετάλλευση φωτονικά ενεργοποιούμενων μηχανισμών σε ένα στοιχείο ολοκληρωμένου κυκλώματος, όπως αυτή που πραγματοποιήθηκε εδώ, είναι μια απόδειξη της ανταγωνιστικότητας της προσέγγισης υβριδικών μοριακών/CMOS προς παραγωγή χαμηλού κόστους τεχνολογία αιχμής.

Το παράθυρο μνήμης εκτοξεύεται με τον τρόπο αυτό πάνω από τα 7.0 V, ενώ κάθε στοιχείο μνήμης ενσωματώνει περίπου $9 \times 10^{12}\ cm^{-2}$ μοριακούς νανοκρυστάλλους που αντιστοιχούν σε $4 \times 10^{14}\ cm^{-2}$ κόμ-

βους αποθήκευσης, ικανούς να αποθηκεύσουν φορτίο 65-195 $\mu$Cb/$cm^2$. Η δομή αυτή έχει πολλαπλές φορές την πυκνότητα φορτίου ενός τυπικού πυκνωτή DRAM capacitor (1-2 $\mu$Cb/$cm^2$) ενώ καταγράφηκαν ταχύτητες εγγραφής της τάξεως των 10 ns για το πακεταρισμένο κελί μνήμης.

Οι παραγόμενες μη πτητικές μνήμες υψηλής απόδοσης είναι η πρώτη καταγεγραμμένη μοριακή χωρητική μνήμη του είδους της που ικανοποιεί το κριτήριο διατήρησης πληροφορίας για 10 έτη και έχει CMOS-συμβατότητα.

Το επίτευγμα αυτό είναι ένα σημαντικό βήμα προς την εμπορική αξιοποίηση των λειτουργικών οξειδίων και των μοριακών υβριδικών υλικών και την σαφή κατηγοριοποίηση τους ως υψηλής προστιθέμενης αξίας-χαμηλού κόστους μη πτητικές μνήμες για προηγμένες εφαρμογές.

## ΜΟΡΙΑΚΑ ΑΥΤΟΡΥΘΜΙΖΟΜΕΝΑ ΔΙΚΤΥΑ ΓΙΑ ΛΟΓΙΚΕΣ ΠΡΑΞΕΙΣ

Η λογική που ακολουθήθηκε μέχρι εδώ είναι αυτή των κυκλωμάτων που ακολουθούν δοσμένους σχεδιαστικούς κανόνες. Από την άλλη, μία ματιά στη φύση θα μας πείσει ότι η ίδια λειτουργεί ελαφρώς πιο χαοτικά, εκμεταλλευόμενη όποιες ιδιότητες υπάρχουν διαθέσιμες και αξιοποιώντας τη παράλληλη δράση πολλών τοπικά ενεργών στοιχείων σε μια λογική δικτύου. Τα εμπνευσμένα από τον εγκέφαλο νευρωνικά συστήματα, και η δεδομενο-κεντρική non-Von Neumann επεξεργασία είναι ανάμεσα στις τελευταίες τάσεις όσον αφορά τις μη συμβατικές προσεγγίσεις της βιομηχανίας ημιαγωγών.

Προς τη κατεύθυνση αυτή επικεντρωθήκαμε σε υβριδικά δίκτυα οξειδο-αναγωγικών μορίων-νανοσωματιδίων, τα οποία σχηματίζουν έναν επίπεδο χαοτικά δομημένο πίνακα και στα οποία η ηλεκτρική αναφορά γίνεται μέσω λιθογραφημένων (με λιθογραφία ηλεκτρονικής δέσμης) νανοηλεκτροδίων. Σε μια τέτοια τοπολογία οι αναφερόμενοι κόμβοι δεν είναι αυστηρά καθορισμένοι ενώ η λειτουργικότητα προκύπτει από τις αμοιβαίες ηλεκτροστατικές αλληλεπιδράσεις (εν είδη capacitive cross-talking) μεταξύ διασυνδεδεμένων με μόρια κόμβων νανοσωματιδίων οι ιδιότητες κάποιων από τους οποίους τοπικά μεταβάλλονται.

Μετά την εξέταση διαφόρων τεχνικών αυτο-οργάνωσης και δόμησης τέτοιων δικτύων, μελετώνται οι ηλεκτρονικές ιδιότητες επίπεδων δικτύων μοριακών πολυδιόδων αποτελούμενων από νανοσωματίδοα χρυσού μέσης διαμέτρου 1.4 nm ηλεκτρονικά συζευγμένων με μόρια φθαλοκυανίνης χαλκού υποκατεστημένης με μόρια 3-διαιθυλαμινο-1-προπυλοσουλφαμιδίου και θειικού οξέος (CuPcSu). Μετά τη διάσταση των υποκαταστατών σε υδατικό διάλυμα οι ελεύθερες θειικές ομάδες

δημιουργούν ισχυρούς δεσμούς με τον χρυσό των νανοσωματιδίων εξασφαλίζοντας ηλεκτρονική σύζευξη μεταξύ των κόμβων του δικτύου.

Όταν ηλεκτρόνια εγχέονται μέσω των ηλεκτροδίων σε μη-συζευγμένα νανοσωματίδια, εντοπίζονται στην επιφάνειά τους και δέχονται έντονη άπωση Coulomb. Ο εντοπισμός των ηλεκτρονίων αυτών είναι αρκετά ισχυρός και το μήκος εντοπισμού (localization length, ξ) υπολογίζεται ότι ανέρχεται σε 0.7 nm. Αυτό πρακτικά σημαίνει ότι τα ηλεκτρονικό νέφος δεν εκτείνεται εκτός του όγκου των νανοσωματιδίων.

Σε δυναμική διέγερση τάσης (κατάσταση μακράν της ισορροπίας) το σύστημα άγει κβαντισμένα, υποκείμενο σε ταλαντώσεις Coulomb. Η εισαγωγή των συνδετικών μορίων CuPcSu οδηγεί στο σχηματισμό πολλαπλών διόδων μορίων-νανοσωματιδίων δημιουργώντας ένα δίκτυο με νέες ιδιότητες στο οποίο η αγωγιμότητα αυξάνεται κατά 5 τάξεις μεγέθους επιτρέποντας δυνατότητες λειτουργίας σε τάσεις κάτω του 1 Volt.

Αυτή η λειτουργία τύπου διακόπτη των μορίων στηρίζεται σε αντιστρεπτές οξειδοαναγωγικές αντιδράσεις που λαμβάνουν χώρα κατά την αγωγή ρεύματος και εξωθεί τους φορείς σε μια κατάσταση ασθενέστερου εντοπισμού σε σχέση με το «γυμνό» (χωρίς συνδετικά μόρια) δίκτυο. Σε αυτή την κατάσταση τα ηλεκτρόνια απεντοπίζονται σε περισσότερες διόδους και όλες οι καμπύλες ρεύματος τάσης όταν κανονικοποιηθούν κατάλληλα με τη θερμοκρασία ($J/T^{1+a}$ vs eV/kT), καταρρέουν σε μια κοινή καμπύλη, η οποία χαρακτηρίζει το δίκτυο και την έκταση της αταξίας του.

Με τον τρόπο αυτό ποσοτικοποιείται η δομική αταξία μέσω του παράγοντα $a$ και παρέχεται η δυνατότητα συστηματικού ελέγχου της προς τροποποίηση των ηλεκτρονικών και τελικά ηλεκτρικών ιδιοτήτων τέτοιων δικτύων κατά βούληση.

Βασισμένοι στα παραπάνω δίκτυα θέτουμε τον στόχο κατασκευής λογικών πυλών. Ωστόσο, η απόκριση ρεύματος-τάσης των παραπάνω δικτύων είναι μονοτονική. Απόκριση τύπου αρνητικής διαφορικής αντίστασης είναι ένα από τα προαπαιτούμενα για να υπάρξει η δυνατότητα εμφάνιση λειτουργίας λογικής πύλης σε μια δομή.

Η λειτουργία αυτή μπορεί να επιτευχθεί σε δίκτυα drop-cast στα οποία τα νανοσωματίδια διασπείρονται σε 3 διαστάσεις (και δεν παραμένουν περιορισμένα στο επίπεδο όπως προηγουμένως) και είναι ασθενώς συζευγμένα. Σε τέτοιες περιπτώσεις ευνοείται η αποθήκευση φορτίου, οι μεταβολές διευθέτησης κατά το στρες και, λόγω αυτών, η υστερητική απόκριση. Το κατώφλι αγωγιμότητας και η ίδια η αγωγιμότητα του δικτύου εξαρτώνται από τη στοχαστική διεργασία φόρτισης των νανοσωματιδίων.

Έτσι η αγωγή ηλεκτρονίων χαρακτηρίζεται από ένα συλλογικό κατώφλι αγωγής (percolation), κάτω από το οποίο επικρατούν συλλογικά φαινόμενα παρεμπόδισης Coulomb τα οποία εντοπίζουν τα ηλεκτρόνια και παρακωλύουν τη μεταφορά τους. Σε αυτές τις περιπτώσεις και για μεγάλη τάση πάνω από το κατώφλι Coulomb οι χαρακτηριστικές I-V ακολουθούν μια σχέση της μορφής $((V–V_{TH})/V_{TH})^{\alpha}$ με $\alpha = 2.93$. Η συμπεριφορά αυτή αναδύεται σαν συνέπεια της αγωγής ηλεκτρονίων από πολλούς κλάδους ταυτόχρονα.

Με βάση την ισχυρά μη γραμμική συμπεριφορά των νανοδιόδων και τις μεταξύ τους αλληλεπιδράσεις η οποίες οδηγούν στην εμφάνιση τάσης κατωφλίου 0.42 V και $a = 2.93$ μπορεί κανείς να διερευνήσει περαιτέρω την συμπεριφορά τους σε λειτουργία λογικών πυλών. Το δίκτυο μπορεί να «εκπαιδευτεί» να άγει φορείς συλλογικά στην ίδια πάντα κατεύθυνση ανεξαρτήτως της πόλωσης της τάσης. Επιπλέον, «μαθαίνει» να μεταβάλλει την αντίστασή του μεταξύ δύο επιπέδων/τιμών ανάλογα με την πόλωση του παλμού εγγραφής. Και τα δύο επίπεδα μπορούν να διαβαστούν σε πραγματικό χρόνο με ένα ζεύγος ηλεκτροδίων και χαμηλή τάση ανάγνωσης της τάξεως των 500 mV.

Με όρους σήματος εισόδου-εξόδου $V_{IN}$ (t) and $I_{OUT}$ (t) το δίκτυο αποκρίνεται ως μια λογική πύλη δύο εισόδων με λειτουργικότητα "then-if". Συνοπτικά, η μεταβολή των τοπικών ιδιοτήτων του δικτύου (φόρτιση, αλλαγή μεταξύ διακριτών σταθμών αντίστασης) αποδίδεται σε χωρητική σύζευξη μεταξύ των κόμβων του δικτύου. Το λογικό στοιχείο που προκύπτει βασίζεται εξολοκλήρου σε τοπικά ενεργά αλληλεπιδρώντα στοιχεία και ακολουθεί μια μη-σχεδιαστική λογική αυτοοργάνωσης. Με τον τρόπο αυτό, η χωρητική σύζευξη, ένα τυπικά ανεπιθύμητο πλευρικό φαινόμενο αναδεικνύεται εδώ ως μια εκμεταλλεύσιμη φυσική ιδιότητα που οδηγεί σε υπολογιστική λειτουργικότητα.

Τα παραγόμενα δίκτυα είναι πολλά υποσχόμενα για εφαρμογές μαζικής παρασκευής φτηνών και αξιόπιστων αυτοοργανούμενων στοιχείων κυκλωμάτων από διάλυμα όπως η εκτύπωση με ψεκασμό.

# Contents

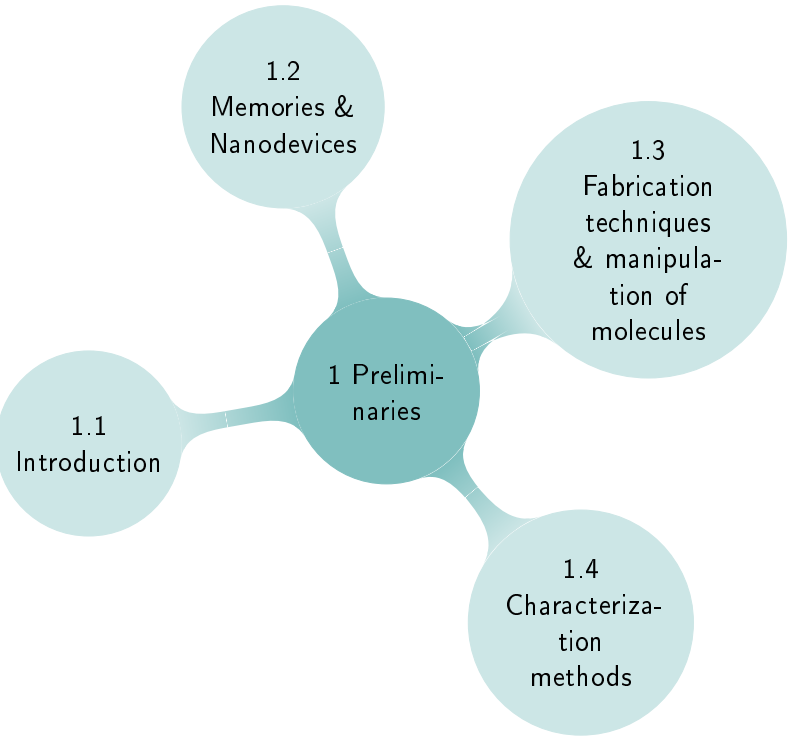


# 1

# Preliminaries

*The reasonable man adapts himself to the world; the unreasonable one persists in trying to adapt the world to himself. Therefore, all progress depends on the unreasonable man.* – George Bernard Shaw

---

## 1.1 Solid State Memories & Electronic Nanodevices – An Introduction

### 1.1.1 Why Go Small? The Driving Forces behind Technology Scaling

One can argue that way too much effort has been invested in recent years on the miniaturization of integrated circuit components. Up to now, though, there certainly are several good reasons for it!

Speaking with numbers, since the 1960s the price of one bit of semiconductor memory has dropped 10 trillion times (from 8,192,000,000,000.00 $ per GigaByte of RAM in 1966 to 0.50 $ in 2015) and the trend still continues. The cost for a logic gate has, similarly, undergone a dramatic drop, stimulating an increasing number of new applications for semiconductor devices.

As far as memory and processing units are concerned, by making transistors and interconnects smaller, more circuits can be fabricated on each silicon wafer and, therefore, each circuit becomes cheaper. Miniaturization has also been instrumental in improving speed and power consumption.

In the field of integrated photonics and sensors that also use semiconductor processing techniques to realize advanced information handling, optoelectronic and sensing functions, miniaturization of functional elements using standard wafer-level processing tools boosts applications range and contributes to cost reduction, while shedding new light on sectors like the radical redesign of packaging and assembly [1].

Historically, a new technology node is introduced approximately every three years. At each new node, the various feature sizes of circuit layout are 70% of the previous node. Main gain when introducing a new technology node is the reduction of circuit size by 2, as 70% of previous line width is translated in ~50% reduction in area, i.e. 0.7 × 0.7= 0.49. Since nearly twice as many circuits can be fabricated on each wafer with each new technology node, the cost per circuit is reduced significantly.

Other parameters besides line width, also reduced via scaling are the MOSFET gate oxide thickness and the power supply voltage. The reductions are chosen such that the transistor current density (Ion/W) increases with each new node. At the same time, smaller transistors and shorter interconnects lead to smaller capacitances, causing the circuit delays to drop according to Eq.1.1, [2].

$$\tau_{delays} = \frac{CV_{dd}}{4}\left(\frac{1}{I_{d,sat,N}} + \frac{1}{I_{d,sat,P}}\right) \tag{1.1}$$

The equation gives the CMOS propagation delay, i.e. the time delay for a signal to propagate from one gate to the next in a chain of identical gates. $V_{dd}$ is the supply DC voltage and $I_{d,sat,N}$, $I_{d,sat,P}$ are taken at Vgs = Vdd and Vgs = -Vdd respectively and are the on-state current, of the NFET and the PFET. Historically, integrated circuit speed has increased roughly 30% at each new technology node.

Total power consumption for a MOSFET is expressed through the equation [2]:

$$P = 1.2 \cdot CV_{dd}^2 f + V_{dd} I_{off} \tag{1.2}$$

showing that reducing capacitance (C) and, especially, the power supply voltage ($V_{dd}$) effectively lowers power consumption. Thanks to the reduction in C (It represents the sum of all the capacitances that are connected to the output node of the inverter. It consists of the input capacitance of the next inverter in the chain, all the parasitic capacitances

of the drain, and the capacitance of the metal interconnect that feeds the output voltage to the next inverter) and $V_{dd}$, power consumption per chip has increased only modestly per node in spite of the rise in switching frequency, f, and the doubling of transistors per chip at each technology node.

Had it been no scaling, the job of a single microprocessor running 500 M transistors at 2 GHz using 1970 technology would require the electrical power output of a medium-size power generation plant.

By now it became clear how scaling improves cost, speed, and power per function with every new technology generation. All of these attributes have been improved by 10 to 100 million times in four decades, an engineering achievement never been attained before!

As we dig deeper and deeper in the nanoscale, though, scaling becomes increasingly expensive. Sophisticated precision nano-fabrication tools counterbalance by far the gain from circuit densification, while higher mobility materials like III-V semiconductors and Ge [3] that would overcome the inherent limitations of silicon and enhance drive current [4] emerge as a pressing need.

This is the point where emerging memory technologies and epitaxial growth of new materials on the well-established Si platform [3] come into play in order for Moore's law to march on a bit longer.

#### Memory Technologies – The Key to Revolutionize Transistor Density

According to ITRS [3] memory technologies will continue to drive pitch scaling and highest transistor count and will always be the drivers of Moore's scaling law. As DRAM products are expected to reach their scaling limits by 2024 unless some major breakthrough occurs, Flash memory will lead the semiconductor industry towards the next revolution in transistor density [3].

### 1.1.2 Solid State Memories & Charge Trapping Operation

#### Solid State Memories' Concepts

Data storage devices can be classified based on several functional criteria (storage mechanism, material, power supply autonomy, etc.).

Silicon-based semiconductor memories are typically categorized into two: volatile and nonvolatile [5], according to whether an active power source is required to maintain data. In volatile memories, the information eventually fades when power supply is turned off (i.e. static random-access memory (SRAM)) unless the devices are periodically refreshed

(i.e. dynamic random-access memory (DRAM)). On the other hand, non-volatile memories (i.e. Flash memories) retain the stored information even after power supply is turned off. The general classification scheme can be seen in Fig.1.1.

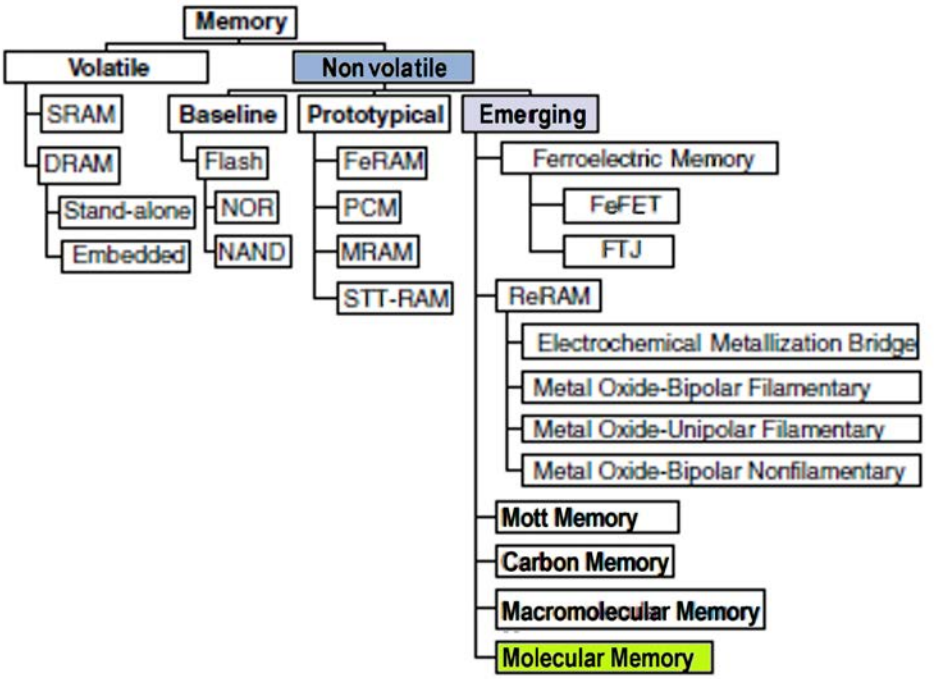


Figure 1.1: Classification of memory technologies (adapted from the 2013 ITRS ERD according to [5])

DRAM, SRAM, and Flash are today's dominant solid-state memory technologies with Flash being the youngest, at 29 years. Their distribution on an actual integrated server along with their role and typical access latency in processor cycles is presented in Fig.1.2.

The system performance scales with Memory Capacity, Latency & Bandwidth. When comparing DRAM memory with NAND storage units the bandwidth relation is 10 GB/sec for DRAM to 250 MB/sec for NAND. A Flash bit is cheaper and more energy efficient but lacks in endurance, bandwidth and latency when compared to DRAM [6]. Each memory type has its own unique role during processing cycles.

Besides the aforementioned mature products, prototypical memory technologies like spin transfer torque RAM (STT-RAM) and phase change RAM (PCRAM), have made improvements in recent years and are already being commercially produced for niche markets.

According to [6] the main focus is to be put on high density MLC

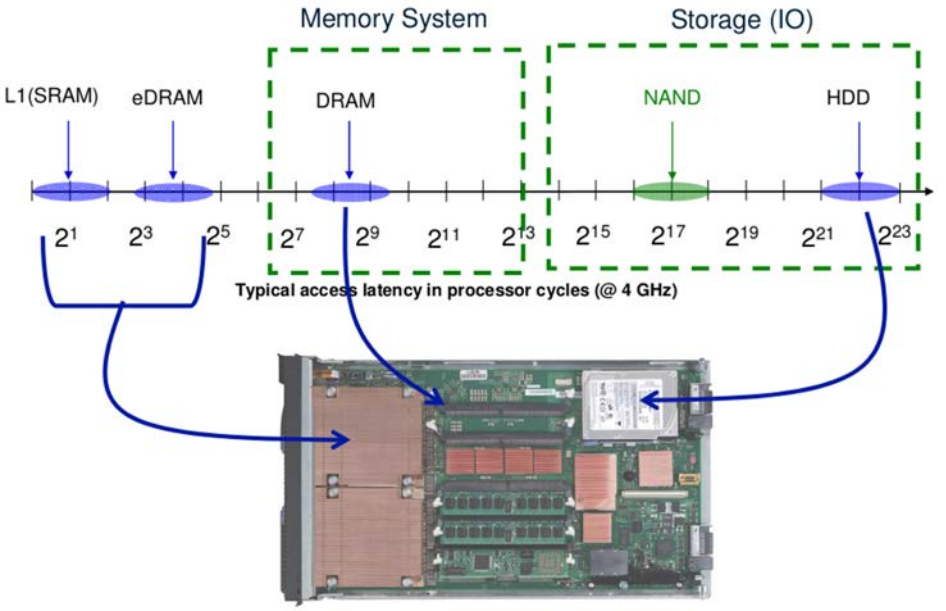


Figure 1.2: Where Memory is in a System according to [6])

(Multi-Level Cell)-based flash storage solutions as well as on innovations in server architecture, which will enable benefits from Emerging Memory Technologies as they become mature.

### State of the Art–Emerging Memory Technologies

Emerging memory technologies, especially resistance switching memories (RRAM) have made rapid advancements in the past decade and offer the possibility of greater scaling and performance than prototypical or baseline technologies. RedoxRAM (ReRAM) technologies have advanced at a particularly high rate in recent years, both in the scientific understanding and technological development of working prototype chips [5].

Building on the success of organic electronic devices, such as light-emitting diodes and field-effect transistors, procedures for fabricating non-volatile molecular memory devices are now being increasingly explored.

Implementing on-chip non-volatile molecular memories has been a long-term goal and the community's strenuous perseverance on the field is certainly not without a good reason.

Except from fulfillment of the ITRS-dictated CMOS compatibility criterion, they are targeted due to a vast range of advantageous properties. Among these are: their solution processing ability (low cost, injection-

printing friendly), the conceptual compatibility with photonic addressing due to molecular photosensitivity, multilevel storage, high information density, quick write-read operations, low power consumption, mechanical flexibility, biocompatibility, bottom-up fabrication logic (overcoming the lithographic patterning constrains) and properties tunability through simple chemical tailoring.

Their functionality is based upon charge-trapping on their red-ox active centers, often in conjunction with their ability for facile 3-d organization from solution, with both characteristics being hot features for next-generation memory devices [7].

### Charge Trapping Operation

A charge trapping type memory cell uses a variable charge between the control gate and the channel to change the threshold voltage of the transistor. The mechanisms exploited to modify and read this charge are very similar to the floating gate memory cell [8] the architecture commonly used in standard FLASH memory design (see Fig.1.3 schematics). In a floating gate MOS the electrically isolated gate creates a floating node in DC and is only capacitively connected to the secondary gates or inputs. In a charge trapping flash electrons are stored in a trapping layer just as in the floating gate, EEPROM (electrically erasable programmable read-only memory), or EPROM (erasable programmable read-only memory). The key difference is that the charge trapping layer is an insulator, while the floating gate is a conductor.

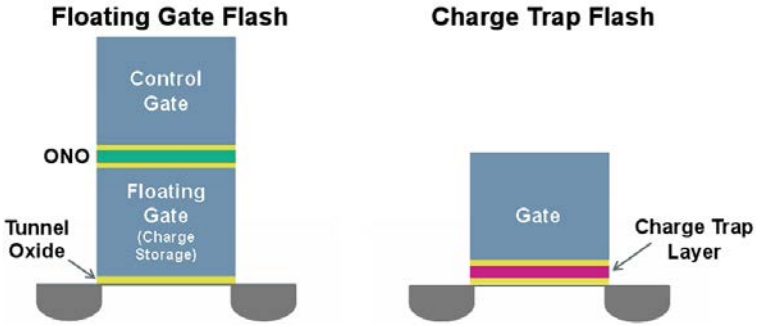


Figure 1.3: Floating Gate vs Charge Trapping Flash

High write loads in a flash memory cause stress on the tunnel oxide layer creating small disruptions in its structure called oxide defects. A large number of such disruptions causes development of a short circuit between the floating gate and the transistors channel and the floating gate can no longer hold a charge. This is the root cause of flash wear-out,

degrading the chips endurance.

In order to reduce the occurrence of such short circuits, floating gate flash is manufactured using a thick tunnel oxide (~10 nm), but this slows erase when Fowler-Nordheim tunneling is used and forces the design to use a higher tunneling voltage, which puts new burdens on other parts of the chip.

A charge trapping cell is relatively immune to such difficulties, since the charge trapping layer is an insulator [8]. A short circuit created by an oxide defect between the charge trapping layer and the channel will drain off only the electrons in immediate contact with the short, leaving the other electrons in place to continue to control the threshold voltage of the transistor. Since short circuits are less of a concern, a thinner tunnel oxide layer can be used (3-7 nm) increasing the trapping layers coupling to the channel and leading to a faster program speed (with localized trapped charges) and erasing with lower tunneling voltages. The lower tunneling voltages, in turn, place less stress on the tunnel oxide layer, leading to fewer lattice disruptions.

Another important benefit of charge trapping cells is that the thin charge trapping layer reduces capacitive coupling between neighboring cells, improving performance and scalability [8].

### Write Function

Electrons are moved onto the charge trapping layer similarly to the way that floating gate NOR flash is programmed, through channel hot carrier (electrons) injection. In brief, a high voltage is placed between the control gate while a medium-high voltage is applied on the source and the drain while a current is induced from the source to the drain. Those electrons that have gained sufficient energy in traversing through the high-field region near the drain will boil off from the channel to be injected into the charge trapping layer where they come to rest.

### Erase Function

Charge trapping flash is erased via hot hole injection as opposed to the Fowler–Nordheim (FN) tunneling approach used in both NAND and NOR flash for erasure. This process uses a field, rather than the current used in FN, to move holes toward the charge trapping layer to remove the charge.

### 1.1.3 Electronic Nanodevices – Operating in Networks of Nanocomponents

It is possible to raise performance in a way different than scaling the MOSFET, that is following non-conventional architectures.

One of the central objectives of recent research in devices beyond silicon transistors consists in the development of novel logic switches that might replace the silicon transistor as the device driving technological development within the semiconductor industry.

Such a replacement is thought potentially to be viable if one or more of the following capabilities is afforded by a novel device [3]:

(1) an increase beyond CMOS in device density,

(2) an increase beyond CMOS in switching speed, e.g., through improvement of normalized drive current or reduction in switched capacitance,

(3) a reduction beyond CMOS in switching energy (lower consumption), or

(4) the enabling of novel information processing functions that cannot be performed as efficiently using conventional CMOS.

In the latter case non-binary data representation and non-Boolean logic may be also required to employ a new device for information processing [3]. Brain-inspired, neural systems performing in networks and Data-centric non-Von Neumann processing are among the latest trends for non-conventional approaches in the semiconductor industry race.

Towards this direction we will focus our quest on hybrid molecular-nanoparticle networks electronically addressed as a planar low dimensional matrix. Such configurations aim at exploiting the massive parallelism of interconnected networks of locally active components.

The approach is based on designless nano-component arrangement on CMOS compatible platforms, obviating the need for expensive lithographic steps. Disorder can be incorporated to alter the electronic properties of the networks in a rational way. Moreover, common miniaturization bottlenecks such as capacitive crosstalk, are embraced as exploitable physical processes, that can lead to robust computational functionality.

The strongly nonlinear single-electron transistor behavior that emerges from interconnected metal nanoparticles can be configured in situ to perform logic gate operations, thus enabling novel functions promising for future technologies.

## 1.2 Current International Technology Roadmap for Semiconductors & Outline of this Thesis

We are experiencing an era where silicon-based devices are approaching their physical limits. The current leap for semiconductor industry after the 10-nm process node is 7 nm. In July 2015 IBM announced successful production of 7-nm test FinFETs with silicon-germanium (SiGe) alloy channels [9]. This new alloy is apparently one of three advancements that made the 7-nm test chip possible, the others being self-aligned quadruple patterning and an EUV light source with a wavelength of 13.5 nm. Given that we're still waiting on 10-nm products from other manufacturers, it'll likely be a long wait till commercial products based on a 7-nm process will come to market, but it seems as if Moore's Law could march on a little longer yet.

Nevertheless, it becomes more than clear that miniaturization of chip size is a process fundamentally constrained. Quantum mechanical effects like direct source-drain tunneling, quantum mechanical reflection and interference, increased leakage current, cross-talking between integrated components and local overheating, throw the validity of Moore's law into question for the years to come. Although approaches like recessed channel and vertical transistors could allow for continuation of miniaturization and increase of component density, the adoption of new materials like InGaAs seem inevitable in order to proceed even further. Indeed silicon had to be abandoned already in order to reach the 7-nm milestone.

Replacing silicon in a commercial scale, though, would still be a formidable task because all the electronics industry is adapted on it. What is, consequently, emerging as a pressing need is the development of alternative approaches and new architectures that will boost the performance of conventional silicon-based platforms through C-MOS compatible side processes. Heterogeneous integration and components that form heterogeneous systems, such as MEMS, power generation, and sensing devices are amongst the current focus topics of the International Technology Roadmap for Semiconductors [10].

Towards this direction great efforts have been made to integrate molecules as active components for future electronic devices. Molecules, few atom entities spanning sub-nanometer to micrometer sizes offer a vast variety of physical and chemical properties. They can be extremely sensitive in "sensing" their environment or offer effective isolation of their electronic states being structural and electronically stable. Moreover, their properties can be tuned with proper surface or structure modification and can be also handled using grafting groups and field or chemical

interactions. We emphasize here on the development of molecular electronics for non-volatile memory applications with a focus on redox-active molecules, for future low-power and ultra-high-density non-volatile memory applications.

## STATE OF THE ART

MOSFET and related integrated circuits now constitute about 90 % of the semiconductor device market [11]. A nonvolatile memory device based on semiconductors is a typical MOS transistor that has a source, a drain, and a gate. Tunneling is the process by which a nonvolatile memory can be either erased or programmed and is usually dominant in thin insulating layer. Storage of the charge on the floating gate allows the threshold voltage to be electrically altered between a low and a high value to represent logic 0 and 1, respectively. Typical requirement for a non-volatile memory is a ten years data retention time without power supply.

Emerging memory technologies promise storage of more data at less cost than conventional silicon-integrated MOSFET structures and are targeted as potential memory alternatives mainly for popular consumer gadgets including digital cameras, cell phones and portable music players. They are being investigated as potential alternatives to existing memories in future computing systems.

Flash-type charge storage memory is the most suitable structure of non-volatile memory, since one cell consists of only one transistor. It is widely used in consumer electronic products such as cell phones and music players, while NAND Flash-based solid-state disks (SSDs) are increasingly displacing hard disk drives as the primary storage device in laptops, desktops, and even data centers [12]. The state of the art development in emerging non-volatile molecular memory technologies involves mainly the following sectors :

**I)** Molecular Switching Devices based on Metal/Molecule/Metal nanojunctions in Crossbar or
**II)** Planar (Multi-junction Networks) architecture,
**III)** Hybrid CMOS/Molecular Memory Devices both in Liquid (Electrochemical Cell Deployment) and
**IV)** Solid State (Hybrid CMOS/Molecular Solid State Memories),
**V)** Nanotube and/or Nanowire-based Molecular Memories.

There are two fundamentally different approaches used to fabricate molecular electronics, figuratively termed top-down and bottom-up. Stead

of top-down, which refers to making nano-scale structures by shaping macrosopic size bulk material through machining and etching techniques, the bottom-up approach takes advantage of molecule self-assembly and hyperstructuring using nanoscale building blocks. Bottom-up refers to building complex organic or inorganic structures atom-by-atom or molecule-by-molecule. In the past few decades, research on molecular electronics has been focusing more and more on the combination of top-down device fabrication (mainly lithography and epitaxial growth) with bottom-up molecule self-assembly.

**IN THIS DISSERTATION** molecular technology is selected as an answer to the stringent performance requirements for thin-film transistors in terms of miniaturization, switching speed, turn-on voltage and energy consumption. In theory the potential of the utilization of molecular building blocks in nano-scale electronics is overwhelming due to the inherent scalability and intrinsic properties of molecular entities [13, 14, 15]. Towards this quest we will have to face major scale-up challenges and disorder-induced mis-performance. We show that careful selection and handling of functional molecules can overcome these difficulties. We particularly focus on molecular memories and sensitive molecular logic switching networks, among all new emerging candidates, which are considered promising particularly due to the reduction of size per cell and the enhancement of memory speed, density and reliability [16, 17].

Throughout this work molecular electronic devices are fabricated following the approach of the combination of top-down device lithography with bottom-up nanofabrication and self-assembly in order to provide a feasible route towards extension of the functional value of current C-MOS platforms. These platforms, despite being relatively outdated compared to alternative lab-level approaches, they still dominate the market. The combination of molecules with semiconductors, metallic nanoparticles and 3D nanostructures in an effort to boost the complementary metal-oxide-semiconductor (CMOS) scaling and performance is discussed and investigated.

This method is proposed as a promising alternative towards overriding the current roadblock of manufacturability of high resolution structures through conventional lithographic processes. The self-assembly of functional molecules could exploit the capabilities of silicon while remaining an economically feasible transition in industrial scale. Moreover, molecular functional components operate by controlling fewer electrons at the molecule scale and, therefore, have potential for low-power devices and ultra-high-density memory applications with a lower fabrication cost. Redox-active molecules have become attractive to replace the floating gate in conventional flash memory, due to their inherent and reliable re-

dox behavior [18, 19, 20] along with the ability for multi-state occupancy.

This work focuses mainly on the investigation of functional red-ox molecules like polyoxometalates and pthalocyanines as core components of hybrid molecule-oxides and molecule-metal devices. The use of molecules offers a viable alternative in the current problems of microelectronics industry and a challenging field for nanotechnology in terms of basic research. The natural size reduction down to the molecular scale and the possibility of exploitation of multiple molecular states with the advantage of low energy consumption and high speed are only some of the appealing aspects of such a concept and will be covered in this work. Three dimensional nanostructuring of the molecular nano-assemblies is also discussed while its impact is investigated on the electric performance of working devices.

New sensors, memories, junctions and quantum traps could be developed using stable structure molecules with reversible red-ox properties such as polyoxometalates (POMs). These molecules, being the molecular analogue of transition metal oxides, are inorganic metal-oxygen cluster anions that are unique in their topological and electronic versatility. Besides their handling flexibility, they are able to attach and delocalize electrons on their metal framework without undergoing structural damage [21], with their electronic properties being chemically tuned. Their additional advantage is the incorporation of their assembly process in early stages of the integrated circuits production line, therefore, reducing the cost and increasing their functional reliability.

Other molecules such as Copper pthalocyanine can have a well-defined planar arrangement in solid state while exhibiting reversible red-ox reactions. These molecules can be utilized in non-conventional 2-D architectures, as in their sulfonated form can serve as conjugated electronic linkers for gold nanoislands.

## OUTLINE OF THIS WORK

The structure of this dissertation is as follows:

In **CHAPTER 1** we will cover some preliminary physical concepts and basic fabrication and characterization methods. These will be used throughout this work without further explanation.

We will see what going nano implies for the macroscopic and mesoscopic observables of devices incorporating nanodimensional active components. The special characteristics of transport as we approach the nanoscale regime are discussed. The problem of variability in nanoscale devices and the techniques used for the introduction of molecular com-

ponents will also be covered in this chapter.

The fabrication methods used in this dissertation for the shaping of nano-devices will be discussed, along with the practices adopted for troubleshooting common problems encountered in nano-dimensional manufacturing and molecules' handling. Finally, the methods used for the structural (AFM, SEM, TEM), spectroscopic (UPS, XPS, FTIR, UV-Vis, SE), electronic (STM) and electrical (*I-V, C-V, C-F, C-t, I-t*) characterization of the realized nanostructures will be briefly presented, along with the specific physical quantities they aim to unveil and determine.

**CHAPTER 2** is dealing with Polyoxometalates as building blocks for functional devices. It demonstrates their superior electronis structure and handling agility as materials able to exhibit tunable valence and conduction bands and, hence, adjustable electronic properties. They are able to form bottom-up solution-derived molecular hyperstructures with great potential for electronic applications.

It is demonstrated that insulator-to-semimetal transitions (SMIT) can be enforced in self-assembled tungsten polyoxometalate (POM) molecular hyperstructures via tuning the extent of crystallization in solution. An one-pot self-assembly process is applied in two stages, in order to separately address intermolecular and molecule-substrate interactions. Intragrain electron-electron interactions are enhanced to the point where itinerary correlated electrons appear in previously strongly localized electronic states, resulting in a dimensional crossover-driven SMIT under vertical transport. In plane, on the other hand, electronic states are always strongly localized, owing to weak inter-crystal coupling.

The produced structures largely preserve their original single-nanocrystal properties on plane, modified only by long range Coulomb interactions between neighbors. Selection between 1-D and 2-D planar transport depends on the choice of addressing leads. Properly incorporating such a material in transistor channels or memory cells will enable substantial modulation of transistor current or injection barrier, respectively, paving the way for solution-printed devices with consistently tunable performance characteristics.

In **CHAPTER 3** the component that is most urgently in need of replacement for most semiconductor devices, the capacitor core, is investigated in detail. Hybrid Complementary Metal Oxide Semiconductor (CMOS)/molecular memory devices based on the parallel plate architecture are fabricated, characterized and tested utilizing the CMOS platform.

The utilization of molecular transition metal oxides known as polyoxometalates (POMs), in particular the Keggin structure anions of the for-

mula $[PW_{12}O_{40}]^{3-}$, as active nodes for potential switching and/or fast writing memory applications is investigated in detail. The active molecules are being integrated in hybrid Metal-Insulator/POM molecules-Semiconductor capacitors, which serve as prototypes allowing investigation of critical performance characteristics towards the design of more sophisticated devices. The incorporated POM molecular assemblies are designed in a rational way in order to have pre-specified electrical properties and are incorporated with only minor modification of existing fabrication methods. Each memory element contains a planar hyperstructure of molecules (typically some millions) that can store charge; this process yields a structure that has multiple times the charge density of a typical DRAM capacitor, obviating the necessity for a trench or stacked capacitor geometry.

The charging ability as well as the electronic structure of the molecular layer is probed by means of electrical characterization, namely: capacitance-voltage and current-voltage measurements, as well as transient capacitance measurements, C (t), under step voltage polarization. It is argued that the transient current peaks observed are manifestations of dynamic carrier exchange between the gate electrode and specific molecular levels, while the transient C (t) curves under conditions of molecular charging can supply information for the rate of change of the charge that is being trapped and de-trapped within the molecular layer.

Structural characterization via surface and cross sectional scanning electron microscopy as well as atomic force microscopy, spectroscopic ellipsometry, UV and Fourier-transform IR spectroscopies, UPS and XPS contribute to the extraction of accurate electronic structure characteristics and open the path for the design of new devices with on-demand tuning of their interfacial properties via the controlled preparation of the POM layer.

**CHAPTER 4** is dealing with transition-metal-oxide hybrids composed of high surface-to-volume ratio $Ta_2O_5$ matrices and tungsten POMs as a charge storage medium in molecular nonvolatile capacitive memory cells.

The POM molecules are electrostatically self-assembled on a low-dimensional $Ta_2O_5$ matrix, functionalized with an aminosilane molecule with primary amines as the anchoring moiety. The charge trapping sites are located onto the metal framework of the electron-accepting molecular entities as well as on the molecule/oxide interfaces which can immobilize negatively charged mobile oxygen vacancies.

The memory characteristics of the nanocomposite are tested using no blocking oxide for extraction of structure-specific characteristics. The

film is formed on top of the 3.1 nm-thick $SiO_2$/n-Si(001) substrates and has been found to serve as both $SiO_2$/Si interface states reducer (i.e., quality enhancer) and electron storage medium. The device with the polyoxometalates sandwiched between two $Ta_2O_5$ films results in enhanced internal scattering of carriers resulting in a memory window of 4.0 V for the write state and a retention time around $10^4$ s without blocking medium.

Differential distance of molecular trapping centers from the cells gate and electronic coupling to the space charge region of the underlying Si substrate are being identified as critical parameters for enhanced electron trapping for the first time in such devices.

A numerical electrostatic model incorporating structural and electronic characteristics of the molecular nodes derived from scanning probe and spectroscopic characterization interprets the hybrids electrical response and provides insight into the electrostatics of the trapping medium.

**CHAPTER 5** addresses one of the main factors putting the skids on the realization of silicon-competitive molecular memories. The difficulty in acquiring a molecular-friendly blocking oxide. This hinders long-term retention of the stored bytes and renders the cell prone to cross-talking. At the same time, even though multilevel storage is commonly highlighted as a flagship feature of molecule-based memories, an experimental realization of a multi-state capacitive memory cell still remains elusive. This stems, among others, from the difficulty of addressing discrete molecular levels at the mesoscopic scale. Ideally, high storage density, fulfillment of the current commercial threshold of 10-years-data-retention-guarantee in ambient conditions, ability of multi-state addressing, and CMOS-compatible fabrication processes should be collectively met for commercially-valuable non-volatile capacitive memory devices.

An elegant way to address such a multi-aspect problem is presented through the incorporation of multiple functionalities in one "clever" material. Utilizing a stack of such materials and taking advantage of the power of multiple interfaces, molecules and transition metal oxides it is possible to built a so-called functional oxide stack; ultimately, a complex material that meets all the aforementioned requirements, while taking advantage of photonically-addressed phononic modes to boost information storage and reach molecular states that were previously non-available.

Capacitive memory cells based on this material are being fabricated with only minor modifications of the standard CMOS-line protocol. These high performance non-volatile memories are the first documented CMOS-compatible long term retention molecular capacitive cell of its kind, blazing the trail for the commercial exploitation of functional oxide and

molecular hybrids as a high-end non-volatile memory product.

In **CHAPTER 6** a different architecture utilizing multiple metal/molecule/metal junctions is investigated. It attempts to rationalize the emergent electronic characteristics of designless multijunction networks realized through the bottom-up self-organization of hybrid metal-organic nanosize units. This includes the incorporation of disorder in the modeling of their electrical behavior and the exploitation of collective behavior of interacting nano-components.

It is demonstrated that this way can lead to forms of computational functionality. The rich behavior of interconnected metal nanoparticles, which act as strongly nonlinear single-electron transistors is exploited, making clear that this nanoscale architecture can be configured on-flight to perform Boolean logic functions.

Precision control of charge transport is essential in providing a solid basis for the design of materials with novel properties. The impact of the bottom-up fabrication processes on the functionality of the final structure is investigated and the electronic properties of molecular multijunction networks comprising of ultra-fine gold nanoparticles (AuNPs) of diam.~1 nm, electronically linked by means of copper 3- diethylamino-1-propylsulphonamide sulfonic acid substituted phthalocyanine (CuPcSu) molecules are studied.

When electrons flow through the non-linked nanoparticle arrays, they experience on-site Coulomb repulsion and are strongly localized, with localization length ($\xi$=0.7 nm). Under dynamic excitation the system undergoes Coulomb oscillations, while the introduction of CuPcSu molecules results in the formation of a network of multiple molecular/Au nanojunctions and conductance increases by 5 orders of magnitude.

This switching behavior functions on reversible red-ox reactions and pushes carriers in a weak localization state. In this state electrons spread over several junctions and all temperature scaled current vs voltage curves, $J/T^{1+\alpha}$ vs eV/kT, collapse in one universal curve, characterizing the network and the extent of its disorder.

Utilizing this property we demonstrate the effect of inter-electrode distance on the conduction nodes' topological disorder. The fabricated networks consist a promising candidate for designless Au NPs-based networks with tunable properties wherever solution-based fabrication methods, such as injection printing, are envisioned.

## 1.3 How to Fabricate Nanostructured Devices & Manipulate Molecular Components

Since one of the dominant trends according to the 2015 ITRS 2.0. guidelines is the extension of functionality of the CMOS platform via heterogeneous integration of new high-speed, high-density, and low-power memory technology onto the CMOS platform, conventional CMOS line patterning methods like photolithography come into play, albeit with properly modified procedural protocols in order to be compatible with molecular matter.

### 1.3.1 Optical lithography

In general, the processes used to make an IC fall into three categories: film deposition, patterning and semiconductor doping [22]. Fundamental to all of these processes is lithography, i.e. the formation of three-dimensional relief images on the substrate for subsequent transfer of a pattern and, utilizing this, a localized process like subtractive transfer (etching), additive transfer (selective deposition) or impurity doping (ion implantation) into and/or onto the substrate.

#### Photoresists–Positive, Negative & Image Reversal

Positive resists form an indene-carboxylic acid ($x(C_9H_8) - y - (COOH)$) during exposure making them soluble in aqueous alkaline solutions. Therefore, positive resists develop where they have been exposed, while the unexposed areas remain on the substrate. Since positive resists do not cross-link, the resist structures rounden beyond their softening point of typically $100 - 130^o$ C. The mask, therefore, contains an exact copy of the pattern which is to remain on the wafer for subsequent processing.

Negative resists cross-link after exposure and a subsequent baking step, while the unexposed part of the resist is dissolved in the developer. The crosslinking makes the resist thermally stable, so even elevated temperatures will not deteriorate the resist profile. However, towards higher and higher process temperatures, the degree of crosslinking increases and it becomes hard or even impossible to wet-chemically remove the resist. Masks used for negative photoresists, therefore, contain the inverse or photographic "negative" of the pattern to be transferred.

Image reversal resists can either be processed in positive or negative mode. In the positive mode, the process sequence is the same as for positive resists. In the image reversal mode, an image reversal bake after the exposure followed by a flood exposure without mask is required. Even

in the negative mode, the degree of crosslinking of the resist is rather low, so the resist structures will rounden beyond the softening point of typically 130°C.

### What we Use

In our case AZ Image reversal photoresist comprised of a novolak resin (phenol-formaldehyde resin with a formaldehyde to phenol molar ratio of less than one) and naphthoquinone diazide as photoactive compound (PAC) capable of image reversal (IR) resulting in a negative pattern of the mask is used. The image reversal capability is obtained by a special crosslinking agent in the resist formulation which becomes active at temperatures above 110řC and - what is even more important - only in exposed areas of the resist. The crosslinking agent together with exposed PAC leads to an almost insoluble (in developer) and no longer light sensitive substance, while the unexposed areas still behave like a normal unexposed positive photoresist. After a flood exposure (no mask required) this areas are dissolved in standard developer for positive photoresist, the crosslinked areas remain. The overall result is a negative image of the mask pattern.

### How we Apply

Spin-coating is the most common coating technique for resists and is used here due to its ability to allow for very smooth and homogeneous resist films. The attained resist film thickness goes with the reciprocal square root of the spin speed and thus is adjustable in a certain range for each resist. However, since the edge bead becomes more pronounced towards low spin speeds, for attaining thick films it is recommended to use highly viscous resists as well as suited (i.e. not extremely low) spin profiles. Alternative coating methods such as spray coating are occasionally used for arbitrary shaped and textured substrates or dip coating for larger, rectangular shaped substrates with demand for minimum resist consumption per coated area.

### Stripping Tips

After the imaged wafer has been pattern transferred the remaining photoresist must be removed. There are two classes of resist stripping techniques: wet stripping using organic or inorganic solutions, and dry (plasma) stripping.

Common organic stripping procedures utilize acetone and isopropanol. Although commonly used, solvents tend to disrupt the deposited

molecular material through side penetration causing structural decomposition and/or swelling. Moreover the high possibility for residues on the wafer are turning the method unacceptable for molecule-involving processing.

A viable alternative is to follow a wet strip by a plasma etching step to completely clean the wafer of resist residues while avoiding penetration of solvent in the sensitive molecular parts at final stages of the stack's side-walls exposure. Oxygen plasma is the method of choice since it is highly reactive toward organic polymers [22] but leaves most inorganic materials under the photoresist untouched.

The process details of resist application are the following:

(1) Surface Preparation/Cleaning,

(2) Coating (via spin casting),

(3) Pre-Bake (Soft Bake, Used to evaporate the coating solvent and to densify the resist after spin coating. Typical thermal cycles: 90 – $100^oC$, 20 min in a convection oven,

(4) Performation of Mask alignment and Expose of resist to UV light,

(5) Development of sample,

(6) Post-Bake (Hard Bake, Used to stabilize and harden the developed photoresist prior to processing steps that the resist will mask. Main parameter is the plastic flow or glass transition temperature. Post-bake removes any remaining traces of the coating solvent or developer and eliminates the solvent burst effects in vacuum processing. Longer or hotter postbake makes resist removal much more difficult),

(7) Processing Using the shaped Photoresist as a Masking Film,

(8) Stripping/ Cleaning (With the final stripping being oxygen plasma etching).

**Photomask & Aligner**

Photomasks are high precision plates containing microscopic images of electronic circuits. They are made from very flat pieces of quartz or glass with a layer of chrome on one side. Etched in the chrome is a portion of the electronic circuit design to be developed.

Photomasks are generally manufactured using four main types of material: quartz (most common/expensive), LE, soda lime, and white crown.

The utilized mask aligner is a projection Perkin-Elmer Micralign aligner. Mask image is projected a distance from the mask and demagnified to a smaller image: 1:4-1:10 magnification.

Advantages: It can be quite high resolution (~0.07 $\mu$m or better), circumvention of mask contact results in almost no mask wear and mask defects or particles on mask are reduced in size on the wafer.

Disadvantages: Expensive and complicated equipment while diffraction effects can limit the accuracy of pattern transfer.

### Developer etchants

Wet chemical etching requires an optimized adhesion to the substrate. For this purpose, standard aqueous basic solution formulated with an organic amine (aqueous Tetramethylammonium hydroxide (TMAH) solution 0.26 N) diluted at least 100 times with deionized water is used as a developer (AZ resist etchant).

TMAH is also a silicon etchant, so development times should be kept with care in order to avoid undesired etching of substrate. HF-containing etchants sometimes cause large-scale resist peeling as a consequence of HF-diffusion through the resist towards the substrate underneath. In this case, its generally beneficial to increase the resist film thickness via using lower dilution.

Lift-off processes recommend an undercut resist profile which can be attained with image reversal resists or negative resists. Additionally, these resists are thermally stable and therefore help to prevent a rounding of the resist structures during coating.

If the mask design requires positive resists for lift-off application, the resist sidewalls should be as steep as possible in order to prevent a coating of these sidewalls. For this purpose thermally stable resists like AZ 6600 resists, or the high-resolution AZ 701 MiR are often used.

A T-shaped profile can be achieved by the following process sequence: The prebaked AZ 5214E photoresist is flood exposed (no mask) with a small amount of UV energy, just to generate some exposed PAC at the surface. Now the reversal-bake is performed to partially crosslink this top areas. By this treatment a top layer with a lowered dissolution rate compared to the bulk material is generated.

After this the resist is treated like a normal positive photoresist (imagewise exposure and development) to generate a positive image! Due to the lower dissolution rate in the top layer a T-shaped profile with overhanging lips will be the result.

#### Developing light wavelength

The most important light types include UV, DUV (Deep UV), and the g and I lines having wavelength of 436 nm and 365 nm respectively of a mercury-vapor lamp. This particular parameter is closely related to the thickness of the applied photoresist, with thinner layers corresponding to shorter wavelengths, permitting a reduced aspect ratio and a reduced minimum feature size. This is important in microelectronics and especially the ITRS reduction in minimum feature size.

### 1.3.2 E-beam lithography

#### A High-Precision Tool for Non-Conventional Device Architectures

In the case where lab-grade emerging technology devices are involved it is often the case that materials that are not always appropriate for processing in C-MOS-dedicated infrastructure. It is also a frequent occurrence that the feature resolution desirable for such apps requires precision lithography, but without the need for large scale production (when still in the R&D stage). For such cases electron-beam lithography (often abbreviated as e-beam lithography) is the tool of choice.

The method utilizes a focused beam of electrons to draw custom shapes on a surface covered with an electron-sensitive film (resist). Similarly to UV-lithography the electron beam alters the solubility of the resist, enabling selective removal of either the exposed or non-exposed regions of the resist by immersing it in a solvent. The interested reader can find more about electron beam lithography and the patterning of nanostructures in a plethora of textbooks. I will indicatively cite here the handbook of Wiederrecht [23]. The primary advantage of electron-beam lithography is the formation of direct-write custom patterns (maskless lithography) with sub-10 nm resolution.

#### The Importance of the Resist

The polymer most commonly used as e-beam resist, and also used for the lithographies of this work, is Poly (methyl methacrylate) (PMMA). The significance of the resist and its handling can be understood from the fact that the ultimate resolution of electron beam lithography is not set by the resolution of electron optical systems, which can approach 0.1 nm, but by the resolution of the resist (determined among others by forward scattering and secondary electron travel in the resist) and by the subsequent fabrication process [24] involving resist stripping and/or lift-off and so on.

The forward scattering can be decreased by using higher energy electrons or thinner resist, but the generation of secondary electrons is inevitable. The use of double patterning allowed the spacing between features to be wide enough for the secondary electron scattering to be significantly reduced.

As a measure of electron blur, electrons with energy 50-100 eV easily penetrate beyond 10 nm of resist thickness (PMMA or commercial resist) causing charge build-up and, in prolonged exposures, dielectric breakdown discharge [25].

### Nano-electrode Fabrication

In order to address nanostructured objects, such as the hybrid networks discussed in Chapter 6 on plane, nano-electrodes with few nm separation are necessary. In order to produce comparable platforms of low variability and enable investigation of electrode gap dependence methods like break junctions were avoided and EBL was utilized instead. Topographies and the basic process steps are summarized in Fig.1.4.

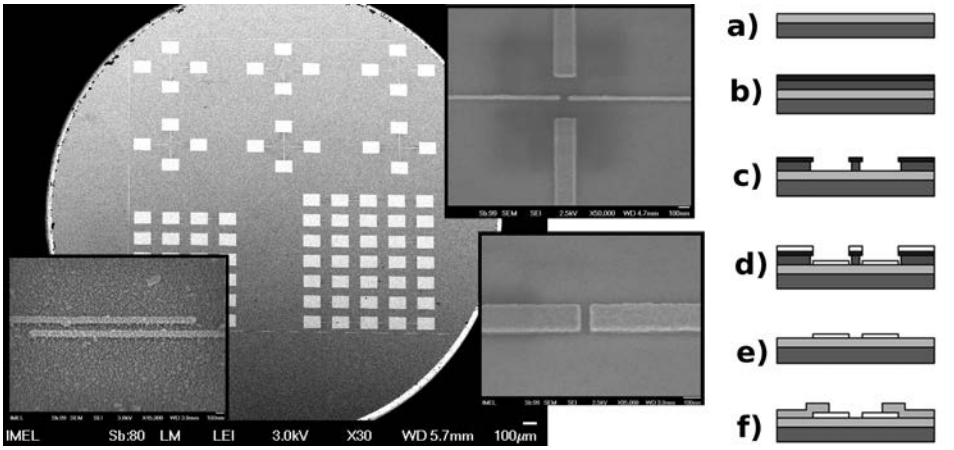


Figure 1.4: SEM micrographs of the EBL-fabricated nanoelectrode-bearing chip and magnifications of the different contact pairs. On the right: a schematic overview of the EBL nano-electrode fabrication process: a) Substrate, b) PMMA bi-layer resist spin-on, c) exposure and development, d) evaporation of metal, e) lift-off, and f) contacting pads fabricated with standard photolithography on top.

Two different high resolution positive electron beam resist layers based on PMMA with different sensitivity to electron irradiation were employed in order to obtain an undercut profile, which is necessary for the subsequent lift-off process.

### 1.3.3 Self-assembly as a molecule manipulation technique

#### Added Value

Nature itself has chosen the self-assembly route for building highly organized structures and organisms. This is partly because it provides an evolutionary path to complexity, and partly because its inherent modularity means structures can be created, disassembled, and their building blocks reused with low energetic cost [26].

A long-term goal of molecular electronics is to borrow nature's methods in order to build complex circuits or other electronically active units by molecular self-assembly from solution. Because the components are in a minimum energy configuration and often align with atomic precision, self-assembled devices should be more robust and reproducible than devices made by traditional approaches.

They can be biocompatible and chemically responsive, and they use much less power because the transfer of only one or a few electrons is often enough to cause the desired effect. They can be designed to work massively in parallel, and can be much less expensive to produce. Finally, self-assembled structures can bridge between the length scales accessible by covalent synthesis (up to a few nm) and by top-down patterning (down to tens of nm).

Self-assembly can be driven by a number of forces, including hydrogen and metal-ligand bonding, electrostatics, charge transfer, van der Waals attractions, hydrophobic interactions, and pi-stacking. This last type of interaction describes the weak bonding between planes such as layers of graphite or the rungs in the helical DNA ladder. Usually, some sort of trigger is necessary to drive the self-assembly forward, such as a change in the concentration, temperature, pH, light, or the ionic strength or polarity of the solution [27].

#### Forms of Assembly Utilized to Obtain Different Organization Levels within a Single Device

In this work I will commend on the use of molecules that are ionized to end up with a positively or a negatively charged center, in polar solvents. These molecules will be alternated (i.e. first positive then negative) to interact and form thin film structures (see LbL nanofabrication [28]). According to its functional groups and structure as a whole, each molecule is assembled driven by various types of intermolecular forces (ion-dipole and ion-induced dipole forces, covalent bonding, Van der Waals forces, elecrostatic attraction/repulsion, hydrogen bonding). They are occasionally post-modified after deposition in order to establish the appropriate

bonding type with the substrate, i.e. they are post annealed in order to obtain silanization, thus covalent, bonding with the substrate or just rinsed to remove weakly physisorbed entities.

Another self-assembly technique is applied on uniquely charged highly symmetric molecules isolated in solution. These molecules, under appropriate control of the quantity of counterbalancing ions in sol (here via pH control), self-organize to lower the total free energy of the system (molecules plus solution): Symmetry-matched interactions and complex electrostatic and Van der Waals forces interaction between molecules and their clusters [29, 30] lead to the nanocrystallization of these molecules in solution in a controllable manner. Electrostatic forces develop due to the reduction of POMs in the acidic medium and subsequent proton-mediated crystallization. At this stage the secondary structure of the heteropoly-acids is largely determined by hydrogen bonding of the polyoxometalate anions via water and hydrated proton species [29]. Attractive van der Waals forces between aggregates become appreciable when the POM units are in close proximity. This way higher density solutions involve formation of larger aggregates. Charge balancing cations (protons) control the extent of crystallization in solution and, finally, the solid state output [31]. Cation availability is directly affected by the pH (kept constant) and the diffusion constant (directly related to molarity) in the precursor solution. This implies that molarity can be used to tune the crystallization extent of POM nanocrystals (NCs) in solution. With this latter method we construct the molecular building blocks that are, subsequently, post-assembled with the first (LbL) method.

### 1.3.4 Fabrication of an integrated molecular cell

The fabrication process is C-MOS compatible and consists of standard photolithography on top of wet-oxidized n-type Si substrates which defined square patterns with edges ranging from 50 to 300 $\mu$m) that would act as the active device areas.

The process consists of the following steps:

(1) Cleaning the wafer with acetone ($(CH_3)_2CO$) and isopropanol ($C_3H_8O$). Acetone removes debris, photoresists and physisorbed organic impurities from the chip substrate, and is particularly apt for dissolving oily or greasy contaminants. However, due to its rapid evaporation, acetone alone would result in the partial redeposition of the dissolved impurities. This is prevented through the subsequent utilization of isopropanol, an excellent rinse agent for contaminated acetone that lifts and removes remnant particles.

(2) Piranha cleaning. Piranha is a mixture of sulfuric acid ($H_2SO_4$) and hydrogen peroxide ($H_2O_2$) used here in a mixture ratio of 1:1 (v/v) and applied for 15 min. It is used to clean organic residues off substrates as well as to remove alkali ions, heavy and transition metals in order to meet the requirements of high performance C-MOS devices. It is essential that the previous cleaning step precedes, as large amount of contaminant would cause violent bubbling and gas release, posing explosion risk. As the mixture is a particularly strong oxidizing agent, it removes most organic matter, and also hydroxylates most surfaces (adds -OH groups), making them highly hydrophilic (water compatible). The etched wafer is cleaned thoroughly with deionized water.

(3) Oxidation of the wafer under the presence of $H_2O$ vapor. $N_2$ steam with a volumetric flow rate of 3.5 standard liters per minute (slm) under standard chamber environment conditions (1 atm, $20^0C$) is directed trough the $H_2O$ vapors creating a flow of $H_2O$ vapor just above the wafer surface. The substrate is heated at a temperature of $1050^oC$. The oxide growth is realized via the following reaction:

$$Si + 2H_2O \rightarrow SiO_2 + 2H_2(g)$$

A 500-nm-thick wet thermal oxide layer is created on top, as depicted in Fig.1.6a.

(4) Positive resist photolithography for the definition of the capacitor's active region (Fig.1.6d). The resist used here is AZ image reversal resist, processed as normal positive photoresists (see Subs. 1.3.1).

(5) BHF etching of exposed area and creation of the central cavity (Fig.1.6e).

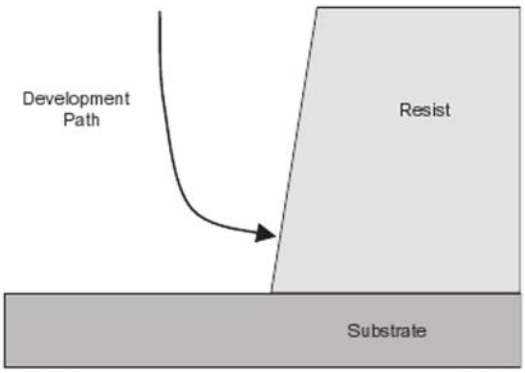


Figure 1.5: Typical wet etching profile

The actual profile can be seen in Fig.1.5. At this stage non-perpendicular side walls are desirable, since they prohibit shadowing of the active region during subsequent deposition steps, while facilitating upcoming wet processes.

(6) Repetition of cleaning steps 1, 2.

(7) HF last process. In this step Hydrofluoric acid (HF 2%) is applied on the wafer in order to remove the native oxide along with a monolayer of Si, forming gaseous or water-soluble silicon fluorides through the following reactions:

$SiO_2 + 4HF \rightarrow SiF_4(g) + 2H_2O$

$SiO_2 + 6HF \rightarrow H_2SiF_6 + 2H_2O$

This process renders the wafer hydrophobic, making uniform hydrophobicity a safe measure of total native $SiO_2$ consumption. HF passivates the clean Si surface with a H termination monolayer, reducing organic pickup from air for several hours.

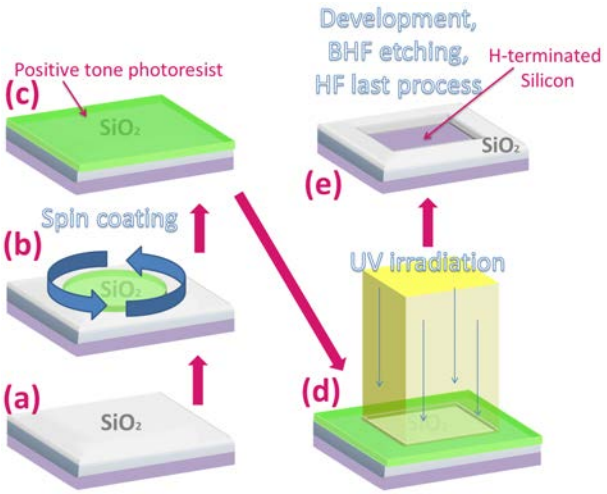


Figure 1.6: Processing steps 1-7

(8) Oxidation of the wafer under the presence of $O_2$ vapor. $O_2$ steam with a volumetric flow rate of 3.5 slm under standard chamber environment conditions is supplied right above the wafer surface while the substrate is heated at a temperature of $850^oC$. The oxide growth is realized via the following reaction:

$Si + O_2 \rightarrow SiO_2$

A 3.1-nm-thick dry thermal oxide layer is created on top, resulting in the structure appearing in Fig.1.7f.

(9) Application of the layer by layer self assembly process (LbL) on the exposed $SiO_2$ surface for the formation of the active molecular region. The process consists of hydrophilization of the oxide surface via the creation of -OH surface groups using mild oxygen plasma treatment (Power = 800 W, Pressure = 1.33 Pa, $O_2$ = 100 sccm, Bias = 0 V for 2.5 min). This highly hydrophilic surface is subsequently chemically modified via the silanization of the exposed O atoms resulting in the covalent bonding of the silane group of 3-aminopropyl-triethoxysilane (APTES) molecule with the deprotonated -OH groups.

APTES aqueous solution (2% v/v, pH 7) was deposited on the surface at full coverage and room temperature (RT) for 20 min, rinsed cautiously with de-ionized water, and dried under low pressure (2 bar) $N_2$ steam. Silanization of the $SiO_2$ substrate was obtained during thermal treatment at $120^oC$ for 20 min on hot plate covered with tin foil coated ceramic for uniform heating conditions. Heating activates the silanization reaction between the silane groups of strongly physisorbed APTES molecules and deprotonated surface -OH groups. The exposed amine groups are protonated in solution, forming a positively charge molecular template on the $SiO_2$ surface. What follows is the electrostatic assembly of reduced POM molecules in acidic solution which are negatively charged via the attachment of 1-3 electrons onto their framework. Their self-assembly is an interplay between repulsive (among them) and attractive (between them and the amine groups) electrostatic forces and can result in a great variety of nanomorphoogies as we will see later on. The preservation of highly acidic PH (0.5) is crucial in retaining the highly symmetric Keggin structure of the POM anions in the molecular assemblies. Finally an amine monomolecular film is applied on top, after the immobilization of POMs as a capping layer providing oxidation protection of the upcoming Al layer and electronic decoupling of POMs from the gate.

(10) 400 nm Al deposition on top via sputtering without substrate heating.

(11) Positive resist photolithography for the definition of capacitor gate electrodes.

(12) Al etching.

(13) In order to avoid further wet etching processes after the definition of the capacitive structures plasma etching is used. Liquid etchants can have a penetration depth comparable to the device lateral oxide dimensions and are, thus, avoided from now on. Oxygen plasma

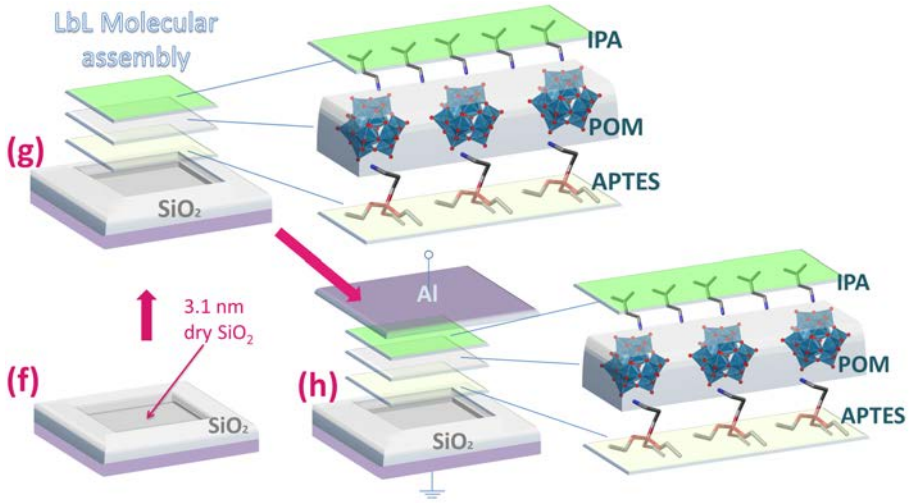


Figure 1.7: Processing steps 8-10

etching is used for the removal of native oxide on the back side of the wafer. During the process the sample is placed on grounded electrode under $O_2$ ambient (100 scc) and a 800 W plasma discharge is accelerated under application of 10 V voltage between the beam and the grounded sample. The whole process lasts around 10 min, or until the back surface becomes hydrophilic.

(14) Deposition of 400-nm-thick Al backgate on the plasma treated backside of the wafer.

The samples acquired a protective 3.5 nm-thick gate oxide by dry oxidation. N-O linked tungsten polyoxometalates on p- and n-type Phosphorous doped Silicon substrate were formed via electrostatic interaction of polyoxometalate anions with a single atomic layer of $H_2N(CH_2)_3Si(OC_2H_5)_3$ (APTES) cations. The APTES compound is used for chemical modification of the silicon substrate in order to ensure a chemically stable molecular layer. This way the POM monolayers were organized by the Layer by Layer method (LBL), via a SAM of 3-aminopropyltriethoxysilane (APTES) onto the active areas [28]. All samples were covered with a thick Al film and the contact pads were defined by a second lithographic step. This particular process ensured the encapsulation of the sensitive molecular layers and resulted in their longevity, robustness and high yields.

## 1.4 Characterization methods – Tips & Workarounds

### 1.4.1 UV-Vis absorption spectroscopy

Within the overall range of electromagnetic radiation UV- and VIS- occupy only a very narrow frequency region. Nevertheless, this range is of extreme importance for spectroscopy, since the energy differences falling into this regime correspond to those of the electronic states of atoms and molecules [32].

Moreover, under the framework of Mie theory, UV- and VIS-absorption spectroscopy can be used to determine particle size and size distribution of noble metal nanoparticles and characterize the kinetics of their formation as well as final colloid stability [33].

**TOPIC: Origin of Peak Broadening for molecules and NPs – Can it be Useful ?**

Since the energies of the orbitals involved in electronic transitions have fixed quantized values, one would expect that absorption peaks in ultraviolet/ visible spectroscopy should be sharp peaks.

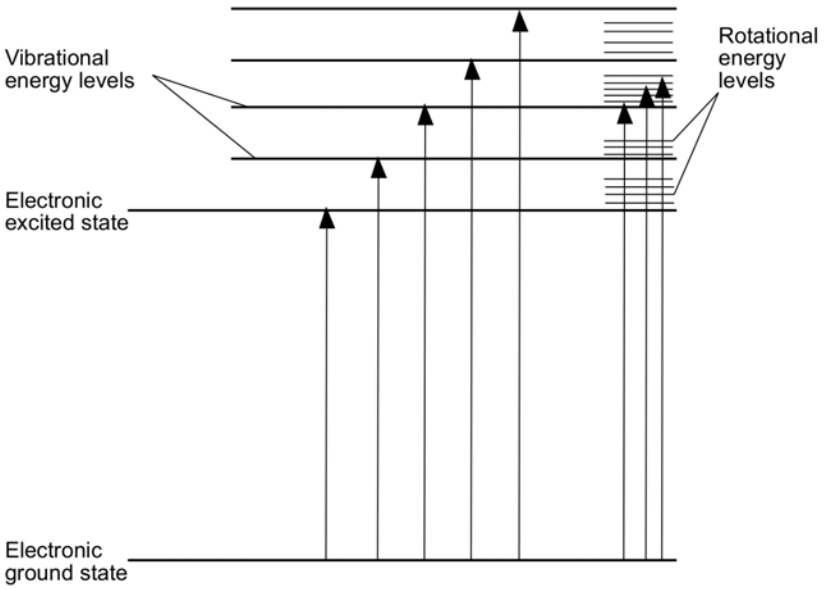


Figure 1.8: Electronic vibrational and rotational levels in UV-Vis transitions

However, this is rarely the case and broad absorption peaks are observed instead. This is because a number of vibrational energy levels are

available at each electronic energy level, and transitions can occur to and from the different vibrational levels as well resulting in peak broadening. This is further complicated by the presence of rotational energy levels in absorbing materials (Fig.1.8). The energy scales of the corresponding level differences are $\sim 100 kJmol^{-1}$ for transitions between electronic levels, $\sim 1 kJmol^{-1}$ for vibrational levels and $\sim 0.01 kJmol^{-1}$ for rotational levels [34].

In the case of noble metal NPs there is a relationship between the optical absorption spectrum caused by surface plasmon absorption, in particular the plasmon resonance (coherent excitation of all the 'free electrons within the conduction band) frequency and its broadening and their sizes. When particles aggregate the conduction electrons near each particle surface become delocalized and are shared amongst neighboring particles. When this occurs, the surface plasmon resonance shifts to lower energies, causing the absorption and scattering peaks to red-shift to longer wavelengths.

As the particles destabilize, the original extinction peak will decrease in intensity (due to depletion of stable nanoparticles), and often the peak will broaden or a secondary peak will form at longer wavelengths (due to aggregate formation).

Molecules adsorbed on noble nanoparticles will also cause a pronounced broadening and damping of the surface plasmon resonance [35].

The interested reader can find the basic principles of the method as well as advanced measurement and analysis methods in various textbooks as well as in [32].

### 1.4.2 FT-IR reflectance spectroscopy

IR spectroscopy is utilized to identify chemical compounds and structure because molecular bonds and functional groups give rise to characteristic IR bands in terms of both intensity and frequency.

The absorptions are resonant frequencies, characteristic of the bonds or groups that vibrate. The energies match the shape of the molecular potential energy surfaces, the masses of atoms, and the associated vibronic coupling.

In order for a vibrational mode in a molecule to be "IR active", it must be associated with changes in the dipole moment, not necessarily involving permanent dipoles [36].

#### TOPIC: Practices for Signal to Noise Ratio Improvement

One of the major advantages FTIRs enjoy over other infrared spectrometers is the ability to measure spectra with high signal-to-noise ratios due

to their throughput (Jacquinot) advantage [37]. The amount of signal in a spectrum depends upon the amount of light hitting the detector; the more light the better. Throughput is a measure of the amount of light from the source that makes it to the detector.

In an FTIR the infrared beam does not pass through a prism, grating, or slit (in the traditional sense) to achieve resolution, as in non-FTIRs (dispersive) spectrometers. Thus, a high-intensity infrared beam impinges on the detector increasing the signal level. Therefore, you get much higher throughput with an FTIR than you do with a dispersive instrument.

A second advantage of FTIRs is the multiplex (Fellgett) advantage. Owing to its interferometric principle, in FTIR all wavenumbers are observed at once. The Signal to Noise Ratio (SNR) of a spectral region is proportional to the square root of the amount of time (t) spent observing the intensity of light in that region. This gives [37]:

$$SNR \propto t^{1/2} \tag{1.3}$$

Where SNR =Signal-to-Noise Ratio and t =Observation time determined by the number of scans added together. So, there is a relationship between the number of scans used to measure a spectrum (N) and observation time. Since N is proportional to time we can rewrite Equation 1.9 as follows:

$$SNR \propto N^{1/2} \tag{1.4}$$

This consists the practical expression of the multiplex advantage, and it tells us that adding more scans together is a way of improving the SNR of a spectrum measured with an FTIR. For example, a spectrum measured using 100 scans, the square root of which is 10, will have a ten times better SNR than a spectrum measured with only one scan. Thus, increasing the number of scans used to measure a spectrum is a convenient and straightforward way of improving spectral quality.

Since, however, more scans require extra acquisition time, one should take this in mind when planning the scan duration in cases of non-steady ambient conditions like time-varying $H_2$, $H_2O$ and $CO_2$ content.

A third advantage FTIRs enjoy over other infrared spectrometers is wavenumber precision [37], with spectral resolution being determined by the maximum achievable value of optical path difference in the interferometer. This allows wavenumbers to be determined with precision of the order of $\pm 0.5 cm^{-1}$.

When the resolution level is increased (via utilization of a narrower aperture) light intensity drops. This results in the apparent level of noise increasing by an amount corresponding to the decrease in light intensity;

so, with a high-resolution measurement, it is necessary to set a sufficiently high number of integrations to obtain clear spectra.

### 1.4.3 Photoluminescence

Luminescence denotes the emission of radiation by a solid in excess of the amount emitted in thermal equilibrium. It is a non-equilibrium phenomenon excited by light, electron beams, current injection, etc.

Processes competing with luminescence are: radiative transfer to another ion and non-radiative transfer (multiphonon relaxation and energy transfer between different ions or ions of similar nature) [38].

Speaking in terms of materials, photoluminescence (PL) can either originate from relatively large-scale inorganic materials, mainly exhibiting phosphorescence, or smaller dye molecules and small-particle inorganic nanomaterials, which can either fluoresce or phosphoresce.

In general, fluorescence is a "fast" process (ns time scale), while phosphorescence is "slow" (longer time scale, up to hours or even days).

#### TOPIC: Exploitable Photoluminescence Processes in the Case of Subgap Excitation Energies

Typically, the laser wavelengths utilized to produce photoluminescence in the case of materials with bandgap correspond to energies larger than the gap.

Nevertheless, excitons pumped just within the optical gap can also decay by luminescence and can be excited resonantly to provide useful information regarding the different mechanisms contributing to a general broad (non-resonant) photoluminescence band [39].

In general, using energies less than the band gap selectively excites the internal defects rather than the material itself. The resulting excitons are self-localized, giving a clear fingerprint of their intragap energy and type.

Owing to the aforementioned localization of carriers [40], certain defects are more efficiently excited by particular laser wavelengths. For example, most PL peaks of diamond in the 900-1000 nm range are more intense when activated by a 785 or 830 nm laser than by a 325 nm laser [41]. Hence, PL spectra using lasers of appropriate wavelength can enhance the collected information.

Localized oxygen vacancies and oxygen interstitials, which are of interest for the oxides utilized in this work, have been known to emit in the visible part of the spectrum when excited, owning to the provision of alternate paths for the photo-induced carrier generation and recombination,

leaving their fingerprint on both PL and photoabsorption characteristics [42, 43, 44].

Disorder can also lead to localization of carriers and, hence, drastically increase the photoluminescence life times as localized carriers cannot as easily find nonradiative recombination centers as can free ones.

Hence, sub-gap energy (wavelength) lasers can become a useful tool of approaching weakly luminescent localized defects.

### 1.4.4 Spectroscopic ellipsometry

Ellipsometry is a standard optical technique for measuring the complex dielectric function or the complex optical constants $\mathbf{n} + i\mathbf{k}$ of bulk materials and thin films. It monitors the change of light polarization upon reflection or transmission and fits it according to a specified model [38].

The incident beam of polarized light reflects and refracts at each interface of the encountering material/film stack of incidence, leading to multiple beams in a thin film. Interference between beams depends on relative phase and amplitude of the electric fields. Fresnel refection and transmission coefficients can be used to calculate the response from each contributing beam.

Each film's optical parameters are calculated via fitting of the acquired relative phase ($\Psi$) and relative amplitude ($\Delta$) spectroscopic values (relative phase and amplitude of the parallel and perpendicular component of the reflected wave, expressing the state of polarization of the light as it is reflected from the sample). In this work the assumptions of an isotropic and non-depolarizing sample were made.

It is also applied to characterize composition, crystallinity, roughness, doping concentration, electrical conductivity and other material properties associated with a change in optical response.

#### TOPIC: Determining the Thickness of Ultrathin Absorbing Films

Absorbing films, such as POMs, are more difficult to characterize because the absorbing region must account for both real and imaginary (absorption-related) optical constants increasing the problem's free parameters, while the optical constants (n and k) are often correlated with film thickness. This calls into question the uniqueness of the results, especially for very thin coatings.

One approach to resolving the problem of non-unique solution to the $\epsilon_1$, $\epsilon_2$ and thickness determination for ultra-thin films [45], such as the POM molecular layers, is to obtain further data by varying a system parameter.

It has been here chosen to modify the thickness of the molecular layer slightly between two samples ensuring they still posses common dielectric function, as monitored via the shape parameters, onset and peak energy of the main absorption peaks and the absorption coefficient. This technique would in principle allow multiple samples to be fit simultaneously with some of the fit parameters common to all samples (in this case the diel. function) and other fit parameters (here thickness) allowed to vary between points.

In order to retrieve the shared dielectric function and different thicknesses of films the multiple sample analysis mode of WVase software for SE [46] is applied and the molecules response function is modeled with appropriate (type, amplitude, broadening, and center energy) oscillators with respect to its optical absorption spectrum. Kramers-Kronig consistency is then used to calculate the shape of the real component after the imaginary behavior is described by the oscillator. Iterative non-linear regression should result in convergence of the fitting.

### 1.4.5 UPS, XPS photoelectron spectroscopy

X-ray photoelectron spectroscopy (XPS) is a surface-sensitive quantitative spectroscopic technique that measures elemental composition, empirical formula, chemical and electronic state of the elements within a material.

A source of soft X-rays (in this work the unmonochromatized Mg Ka line at 1253.6 eV) is being used to remove core electrons and evaluate the kinetic energy and number of those that escape from the top 1 to 10 nm of the material being analyzed.

Far ultraviolet radiation, on the other hand, suffices to remove valence electrons (using here the He I (21.2 eV) excitation line) from atoms and molecules and is used in the technique known as Ultraviolet Photoelectron Spectroscopy (UPS). UPS measures the kinetic energy spectra of photoelectrons emitted by the outer 1-5 nm of entities that have absorbed ultraviolet photons, in order to determine orbital energies in the valence region.

Although XPS can sample both valence and core electrons, the photon energy used in UPS is more closely matched to the valence electrons' binding energy and is, thus, far more sensitive to the valence region [47].

#### TOPIC: Fermi level alignment in the case of ultra-thin materials

Traditionally, the determination of the Fermi level and work function is performed through UPS. To accurately elucidate the Fermi level alignment in the case of ultra-thin materials, a combined technique of work function measurement by monitoring secondary electron cutoff with both

UPS and XPS core-level measurements can be proven extremely useful [48, 49].

The poor spectral resolution of X-rays in the low energy region of valence bands cannot provide a detailed view of the band com- ponents. This is why UPS is commonly used for workfunction estimation.

Nevertheless, with XPS we can occasionally observe striking shifts of the cut-off energy even when ultrathin molecular layers are deposited, a fact not always observed in the respective UPS spectra.

The above response can be, for example, related to the photo-sensitivity of molecular matter in the UPS-probed energy window. This photo-sensitivity of certain films can hinder the impact of non photosensitive ultrathin films in their vicinity. Nevertheless, the combination of the two techniques can help resolve such issues.

### 1.4.6 Scanning tunneling microscopy

Scanning tunneling microscopy (STM) provides a means to "see" individual atoms and to visualize the physics of their interactions.

An atomically sharp tip is brought in close proximity to the sample until, under voltage application, a current of typically 1 nA is detected. This signifies the initiation of electron tunneling through the medium separating the tip-sample system.

The tip can be subsequently raster scanned at a constant current over the sample surface to produce atomic resolution images. The tip is attached to piezoelectric crystals which, utilizing electronic feedback control, can position the tip precisely relative to the sample beneath it.

#### Constant Current Maps

In this technique the tip is ordinarily kept between 5 and 15 Å away from the sample (measuring the distance from the nucleus of the apex atom of the tip to the nucleus of the sample atom). Typically, the tunneling currents are in the nanoampere range (0.1-5 nA) and the voltage applied across the barrier ranges from 10 mV to 10 V. Equi-current contours are generally the contours of constant tip-sample interaction strength [50].

The tunneling current depends on the density of states of the tip (assumed constant if metallic) and that of the sample. This can be well-visualized in the framework established by Bardeen for the case of independent tip-sample densities of states. The one-dimensional tunneling process is then described by [51]:

$$I = \frac{4\pi e}{\hbar} \int_0^{eV} \{f(E-eV) - f(E)\} \cdot \rho_{SAMPLE}(E) \cdot \rho_{TIP}(E-eV) \cdot |M|^2 \cdot dE \quad (1.5)$$

V is the applied sample-tip voltage. M is the tunneling matrix describing how the barrier affects the tunneling process. f(E) is the Fermi distribution of electronic states at a given energy and $\rho(E)$ represents the LDOS in the tip or the sample at a given energy.

Another approach, known as the scattering approach, involves solving the Schrödinger equation by matching an incoming wave with a reflected and a transmitted one. The current is obtained by adding the transmission probabilities of the relevant incoming waves. Simmons (1963) solved this problem in one dimension assuming the WKB approximation and a free electron metal [52].

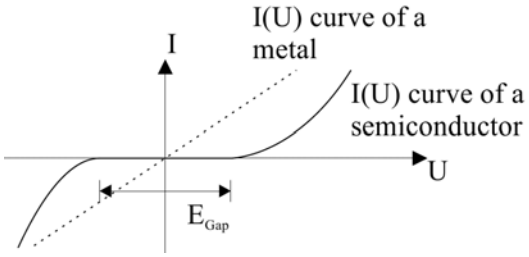


Figure 1.9: I-V spectra of a semiconductor contrasted to a metal.

### Approximations

For a metallic tip with relatively flat density of states near the Fermi energy ($E_{Fermi}$), the density of states of the tip can be approximated as a constant over energy, enabling its removal from the integral.

For small bias voltage ($eV << \phi$ and $eV << E_{Fermi}$) the tunneling matrix, M, is the direct overlap of the wavefunctions of tip and sample and can be approximated as constant over energy, enabling its removal from the integral.

Within the WKB approximation the tunneling matrix can be simplified to a dependence only on the width of the barrier. The current is then proportional to the integral of the LDOS and Fermi distribution of the sample at a given barrier width, given by:

$$I \propto \frac{4\pi e}{\hbar} \int_0^{eV} \{f(E - eV) - f(E)\} \cdot \rho_{SAMPLE}(E) \cdot dE \tag{1.6}$$

### Local Density of States

The tunneling current decays exponentially with the sample-tip distance and is strongly affected by the DOS of the sample at the Fermi level,

$p_{SAMPLE}$ ($E_{FERMI}$). The ability to characterize the local density of states is employed in the scanning tunneling spectroscopy (STS) mode. By keeping the tip location fixed and varying the tip-sample bias a complete characteristic of LDOS close to the Fermi energy can be obtained.

Differentiating 1.6 and normalizing the derivative of the signal we get rid of the tunneling matrix, M, and the tip characteristics and, provided that the assumptions made hold the result is mostly dependent on the local density of states of the sample:

$$\frac{dI/dV}{I/V}(V) \propto \rho_{SAMPLE}(eV) \tag{1.7}$$

The (dI/dV)/(I/V) is a typically used quantity, derived in this work via numerical integration of the I/V curves. Note that the assumptions made prevent the extraction of absolute LDOS values [53].

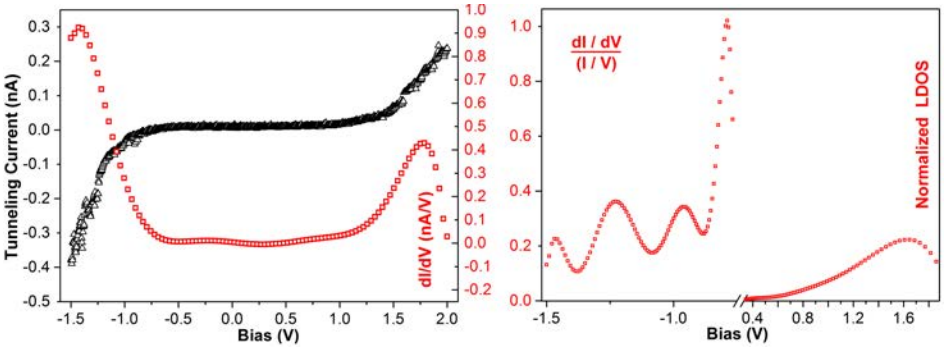


Figure 1.10: Local density of states and normalized local density of states spectra of a semiconducting POM molecular epilayer on $SiO_2$ on Si (n++). Bonding states detected in the LDOS spectrum correspond non-linear I-Vs at the respective applied voltages.

### Vibrational Modes

Inelastic tunneling, typically caused by molecules adsorbed on the surface and scattering of tunneling electrons can excite molecular vibrations similar to infrared spectroscopy data and can be therefore obtained from STS data [53].

If a vibrational mode with energy $\hbar\omega$ is excited during STS spectrum acquisition, a small conductance change can be observed in dI/dV characteristic at voltage $\hbar\omega/e$. This effect is even more pronounced for the second derivative of the I/V characteristics, i.e. for $d^2I/dV^2$.

This method has been proven to offer the possibility of chemically resolving different light molecules, often of organic character. However,

for real chemical identification, specialized equipment is often necessary, including a lock-in based hardware support for obtaining the derivative signal and an increased range of energies of electrons used for tunneling [53].

**TOPIC: Obtaining an Image of Molecular Arrangements under Ambient Conditions**

Having dimensions of the order of few Å and electronic properties strongly characterized by localized electron states, molecular monolayers are typically imaged under UHV conditions. Surface contamination and moisture interference on conductivity would otherwise significantly disturb the obtained image, if any.

Moreover, capillary forces due to adsorbed $H_2O$ would result in the decoupling of the tip from the surface as the excess conductance monitored from the feedback loop during scan is interpreted as peak on the surface profile followed by detraction of the tip.

Nevertheless, if one is forced to use ambient STM either due to equipment restrictions of due to the resemblance of the obtained characteristics to the actual device response, this problem should be overcome.

One solution would be to create an inert atmosphere inside the STM hood such that the $H_2O$ content on the surface would significantly diminish. In practice a 2 bar $N_2$ overpressure inside the hood after a 15 min $N_2$ flow is enough for a clear image to be obtained.

### 1.4.7 Atomic force microscopy

Atomic force microscopy (AFM) is a force feedback technique [54] (in contrast to STM which utilizes current feedback) for preserving constant tip-sample distance and obtaining a surface topography.

**Ambient Imaging & The Effect of Humidity**

Ambient conditions imaging comes along with the observation of effects of capillary forces. Such forces could have a detrimental effect in the case of a surface-sensitive force feedback technique like AFM (this not being the case for specialized high throughput techniques like immersion AFM [55]). Even for very small relative humidity, a thin water layer is adsorbed on hydrophilic surfaces. Water layers were reported for humidities in the range of 10%. Above $\sim$ 15% droplets are already forming and for even higher humidities a continuous film is formed (depending on sample hydrophobicity), with a thickness around 10-12 nm for 50% relative humidity [54].

Capillary forces can be relatively high and if cantilevers with smaller stiffnesses are used (below 1 N/m) they can be higher than the spring force coming from cantilever, which certainly affects AFM imaging [54].

The problem is addressed in this work via:

(1) utilization of tapping (and not contact) AFM mode,

(2) the utilization of an ultra-high resolution diamond-like carbon tip (curvature radius 1-3nm which besides increasing resolution constrains capillary interactions on a smaller area) ,

(3) with a typical force constant of 11.5 N/m for the tip (outbalancing capillary forces),

(4) with Au reflective side which is superior than Al or Ag in the utilized laser window (620-680 nm), thus, permitting slightly larger working distances and weakened capillary forces,

(5) with a 2 bar $N_2$ overpressure inside the hood in order to reduce $H_2O$ concentration inside the working area.

**Fractal Analysis of AFM topographies**

Traditional roughness parameters obtained via AFM topography, such as the average rms roughness ($R_q$) are limited to information on merely the "vertical" magnitude of the roughness without providing any insight of the spatial complexity of surfaces or profiles [56].

Valuable information regarding complexity, hidden symmetries, correlations between structures, and quantitative information regarding the physical mechanisms and kinetics of the methods used for growth are not pictured in $R_q$.

Fractal analysis, on the other hand, is capable of providing an insight to all these questions. Fractal geometry suggests that most surfaces obey, at least up to some scale regime, the fractal self-affine symmetry, i.e. they remain statistically invariant under anisotropic scale transformations [57].

The parameter quantifying this symmetry is the fractal dimension ($d_F$), which indicates the relative contribution of high frequency surface fluctuations to the total roughness [58].

The connection of a profile h(x) with the concept of fractal self-affine symmetry comes from its remaining invariant under anisotropic scaling transformations of the form:

$$h(x) = b^{-\alpha} h(bx) \tag{1.8}$$

with b being the scaling factor and the exponent $\alpha$ indicating the anisotropy of the transformation.

This power law dependence is transferred to the dependence of the rms value of the height profile, $R_q$, on its horizontal length, L, as [58]:

$$R_q(L) \sim \left\{ \begin{array}{ll} L^{\alpha}, & \text{for } L \leq L_{correlation} \\ R_q, & \text{for } L > L_{correlation} \end{array} \right\}$$

The exponent $\alpha$ defines the power law dependence of the rms value of the height fluctuations on the scale used for its measurement and is usually called roughness exponent. It is indicative of the "jaggedness" of the topography and signifies the relative contribution of high frequency fluctuations on roughness [59]. It is related to the box counting fractal dimension $d_F$ via $\alpha = 2\text{-}d_F$ for profiles and $\alpha = 3\text{-}d_F$ for surfaces [58].

The correlation length ($L_{correlation} = \xi$) is defined as the distance above which the normalized autocorrelation function becomes lower than 1/e. In practice, the dependence of rms value on the profile or surface size L is extended until $10\xi$ [60].

When speaking of real world surfaces, this fractal self-affine symmetry and the concomitant power law dependencies are limited to a finite regime with bottom limit determined by the molecular structure of film materials and upper limit related to the correlation length of the profile (i.e. $10 \times \xi$).

This is exactly the concept described with surface fractality in Chapter4. There, although at first sight thin film morphology appears to be random, a close analysis reveals regimes of correlated properties.

In fact, depending on the feature dimension which is parallel to the rough surface, the subsequently deposited molecular epilayer can be substrate-determined or structural unit self-determined. This dependency is quantified and described by the value of the fractal dimension, which means that fractal dimension controls the impact of roughness on the variability of the molecular epilayer features and, hence, final device performance [58, 61].

2-D AFM topographies are analyzed with a box counting algorithm and in case they are found to exhibit scale invariance, the algorithm converges and a computable $d_F$ is determined.

This, in the case of solution-deposited POM molecular entities is found to be indicative of the prevailing growth mechanism in sol. In this manner fractal analysis can be use as a sensitive post-growth non-destructive technique for the evaluation of the actual mechanisms that determine solid state structure.

Another way of probing structure correlations and thin film morphology is the autocorrelation function (ACF) [62]. Spatial autocorrelation

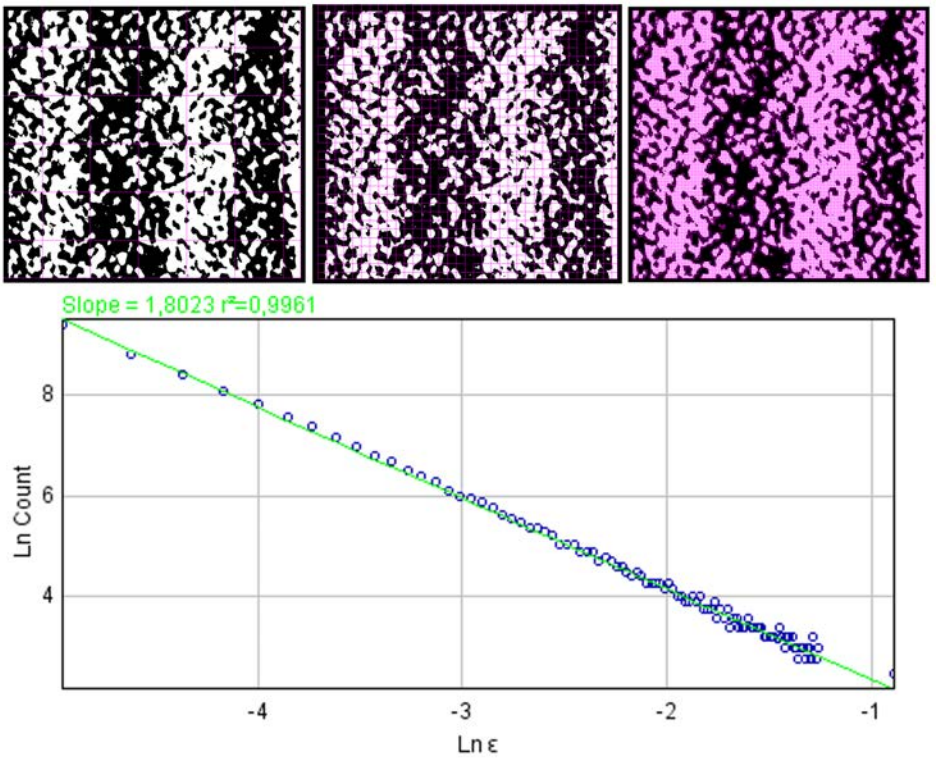


Figure 1.11: On top: Box counting process instances where series of grids of decreasing caliber (the pink boxes) are laid over the image. The counting process records how many of the boxes in each grid have part of the important detail of the image in them. In the image shown here, the important detail is the white pixels, which are on the unimportant black background. On bottom: Obtained logarithmic regression line for counts vs box size used to determine the fractal dimension for the examined topography.

measures the extent, to which the occurrence of an event (i.e. a profile peak) in a designated unit constrains, or makes more probable, the occurrence of an event in its neighboring unit.

As one can see in Fig.1.12, ACF provides qualitatively as well as quantitatively a morphological measure much more profound than the mere $R_q$ value.

The shape of ACF provides valuable information regarding the distribution of structural units on surface while the $L_{correlation}$ (correlation length) parameter, indicating the basic repeating pattern, if any, can be determined using the bottom right diagram. The parameter represents the length of correlation in a chosen direction on plane and corresponds

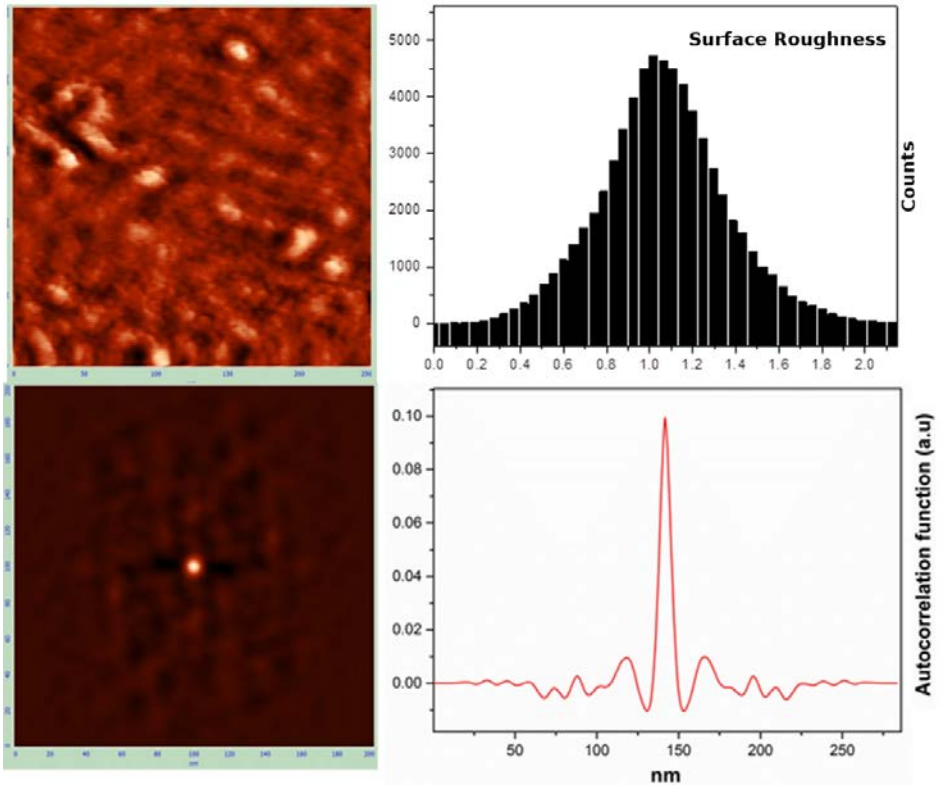


Figure 1.12: From top left, clockwise: Tapping mode obtained AFM topography of POM molecular hyperstructure on $SiO_2$, mean surface roughness distribution, 2-D autoccorelation function (ACF) and random line profile of the ACF function indicating surface isotropy.

to the value of the coordinate, at which the function decreases by e times.

In other words, the autocorrelation function can be used to detect non-randomness in surface data as well as to identify an appropriate space or time series model if the data are not random. In this respect it contains information also contained in $d_F$. However, the close interconnection of fractal dimension and thermodynamic growth conditions of films renders $d_F$ one of the most valuable surface measures for thin film analysis [59] when the physical drives of a specific structure formation are of concern.

### 1.4.8 Electrical Characterization Techniques for the Evaluation of Capacitive Memories & the Investigation of Active Charge-Trapping Sites

Electrical characterization techniques are used for both the evaluation of transport and charging mechanisms of an electronic device performing under voltage application and its evaluation as a memory cell.

They are core measurements in understanding the device physics, extracting modeling parameters [63] and getting real-operation feedback towards better engineering and re-design of devices [64].

Memory cell evaluation includes memory window determination, speed, retention and endurance, while transport/charging investigation includes interface, fixed and ionic charge determination, trap nature and lifetimes, conduction mechanisms evaluation according to I-V characteristics, extent of carrier localization and disorder quantification from I-Vs. The following refer to the evaluation of charge-trapping and floating gate non-volatile memories, where the active cell (charge-trapping medium or floating gate) is coupled to the control gate via capacitive coupling.

#### Memory Performance: Memory Window

The window of a memory device is the shift in the flat band (or threshold) voltage when the device switches after a bidirectional sweep or after appropriate pulse application from the "fresh" (neutral state) to a written state. For practically useful non-volatime memory (NVM) devices it is essential that the written information can also be erased and the device returns again in its neutral, uncharged state.

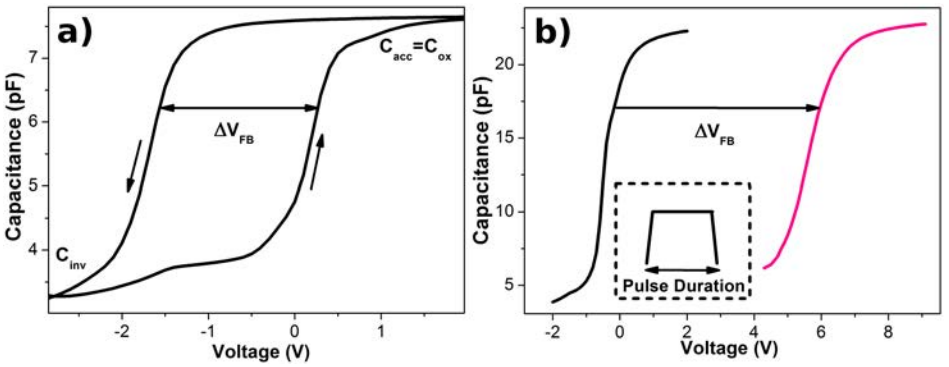


Figure 1.13: Memory windows along a double sweep (a) and after pulse application on gate (b).

In order to shed some light on the electron injection/trapping process

during programming operation, the incremental-step-pulse programming (ISPP) method was employed. More specifically, programming (positive) voltage pulses with constant increasing step height are successively applied on gate keeping the backgate grounded and the flat band voltage ($V_{FB}$) is measured between two successive pulses [65].

Fig.1.14a shows the programming memory windows obtained for MIS type capacitive cells after application of the ISPP method using square voltage pulses extracted with respect to the $V_{FB}$ of a virgin device.

### Memory Performance: Speed of Write/Erase Function

The write/erase speed of a memory device is the duration of the voltage pulse required for the device to switch to a written or erased state. For good NVM devices this time is usually less than 10 ms [63].

The technique applied in this work involves application of programming pulses of different widths (durations) to the gate of the device and measurement of the flat band voltage shift on the capacitive core when compared to the "fresh" state of the device (see Fig.1.14b).

Two typical responses of flat band voltage shifts vs applied pulse height diagrams for a 100 ms pulse are presented in Fig.1.14a.

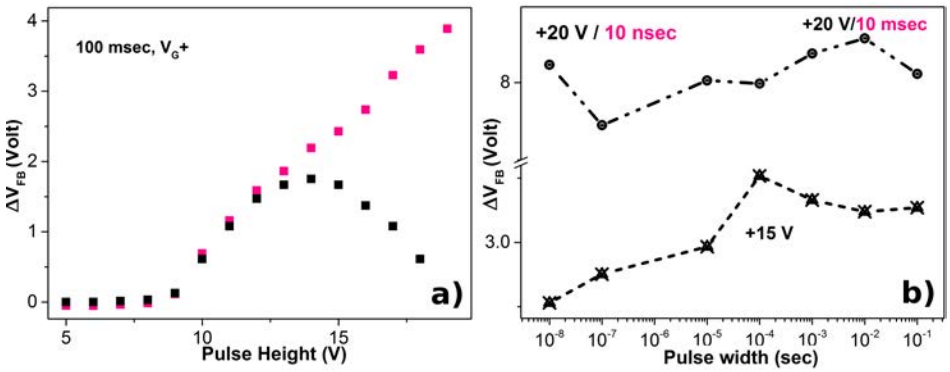


Figure 1.14: (a) Memory windows expressed as shift in the flat band voltage across the memory stack after 100 ms pulse application of varying amplitude on gate and (b) speed performance expressed as shift in the flat band voltage after after +20 V and +15 V pulse application of varying width on gate.

In the black curve we observe a memory window saturation for +14 V pulses, while in the pink curve case we have a continuously expanded memory window. This difference accounts on the presence of either a discrete trapping layer (first case) or an extended spatial distribution of trapping centers (second case) [61].

### Information Retention

Retention measurements test the ability of a non-volatile memory device to keep charge stored in the charge trapping layer for long periods of time.

A program pulse of a set width and amplitude is applied on gate and then the flat band voltage is measured after specified varying time intervals (usually the duration of time intervals is exponentially prolonged). The flat band voltage trend is then extrapolated up to the commercially imposed retention criterion of 10 years retention time.

For nm-size memory cells the stochastic character of the charging process manifests itself as a significant reduction of the retention time. The retention time distribution as calculated in [66] for various numbers of electrons per bit is presented in the right part of Fig.1.15.

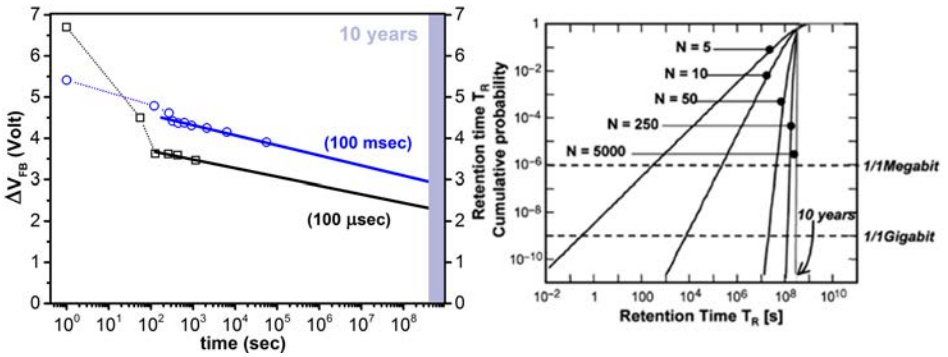


Figure 1.15: On the left: Retention characteristics of a MIS capacitive cell for two applied "write" pulses on gate and cumulative probability of retention time of memories with reducing number of electrons per bit on the right.

### Endurance under Multiple Cycles of Operation

Endurance is the parameter that specifies the cumulative program/erase (P/E) cycling capability of any individual sector within a device.

Each sector erase operation can possibly introduce defects into the memory cell structure, which may accumulate over time. At some point, these defects may even prevent a cell from programming, erasing or reading. When such a failure occurs in a cell that contains critical data, the loss of data may cause system failure. The sector in which the failure occurs is effectively the end-of-life.

Endurance is reported in terms of the number of P/E cycles. In practice, different blocks may undergo a different number of P/E cycles

based on the workload and Flash Translation Layer behavior.

Endurance usually refers to up to 5 years of activity. This 5-year service life allows examination of the impact of P/E cycles on endurance well before retention related reliability problems arise (the retention period of flash is 10-20 years [67]).

### High-frequency C-Vs

High frequency C-V profiling uses a metal-semiconductor (Schottky barrier) or a p-n junction [68] or a MOSFET to create a depletion region, a region empty of conducting electrons and holes, that may contain ionized donors and electrically active defects or traps. By varying the voltage applied to the junction it is possible to vary the depletion width. The dependence of the depletion width upon the applied voltage provides information on the semiconductor's internal characteristics, such as its doping profile and electrically active defect densities [69, 70]. Measurements are most typically done using both DC (giving the voltage step) and a small-signal AC signal [70, 71] in order to induce signal on a pick-up measuring coil.

High frequency capacitance-voltage characteristics determine the parameters of interface and near-interface traps, the fixed oxide charge, the mobile ionic charge and the oxide trapped charge, the effective oxide thickness and, based on complementary measurements, the actual oxide thickness or its dielectric constant, the semiconductor doping and fixed oxide charge. The technique details and all related equations can be found in [72, 73].

### Gp/$\omega$-f Characteristics

The conductance (Gp) method makes use of the investigation of frequency (f) dispersion of the conductance connected with the presence of interface traps. If the measured frequency range exceeds the reciprocal of the time constant of minority carriers at the surface of the semiconductor, i.e. exceeds a few Hz and if the series resistance of the capacitor equals zero, then the conductance of the structure can be attributed almost exclusively to the presence of interface traps. Therefore, one can expect that conductance measurements are more accurate than the capacitance methods as far as interface traps are concerned [74]

The contribution of bulk traps manifests itself in the state of the weak inversion. In that range this effect can limit the sensitivity of the method, although simultaneous measurement of high frequency capacitance makes it possible to isolate the origin of losses. When the losses

related to change of the population of the bulk traps dominate, the conductance as a function of the gate voltage does not show a characteristic peak in the range of weak inversion and at the same time in the inversion the capacitance of the structure increases[75, 74].

### C-t Characteristics

Transient capacitance characteristics are typically obtained after the MOS capacitor is pulsed into deep depletion. The capacitance over time curve is measured (usually at room-temperature), with the capacitance relaxation determined by thermal electron-hole pair (ehp) generation.

ehp generation parameters (such as carrier lifetimes) for both the space-charge region and the surroundings can be obtained using the so-called Zerbst transient capacitance method [72]. A modification of this method can be found in Chapter 3.

### Dielectric Spectroscopy

Dielectric spectroscopy is a technique utilizing measurement the admittance, i.e. capacitance and conductance over a range of frequencies.

Physically, the real part of the material's dielectric function represent the charging and is a measure of the energy stored from the applied electric field in the material identified the strength of alignment of dipoles in the dielectric, while the imaginary part the loss current, i.e. the energy dissipated in the dielectric due to frictional dampening that prevents displacements of bound charge from remaining in phase with the field changes [76].

### TOPIC: Measuring at Low Temperatures Means Probing the Fermi Level

The mean charge density dynamically transfered into the POM nanostructures was monitored during forward Current-Volttage sweep and various ramp rates. The trap density of the POM sheet deduced from those experiments at cryogenic temperatures (i.e. 140 K, where thermal fluctuations were adequately suppressed) was $D_t = 2 * 10^{12} cm^{-2}$. The corresponding Fermi wavelength is of the order of 18 nm.

For this temperature the thermal energy of electrons is much less, corresponding to a wavelength of 102.8 $\mu m$. We expect thus, that the electrons mainly contributing to conductance are the electrons with energy close to the Fermi energy.

Generalizing, low temperature low bias measurements are an excellent method for investigating mesoscopic transport phenomena, because

under such conditions the current is carried only by electrons at the Fermi energy. This is analogous to doing optical experiments with a monochromatic source [4].

On the other hand, the commercial market for 'low temperature low bias devices' is severely limited. Real world devices usually operate at room temperature under high bias such that transport occurs over a broad band of energies. Moreover, scattering processes are much stronger at higher temperatures.

Nevertheless, for experimental purposes it is always useful to scan the response of a system under such conditions, since useful system parameters can be extracted without the "noise" of thermal scattering. This is crucial for device engineering and optimization in the nanoscale.

For an electron density of $5 \times 10^{11}/cm^2$, the Fermi wavelength ($\lambda_f = 2\pi/k_f = \sqrt{2\pi/n_s}$) is about 35 nm. At low temperatures the current is carried mainly by electrons having an energy close to the Fermi energy so that the Fermi wavelength is the relevant length. Other electrons with less kinetic energy have longer wavelengths but they do not contribute to the conductance.

The mobility at low temperatures provides a direct measure of the momentum relaxation time (average time between scattering events) as limited by impurities and defects. Once the mobility is known, the momentum relaxation time (related to the mean free path, $L_m$ via $L_m = v_f \tau_m$ ) is readily deduced from:

$\mu = \frac{q}{m^*}\overline{\tau}$.

Electron-electron scattering is the dominant source of dephasing at low temperatures. An electron with a small excess energy ($E - E_F$) has very few states to scatter down into since most states below it are already full. Since the average excess energy of electrons is $\sim k_B T$ at low bias, $\triangle \sim k_B T$ and $\tau_\phi \propto (1/T^2)$ [77]. For high-mobility semiconductors $\tau_\phi \simeq \tau_m$, while for semiconductors of low mobility $\tau_\phi \gg \tau_m$. In low-mobility conductors the phase-relaxation time is usually obtained from weak localization experiments.

**TOPIC: The nature of dielectric function in molecular nano-assemblies**

The permittivity of a material is a physical property of paramount importance when any type of capacitive or electromagnetic wave propagation devices come into play. When the focus comes to molecular materials in the sense of hyperstructures formed from molecular building blocks the situation becomes a bit more complicated comparing to covalently-bonded single face bulk materials.

In molecular assemblies, and especially in cases like LbL-fabricated

heterolayers, distributed electric charge carriers on the electrostatically-formed interfaces, permanent (i.e. crystallization water in POM nanocrystalls, imbalance in charge distribution within the molecular framework) and/or field-induced molecular dipoles (i.e. differential localization of HOMO-LUMO states in POMs under uniaxial field application) and mobile ions can be displaced by an electric field. The charges become polarized to compensate for the electric field such that the positive and negative charges move in opposite directions. Moreover, dipole orientation and ionic conduction interact strongly at microwave frequencies, while permanent dipoles rotate to follow an alternating electric field.

Such mechanisms contribute drastically to the overall dielectric behavior and are quite lossy. For example the friction accompanying the orientation of the dipole will contribute to the dielectric losses. The dipole rotation causes a variation in both $\epsilon'$ and $\epsilon''$ at the relaxation frequency which usually occurs in the microwave and radio frequency region.

On the other hand, atomic and electronic mechanisms are relatively weak, and usually constant (i.e. they don't resonate) over the microwave region. Far below resonance, the electronic and atomic mechanisms contribute only a small constant amount to $\epsilon'$ and are almost lossless. The resonant frequency is identified by a resonant response in $\epsilon'$ and a peak of maximum absorption in $\epsilon''$. Above the resonance, the contribution from these mechanisms disappears.

In general as frequency increases, the slow mechanisms drop out in turn, leaving the faster ones to contribute to $\epsilon'$. The loss factor ($\epsilon''$) will correspondingly peak at each critical frequency. Water has a strong dipolar effect at low frequencies – but its dielectric constant rolls off dramatically around 22 GHz. Teflon, on the other hand, has no dipolar mechanisms and its permittivity is remarkably constant well into the millimeter-wave region.

Another important factor directly affecting the complex dielectric function is the relaxation time $\tau$, a measure of the mobility of the molecular dipoles that exist in the material. It is the time required for a displaced system aligned in an electric field to return to 1/e of its random equilibrium value (or the time required for dipoles to become oriented in an electric field). Constant collisions cause internal friction so that the molecules turn slowly and exponentially approach the final state of orientation polarization with relaxation time constant $\tau$. When the field is switched off, the sequence is reversed and random distribution is restored with the same time constant.

The relaxation frequency fc is inversely related to relaxation time: At frequencies below relaxation the alternating electric field is slow enough that the dipoles are able to keep pace with the field variations. Because the

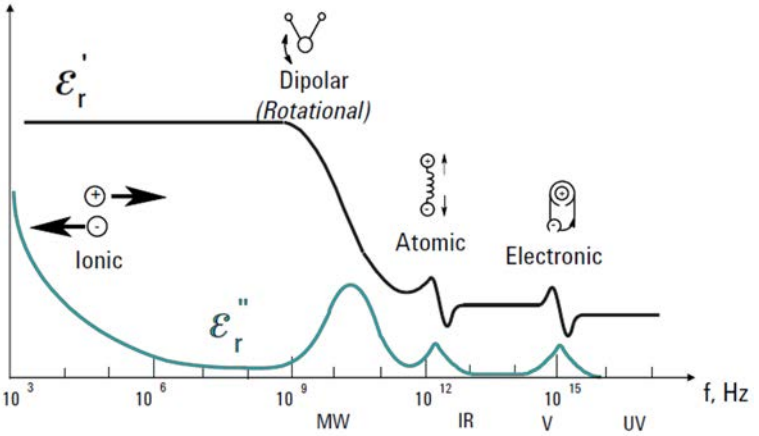


Figure 1.16: Frequency response of dielectric mechanisms.

polarization is able to develop fully, the loss ( $\epsilon$") is directly proportional to the frequency (Figure 9). As the frequency increases, $\epsilon$" continues to increase but the storage ($\epsilon$') begins to decrease due to the phase lag between the dipole alignment and the electric field. Above the relaxation frequency both $\epsilon$" and $\epsilon$' drop off as the electric field is too fast to influence the dipole rotation and the orientation polarization disappears.

Materials that exhibit a single relaxation time constant can be modeled by the Debye relation, which appears as a characteristic response in permittivity as a function of frequency (Fig.1.17).

$$\epsilon(\omega) = \epsilon_{\infty} + \frac{\epsilon_s - \epsilon_{\infty}}{1 + j\omega\tau} \tag{1.9}$$

$\epsilon$' is constant above and below the relaxation with the transition occurring near the relaxation frequency (22 GHz). Additionally, $\epsilon$" is small above and below relaxation and peaks in the transition region at the relaxation frequency.

In calculating the above curves the static (DC) value of the dielectric constant is $\epsilon s = 76.47$, the optical (infinite frequency) value of the dielectric constant is $\epsilon\infty = 4.9$ and the relaxation time $\tau = 7.2$ ps.

The measured loss of material can actually be expressed as a function of both dielectric loss ($\epsilon$d") and conductivity ($\sigma$). $\epsilon" = \epsilon d" + \frac{\sigma}{\omega\epsilon_o}$ At low frequencies, up to 1MHz, which is the case of interest for most standard MOS-related tests, ionic conductivity is the most prevalent mechanism in moist and solution-deposited materials. $\epsilon$" is dominated by the influence of electrolytic conduction caused by free ions which exist in the presence of a solvent (usually water). Ionic conductivity only introduces losses into a material. At low frequencies the effect of ionic conductivity is inversely

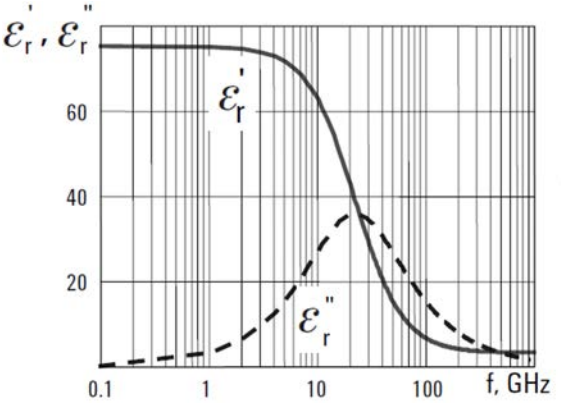


Figure 1.17: Debye relaxation of water at 30° C.

proportional to frequency and appears as a 1/f slope of the $\epsilon''$ curve.

Electronic, atomic, and orientation polarization occur when charges are locally bound in atoms, molecules, or structures of solids or liquids. Charge carriers also exist that can migrate over a distance through the material when a low frequency electric field is applied. Interfacial or space-charge polarization occurs when the motion of these migrating charges is impeded. The charges can become trapped within the interfaces of a material.

Motion may also be impeded when charges cannot be freely discharged or replaced at the electrodes. The field distortion caused by the accumulation of these charges increases the overall capacitance of a material which appears as an increase in $\epsilon'$. Mixtures of materials with electrically conducting regions that are not in contact with each other (separated by non-conducting regions) exhibit the Maxwell-Wagner effect at low frequencies.

If the charge layers are thin and much smaller than the particle dimensions, the charge responds independently of the charge on nearby particles. At low frequencies the charges have time to accumulate at the borders of the conducting regions causing $\epsilon'$ to increase. At higher frequencies the charges do not have time to accumulate and polarization does not occur since the charge displacement is small compared to the dimensions of the conducting region.

As the frequency increases, $\epsilon'$ decreases and the losses exhibit the same 1/f slope as normal ionic conductivity. Many other dielectric mechanisms can occur in this low frequency region causing a significant variation in permittivity. For example, colloidal suspension occurs if the charge layer is on the same order of thickness or larger than the particle dimensions. The response is now affected by the charge distribution of

adjacent particles.

Taking into account the above molecule-originating mechanisms will help to engineer better hybrid solid state/molecular materials with desirable dielectric properties, i.e. low loss factor ($\epsilon''$) and high energy storage capacity ($\epsilon'$) for molecular charge regulators and non-volatile memory applications.

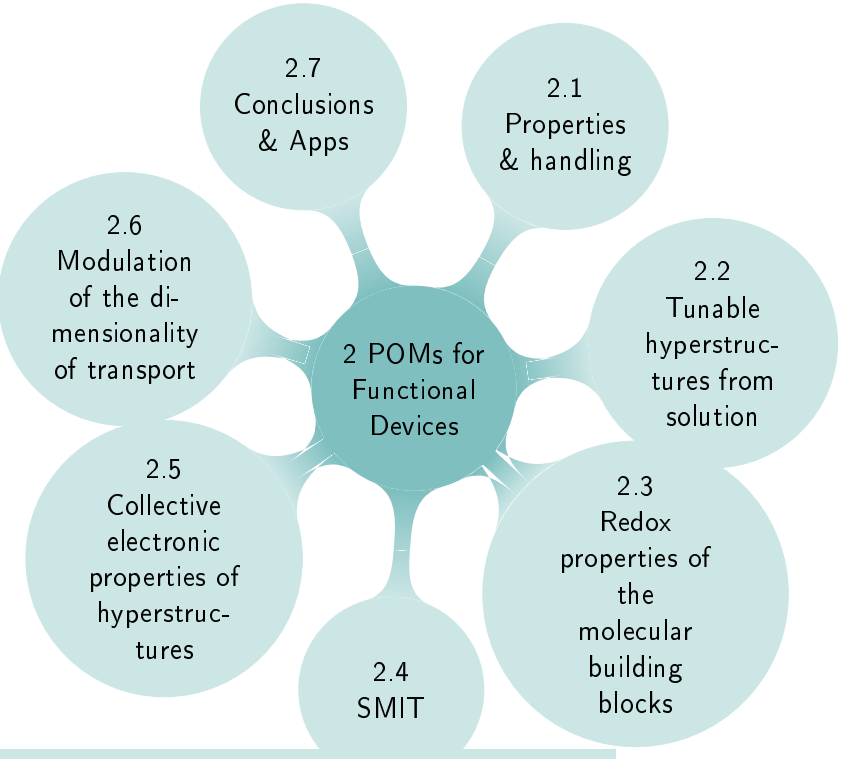


# 2

# Polyoxometalates as building blocks for functional devices

*Next generation electronics are likely to incorporate agile materials that will be able to exhibit tunable valence and conduction bands and, hence, adjustable electronic properties. This concept has reignited interest in bottom-up designer materials, such as solution-derived molecular components, whose potential for electronic applications has not been adequately capitalized on. This chapter demonstrates that low dimensional molecular transition metal oxide hyperstructures with tunable work function, HOMO-LUMO levels and localization extent are presented as components that can minimize injection barriers in hybrid molecular-metal-oxide-semiconductor (MOS)-type memories and enhance interfacial electron/hole injection in organic photovoltaic (OPV) stacks. Polyoxometalate molecules (POMs) are being self-arranged both on nanocrystal (NC) and hyperstructure level in layers of tunable (application optimal) spatial correlation length. An one-pot self-assembly process is applied in two stages, in order to separately address intermolecular and molecule-substrate interactions. Following the logic of strongly correlated materials, POM hyperstructures exhibit electronic properties vigorously determined by electron-electron interaction, varying dramatically by virtue of structurally-driven electronic tuning. The films are addressed to work under ambient conditions vertically or on plane, massively in parallel or in few chains mode exhibiting single electron transport characteristics. Individual POM nodes of controllable crystallization are electronically addressed for the first time on chip-grade oxidized silicon, using STM probes under ambient conditions. By adapting POM NC size in solution, we obtain current modulation of up to 4 orders of magnitude on a single*

*NC on $SiO_2$ at voltages as low as 3 Volt. Critical concepts such as structurally-driven insulator-to-semi-metal transitions (SMIT), extreme density of states modification and size-dependent current regulation on plane are demonstrated and examined with an eye on the corresponding stereochemical changes accompanying the molecular entities. This extends the value of self-assembly as a tool for correlation length and electronic properties tuning and demonstrates the possibility for on-chip single molecule electronic characteristics under ambient conditions. Properly incorporating such a material in transistor channels or memory cells will enable substantial modulation of transistor current or injection barrier, respectively, paving the way for solution-printed devices with consistently tunable performance characteristics.*

## 2.1 What exactly are POMs? Properties & Handling

Owing to benefits stemming from their inherent properties, molecules have long now been envisioned as a possible replacement of conventional top-down lithographically patterned components. Much effort has been devoted to their utilization as functional parts of solid-state electronic devices in an attempt to meet the stringent performance requirements for complementary metal-oxide-semiconductor devices in terms of miniaturization, speed, information density and power consumption [78]. This has already contributed to significant performance breakthroughs, particularly in the field of single-molecule devices [79], multi-state memories [80, 81] and organic light-emitting diodes (OLEDs) [82], with the later gaining commercial foothold. In other molecular device concepts, however, this success is not of comparable impact [83] due to major scale-up and fabrication challenges like disorder and contact induced smearing of isolated states [84, 85] cross talking [86], poor coupling to the addressing leads [87, 88] and low device yield [89, 90]. In this chapter we will discuss the self-assembly of tungsten polyoxometalates (POMs), a class of heteropolyanionic inorganic molecules with an unmatched range of physical and chemical properties [91] as a viable C-MOS compatible solution[81].

### Structure

Polyoxometalates (abbreviated as POMs) are a particularly large group of ionic clusters, usually anions, with frameworks built from transition metal oxoanions linked by shared oxygen atoms. In most cases the oxo-

anions reside in the form of clusters of metal oxides forming $MO_6$ octahedra with shared vertices and edges [92].

This class of compounds offers a vast amount of formations and isotopes among which the $[XM_{12}O_{40}]^{n-}$ compounds, which adopt the well-known Keggin stereochemical structure. The latter is a molecular architecture of high symmetry (tetrahedral) consisting of three or more transition metal oxyanions linked together by shared oxygen atoms to form a large, closed 3-dimensional framework. In the aforementioned chemical formula X is the so-called heteroatom which could be any of the 4-coordinate elements $Al^{III}, Si^{IV} or P^{V}$, while M is a transition metal commonly addressed as addenda element.

More thoroughly, the heteroatom of the Keggin structure is surrounded by four oxygens to form a tetrahedron (Fig2.1). It is located centrally, caged by 12 octahedral MO-units linked to one another by the neighboring oxygen atoms. There are a total of 24 bridging oxygen atoms that link the 12 addenda atoms. The metal centers in the 12 octahedra are arranged on a sphere almost equidistant from each other, in four MO units (four trimeric metal-oxygen subsets), giving the complete structure an overall tetrahedral symmetry.

The bond length between atoms varies depending on the heteroatom (X) and the addenda atoms (M). For the phosphotungstic acid primarily used in this work Keggin determined the bond length between the heteroatom and each the four central oxygen atoms to be 1.5 A. The bond length form the central oxygen to the addenda atoms is 2.43 A. The bond length between the addenda atoms and each of the bridging oxygen is 1.9 A. The remaining 12 oxygen atoms that are each double bonded to an addenda atom have a bond length of 1.7 A.

The octahedra are, therefore, distorted [93]. This structure allows the molecule to hydrate and dehydrate without significant structural changes and grants the molecule significant thermal stability in the solid state[93, 92].

The most typical addenda elements that form molecular metal oxides are $M^{VI}$, $Mo^{VI}$ and $W^{VI}$ or mixtures of these elements in their highest oxidation states with $d^0$ electronic configuration because their ionic radii and charge are then suitable for the formation of bonds with O [94].

In Fig2.1 the a-Keggin phosphotungstic acid POM used in this work is shown in three different representations, highlighting its structure, symmetry and chemical composition.

The corner-sharing trimetallic fragments are assembled according to a $T_d$ symmetry with all metal centres in the structure being equivalent [95]. Each $MO_6$ octahedron shares two edges with two octahedra of the same trimer and is connected by two corners with octahedra from other

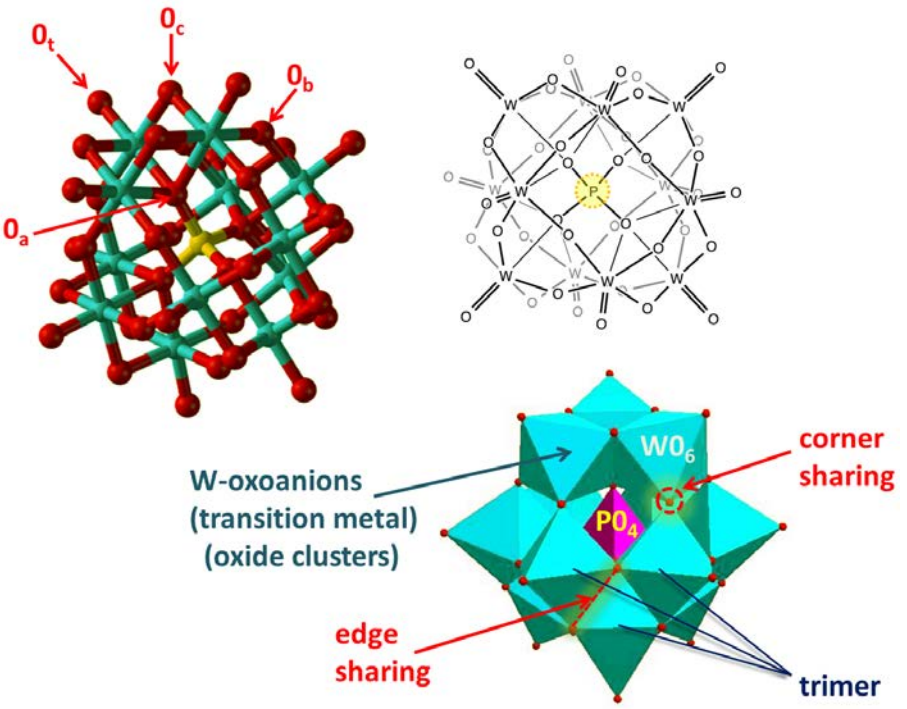


Figure 2.1: Structure of the a-Keggin tungsten polyoxometalate with a phosphorus heteroatom $[PW_{12}O_{40}]^{3-}$ and framework oxygen annotation.

trimers. Three octahedra from the same trimer have one common oxygen atom, and four such atoms form a tetrahedral environment for the X heteroatom. According to the annotation of Fig2.1 $O_a$ is the central oxygen involved in the heteroatom tetrahedron, $O_b$ the bridging oxygen that links two corner-sharing octahedra, $O_c$ the bridging oxygen that links two edge-sharing octahedra, and $O_t$ the terminal (outermost) oxygen of the Keggin POM structure.

Other isomers of the Keggin structure include the b-, c-, d- and e-isomer, which are structurally related to a- by the rotation of one or more of the four trimetallic groups by 60 degrees. Due to the richness of their structural and electronic properties, the Keggin-structure POMs have been extensively applied in quite diverse fields of research such as catalysis, biology, medicine, photochemistry and materials science[94]. On account of their high oxidation states and stability, POM-based architectures have sparked real life applications in catalysis [96], magnetic materials [97], electronic materials [98, 61] and nanocomposites [99]. Furthermore, POMs are promising candidates for drug-carrier approaches on the way to new composite drugs because they have long been known

for their multifaceted bioactivity that encompasses antiviral, anticancer, antibacterial and herbicidal properties [100].

POMs (Fig2.1) were opted as the functional molecules in electronic devices because of their unique combination of properties: they are stable molecules of well-defined structure and fixed size (1 nm), they can accept one or more electrons without significant structural changes, and these electrons can be de-localized over several metal centers of their framework. In other words, POMs can be viewed as zero-dimensional n-type semiconductors with low charging energies (from the Fermi level of Al or Au electrode to their lowest unoccupied molecular orbital, LUMO, level) in the range of 0.1-0.4 eV, i.e. with discrete electronic levels at room temperature. For semiconductor/molecule junctions, the corresponding barrier height is the energy difference between the edge of the conduction or valence band and the LUMO or HOMO respectively, depending on the semiconductor doping and can be tuned by changing the semiconductor doping type [101]. These properties together with their advantageous size can make them a promising candidate for high-density electronic devices in which the main operating element could be a single molecule.

### Electronic Properties of the Fully Oxidized Anion $[PW_{12}O_{40}]^{3-}$

For Keggin anions without paramagnetic ions such as $[PW_{12}O_{40}]^{3-}$ the ground-state configuration is typical of a fully oxidized polyoxoanion with a large energy gap between the HOMO, formally delocalized over oxo-ligands, and the LUMO, delocalized over the d-shells of tungstens (see Fig2.2). The electronic properties of $PW_{12}O_{40}]^{3-}$ involve primarily the metal and oxygen orbitals, while the heteroatom only slightly affects the POM reactivity [102] serving mainly to stabilize the structure, according to its coordination number.

The metal-oxygen bonds in an $\alpha$-Keggin framework can be divided into three sets according to whether their oxygen atoms is tetrahedral, bonding or terminal. In addition, there is a fourth metal-oxygen bond between the heteroatom and tetrahedral oxygens [104].

The Fully Oxidized Anion $[PW_{12}O_{40}]^{3-}$ can undergo several rapid one- and two-electron reversible reductions of the addenda or peripheral metal centers to produce the so-called heteropoly blue [105, 95]. This term is used in a typical manner for reduced polyanions irrespectively of their true color. For the one-electron-reduced species EPR spectra at different temperatures suggest that the spin is rather partially localized at quite low temperatures but is delocalized at higher temperatures [104]. NMR investigation [106] as well as ab-initio calculations[107] indicate that the doubly reduced $\alpha$-Keggin phosphotungstate is diamagnetic, owing to

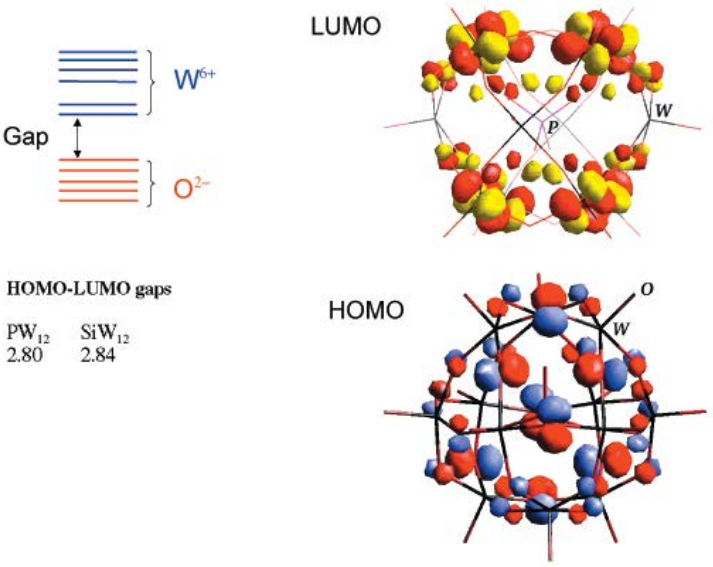


Figure 2.2: Schematic orbital diagram, HOMO-LUMO energy gaps (in eV) and 3D representations of one of the two doubly degenerate components of the HOMO and LUMO of the fully oxidized $[PW_{12}O_{40}]^{3-}$ anion. The contribution of oxo-ligand orbitals to the LUMO is ~95%, and for the HOMO the highest weight is for d-W orbitals with a contribution of~73% [103].

the strong antifferomagnetic coupling of electrons in the reduced anion. This paired singlet is stabilized due to electron delocalization and electron repulsion. According to first principle calculations [107] the $O_a$ (see Fig2.1) oxygens do not support any pathway for electron transfer and delocalization occurs only through the orbitals of the O ions being shared by two octaedra (i.e. the $O_b$ and $O_c$).

Delocalization is an essential prerequisite in order to obtain electron transfer pathways between the POM nodes, while strong localization is a quality highly desirable for charge trapping applications.

The energy and composition of the lowest unoccupied orbitals, delocalized over the addenda atoms, are of paramount importance since they determine the redox properties of a polyoxometalates. The energy gap between these occupied states and the unoccupied band in fully oxidized Keggin anions is almost independent of the nature of X. In (Fig2.3) one can see the unoccupied orbitals of fully oxidized Keggin anions which are symmetry-adapted d-metal orbitals with some antibonding participation of oxygen orbitals.

As indicated in (Fig2.3) the $MO_6$ units do not retain a perfect octahe-

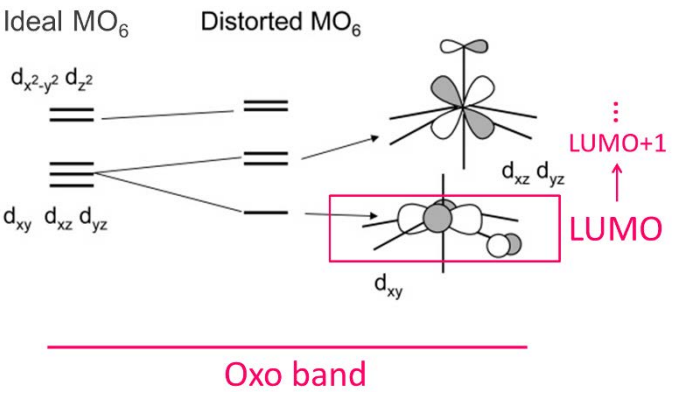


Figure 2.3: Scheme depicting the distortion of metal d orbitals in realistic POM structures due to the antibonding participation of oxygen p orbitals [108, 95].

dral symmetry in the structure, since the metal atoms are displaced due to the M=O pi-bonding towards the vertices that form the surface [109]. Thus, $d_{xy}$, $d_{xz}$ and $d_{yz}$ orbitals are destabilized by antibonding interactions with appropriate symmetry p oxygen orbitals. The negative overlap is notably higher for terminal than for bridging oxygens because the metal-oxygen bond lengths are shorter and the orientations are more favorable. The resulting splitting of degenerate d orbitals due to the interaction with the O antibonding states can be seen in Fig.2.3. It follows that, upon reduction, the unpaired electrons are essentially delocalized over the lower energy $d_{xy}$-like orbital of each of the W ions [107]. The LUMO+1 is a triply degenerate orbital of symmetry t1 [104]. The energy gap between LUMO and LUMO+1 is 280 meV [107] (DFT-derived) or as determined from polarographic measurements 243 meV [110]. This large energy gap is, essentially, the origin of the diamagnetic properties of the two-electron-reduced Keggin anion compound [107].

### Chemical & Thermal stability

An important property, and one of the core prerequisites for electronic device operation, is chemical and thermal stability, in order to be able to withstand both the CMOS line fabrication processes as well as multiple operating cycles (at device level) while maintaining function reliability.

POMs are recyclable, in the sense that they can be repeatedly used in a closed system [111]. This stems from their reversible redox activity. Moreover, they are inherently stable towards strong oxidants, while they retain their structure at high temperatures [102]. Tungsten, in particular,

outbalances Mo in thermal stability [112] and this is the main reason that phoshotungstates were mainly utilized in this work.

The a-Keggin isomer is selected for similar reasons, due to its being the most stable Keggin form amongst polyoxometalate anions. Moreover, its highly symmetric framework renders it an agile building block for substrate-specific handling and assembly.

In aqueous (or non-aqueous) solvents the stability of POMs is a more complicated issue, directly and more intensely affected by the pH (or the reactivity of solvent) and is generally measured by their ability to retain their structural identities and avoid degradation or transformation to other forms.

The treatment of Keggin-type POMs with alkaline solutions under appropriate experimental conditions (e.g., pH, temperature, concentration) leads to loss of one to several metal centers. This yields what is called lacunary POM species, a deformed structure which, nevertheless, still belongs to the Keggin series. For example, both lacunary species $XM_9$ and $XM_{11}$ which are being formed from the degradation of Keggin $XM_{12}$ are still relatively stable members of the Keggin family and widely used in subsequent syntheses [113]. The formed lacunary species have also several isomers [114]. The lacunary Keggin POMs can react with transition metals (e.g., FeIII, MnII, CoII, NiII, ZnII) or other elements with close properties (e.g., WVI, MoV, VV) to fill out the vacant sites and form substituted Keggin POMs [113].

### Analogy to transition metal oxides

POMs can be considered the molecular analogue of transition metal oxides and, as such, their structural bonding straddles the subtle boundary between covalent, ionic and metallic. This hybrid bonding character is often the origin of a rich variety of physical phenomena, ranging from high-Tc superconductivity in layered cuprates, colossal magnetoresistance in perovskite manganites, to the coexistence of magnetism and ferroelectricity.

As we already saw in Fig.2.1 the basic structural units of the POM framework are $M0_6$ octahedra, a typical coordination form for transition element oxides. The central heteroatom can be neglected in this comparison as it does not generally alter the electronic structure details of the anions. This is reflected to the similarity in optical and electronic properties of polyoxometallates and aggregates of various metal oxides [115]. The central heteroatom does influence, though, the overall stability of the structure [116] and shifts the threshold for reduction of the anion according to its size. This explains why POM clusters are more difficult

to reduce with decreasing size of the central heteroatom within a given family of Keggin-type heteropolyanions carrying the same overall negative charge [117]. The metal-d orbitals (Md) overlap with the ligand 2p orbitals (O2p) forming the POM molecular orbitals as shown in Fig.2.4.

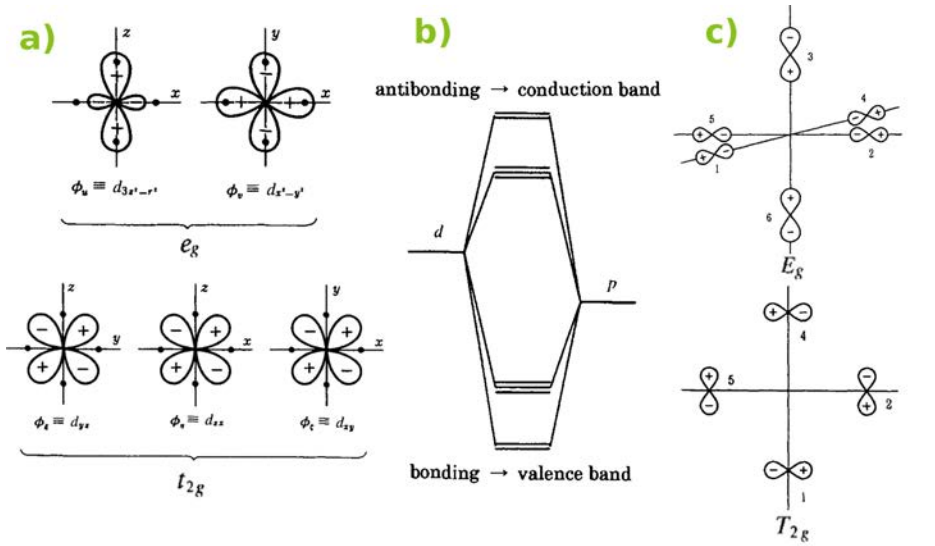


Figure 2.4: Schematics of $d\epsilon(T2g)$ and $d\gamma(Eg)$ orbitals of octaedrally arranged metals when ligand oxygen ions are approximated by negative point charges and O2p orbitals of T2g and Eg symmmetry in the $MO_6$ cluster. Their combination, depicted in the center as mixed energy levels, represents the ideal $MO_6$ POM oxoanion comprised of bonding and antibonding contributions of the O2p and Md orbitals, respectively, as well as of their hybridized states [108, 95].

Usually O2p levels are lower than M5d levels and as a result, the bonding orbitals are mainly composed of O2p orbitals whereas the antibonding orbitals are mainly composed of M5d orbitals.

In conventional transition metal oxides, the orbitals are often (i.e. in the LCAO or tight binding approximation) approximated by linearly combining the atomic orbitals with a phase factor which satisfies the periodic boundary condition. In direct analogy to a POM molecule, in a typical transition element oxide the conduction band is a d band and the valence band is a p band.

The well-studied physical and stereochemical properties of transition metal oxides [118, 119] can be of immense help towards the effort of rationalizing the engineering of POM molecular solids and hyperstructures. For example, it is now known that the band picture of electrons in transition metal oxides fails when various interactions, which were

neglected in the band calculation, become larger than the band width. These are non-periodic potentials, electron-phonon interactions and parts of electron-electron interactions.

One additional characteristic of transition metal oxides is that many of their properties strongly depend on materials defects like vacancies, dislocations, stacking faults and grain boundaries. These defects affect local oxygen bonding [120] and influence their chemical properties. The relative acidity and basicity of the atoms present on the surface of metal oxides are also affected by the coordination of the metal cation and oxygen anion, which alter the catalytic properties of these compounds. For this reason, structural defects in transition metal oxides greatly influence their catalytic and physicochemical properties. Along the same lines as with transition metal oxides, there is a really strong impact of stacking and local environment on their properties.

The aforementioned characteristics will be directly exploited during the manipulation of POM molecules from solution in order to fabricate/tune electronically active molecular hyperstructures with on-demand electronic properties.

## 2.2 Making tunable hyperstructures from solution

### 2.2.1 Motivation & State of the Art

Next generation electronics are likely to incorporate agile materials that will be able to exhibit tunable valence and conduction bands and hence, adjustable electronic properties. This concept has ignited interest in bottom-up designer materials, such as solution-derived hyperstructures, that may lead to resolution and fabrication strategies not possible with top-down methods, while exhibiting potential for electronic applications that extends far beyond their currently established role [121, 122].

Molecular and 2-D bottom-up assemblies from solution are both targeted as a replacement for conventional top-down lithographically patterned components due to their superior opto/electronic properties as well as low cost [123]. Much effort has been devoted to their utilization as functional parts of solid-state electronic devices in an attempt to meet the stringent performance requirements for complementary MOS devices in terms of miniaturization, speed, information density, power consumption and added functionalities [124]. This has contributed to significant performance breakthroughs in all fields of molecular and polymeric organic field-effect transistors (OFETs) [125], single-molecule devices [126], resistive memories [127, 128] and organic light-emitting diodes (OLEDs),[129] with the later gaining commercial foothold.

However, in other mesoscopic CMOS-molecular electronic device concepts this success is not of comparable impact [130] due to major scale-up and fabrication challenges. These include disorder and contact induced smearing of isolated states [131, 132] cross talking, [133] poor coupling to the addressing leads, [134, 135] high resistivity and low device yield [136, 137].

In an effort to address these issues in an elegant manner and exploit the design opportunities offered by bottom-up-built materials we investigate the nested two-stage self-assembly of tungsten polyoxometalates (POMs). This class of heteropolyanionic inorganic molecules has an unmatched range of physical and chemical properties [138] and is investigated herein as a viable C-MOS compatible solution [128] able to overcome the limitations of a topologically fixed structure.

Devices based on self-assembled molecular films are more robust and reproducible over single-molecule junctions, and are more likely to be compatible with future mass production and integration [91, 139, 139]. Moreover, the non-covalent grafting scheme they rely on is considered a particularly attractive route towards the design of new supramolecular assemblies [140, 141], offering more power than traditional covalent synthetic strategies [140]. Our group has investigated the possibility of utilizing self-assembled POM molecules under various topologies [142, 143, 144, 145] demonstrating that, depending on the directionality of addressing (planar or vertical), different transport properties can be probed.

Despite the rigorous investigation of POM device possibilities both on experimental and theoretical level [128], purely inorganic POM-only designer hyperstructures with tunable localization extent have not yet been electronically addressed. In the case where electrons are being localized, the characteristic feature of the hyperstructure appears in the form of dielectric properties. For such applications, the conductivity can be detrimental to the desired functionality[146]. This is the limit of interest for hybrid CMOS-molecular memory applications. In the case of itinerary electrons and delocalization the applicability of the film as a carrier extraction layer for OPVs is more appropriate, with the work function and HOMO-LUMO tunability being the relative advantage over existing transition metal oxide solutions [147].

In this chapter we show for the first time that POM assemblies, based upon pre-organized molecular species in solution, exhibit highly tunable electronic properties directly related to the extent of crystallization of their building blocks. POMs are being self-arranged both on nanocrystal (NC) and hyperstructure level in a rational way resulting in layers of tunable spatial correlation length. Precision control over crystallization

is a major asset for devices, since the electronic coupling between adjacent molecules and the intrinsic mobility are primarily governed by the molecular packing arrangement [148, 149].

Being able to transport or confine charge at will, these hyperstructures constitute ideal candidates for alternative molecule-based circuitry components and transistor channels. Moreover, the structures realized this way have properties particularly tolerant in disorder. Due to their highly symmetric Keggin structure [150, 151] they are able to form self-assembled films with building blocks of controlled crystallization extent and collective electronic properties on par with their molecular building blocks.

They are, thus, promising for solution-printed molecular semiconductor films with electronic properties of noticeable tunability, high stability and predictability.

### 2.2.2 A two-stage one-pot fabrication scheme

The principles of Layer-by-Layer self-assembly have been discussed in Subs. 1.3.3. What has yet to be explored, though, is in which extent is possible to gain control over the molecular assembly process already in the precursor solution under constricted modification of simple interrelated parameters such as POM concentration and pH.

#### Nature of interactions in solution

The form of interaction between molecules, or in other words, the forces we can utilize in order to assemble POM molecules inside the solution are directly dependent (among other things) upon the intermolecular distance. For distances of the order of 1 $\mu$m and if the bodies are charged, we might be able to measure electrostatic force among them or, in case they are magnetized, we could observe magnetic interaction. There will not probably be any significant energy transfer, except for radiative heat transfer in case that the constituents' temperatures differ significantly, but this effect will be rather small as well. After the initiation of this first electromagnetically driven approach, when the bodies will come closer up to distances of 10-100 nm, they will start sensing some other long range interactions, like van der Waals forces [54].

Even closer, the first water bridges can appear giving rise to the primary POM crystallization process. Convective heat transfer due to the surrounding liquid can also appear to some extent. When molecules reside at distances 1-10 nm, charge transfer via tunneling becomes possible, while van der Waals forces can become dominant, giving rise to

secondary POM crystallization resonsible for the formation of larger aggregates. Upon molecular contact repulsive interactions due to the Pauli exclusion principle determine the bonding nature (i.e. hydrogen bonding) while charge and heat transfer is observed. Mechanical properties also play a role, especially in solution, where adhesion and hydrophilicity-influenced diffusion can play a major role on the stereoscopic structure of the complexes. An illustration of the spatial range of dominance of fundamental forces developed between fully oxidized POM anions in aqueous solution can be seen in Fig.2.5.

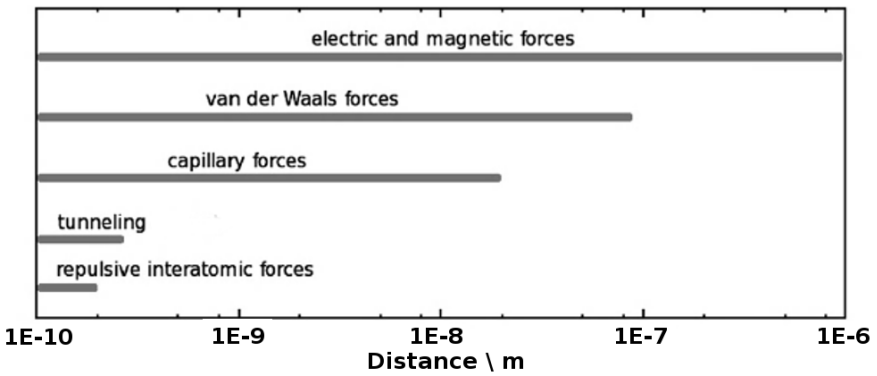


Figure 2.5: Dominant interactions between POM molecules in sol [54].

The following basic strategy is used for describing or analyzing the solid-state structure. One decomposes the hyperstructures into elementary building blocks (aggregates of polyhedra) and then tries to identify and explore the local matching rules according to which the building blocks are to be assembled to yield the objects considered. These nanosized polyoxomolybdate clusters could also provide model systems for studies on the initial nucleation steps of crystallization processes.

### Manipulating interactions via a two-step process

The developed process is a simple one-pot self-assembly procedure in HCl-acidified deionized water. Key detail is the division of the process in two strictly separated stages during which inter-molecular (stage A, Fig.2.6a) and substrate-molecular (stage B, Fig.2.6b) interactions dominate successively.

During stage A, by tuning the concentration of molecules in the precursor solution, while maintaining a constant pH of 0.5, a controlled crystallization following aggregation of POMs is attained. In this case the HCl concentration in the POM solution should be modified accordingly, in close synergy with the concentration of heteropoly compounds which

are strong Brönsted acids, in order to maintain a stable acidic pH (i.e. 0.5) in the precursor for all molarities. Maintenance of highly acidic environment during the process is crucial in preserving the Keggin structure of the molecules which, in turn, enables high symmetry crystallization [152].

In sol molecule-substrate interactions are at a minimum, thus intermolecular interactions dominate, resulting in the molecules adopting a minimum energy packing [153]. The self-arrangement of hydrophilic POM molecules to form crystalline clusters in polar solvent [154, 155] is governed by electrostatic and van der Waals forces between molecules and their clusters [156, 30]. Electrostatic forces develop due to the reduction of POMs in the acidic medium and subsequent proton-mediated crystallization. At this stage the secondary structure of the heteropolyacids is largely determined by hydrogen bonding of the polyoxometalate anions via water and hydrated proton species [156] (Fig.2.6a).

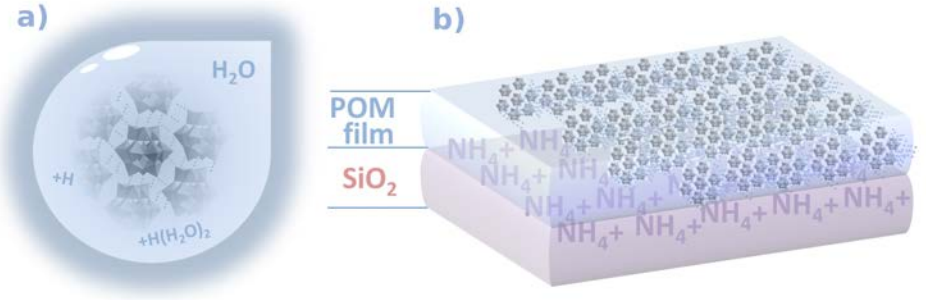


Figure 2.6: Schematics of two stage (a, b) one-pot self-assembly of POM hyperstructures.

Attractive van der Waals forces between aggregates become appreciable when the POM units are in close proximity, so that higher density solutions involve formation of larger aggregates. Counter ion-mediated attraction and hydrogen bonding are primarily responsible for this unique associative behavior [157]. In other words, charge balancing cations control the extent of crystallization in solution and, finally, the solid state output [31]. More specifically, clustering and subsequent solid-state network and cluster-of-cluster type assemblies in POM solutions are defined via successive secondary and tertiary cation exchange reactions [31, 158]. Cation availability is directly affected by the pH (kept constant) and the diffusion constant (directly related to molarity) in the precursor solution. This implies that molarity is used here to tune the crystallization extent of POM nanocrystals (NCs) in solution.

During stage B, after the nanocrystallization of the molecular building blocks self-terminates, POM hyperstructures are fabricated from the

same solutions via post crystallization arrangement on high quality dry $SiO_2$. The concentration of molecules in the precursor sol is a direct measure of the final size of the molecular blocks to be used in this stage. For the fabrication of planar hyperstructures the LBL self-assembly method is being used (see Subsections 1.3.3,1.3.4). Prior to assembly the $SiO_2$ substrate is chemically modified with APTES in order to enhance long range molecule-substrate interactions. While in aqueous ambient, the exposed amine end-groups of APTES are being protonated, acting as a 2-D electrostatic template for the assembly of the preformed NCs. After lapse of the reaction time a low dimensional superstructure is being formed (Fig.2.6b).

### 2.2.3 Dependence of (opto)electronic and structural properties of films upon nanoclustering

All-inorganic POM hyperstructures were prepared starting from solutions with concentrations spanning four orders of magnitude ($[1 \times 10^{-4}$, $1 \times 10^{-1}]$ M). UV-Vis absorption spectra of the as-grown films are given in Fig.2.7a. The absorption peak at 270 nm is characteristic of the Keggin structure of $[PW_{12}O_{40}]^{3-}$ anions, and is ascribed to the oxygen-to-metal charge transfer [159]. Its intensity increases linearly with POM concentration in the precursor sol, in accordance with literature [160].

For concentrations below $5 \times 10^{-2}$ M, an additional weak absorption peak emerges, centered at 311 nm (Fig.2.7d), within the POM fundamental HOMO-LUMO gap. This peak, with a linewidth of a few wavenumbers (FWHM $\sim$ 8 nm) and an onset close to the DFT-calculated HOMO-LUMO gap for non-interacting POM molecules [161], is centered only 41 nm away from the oxygen-to-metal charge-transfer band of POM and is more prominent in the case of $1 \times 10^{-4}$ M.

Similarly to the intervalence charge transfer band typically appearing in the visible region [154, 162] this peak can be attributed to the reduction of POM molecules. As such, it is accompanied by the presence of W atoms in oxidation state $<+6$, indicating reduction of POM metallic centers. Normally, phosphotungstic acid suffers rapid re-oxidation in ambient due the presence of $O_2$ which mediates the process [151]; however, in the case of small aggregates quantum confinement becomes important, increasing the electron exchange threshold and hindering re-oxidation.

The bandgaps of both POM films and sols were estimated via Tauc plot analysis of absorption measurements (see Subsection 3.7.2) [163, 164] (Fig.2.7b). It appears that, both in film and sol, the bandgap of clusters depends monotonically on POM molarity in the precursor solutions. In liquid the band gap increases linearly with decreasing $\log[C_{POM}]$ (cf.

Fig.2.7b). This indicates that POM clusters are already formed in sol, while their electronic properties depend in a straightforward manner on cluster size which, in turn, is defined by POM molarity in the precursor solution.

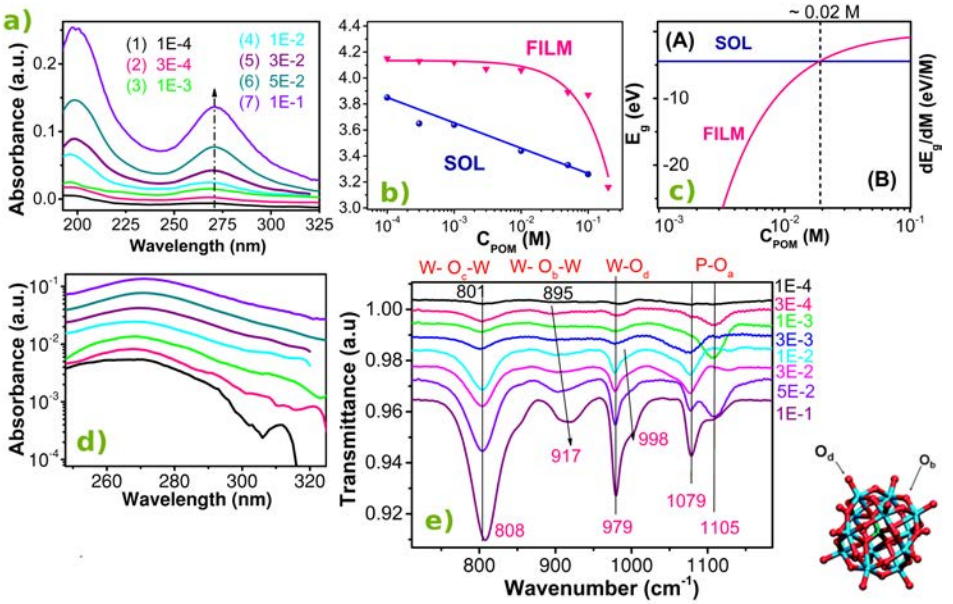


Figure 2.7: (a) UV-Vis absorption spectra of molecular films fabricated from sols of varying POM concentrations; (b) Band gap of molecular aggregates in solution and hyperstructures in the solid state as a function of POM molarity in the precursor sol; (c) Rate of change of band gap vs. molarity for both sols and films; (d) Low energy UV-Vis absorption peak at 311 nm indicating the reduction of POM molecules at low molarities; (e) FTIR transmittance spectra for films of different molarities; Scheme: The POM unit consisting of a framework of twelve octahedral tungsten oxyanions surrounding a central phosphate group.

In solid state (film), the bandgap similarly decreases with increasing precursor concentration; however, it follows an exponential, rather than linear trend with $\log[C_{POM}]$, exhibiting weak changes in the lower $10^{-4}$ to $10^{-2}$ M molarity range. The latter is directly related with the slow variation of the size of POM NCs in this regime (See Section 2.6). Solid state gaps are found to be significantly larger than those measured in liquid, owing to the confinement of the molecules on the plane. This basic electronic structure divergence between the two states is consistent with the different nature of intramolecular electronic interactions reported in solid state and in sol [165, 166] and is a manifestation of cluster immo-

bilization on the substrate and subsequent structural transition towards assembly/packing on plane.

Above a certain precursor concentration, the interactions between nano-crystals immobilized on the substrate predominate over cluster size impact with respect to the exhibited band gap; the transition point can be located by plotting the rate of change of band gap vs. molarity for both sols and films as inFig.2.7c. In Region A, of lower concentrations, the variation rate still depends on cluster size, involving, thus, weakly interacting clusters/NCs up to about $2 \times 10^{-2}$ M, where the two rates become comparable and inter-crystal interactions between clusters take over (region B). Notably, the changing point is related to the vanishing of the extra absorption peak at 311 nm (Fig.2.7d). This peak was thought to signify a dominant reduction of POM molecules assisted by quantum confinement, reflecting the weakening of electronic interactions between POM nano-islands produced from dilute solutions. Thus, inter-crystal interactions influence in a straight forward manner the width of the forbidden gap in solid state and, consequently, the POM oxidation threshold. Quite unconventionally, transition from non-interacting free molecules (i.e. with HOMO-LUMO separation of 2.8 eV, as estimated from ab-initio calculations in [95]) to increasingly interacting molecules in liquid and solid state induces significant broadening of the gap (Fig.2.7b).

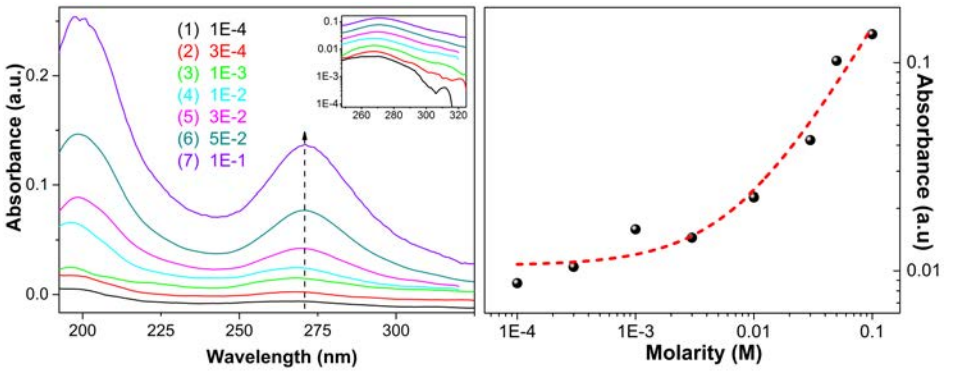


Figure 2.8: On the left: UV-Vis absorption spectra of a number of thin molecular films in solid state. The inset shows the exhibition of a weak absorption peak after 300 nm for low molarities owing to POM reduction. On the right: Absorption Intensity versus molarity in precursor sol.

Transmittance spectra for the employed precursor concentrations, ranging from $1 \times 10^{-1}$ M to $1 \times 10^{-4}$ M, are presented in Fig.2.7e. The compounds exhibit all four characteristic asymmetric stretching vibrational peaks of the POM molecule (see Characterization Methods), indicating that the building blocks of the as-prepared molecular films still retain the

basic Keggin structure.

The increase of molarity affects significantly not only the intensity of the signal, but also the position of the characteristic bands, giving rise to new vibrational modes as well. More specifically, the emergence of a symmetric terminal oxygen (Od) stretching mode [156] around $997 cm^{-1}$ for concentrations above $1 \times 10^{-2}$ M signifies an increase in the W=Od group symmetry due to coordination of the POM anions, indicating the formation of higher symmetry ionic crystals. In Keggin tungstophosphoric acid-POMs, this symmetric stretching mode has A1 symmetry and is, normally, IR-inactive [156, 167] as is the case for low molarity films (Fig.2.7e). However, IR-inactive modes can become active if they are accompanied by a polarization of the bond. This effect is provided here by protonated water, which is typically hydrogen-bonded to the terminal POM oxygen $W = Od \cdots H + (H_2O)_2$ and, along with loosely bound lattice water, assists the crystallization of POM moieties [156]. As a result, a symmetric stretching mode appears as a shoulder. For concentrations higher than $1 \times 10^{-2}$ M, the shoulder becomes more intense, due to expanding crystallization, shifting to higher energies, due to the strengthening of electrostatic anionanion interactions [168].

The blue shift of the W-Ob-W bridges stretching (corner sharing octahedra, 895 to 917 $cm^{-1}$) along with the significant broadening of the band is quite remarkable for concentrations above $3 \times 10^{-2}$ M. The Ob atoms together with the terminal oxygens, (979 $cm^{-1}$), form the outermost part of the POM framework being, thus, prone to interactions emerging from close proximity. This concurs with Fig.2.7c for transition from weakly to strongly interacting NCs. The full width at half maximum (FWHM) of this IR band broadens with increasing concentration, most likely reflecting the heterogeneity of these sites in the aggregated polycrystalline material and/or the involvement of inelastic collisions between molecules in the forming NCs [169, 170].

We note finally the $1105\, cm^{-1}$ peak, which corresponds to the bulk Si-O-Si asymmetric stretching mode [171]. For low concentrations, portions of the silane part of APTES molecules are exposed, giving rise to this band. Improved coverage at higher concentrations suppresses the peak, which reappears at higher molarities, as the arrangement of larger NCs (already formed in sol) on the APTES surface leads again to exposed silane areas.

A more quantitative look at the two concentration extremes ($1 \times 10^{-4}$ M and $1 \times 10^{-1}$ M molarity ranges) contributes to the understanding of the underlying electronic properties emerging from the outspread of crystallization and assembly in POM building blocks. In (Fig.2.9) deconvolution of the complex bands in the vibrational spectra of the high-molarity films

by means of Gaussians highlights the varying contribution of molecular orbitals as the structure transforms from isolated oligomolecular dots to a polycrystalline film.

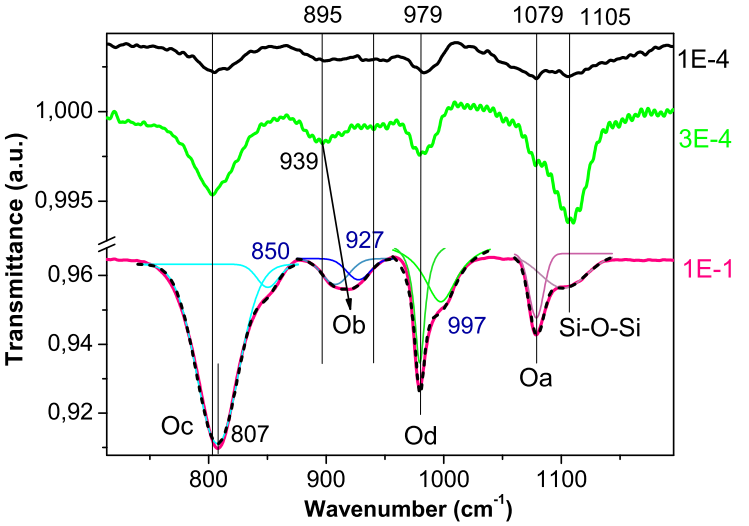


Figure 2.9: FTIR transmittance spectra for films of two molarity extremes. The blue numbering indicates the new peaks emerging exclusively in high molarity films, and were not present for low coverages.

The blue shift of the W-Ob-W bridges stretching (corner sharing octahedra, 895 to 917 $cm^{-1}$) along with the significant broadening of the band is quite remarkable for concentrations above $3 \times 10^{-2}$. A slight blue shift is also the case for the W-Oc-W bridges of corner sharing octaedra Fig.2.9. The bridging orbitals of the O ions residing in these specific positions on the Keggin framework are the ones facilitating delocalization of electrons in the reduced species [107]. Thus, intensification (blue shift of vibrational response) of these bonds in the highly aggregated material directly prompts for enhancing delocalization with increasing molarity.

Fig.2.10 depicts the top view morphology of POM hyperstructures for two characteristic concentrations ($3 \times 10^{-2}$ and $1 \times 10^{-4}$ M) as obtained via tapping mode AFM. Although NC size increases with POM concentration in the precursor solution (Fig.2.10a), aggregates retain their nanotexture. Fine NCs forming larger aggregates can be observed for both $3 \times 10^{-2}$ and $1 \times 10^{-4}$ M films (Fig.2.10a,Fig.2.10c and Fig.2.10d). According to the derived 2-D autocorrelation function of i.e. $1 \times 10^{-4}$ films in Fig.2.10e,Fig.2.10f, POM formations are isotropically distributed [172] on plane. The autocorrelation function has a circular symmetry with re-

spect to the origin, an evidence of surface isotropy. This stems from both the symmetry of the POMs Keggin structure, enabling isotropic coalescence/crystallization in sol, and the amorphous substrate. Random profiles of 250-nm-width line scans are presented in Fig.2.10b. Although, at first sight, the film morphology appears to be random, quantitative analysis reveals terraces of spatially correlated properties. Roughness analysis reveals a Gaussian root mean square roughness distribution around 1nm, i.e., the size of a single POM molecule [156].

The shape and periodicity of the line profile of the autocorrelation function in Fig.2.10f is indicative of non-randomness in the surface data. The topographical self-similarity of POM NCs, as revealed upon scanning different magnifications and/or spanning different molarities (Fig.2.10), implies the existence of a fractal structure. This self-affine symmetry and the concomitant power law dependencies of height profiles to the horizontal length [60] have as lower limit the size of the POM molecular building block (1nm) and as upper limit the spatial correlation length of the surface profile [60] ($L_c = 10\xi$) ($\xi = 6.7nm$ for $1 \times 10^{-4}$ M and $\xi = 18.1nm$ for $3 \times 10^{-2}$ M). $\xi$ is directly related to the size of the basic grain unit, while the periodicity in the 1D autocorrelation function (Fig.2.10f) reflects the mean spacing between units, which is of the order of 15 nm for $1 \times 10^{-4}$ M films.

Fractal analysis of the obtained topographies confirms the presence of self-similarity and provides information on hidden symmetries and the correlation of these symmetries to the growth process and system dynamics [60]. Both surfaces presented in Fig.2.10 (i.e. of the $3 \times 10^{-2}$ and $1 \times 10^{-4}$ M layers) were analyzed using a box-counting algorithm [173] and have been found to exhibit scale invariance, possessing a fractal dimension (df) of 1.8 for the 0.03 M (and higher molarity i.e. 0.05 M layers) and 1.7 for the $1 \times 10^{-4}$ M (For raw curves and error estimation see Appendix Section 8.4).

In fact, whenever intra-grain resolution is preserved df is 1.7, while for higher roughness thresholds, where intra-grain information is lost, df is 1.8 and is related to the ordering of grains towards formation of a hyperstructure. The obtained df values are consistent with an off-lattice diffusion limited aggregation process of molecular cluster formation [174] and provide a post-process link to the crystallization mechanism of POMs in solution.

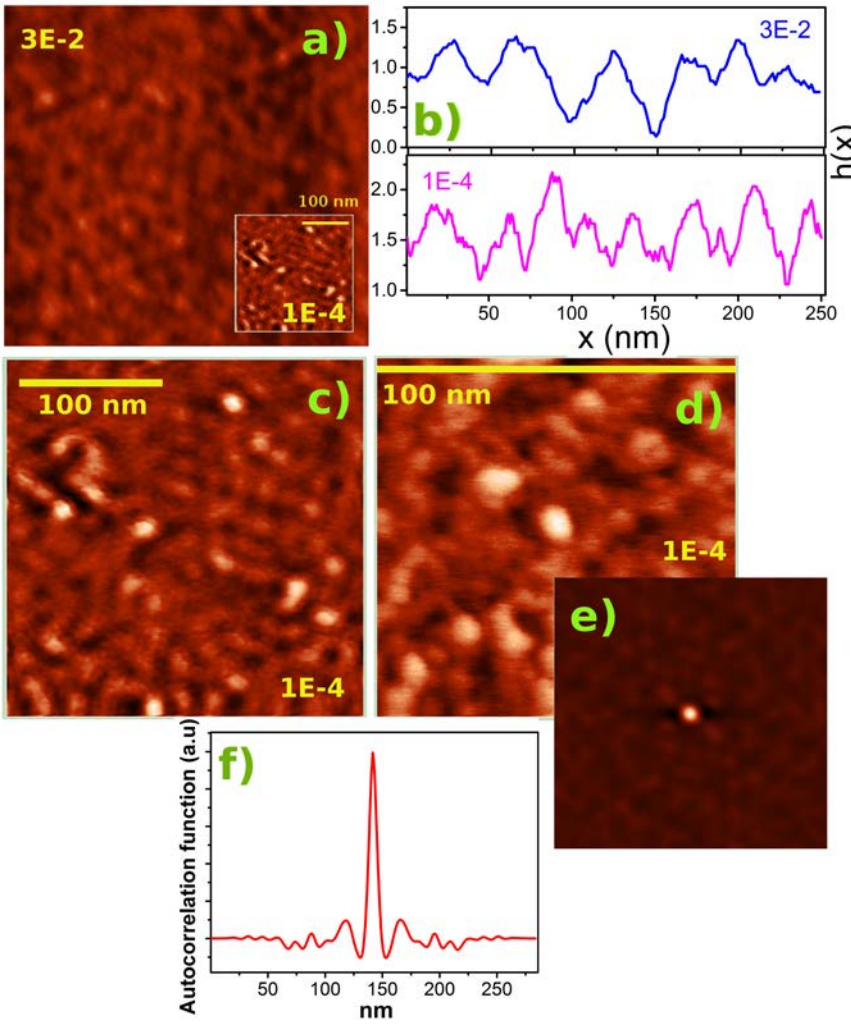


Figure 2.10: (a) Top view of the fabricated POM hyperstructures for two concentrations ($3 \times 10^{-2}$ and $1 \times 10^{-4}$ M) as obtained via tapping mode AFM. (b) AFM Height profiles for 250 nm-width line scans of two different POM molarities. (c) 250 × 250 nm and (d) 100 × 100 nm line scans of a POM $1 \times 10^{-4}$ M film self-assembled on native $SiO_2$, and (e) corresponding 2-D autocorrelation function of the 250 × 250 nm scan; (f) Line profile of the autocorrelation function, indicating its symmetry with respect to the origin. The periodic peaks and humps are a signature of self-affinity.

## 2.3 Redox properties of the fabricated molecular building blocks

The electronic properties of POMs in solution provide clear indication of the reversibility of re-dox reactions occurring on its framework. Different as this system might be from its solid state (i.e. molecular film) analogue, it is a facile way of probing the chemical reactions accompanying electron trapping and exchange by the molecules (providing that the basic structural units retain the same stereochemical structures both in liquid and solid state). Indeed, in solution the system is stabilized and the molecular orbitals drop to quite negative energies[108]. This enables facile reduction of the system, permitting investigation of the nature of chemical reactions. On the other hand, this results in the underestimation of LUMO and LUMO+1 energy levels as detected via polarography and, as a result, a direct comparison of these values with their solid state analogues is not possible.

Cyclic voltammetry on various electrodes (Pt, glassy carbon, Ti) was utilized to evaluate the position of HOMO and LUMO energy levels of the molecular nanocrystals directly in the precursor sol [161]. In fair agreement with the literature [166], the cathodic scan on Pt electrode (Fig.2.11a), revealed a two-stage one-one electron reduction of POM at the Epc1 and Epc2 waves.

Having a strongly oxidizing compound, such as POM molecules, one starts a positive voltammetric scan towards reduction of the fully oxidized medium. In fair agreement with the literature [171], the cathodic scan on Pt electrode revealed a two-stage one-one electron reduction of POM at the Epc1 and Epc2 waves. The current is first observed to peak at Epc1 (with value ipc1) indicating the first reduction wave of POM species. This is followed by a second reduction wave Epc2 (with value ipc2, respectively) and then drops due to depletion of the reducing species from the diffusion layer.

During the reverse scan, the reduced clusters at the electrode/sol interface undergo oxidation at the respective anodic waves Epa1, Epa2, involving lower integrated charge compared to reduction, probably because of the surface-limited nature of the oxidation process.

The electrochemical assessment of the band gap of molecular aggregates in sol may rely on the determination of the onset potentials of reduction and oxidation [175] from single cathodic and anodic voltammetric scans, respectively. Here the molecular LUMO is identified with the onsets of the Epc1 wave, while the HOMO is post-located via subtraction of the LUMO energy from the optical band gap (Fig.2.7b). The diagram in Fig.2.11b, indicating the molarity-dependent levels of POM

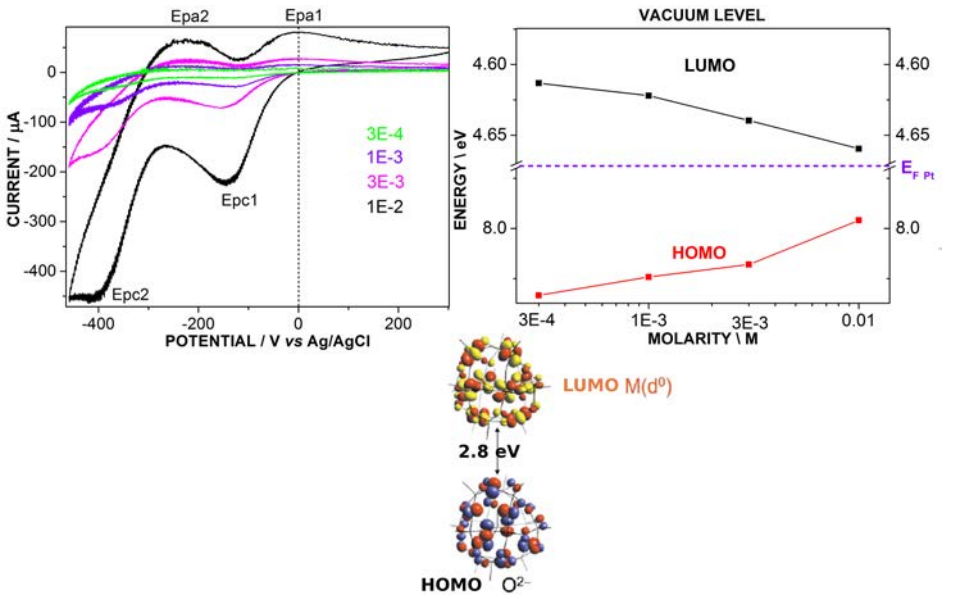


Figure 2.11: a) Cyclic voltammograms at a Pt stationary electrode for aqueous sols with varying POM concentration (scanning from +300 mV to the switching potential, 460 mV, and back at a scan rate of 150 mV/s, room temperature). b) Molarity dependence of energy levels for POM aggregates in sol and HOMO-LUMO spacing for the free POM molecule as estimated from ab-initio calculations in [161].

nano-aggregates was constructed on this basis. Note that charge transfer barriers at the electrode-solution interface may cause an overestimation of the relevant energies.

In any case, lowering of the LUMO level as aggregation proceeds (decreased reduction threshold), accompanied with an increase of the HOMO and a progressively narrower band gap (relative delocalization [176]) is observed. In Fig.2.11b the distance between the Fermi level of Pt electrode and the POM LUMO decreases when moving from small to bigger aggregates. Similarly to n-type doping, the main effect of carrier delocalization with increasing molarity is an increase in the free charge carrier density, which is associated with a shift of the Fermi level towards the molecular LUMO [177]. This practically stems from the reduction of POMs in the crystalized state due to the presence of crystallization water [156].

In order to evaluate the speed and reversibility of the redox process it is common to perform voltage sweeps at a set of different scanning rates. In general, the faster the scanning rate the shorter the diffusion

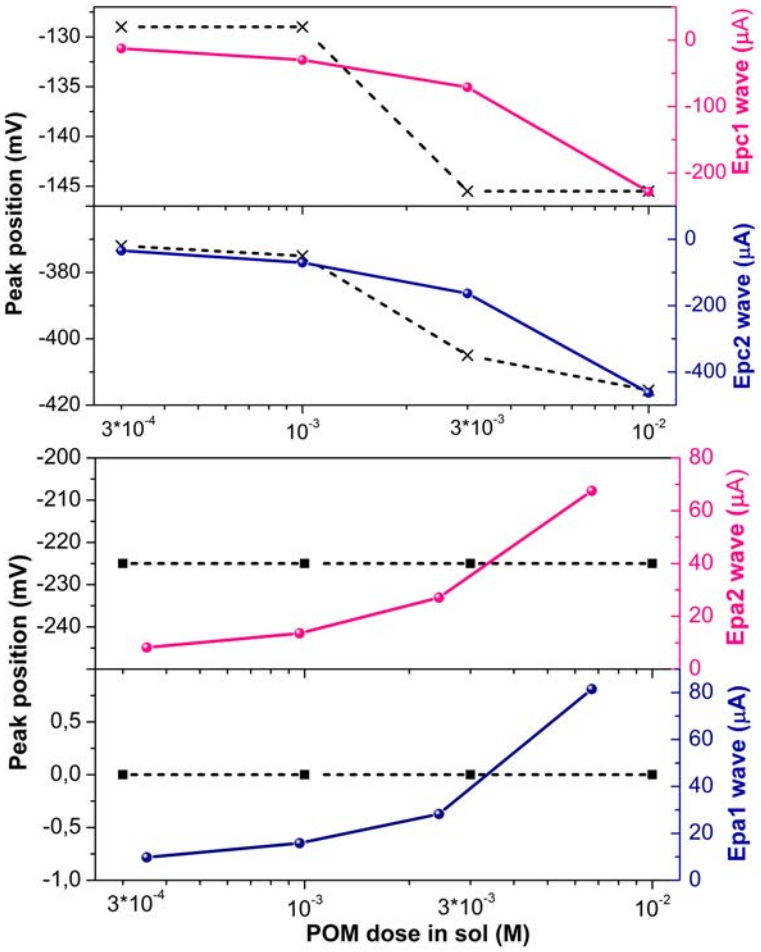


Figure 2.12: Potentials of emergence and current intensities of the two reduction (Epc) and oxidation (Epa) waves appearing on the cyclic voltammogramms versus POM molarity. Pt stationary electrode in aqueous sols, 150 mV/s, room temperature.

layer. In turn, the shorter the diffusion layer the greater the current. This dependency can be further quantified towards the extraction of the diffusion coefficient and, under circumstances, the size of the involved molecular clusters. As demonstrated in Fig.2.13 the Ipc1 peak height increases linearly with the square root of the scan rate, providing evidence for a chemically reversible redox process with rapid electron transfer kinetics.

Taking in mind the above linearity and, thus, assuming that the POM redox reaction does not cause major structural change in the analyte

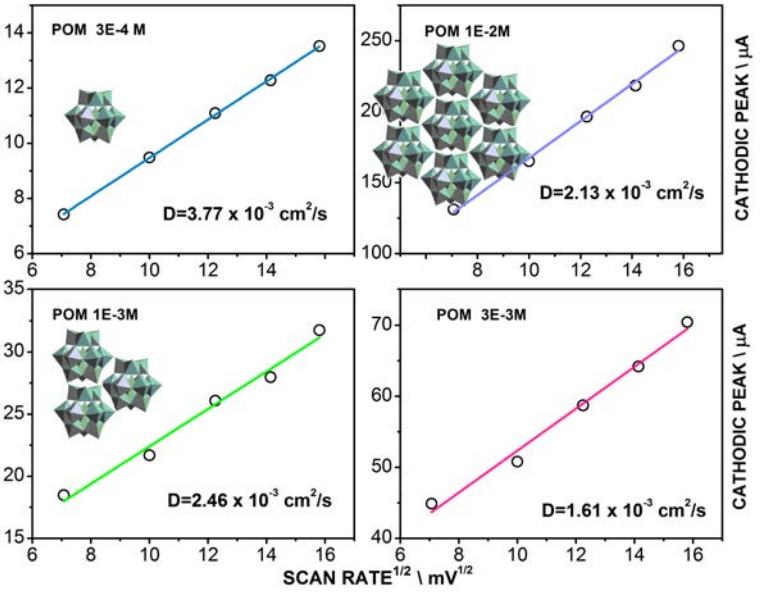


Figure 2.13: Plot of peak height for POM reduction vs the square root of scan rate for various molarities at room temperature. The diffusion coefficient for each molarity is calculated via the slope of the least square linear fit.

and that the electron transfer rate is rapid enough, the current ipc will be directly related to diffusion rate of reduced species from the electrode surface according to the Randles-Sevcik equation [178]:

$$ipc_{peak} = 269 \cdot n^{3/2} A D^{1/2} \left[\frac{dV}{dt}\right]^{1/2} C_{bulk} \qquad (2.1)$$

The peak, though, as already commended in Fig.2.11, does not occur at exactly the same voltage for all rates as in ideal reversible reactions, owing to the modification of the reduction onset due to the different crystallization extent of POM molecules in solution. This response is attributed to the electronic structure modification of the expanding nanocrystals with increasing molarity, and does not imply electrode reactions with slow electron transfer kinetics. The high diffusion coefficients calculated for POM compounds in solution (two orders of magnitude higher than commonly expected for medium size molecules in water) are directly related to the phenomenological loss of electrochemical reversibility, a result that has been recently demonstrated in [179].

For particles or large molecules in a viscous fluid (usually a liquid solution), the Stokes-Einstein equation [180] can be applied:

$$D = \frac{kT}{6\pi\mu r} \tag{2.2}$$

Here, k is the Boltzmann constant, $\mu$ is the solvent viscosity, and r is the radius of the diffusing particle. This equation is derived on the assumption that the particles obey Stokes' law for drag, such that the drag exerted on diffusing molecules, by the solvent molecules, can be computed. To avoid utilization of a viscosity constant we will restrict ourselves in the calculation of the absolute ratios of the effective POM nanocrystal volumes. From the calculated Ds we, thus, get: $V_{3E-4}/V_{1E-3} = 1/3.6$, $V_{3E-4}/V_{3E-3} = 1/12.9$, $V_{3E-4}/V_{1E-2} = 1/5.6$.

The increased D and, therefore, the decreased effective volume in higher concentrations can be understood as result of the increased conductivity (through delocalization enhancement). This is an electronic structure modification accompanying the increase of the size of POM nanocrystals. The concomitant decrease of reduction threshold for large NCs causes a boost on the electrophoretic mobility $\mu_e = v_{drift}/E_{applied}$, which is inversely proportional to the apparent viscosity of the analyte according to the Smoluchowski relation [181]. This is translated as larger value for D.

The increase of the effective surface of the nanocrystals, causing enhancement of electron exchange with the electrode can also amplify the phenomenon. A similar effect has been reported in [182] where thicker compound films exhibited larger D values. Changing the type of electrolyte and/or solvent had no effect on this result. The increase was interpreted as being a result of an increase in the loading capacity of the dopant within the film and the possible existence of channels in the relatively thicker films, which contributes to the increase of electrolyte interaction with the inner parts of the film.

## 2.4 Insulator-to-Semimetal transition under vertical tunneling

### 2.4.1 The utilization of Scanning Tunneling Microscopy

STM constant-current maps illustrating locations of high tunneling current are used to gain information on variations of the Local Density of States (LDOS) and topography of POM-modified $SiO_2$/n+Si surfaces. A tunneling current feedback is used in this imaging mode. When positive bias is applied on the backgate no image is obtained due to electronic occupancy of POM metallic centers and screening, as POMs are

already partially reduced in film [183]. Moreover, the relatively high tunneling barrier of the $SiO_2$/APTES back-stack hinders electronic transport through the structure (Fig.2.14a). However, when negative bias is applied, electrons tunnel from occupied states of the POM molecules towards the tip, and the resulting image exhibits bright regions illustrating the surface distribution of POM charging sites (Fig.2.15b-Fig.2.15d, Fig.2.14e). In Fig.2.15e the film is tipped up locally using an STM tip, revealing the packing of POM NCs in the form of vertically stacked 2-D lattices creating an ordered state.

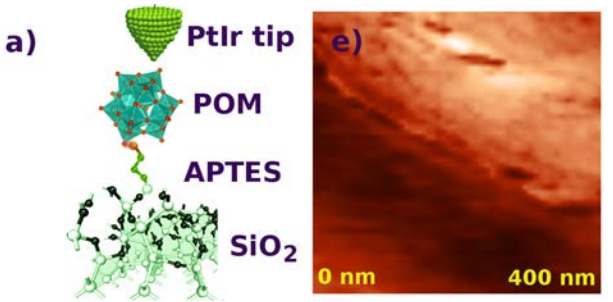


Figure 2.14: (a) Scheme of the tunneling stack. (e) Scratch on the 0.01 film imaged at -1.6V demonstrating the ordered stacking of POM NCs.

The scratch boundary is evident as a dark crevice, enhancing contrast and revealing the films cross section. For precursor concentration $1 \times 10^{-2}$ M (Fig.2.15b) the lateral size of NCs is determined as 10 nm (see Section 2.6), whereas higher POM concentrations, in the order of $5 \times 10^{-2}$ M (Fig.2.15c) and $1 \times 10^{-1}$ M (Fig.2.15d) result in the electronic coupling of POM NCs leading to boundary fusion and a more extended density of states. A concentration-dependent transition is monitored, thus, from a system with strongly localized electron states to one with itinerant electron states on larger areas. Apart from lower film resistivity, the latter can result from stronger coupling to the metallic probe.

The aforementioned structural transformation amplifies the free-carrier concentration and manifests itself as a two-orders-of-magnitude vertical current amplification in the low ($< 2$ V) voltage regime and four orders of magnitude at 3 V between the $1 \times 10^{-1}$ and $1 \times 10^{-4}$ M films (Fig.2.15f). This addresses the long standing challenge of contact formation to molecular components [184, 185] through the tunability of highest occupied molecular orbitals (HOMOs)lowest unoccupied molecular orbitals (LUMOs) of POM assemblies.

The electronic structure of POM NCs upon intermolecular and molecule-substrate interactions is investigated via the differential tunneling conductance (dI/dV, DTC) spectra (Fig.2.15g). DTC plots on single POM

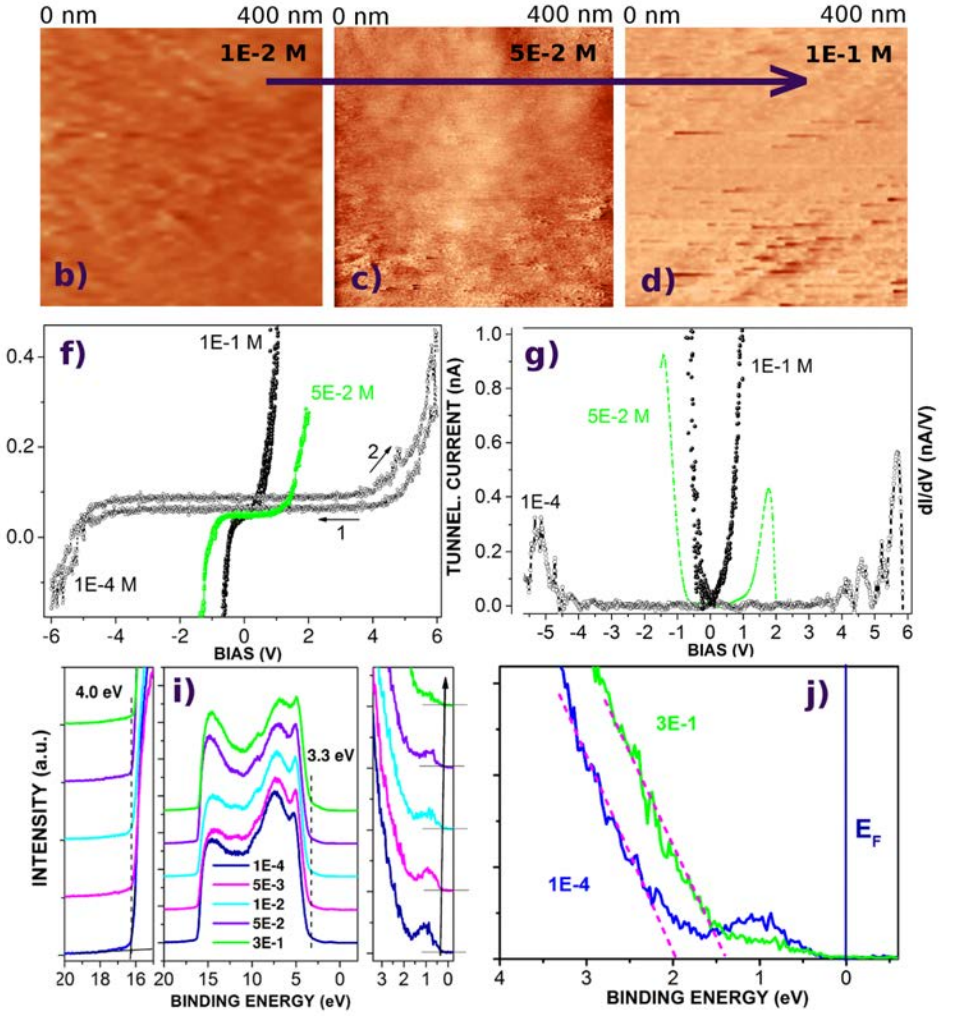


Figure 2.15: (b)-(d) STM topographic images ($400 \times 400 nm^2$, (b) bias: -1.6V, (c) (d) bias:-1.7 V, constant current mode) of 0.01, 0.05 and 0.1 M LbL-grown POM layers respectively, on native $SiO_2$/n+Si. (f) STS I(V) spectra and (g) differential conductance dI/dV spectra on single POM NCs immobilized on $SiO_2$. (i) Valence-band spectra for varying concentration. On the right the region near the Fermi level is shown in magnication, and on the left the high binding energy cut-off. (j) Region around Fermi level for two molarity extremes, depicting the shift of valence band towards $E_F$ and the quenching of localized states.

NCs self-assembled on $SiO_2$ are shown in Fig.2.15g with respect to the applied bias for three different molarities. For low molarity ($1 \times 10^{-4}$ M) the LDOS includes a large gap and five distinct intra-gap peaks, v1, v2 on

the valence band side, and c1 to c3 on the conduction band side, corresponding to the contribution of discrete electronic states. This multiplet structure appears above voltages of approximately 4 V and points to a molecule-like electronic configuration.

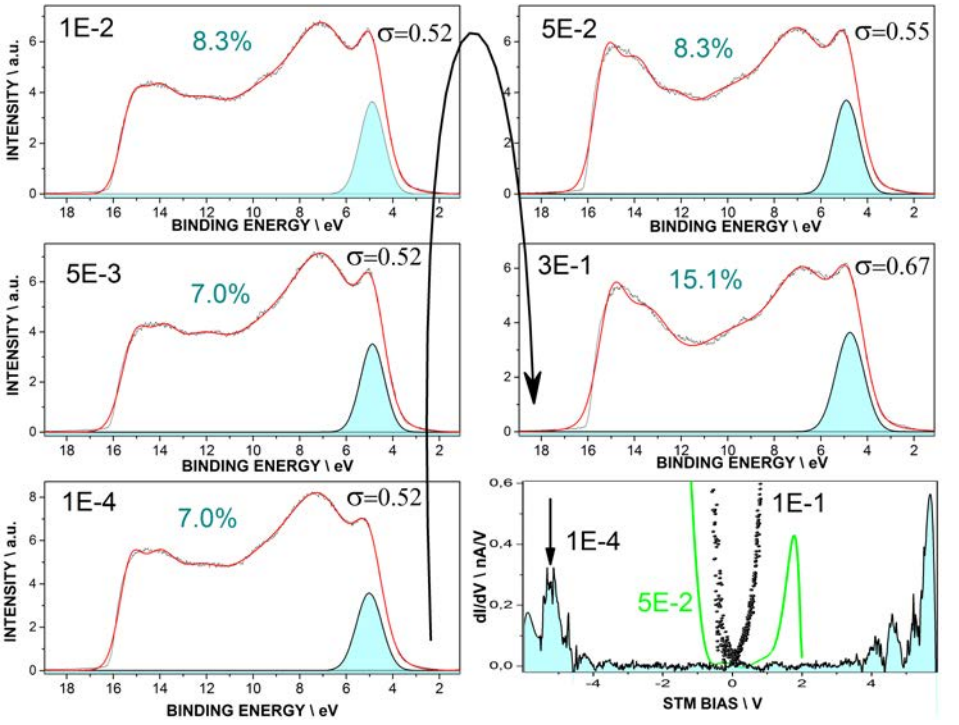


Figure 2.16: Valence-band spectra of molecular hyperstructures with increasing (according to the arrow) concentration. Deconvolution of the signal in the constituent Gaussians [153] probes the shape and contribution of HOMO MOs in light blue; Bottom right: dI/dV STS curves depicting the full local low energy DOS for three different molarities.

The shape of substrate/molecular donor and acceptor states and the resultant bandgap are clearly varying with the concentration of POM molecules in the precursor; as concentration increases and NCs enlarge, the gap gets progressively narrower, with the Ec and Ev almost joining at 0 V for the 0.1 M samples. This is directly related to the presence of itinerant electronic states in STM constant-current maps. There was no evidence of discrete electronic states for high molarity samples. The small asymmetry of the dI/dV plots with respect to zero bias, observed for some clusters, is typical of the presence of contact potential between the cluster and the substrate [155].

The I-V spectra in Fig.2.15 demonstrate the transition from a molecule-

like electron configuration for low POM molarity ($1 \times 10^{-4}$ M) towards itinerant electron configurations for higher molarities at RT.

Since, typically, the main mechanism of energy level formation in transition-metal ions is related to strong Coulomb interactions among d-electrons [186] (here 5-d electrons), these orbitals are further analyzed via XPS. In Fig.2.17 the $W_{4f}$ signal is broadened towards lower binding energies (BEs) with decreasing molarity, suggesting the presence of W in oxidation states lower than 6+ [187].

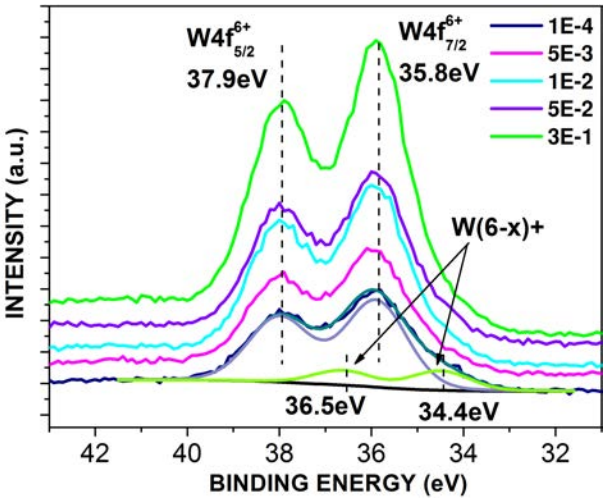


Figure 2.17: XPS W4f core level spectra showing the electronic identity of metallic centers in POM molecules. Contribution of W atoms in oxidation state +5 or lower is evident in the deconvolution of signal for low molarities.

Indeed, deconvolution of the spectrum identified the presence of a second doublet, apart from the major components of W(6+) doublet at 35.8± 0.1 eV ($W_{4f7/2}$) and 37.9 ± 0.1 eV ($W_{4f5/2}$). This is located at 34.4 ± 0.2 eV and 36.5 ± 0.2 eV, corresponding to 20% of the overall W for $1 \times 10^{-4}$ M films. The presence of W in oxidation states (6-x)+ is indicative of a dominant reduction of POM molecules, prominent for on-site Coulomb interactions between nanocrystalls (NCs).

The factor determining whether an atomic multiplet or energy bands (as in higher molarities), will form is the competition between the Coulomb energy and the kinetic energy associated with electrons hopping from site to site in POM hyperstructures. When the two terms compete, complicated electron states as in $1 \times 10^{-4}$ M films (Fig.2.15g) are often observed. These are manifestations of electron correlation [183] directly visualized via scanning tunneling spectroscopy [188].

In Fig.2.16 the valence band spectra of POM hyperstructures on $SiO_2$ exhibits two pronounced low energy emission features at 4.5 and 6.4 eV attributed to O2p-derived band (4.5 eV, HOMO) and O2p-W5d hybridized states (6.4 eV), respectively [189]. The low energy valence band data have been fit using a model of two Gaussian peaks, chosen based on the expected contributions from O2p and O2p-W5d states. The full range valence band fit consists of six Gaussians, a fact justified for empirical reasons; for example, use of a five-peak model does not adequately fit the valence band edge, and a seven-peak model does not further improve the quality of the fits [190].

The HOMO peak position for concentration $1 \times 10^{-4}$ M in the STS is consistent with the HOMO peak position in UPS. For higher concentration films, though, divergence between local and collective electronic properties becomes pronounced, leading to striking differences on HOMO DOS probed with the two methods. This observation lies in the very core of the impact of intermolecular interaction on band formation and is attributed to the increasing influence of long range interactions between nanocrystals for higher molarities.

The HOMO, highlighted in light blue, broadens with increasing crystallization extent due to the larger overlap of the involved molecular orbitals (MOs). The bandwidth is directly related to the spatial spread of MOs [153]. The percentage of these low BE, bulk-related [153] orbitals increases with higher molarity. At the same time, as seen in the XPS spectra of Fig.2.16, the arising intragrain semi-metallic response for molarities above $5 \times 10^{-2}$ M is accompanied with a pronounced enhancement of the percentage of surface (high BE) MOs, directly detected via XPS, highlighting the importance of surface states on the electronic properties of high molarity films.

The UPS, UV-Vis absorbance and UV-Vis reflectance derived electronic structure of the molecular hyperstructures is presented in Fig.2.18, where the transition point for detection of insulator to semi-metal transition in mesoscopic scale is depicted.

## 2.5 Collective electronic properties of POM hyperstructures: Intra- and inter-grain characteristics

A convenient way to quantify the collective electronic response of a granular network is the consideration of characteristic energy scales, such as the mean energy level spacing for a single NC ($\delta$), the Thouless energy ($E_T$), the charging energy, as well as the electron life time within a single NC [191, 192].

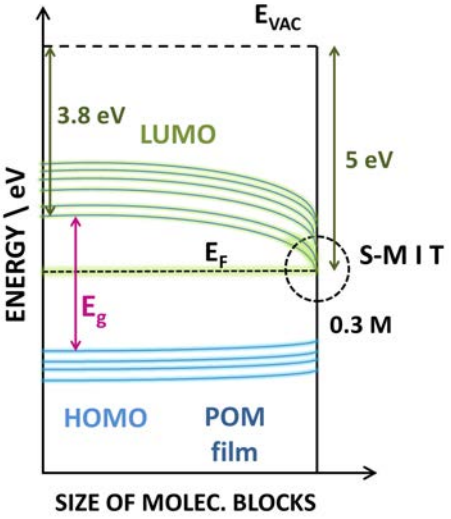


Figure 2.18: Scheme of the spectroscopically-derived electronic structure of POM hyperstructures with varying molarity translated in varying size of molecular building blocks. The point of SMIT transition is highlighted in circle.

The value of $\delta$, corresponding to the average spacing between subsequent single-particle energy levels [193], can be obtained from the density of states ($\nu$) and the NC volume (V) through $\delta = (\nu V)^{-1}$ [191]. In turn, $\nu$ is obtained from the density per unit volume and energy of the number of solutions to Schrödinger's equation (DOS$\sim \sqrt{E}$) and the experimentally obtained dimensions and Fermi level of POM NCs.

At RT (294.5 K) for a POM NC of a mean diameter of 17 nm, corresponding to molarities of $3\times10^{-2}$ M, $n = 8.94\times10^{46}\, cm^{-3}J^{-1}$ and the corresponding $\delta$, 0.027 meV. Since the temperature of the system ($k_B$T=0.025 eV) is quite lower than $\delta$, thermal fluctuations are suppressed and quantum size effects become important. For larger aggregates, though, the appearance of itinerary states (cf. Fig.2.15c, Fig.2.15d and UPS, XPS results) renders this rough approach unreliable and the discreteness of levels unimportant [157].

According to UPS and XPS evidence the POM molecules in $3\times10^{-2}$ M films are already partially reduced [183]. The charging energy, $E_{LUMO+1} - E_{LUMO}$, of the next available charging level for the cluster is higher than $\delta$ and is estimated to be $\triangle E = 0.257$ eV $>> k_B$T according to both electrical and voltammetric measurements [183].

Assuming quasi-ballistic movement of electrons inside the grains (intragrain delocalization), $E_T$ is given from $E_T = 2\hbar v_F/\alpha$, $2\alpha$ being the size of

the grains [192]. From UPS spectra $E_F = 4.42$ eV for POM assemblies on $SiO_2$ [183] and, thus, $T_F = 51291$ K, $v_F = 1.25 \times 10^6$ m/s. From these values we obtain $E_T$ for the electron motion within a grain as: $E_T$=193.11 meV. Under the same assumptions, the elastic scattering time within a single grain is of the order of $2\alpha/v_F$=13.6 fs at RT. Making use of the ratio of $E_T$ and $\delta$ the dimensionless intragrain conductance $g_o$ can be estimated.

$g_o$ is caused by scattering on impurities or on the boundaries of the grains and is, essentially, the physical conductance of a granule in units of the quantum conductance $2e^2/h$ calculated as: $g_o = E_T/\delta$=1715.64 >> 1 [192]. The dimensionless tunneling (intergrain) conductance ($g_T$) is much smaller ($g_T \sim 1 \times 10^{-10}$ to $1 \times 10^{-9} << g_o$) for all molarities, connoting weak coupling between NCs. Thus, whenever the $g_o$ calculation assumptions are valid, electrons are always localized and the main contribution to macroscopic longitudinal resistivity comes from the tunneling barriers between NCs [30].

Collective electronic properties for the films are acquired via measuring the on-plane tunneling conductance $g_T$ for transport through POM NCs under appropriate circuitry (Fig.2.19).

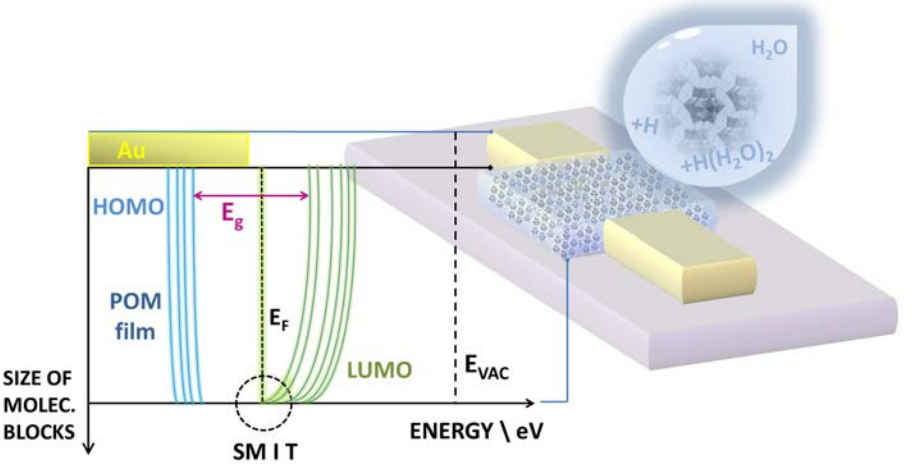


Figure 2.19: Planar nano-electrode addressing scheme and tunability of molecular hyperstructure serving as tunable injection barrier.

In specific, the molecular films are electronically addressed either via opposing nano-leads produced via e-beam lithography (an assembly producing highly non-homogeneous field due to intense fringing effects), or by overlapping parallel nano-leads (producing a relatively homogeneous field in the overlap area). In the first case the possibility of a single (or few) failure/conduction path is favored, while in the second we address

multiple conduction paths in parallel.

For all molarities and nanoelectrode topologies on-plane $g_T$ remains below 10 pS. Such low tunneling conductance ($g_T \sim 1 \times 10^{-10}$ to $1 \times 10^{-9} << 1$) falls in the regime of weak coupling between POM NCs and insulating behavior on plane. The lower the NC size the weaker the inter-crystal coupling.

The conductance of the system is given by $g_T^{-1} + g_o^{-1} \approx g_T^{-1}$, implying that the main contribution to macroscopic resistivity comes from the contacts between POM NCs. Since $g_T << 1$ the width $g_T \cdot \delta$ is smaller than the energy spacing suggesting that the discreteness of levels within grains is the relevant influence. The mean electronic lifetime in i.e. a $3 \times 10^{-2}$ M cluster is $\hbar/(g_T \cdot \delta) = 1.16\ \mu$sec. In short, electrons in POM NCs are always localized on plane, even at RT, implying impeded transport and enhanced Coulomb interactions for a wide range of T and V.

## 2.6 Estimating the Thickness of POM Hyperstructures

In order to obtain a more tangible comparison of the STS curves obtained on the different molarity POM hyperstructures, the thicknesses of these films must be measured.

However, the extraction of an accurate thickness value for the molecular hyperstructures is a non-trivial task. Given the fact that these structures are only weakly sorbed on the substrate (i.e. through electrostatic self-assembly and weak Van den Waals forces) any invasive thickness estimation procedure like contact force AFM would disturb the molecular hyperstructure, giving non-reliable results.

Furthermore, the measurement uncertainty due to the violent tip-film interaction would oversubscribe any thickness differences, particularly in the low molecular density films. Towards this goal other properties characterizing the hyperstructures, together with non-destructive optical and electrical measurements like SE, STM and high resolution tapping mode AFM have to be jointly utilized.

The combination of metrological results is performed on the assumption that the hyperstructure thickness coincides with the diameter length of the POM NC. This is a reasonable hypothesis, since crystallization of POM NCs in liquid is isotropic. The method facilitates the incorporation of results of surface topographies on the calibration of the film thickness.

The NC size estimation is based on the fact that each characterization method is optimal for a specific, usually quite narrow, molarity window. STM constant current mode scanning profiles can provide more

accurate lateral dimension estimations than contact AFM, while tapping mode AFM, is preferred for the determination of z axis profiles. The estimation of tapping mode AFM scanning profile-originating 2-D autocorrelation function provides an accurate estimation of the structural building blocks size, i.e. determines the size of single NCs on the film.

For POM-only hyperstructures, whose constituents framework is based on metal atoms (i.e. W) STM is a useful measurement, for relatively low molarities where clear grain edges are obtained.

### 2.6.1 via STM

For molarities where electrons are localized strictly inside the grain, NC size estimation can be performed from STM height profiles in constant current mode. This measurement, based on single spot electron tunneling during scan, avoids insertion of lateral error due to tip-sample dimension interaction and may give accurate results for limited molarity cases. The profile of the 0.01 M film is presented in Fig.2.20.

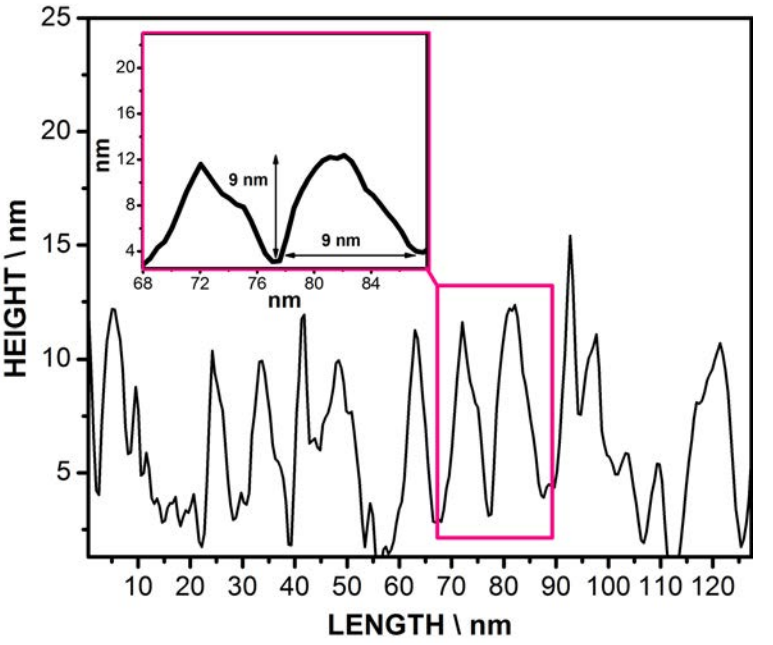


Figure 2.20: Line scan across the scanning direction of a low frequency 0.68 Hz 125×125 nm 0.01 M POM hyperstructure surface scan V=-1.7 V. The dimensions of two indicative grains are depicted in the inset. The mean estimated NC size for this resolution is of the order of 10 nm.

### 2.6.2 via Spectroscopic Ellipsometry

For the data analysis of the SE measurements the distributed POM nanoislands were considered to form a continuous, homogeneous layer. As such, the calculated thickness value for the POM layer corresponds to a mean effective thickness. The films optical parameters are calculated via fitting of the acquired relative phase ($\Psi$) and relative amplitude ($Delta$) spectroscopic values [194] (relative phase and amplitude of the parallel and perpendicular component of the reflected wave, expressing the state of polarization of the light as it is reflected from the sample) under the assumption of an isotropic and non-depolarizing sample. One approach to resolving the problem of non-unique solution to the $\epsilon_1$, $\epsilon_2$ and thickness determination for very thin films, [45] such as the POM molecular hyperstructures, is to obtain further data by varying a system parameter. Here we vary slightly the thickness of the molecular layer between two samples ensuring, though, that they have identical dielectric functions. More specifically, the method was applied for POM layers formed from precursor solutions of concentration 0.03 M and 0.04 M (the molar concentrations in precursor solutions define the resulting thickness in solid state). The concurrence of dielectric functions was suggested from the identical optical band gap [195, 196] as measured via UV-Vis spectroscopy for the layers.

In order to retrieve the common dielectric function and thicknesses we apply the multiple sample analysis mode of WVase software for SE [46] and model the molecules response function with appropriate oscillators with respect to its optical absorption spectrum. Iterative non-linear regression resulted in convergence of the fitting with a mean statistical error of 1.4. The effective thicknesses obtained by this method were 2.08 and 2.15 nm respectively. The resulting common dielectric function for the layers resembles that of the underlying Si, a fact reflecting the previously observed electronic coupling of the molecules to the substrate [197, 61].

In order to retrieve an estimate for the true absolute thickness of the layers we employ the equation $d = \epsilon_{POM} \cdot d_{eff}/\epsilon_{Si}$ that expresses the equivalence of polarizability in the true and the effective systems. The POM dielectric constant is calculated using the fact that its polarizability is mainly originating from the structure's crystallization water and the oxygen/air content of the assembled structure in a 1:1 analogy. After performing the involved numerics we estimate a thickness of 13.5 for 0.03 M and 14 for 0.04 M. Tapping mode AFM indicated that the measured grain size for $1 \times 10^{-4}$ M hyperstructures is half that of the $3 \times 10^{-2}$ M case, giving a rough estimate of 7 nm for $1 \times 10^{-4}$ M. This is in direct accordance to the AFM autocorrelation function analysis of the AFM

images. There, the spatial correlation length of the surface profile [58] ($L_c = 10\xi$) ($\xi$ =6.7 nm for $1 \times 10^{-4}$ M and $\xi$ =18.1 nm for $3 \times 10^{-2}$ M). $\xi$ is directly related to the size of the basic grain unit.

### 2.6.3 via FE-SEM

For the 0.05 M film the NCs are detectable via FE-SEM and a mean diameter of 17 nm is obtained. The NCs are assumed to be spherical due to their isotropic growth in solution. Thus, the film thickness can be estimated through the NC diameter in planar view. The corresponding topography is presented in Fig.2.21.

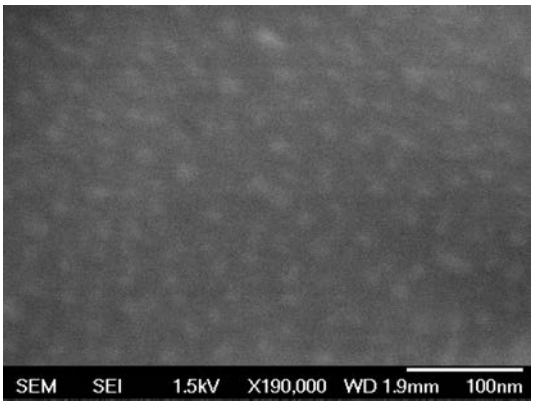


Figure 2.21: FE-SEM image 0.05 M POM, 45°, 1.5kV depicting the size of 0.05 M nanocrystals on $SiO_2$. Due to extended charging effects while scanning with the electron beam the contrast is poor, and NC size is expected to be slightly overestimated. Considering only the sharpest of the edges the top-view 2-D estimation for the size of NCs is 17 nm.

We use these values to extract an empirical thickness versus molarity relation for the self-assembled POM hyperstructures. In Fig.2.22 we can see the agreement of the experimentally obtained thickness values on common graph with the extracted relationship.

The fitting function is selected to be in accordance with the experimentally derived bandgap vs molarity relation for POM films ( Fig.2.23).

Interestingly, the resulting general shape of the bandgap vs thickness relation is in accordance with theoretical predictions for arrays of quantum-confined semiconductor structures with size-dependent band gap obtained using the potential-morphing method PMM within the effective mass approximation and assuming finite-depth square-well confining potentials for both electrons and holes [198].

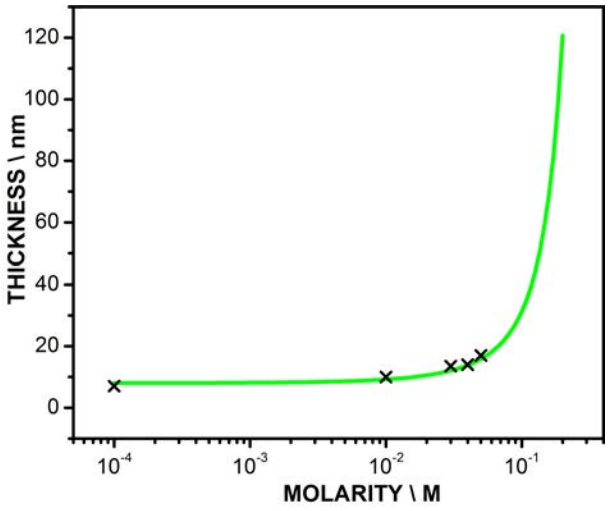


Figure 2.22: Thickness versus molarity derived rule and obtained experimental data spanning three orders of POM molarity magnitudes.

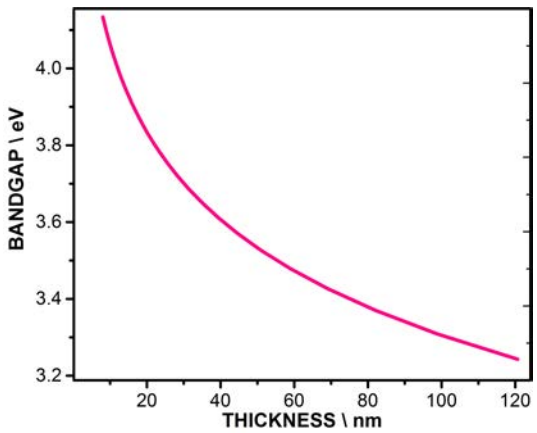


Figure 2.23: Thickness vs bandgap experimentally derived relation.

## 2.7 Size-dependent SET in chains and arrays of POM NCs

Irregularities on grain position and tunneling coupling strength become crucial in the limit of low coupling [30], shown above to be the case between NCs in POM hyperstructures. At the same time, it is vital for few electron based applications that any such irregularities would not nullify Coulomb blockade phenomena and/or single level transport in POM films.

In Fig.2.24a we employ an opposing nanoelectrode configuration to study possible single NC regulation of current on plane. No current is flowing in the absence of the molecular layer at the investigated voltage range. It is estimated that 1 to 4 molecular NC chains participate in transport in all molarity cases under this topology (see Section 2.6). Typical staircase current-voltage (I-V) characteristics for 25-nm-spaced opposing Au nanoelectrodes are illustrated in Fig.2.24a, as measured at 200 K for films of varying molarity.

With increasing bias the current increases in steps, indicating resonant tunneling through single NC levels. Each current step probes a splitting between quantized energy levels in the molecular structures [199]. This splitting becomes smaller with increasing concentration (see Section 2.8), reflecting the increase of the size of molecular clusters and/or the strengthening of inter-island coupling [200].

Registering the differential conductance dI/dV, is illustrative in this connection, since it is proportional to the density of states being occupied at the tunneling electron energy E = $E_F$ + eV. In Fig.2.24b, single electron transport is detected from the differential conductance peaks in electron tunneling through POM NCs [201]. The POM molecular quantum wells are located between source-drain (Au) electrodes and are separated by tunneling barriers (air) in a multi-junction hyperstructure. Since the POM charging energy is quite strong (i.e. LUMO-LUMO+1=257 meV) it forbids double occupancy of the molecular level leading to single level tunneling [201].

We consider the case where we get no charge accumulation within POM NCs, i.e. the shell tunneling regime [201]. This is a rational approximation since electron delocalization in POMs occurs on the external metallic framework. For absence of accumulation the tunneling rate for the first tunneling barrier should be lower than the next [201]. In other words this is the barrier regulating transport. Making these assumptions the FWHMs resulting from the Fermi-Dirac smearing can be analytically estimated as 3.525 kT [201]. We find a linear relationship between the FWHMs and the molarities of POM in films, displayed in Fig.2.24d.

Since the FWHM in dI/dV features is significantly larger than the FWHM expected for single level tunneling due to the thermal broadening (Fermi-Dirac smearing), comparison of the two allows for straightforward estimation of the number of tunneling electrons that enter simultaneously the levels of POMs in NCs [202]. In such a way we get to obtain an estimation of the number of the active molecular sites that are involved in the tunneling process through NCs. The results suggest approximately 4, 5, and 6 discrete sites for the 7nm, 8nm and 12 nm NCs respectively and are indicative of size-dependent SET operation in POM hyperstructures.

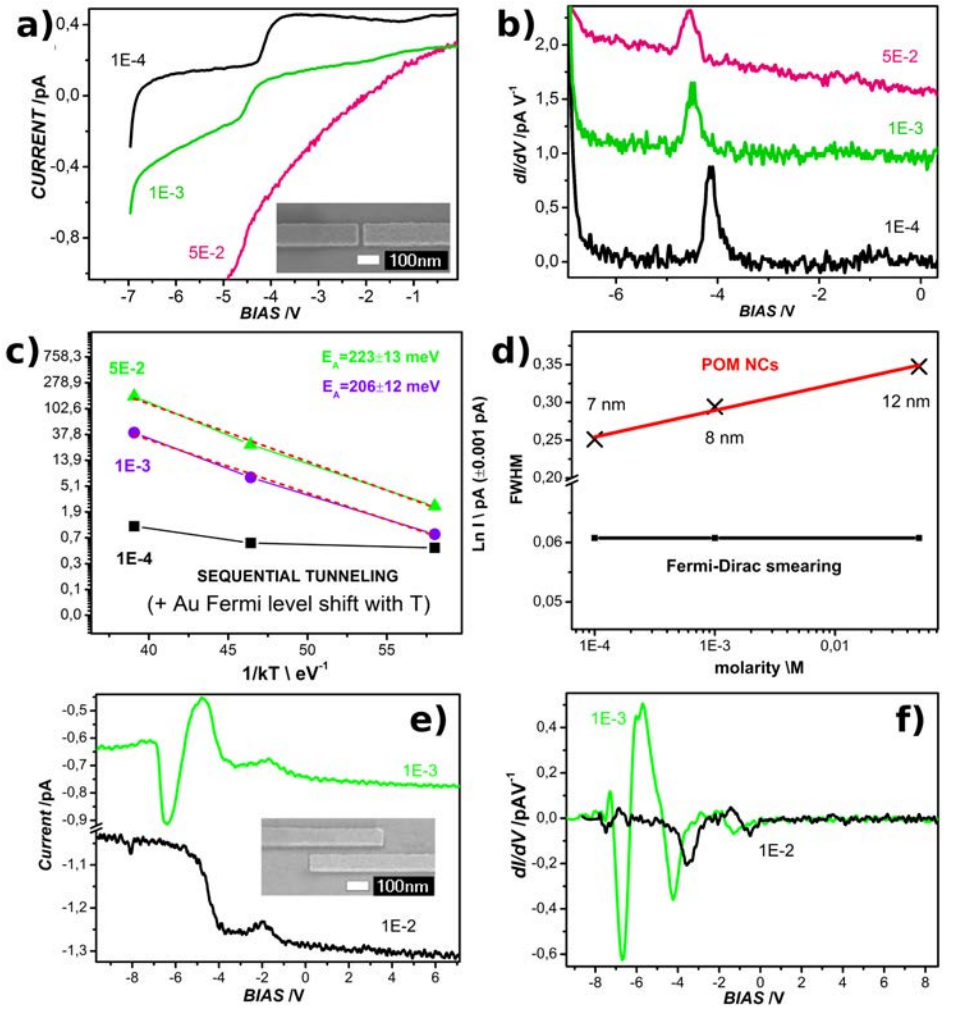


Figure 2.24: a) I-Vs at 200K for three different molarities corresponding to different size of molecular nanoaggregates between 25 nm-spaced opposing electrodes; b) Corresponding dI/dVs; c) Arrhenius plots and extracted activation energies; d) FWHMs of the dI/dV peaks; e) I-Vs at 200K for 50 nm-spaced overlapping nanoelectrodes and f) Differential conductance highlighting the Coulomb oscillation period.

Discrete level tunneling is observed at the scans starting polarity (i.e. here at negative bias) but not at the opposite one (See Section ). This stems from molecular charging and charge retention on POMs and is a demonstration of molecular rectification. In Fig.2.24c Arrhenius plots for hyperstructures of different molarities in the positive voltage regime (+6.9 V) highlight a transition from temperature-activated to sequential

tunneling transport by reducing molarity (i.e. NC size). High molarity structures exhibit common activation energy (Ea) despite their almost 2 orders of magnitude difference in M. The calculated Ea closely matches the LUMO-to-LUMO+1 transition (257 meV) indicating thermally activated transport mediated once again by single molecular levels.

In Fig.2.24e we employ overlapping nano-leads addressing 50 × 500 $nm^2$ arrays of POM NCs. Thus, in this case we massively address a 2-D matrix of several chains in parallel. Two dominant Negative Differential Resistance (NDR) features are being monitored while transport is significantly suppressed. This is a manifestation of discretized charge transfer through inter-crystal barriers within the Coulomb blockade regime [203].

The dominant NDR IV pattern (Fig.2.24e) has a periodicity (Fig.2.24f), reflecting the NC levels spacing ($\Delta$). In this case $\Delta$ is independent from concentration (i.e. from NC size and carrier density), remaining the same for molarities of $1 \times 10^{-3}$ M and $1 \times 10^{-2}$ M. This probes to 2-D transport where the level spacing is independent from carrier concentration [204]. The estimated $\Delta$ (~3 V) corresponds to a self-capacitance of $1.1 \times 10^{-19}$ F for a single NC translated to a droplet of diameter of 6.8 nm. This is exactly the size of spatial correlation length $\xi$ calculated in Fig.2.10f and corresponds to the size of the basic structural unit, when intra-grain topographic information is preserved. With decreasing POM NC size, the resonant tunneling peaks are shifted to higher voltages (quantization enhancement) and higher energy levels become accessible.

For both topologies there is no symmetry under inversion of the I-V curve, implying non-symmetric transmission function. This stems from molecular charging and charge retention on POMs and is a demonstration of molecular rectification in POM hyperstructures. The rectification ratio is increasing with decreasing NC size (Fig.2.24h). The voltage division factor (n) can be estimated from the positions of the first peaks on the negative bias [205] and is 0.5 for 12 nm NCs and 0.2 for 8 nm.

Moreover, the quasi-static I-Vs of the system as the aggregation of POM building blocks proceeds (see Section 2.8 for full I-V characteristics) highlight the amplification of the system's conductance. The effect is sharper in vertical transport, where the current is not affected by inter-crystal coupling, and manifests itself as a two-order-of-magnitude current amplification in the low ($< 2$ V) voltage regime and four orders of magnitude at 3 V between the $5 \times 10^{-2}$ and $1 \times 10^{-4}$ M films. This addresses a significant molecular device problem, namely the efficiency of contacts coupling to molecular components [184, 185].

## 2.8 Low-Dimensional Transport

The number of conducting channels is NC size-dependent. Based on the results of Fig.?? this means that for the case of opposing nanoelectrodes and large molarities (i.e. 0.1 M) a single NC covers the gap and at max 3 NCs can be probed in parallel, while for low molarities (i.e. $1 \times 10^{-4}$ M) a chain of 3-4 NCs bridges the gap while 12-14 chains can, in principle, be addressed in parallel. The morphology of electrodes has been tested extensively with FE-SEM. It has been found that the 25 nm spacing between electrodes always results in well-defined and well-separated electrode fingers. Edge roughness has been measured at ± 3 nm for our electrodes.

The roughness effect on the NC matrix size should statistically cancel out for the 2 $\mu$m overlapping electrode region, where tenths of NC chains are addressed in parallel. For example the radius of low molarity NCs ($\sim$ 3.5 nm) is of the same order as the roughness. So statistically (equal mins and maxs) the total number of NPs within the gap does not change under the presence of roughness for the 0.5 $\mu$m overlapping electrodes. At the same time, several equidistant chains forming a 2-D matrix are addressed in parallel so, undoubtedly, a 2-D system is addressed.

For opposing electrodes, on the other hand, where only few chains are probed, roughness can result in the presence of one NC-shorter conduction paths which would be favored and make a measurable difference in whether transport characteristics would be 1-D or 2-D. If we assume close NC packing and consider 3 equiprobable chain schemes, namely 1) left nanoelectrode periphery height min-to-right nanoelectrode periphery height min, 2) height min-to-height max, 3) height max-to-height max, the nodes favorable for conduction (max-to-max cases) are reduced to 4 (12/3) for low molarities.

This scheme is applicable up to molarities as high as 0.01M (4.5 nm radius) where the number of chains is reduced to 1. For higher POM NC radius roughness plays negligible role, but then we have anyway a max of 3 chains. This means that 1-D DOS features, even though occasionally broadened or disrupted, will be detectable.

Similarly to other two-dimensional (2D) octahedral semiconducting transition metal compounds as dichalcogenides [206, 207], sharp peaks in conductance (DOS divergence) can originate from parallel (band nesting) or very flat conduction and valence band points. It has been proposed that the divergence in conductivity due to band nesting is unique in low dimensional systems [207]. Nesting of the conduction and valence bands in 2D systems leads to a singularity in the joint density of states (JDOS) and corresponding divergence in conductivity [207].

For a single molarity ($5 \times 10^{-2}$ M) the T-regime of temperature-activated conductance as well as the progressive opening of a Coulomb gap under dynamic voltage scan by lowering the temperature can be seen in Fig.2.25.

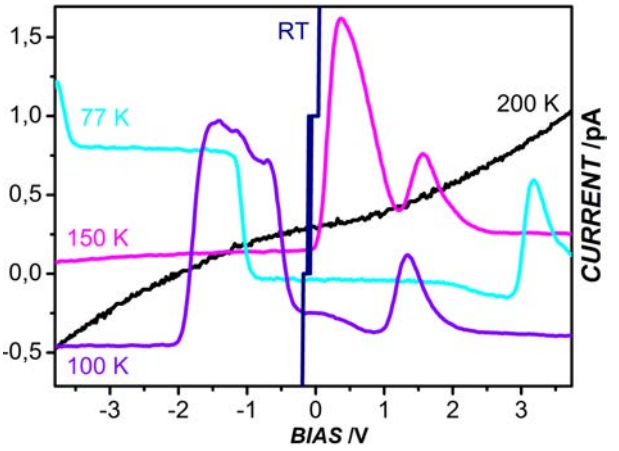


Figure 2.25: I-Vs of $5 \times 10^{-2}$ M films at different temperatures under dynamic voltage scan for opposing electrodes.

Dynamic scan refers to voltage ramp type scanning with a relatively quick scanning rate of 30V/s which does not allow relaxation (i.e. de-excitation) of the molecular structures. Well-developed local maxima and blockade regions are being formed below 200 K.

The tunneling-forbidden region is restricted with increasing temperature, while the Coulomb gap gets progressively narrower, with the conduction peaks almost joining at 150 K. After this temperature thermally activated transport becomes accessible. Variation of blockade regime with temperature proves its Coulomb nature, highlighting the importance of Coulombic forces on bandgap formation mechanism.

For or overlapping electrodes NDR is observed at negative bias (Fig.-2.24f) but not at positive ones. The effect depends on the scanning polarity. The scan starts from negative to positive bias but it could as well be the other way around (i.e. NDR at positive bias) if the scanning direction was from positive to negative. A natural question arising here is why not having NDR at both negative and positive regions since the junction is symmetric. This is a direct consequence of charging.

If one takes a closer look at the I-Vs of Fig.2.24e he can see that, after the specific discrete levels available for charging (through critical points) have been probed (NDR region), slow discharging of POM molecules is observed as leakage current during the opposite polarization scan. This explains the slightly lower resistivity in the opposite polarity region. This

response is a sign of the charge retention ability of POMs.

Naturally, the same non-symmetric response is the case for opposing nanoelectrodes. The full (positive and negative) voltage on-plane I-V characteristics of Fig.2.24a for opposing 25-nm-spaced nanoelectrodes are presented in Fig.2.26.

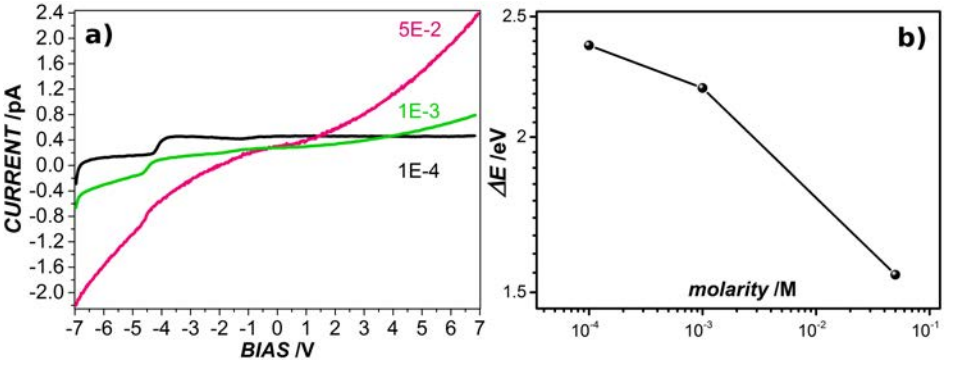


Figure 2.26: (a) Bipolar I-Vs on plane at 200K for three different molarities corresponding to different size of molecular nanoaggregates between 25 nm-spaced opposing electrodes; (b) Variation of energy level splitting in POM hyperstructures of (a) with increasing concentration in the precursor at 200 K under quasi-static voltage scan.

The resolution of HP4041B pA meter is ± 0.001 pA (1 fA). No current is flowing in the absence of the molecular layer at the same applied voltages.

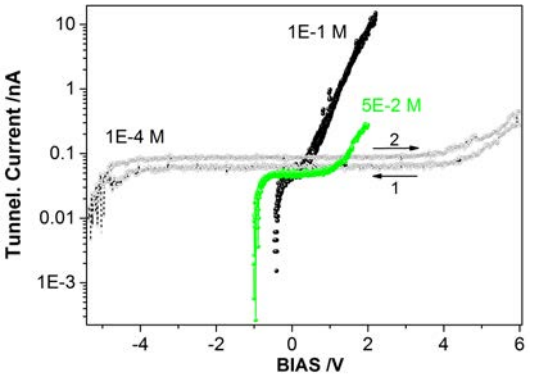


Figure 2.27: Bipolar I-Vs through NC (vertical tunneling) at RT in semi-logarithmic scale highlighting the size evolution of STS spectra.

## 2.9 Conclusions & Emerging Applications

The findings of this work suggest that the two-stage bottom-up self-assembly of tungsten polyoxometalates in ambient conditions represents an alternative approach to produce nanodevices with consistently tunable performance characteristics, bridging the gap between disorder and scaling-up in solution-derived films. Owing to the weak inter-crystal as well as inter-layer coupling, the produced structures largely preserve their original single-NC properties on plane, modified only by long range Coulomb interactions between neighbors. This feature is beneficial for applications related to information storage, where intergrain tunneling and, thus, bit loss should be efficiently suppressed.

By extending the crystallization extent the intra-grain electron-electron interactions are enhanced to the point where itinerary correlated electrons appear in previously strongly localized electronic states and a dimensional crossover driven SMIT is enforced under vertical transport. The extreme electronic bandgap modification for transport through the PtIr/POM/APTES/$SiO_2$/Si stack stems from both intragrain electron-electron interactions and PtIr/POM coupling. This is translated in extreme tunability of the coupling coefficient of POM molecules to the injecting leads by solely dimensional means. Thus, interface alignment and stack performance can be directly tuned via the extent of crystallization in the molecular film. This concept is directly applicable for interfacial electron/hole injection layers to boost carrier separation efficiency in OPV stacks.

Careful control over POM crystallization can yield solution-printed molecular hyperstructures with transport properties of extreme tunability and selectivity and figures of merit on par with their single-NC counterparts. Precision control over crystallization is a major asset for devices, since the electronic coupling between adjacent molecules and the intrinsic mobility are primarily governed by the molecular packing arrangement [148, 149].

For low molecular densities, STM revealed the existence of electronic states strongly localized on plane, owing to very weak inter-crystal coupling. As aggregation proceeds, the increasing influence of intermolecular interactions pushes the system towards a state of progressively increasing correlation under vertical transport. This transformation amplifies the free-carrier concentration and manifests itself as a two-orders-of-magnitude vertical current amplification in the low ($< 2$ V) voltage regime and four orders of magnitude at 4 V between the $1 \times 10^{-1}$ and $1 \times 10^{-4}$ M films.

This addresses a significant challenge, namely the problem of contact formation to molecular components [184, 185] through the tunability of HOMOs and LUMOs of POM assemblies. Being able to transport or confine charge at will, these hyperstructures constitute better candidates for circuitry components and transistor channels.

In plane, on the other hand, electronic states are always strongly localized, owing to weak inter-crystal as well as inter-layer coupling. Thus, electrons in POM NCs are always localized on plane, even at RT, implying impeded transport and enhanced Coulomb interactions for a wide range of T and V.

This is beneficial for information-storage applications where preservation and retention of information is a key feature. Selection between 1-D and 2-D planar transport is possible as well and depends on the choice of addressing leads. This later property can be directly exploited for new efficient bit addressing and reading configurations, paving the way to potentially novel information addressing architectures.

Moreover, the structures realized this way have properties particularly tolerant in disorder. Due to their highly symmetric Keggin structure [150, 151] they are able to form self-assembled films with building blocks of controlled crystallization extent and collective electronic properties on par with their molecular building blocks. They are, thus, promising for solution-printed molecular semiconductor films with electronic properties of noticeable tunability, high stability and predictability.

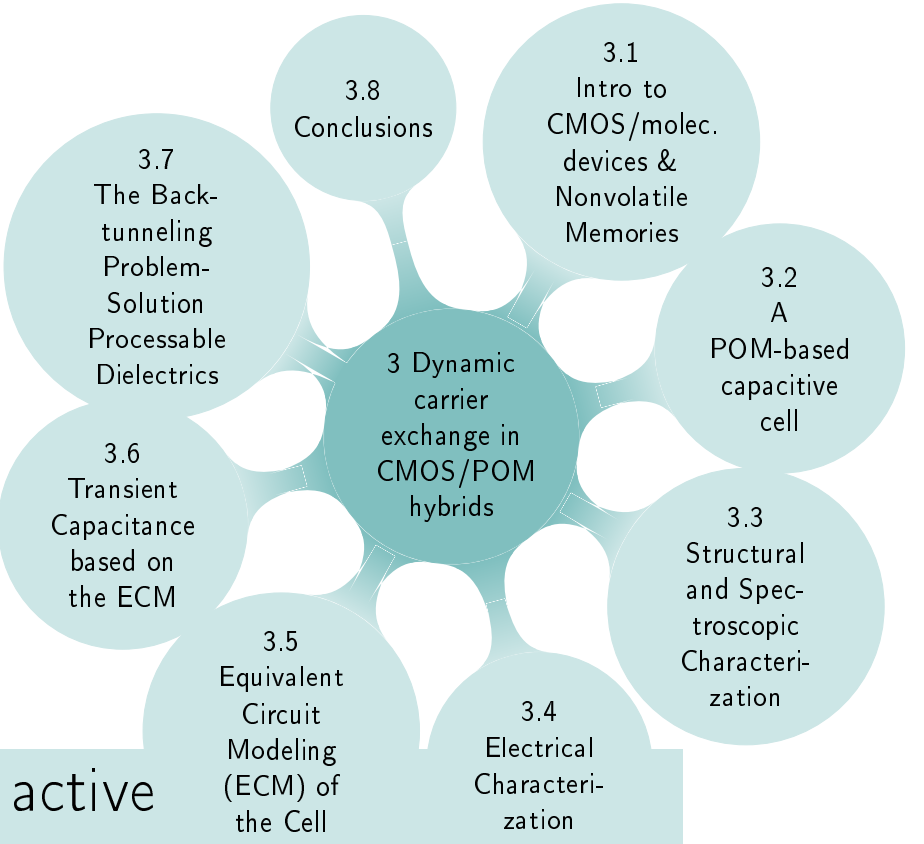


# 3

# POMs as active nodes for dynamic carrier exchange in hybrid CMOS/molecular capacitive cells

*While the creation of a molecular transistor has received the dominant share of attention, the component that is most urgently in need of replacement for most semiconductor devices is the charge storage device, that is, the capacitor.*

*Hybrid complementary metal oxide semiconductor (CMOS)/molecular memory devices are based on the parallel plate architecture and use a well-characterized charge storage mechanism to store information while relying on the intrinsic properties of molecules attached to a CMOS platform.*

*The molecules are designed in a rational way in order to have pre-specified electrical properties and are incorporated with only minor modification of existing fabrication methods. Each memory element contains a planar hyperstructure of molecules (typically some millions) that can store charge; this process yields a structure that has multiple times the charge density of a typical DRAM capacitor, obviating the necessity for a trench or stacked capacitor geometry. The magnitude of voltage required to remove each electron is quantized (typically a few hundred millivolts per state), making it much easier to put molecules in a known state and to detect that state with low-power*

*operation.*

*The incorporation of bottom-up liquid-based processes is introduced in an effort to overcome the lithography limitations and take advantage/combine self-assembly and inject printing in order to make smaller and cheaper devices retaining precision and reliability.*

*In this chapter we study the utilization of molecular transition metal oxides known as polyoxometalates (POMs), in particular the Keggin structure anions of the formula* $[PW_{12}O_{40}]^{3-}$*, as active nodes for potential switching and/or fast writing memory applications. The active molecules are being integrated in hybrid Metal-Insulator/POM molecules-Semiconductor capacitors, which serve as prototypes allowing investigation of critical performance characteristics towards the design of more sophisticated devices.*

*The charging ability as well as the electronic structure of the molecular layer is probed by means of electrical characterization, namely: capacitance-voltage and current-voltage measurements, as well as transient capacitance measurements, C (t), under step voltage polarization. It is argued that the transient current peaks observed are manifestations of dynamic carrier exchange between the gate electrode and specific molecular levels, while the transient C (t) curves under conditions of molecular charging can supply information for the rate of change of the charge that is being trapped and de-trapped within the molecular layer.*

*Structural characterization via surface and cross sectional scanning electron microscopy as well as atomic force microscopy, spectroscopic ellipsometry, UV and Fourier-transform IR spectroscopies, UPS and XPS contribute to the extraction of accurate electronic structure characteristics and open the path for the design of new devices with on-demand tuning of their interfacial properties via the controlled preparation of the POM layer.*

---

## 3.1 A Brief Introduction to the concept of CMOS/ /molecular devices & Nonvolatile Memories

### The concept of CMOS/molecular

As the size of the transistor continuous to shrink, its structural composition is approaching a few hundred atoms and its operation is becoming prohibitively leaky, thereby leading to increased power dissipation. Driven from this constrain, the semiconductor industry seeks a technology to supplement and extend CMOS beyond its fundamental scal-

ing limit and, one day, even to replace CMOS. Since, at that point, a replacement seems quite unrealistic from an economical point of view, parallel efforts have started to develop in order to bridge the gap between long-pursued experimental milestones like all molecular, single atom and quantum computing and the current market-grade state-of-the-art.

This is translated in viable C-MOS compatible solutions, integrating useful functionalities of the aforementioned fields through affordable modifications in the standard line processes at industrial scale.

In the case of memories, C-MOS/molecular topologies can exhibit some distinguished advantages over their conventional floating-gate counterpart [208]. The program/erase states are defined via adding charges to and removing charges from the charge-storage molecular redox layer, similar to a floating-gate memory. However, unlike the floating-gate cell, where charges are mainly stored in the conduction band of the floating gate, in charge-trapping molecular memories charges are located at spatially discrete traps that are either distributed in the band-gap of a generalized charge-trapping layer, or are discrete, ideally non-interacting, semiconducting molecular dots.

C-MOS/molecular topologies are totally compatible with the complementary metal-oxide-semiconductor (CMOS) technology, and readily integrated in the current C-MOS line fabrication process. The simplicity of the concept means that integration into a logic complementary metal oxide semiconductor process flow will be possible with only a few additional non-lithographic steps, while holding promises for all-injection-printed circuitry.

## 3.2 A POM-based capacitive cell

The continuing miniaturization of electronics and the concurrent demand for reduction of fabrication costs has rendered self-assembled molecular systems a promising route towards the realization of novel electronic devices [209, 210]. The natural size reduction down to the molecular scale and the possibility of exploitation of multiple molecular states with the advantage of low energy consumption and high speed are only some of the appealing aspects of such a concept.

However, the development of viable molecular electronic devices is still a challenging task, which requires understanding of the electrical properties from atomistic to mesoscopic scale, precise control of the morphology of the molecular structures and the involved interfaces, as well as stability and device variability reduction [211].

Hybrid devices on semiconducting surfaces are a test bed for molecular layers [212, 213]. In addition, they can be directly exploited for fast

switching, diode and memory applications as well as for chemical sensors or bio-sensors.

Our group has already demonstrated, using planar junctions [214, 215] as well as vertical junctions and STM measurements [216], that the redox properties of the inorganic 12-tungstophosphoric acid ($H_3PW_{12}O_{40}$), a member of the polyoxometalate (POM) class can be, in principle, exploited in novel memory structures. In the current work we extensively investigate the transport mechanisms and the charging states of hybrid organic-inorganic capacitor structures which contain POMs as the charge trapping medium.

The charging effects are studied via quasi-static as well as dynamic electrical characterization (I-V and C-V measurements) in a wide range of temperatures (80-300K). The study of negative differential resistance features, present in the dynamic I-V characteristics, allows the quantification of the trapping efficiency of the POM molecules under device operation. These features provide direct information for the electronic structure of the POM molecular layers.

Temperature dependent quasi-static I-V measurements are used for the identification of the dominant transport mechanisms in each field regime. Transient C-t measurements and subsequent analysis provide the effective generation lifetimes, as a measure of the characteristic response time of POM-functionalized devices under logic signal application.

FE-SEM, AFM, UV-Vis, FTIR, XPS, UPS and SE characterization further completes the picture of the morphology and electronic structure characteristics of the molecular films.

### 3.2.1 Fabrication & Device Band Diagram

Hybrid MIS devices containing POM (in particular $[PW_{12}O_{40}]^{3-}$) as active (trapping and transport control) element were fabricated on wet oxidized (300 nm-thick $SiO_2$) n-Si (1-2 $\Omega$cm) substrates. Square patterns with edges of 100 $\mu$m were defined by photolithography and wet etching on the field oxide and in sequence, a 6.5-nm-thick high quality $SiO_2$, was thermally grown in the device active area (Fig.3.1).

Following a bottom-up Layer by Layer (LbL) self-assembly approach [217] the thermal $SiO_2$ surface was chemically functionalized with 3-aminopropyl triethoxysilane (APTES) providing a template of positively charged amino groups for the formation of an ordered layer of POM anions. POM molecules were subsequently self-arranged on top of the APTES monolayer under pH- and temperature-controlled aqueous environment [215].

After the electrostatic immobilization of POM molecules an isopenty-

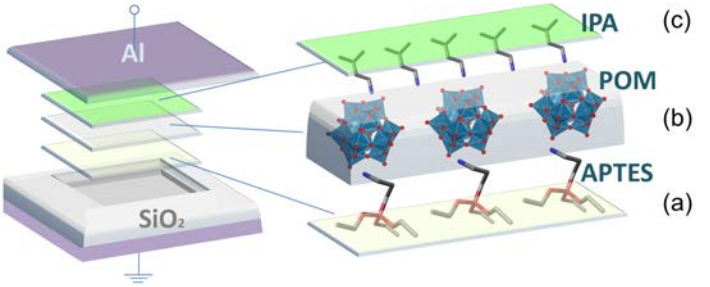


Figure 3.1: Planar MIS and incorporated functional layers. (a) APTES molecules used for $SiO_2$ surface chemical modification, (b) POM molecules self-organized via electrostatic forces on top of the APTES monolayer and (c) IPA molecules electrostatically linked onto the POM structures, used as capping/passivation layer.

lamine (IPA: $C_5H_{13}N$) oligolayer was deposited on top also via LbL in order to passivate the functional POM nodes and serve as cap dielectric. Al was used for the fabrication of both the gate electrode and the substrate backside contact. Metallization ensures the encapsulation of the sensitive molecular layers and results in their longevity, robustness and high yields.

The molecular layers fabrication process parameters as well as the effect of the precursor solution composition on the reproducibility, stability, properties integrity and morphology of the molecular films were monitored by means of UV-Vis absorption spectroscopy, FTIR spectroscopy, spectroscopic ellipsometry, AFM and SEM. Devices with only an APTES SAM were fabricated and used as control samples, while devices with only the gate oxide were used as references.

Sample name convention will be as follows: A: for samples containing $SiO_2$/APTES layers in the active region, AP: for active region functionalized with $SiO_2$/APTES/POM layer stack and API: for the full $SiO_2$/APTES/POM/IPA stack. All electric measurements were performed in shielded probe stations using a HP4041B picoammeter and a HP4284A LCR meter. The band diagram of the basic incorporated layers before contact formation is shown on Fig.3.2 in the flat band model representation, neglecting band bending:

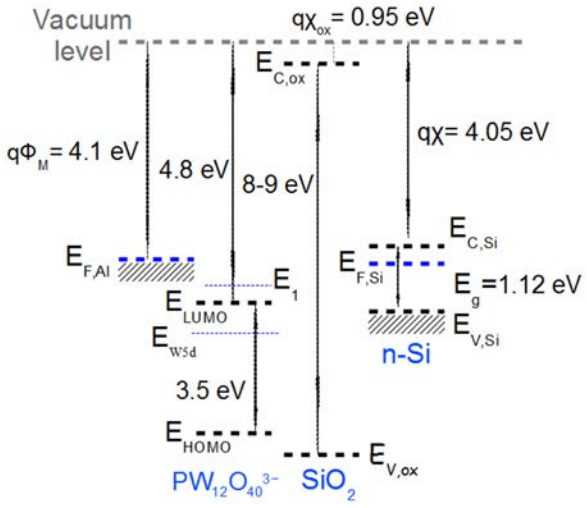


Figure 3.2: Band diagram of the MIS structures layers before contact formation neglecting band bending. The spectroscopically determined HOMO-LUMO gap of $[PW_{12}O_{40}^{3-}]$ is in accordance with [218].

## 3.3 Structural and spectroscopic characterization

First the APTES layer was examined. XPS suggests full surface coverage of $SiO_2$ by the APTES molecular network [217] and AFM scanning indicates sub-nanometer roughness (of the order of 0.5 nm). The thickness of the APTES molecular layer was determined to be 0.95 nm by spectroscopic ellipsometry (SE).

More specifically, the APTES layer was found to be non-absorbent within the energy range of SE measurement (245-998 nm) and, therefore, a Cauchy formula for insignificant absorption dielectrics was applied for its modeling [219, 194]. The fitting was applied under the assumption of an isotropic and non-depolarizing sample. Next the morphology of the POM molecular layer was examined. The topography of the molecule-modified surface obtained via SEM indicates that POMs tend to form uniformly distributed aggregates on the APTES layer and get self-arranged forming nano-islands with a mean diameter of ~17 nm (see Fig.3.3).

Estimation of the thickness of these islands was attempted locally via cross-sectional SEM (see Fig.3.4) and in larger (mm) scale via SE. As shown in Fig.3.4, the height of the grown POM islands (0.05 M) is of the order of few nm (typically 5-14 nm).

For the data analysis of the SE measurements the distributed POM nanoislands were considered to form a continuous, homogeneous layer.

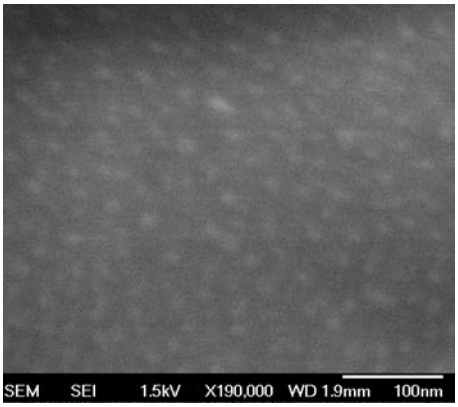


Figure 3.3: FE-SEM topography indicating uniform POM nanoislands with a mean diameter of 17 nm on APTES modified $SiO_2$.

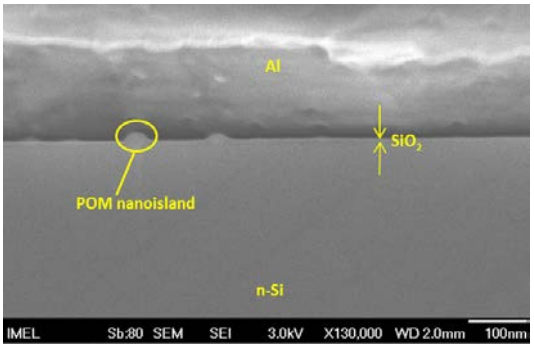


Figure 3.4: FE-SEM image of the hybrid MIS capacitors in cross section (prepared using solutions of POM concentration 0.05 M). POM nanoislands can be sporadically (due to disturbance from the cutting procedure) observed on top of the thin 6.5-nm-thick thermal $SiO_2$ under the Al gate.

As such, the calculated thickness value for the POM layer corresponds to a mean effective thickness. The films optical parameters are calculated via fitting of the acquired relative phase ($\Psi$) and relative amplitude ($\Delta$) spectroscopic values (relative phase and amplitude of the parallel and perpendicular component of the reflected wave, expressing the state of polarization of the light as it is reflected from the sample) under the assumption of an isotropic and non-depolarizing sample.

One approach to resolving the problem of non-unique solution to the $\epsilon_1$, $\epsilon_2$ and thickness determination for thin films [45], such as the POM molecular oligolayers, is to obtain further data by varying a system parameter. Here we vary slightly the thickness of the molecular layer between two samples ensuring, though, that they have identical dielectric

functions.

More specifically, the method was applied for POM layers formed from solutions of concentration 0.03 M and 0.04 M (the molar concentrations in precursor solutions define the resulting thickness in solid state). (Concurrence of dielectric functions was suggested from the identical optical band gap [195, 196] measured via UV spectroscopy for the two molecular layers). In order to retrieve the common dielectric function and thicknesses we apply the multiple sample analysis mode of WVase software for SE [46] and model the molecules response function with appropriate oscillators with respect to its optical absorption spectrum.

Iterative non-linear regression resulted in convergence of the fitting with a mean statistical error of 1.4. The effective thicknesses obtained by this method were 2.08 and 2.15 nm respectively. Fig.3.5 depicts the valence band spectra and the low binding energy (BE) region of the UPS spectrum for the different steps of the hybrid MIS functionalization (samples A, AP, API).

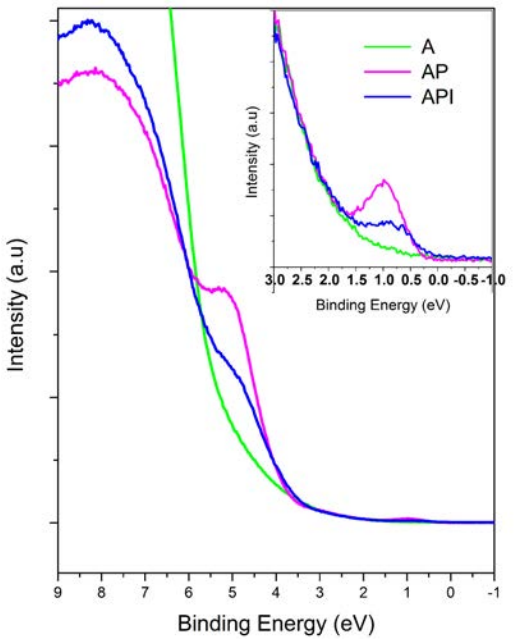


Figure 3.5: UPS valence band spectra of samples A, AP and API along with the magnification of the region near the Fermi level (low BE region) in the inset.

For the UPS measurements the He I (21.2 eV) excitation line was used and a voltage of 12.23 V was applied to the specimens in order to separate the high binding energy cut-off from the analyzer. The valence

band is composed of O2p orbitals and consists of two peaks, one around 4.5 eV, attributed to O2p-derived band and one at 6.5 eV due to O2p-W5d hybridized states [189] while the onset is located 3.5 eV below the Fermi level. The valence band spectra of $PW_{12}$-POM were measured after the electrostatic immobilization of the POM oligolayer (0.5 M) on APTES.

A feature located within the gap, approximately 1.0 eV below the Fermi level, is observed after magnication of the low binding energy cut-off region of the UPS spectrum. The peak extends from 0.5 eV from the Fermi level up to 1.5 eV and is attributed to the W5d band, originating from W atom non-bonding to O (imperfect stoichiometry of POM [189, 220]). The POM LUMO is a mixture of the O2p orbitals and Mo4d orbitals. Since this level has also an antibonding nature with respect to the O-Mo bond [221], electron transfer already occurring via reduction from the APTES template results in a weakening of the corresponding bond. Actually some bridging oxygen species are consumed in this reduction [221, 222]. This is equivalent to the formation of oxygen vacancies in the close vicinity of the molecular lacuna.

Oxygen vacancies are a common defect in $WO_3$ films as well (the oxide analog of POMs) and result in negative charge accumulation in order to compensate the electronegative oxygen ion vacancy [189]. Such charge inserts a donor-like level below conduction band minimum. The observed peak decreases in intensity after the IPA adsorption on POM layer but in all cases suggests the insertion of gap states, as a result of tailing of the electron-rich orbitals of defective POM structures [189] within the gap.

In Fig.3.5 the role of IPA molecular layer as capping/passivation component is not directly accesible. The low binding energy cut-off in UPS spectra is practically the same for both POM and IPA terminated stacks implying no measurable impact of IPA on the UPS estimated workfunctions. This seems to contradict the initial passivation hypothesis.

In order to resolve this issue the XPS cutoff will be utilized. To accurately elucidate the Fermi level alignment in the case of ultra-thin materials, a combined technique of work function measurement by monitoring secondary electron cutoff with both UPS and XPS core-level measurementS can be proven powerful [48, 49].

Note that the poor spectral resolution of X-rays in the low energy region of valence bands cannot provide a detailed view of the band components. This is why UPS is commonly used for workfunction estimation. Nevertheless, in the XPS case we can observe a striking shift of the cut-off energy when IPA layer is deposited on POM, a fact not observed in the respective UPS spectra. This is directly related to the photosensitivity of POMs in the 4-6 eV energy region scanned during UPS spectra

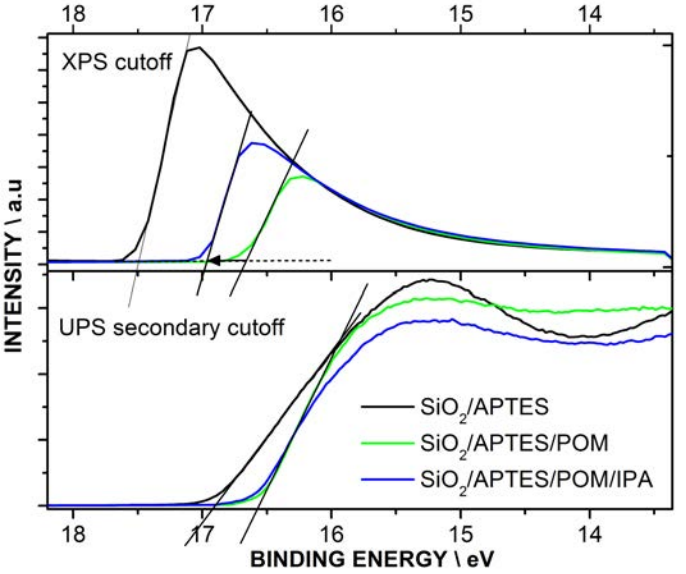


Figure 3.6: XPS and UPS cut-offs for samples A, AP and API.

aquisition. IPA, on the other hand, does not absorb in this regime a fact weakening its relative impact on the obtain spectrum. Nevertheless, since the low binding energy limit of the photoemission spectrum of a level accounts for the completely relaxed final state [223], this problem can be overcome. Thus, the high BE spectra cut-off shift detected in XPS is a direct proof of POM passivation upon IPA deposition, serving for the electronic decoupling (i.e. as dielectric spacer) of POM from the subsequently deposited Al gate.

## 3.4 Electrical & electronic structure considerations

### 3.4.1 Quasi-static I-Vs and more

The quasi-static I-V characteristics under staircase sweep conditions were recorded for three types of devices: (a) only APES functionalization of the active region (samples A) (b) POM molecules over the APTES layer (samples AP) and (c) the IPA overlayer included (samples API). The I-V characteristics of the fabricated MIS structures proved to be highly asymmetric and exhibit pronounced hysteresis under gate injection currents within the [-2, 2] V cycle (see Fig.3.7). Negative resistance effects were only observed in the case of AP & API samples at room temperature, in analogy with other cases of MIS-type devices containing quantum dots [224].

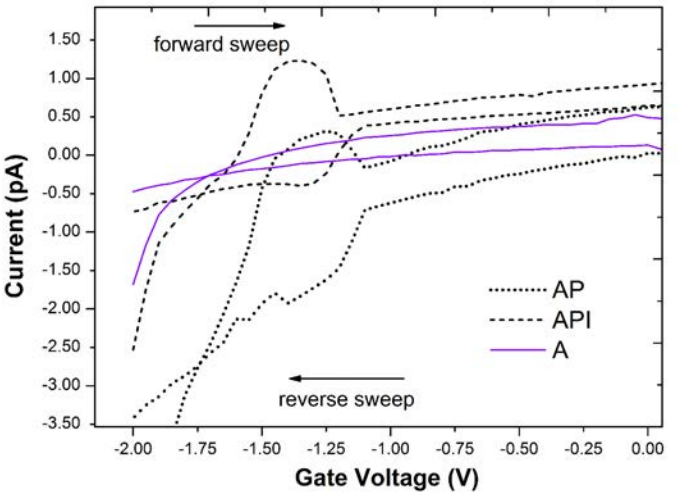


Figure 3.7: Current-voltage characteristics monitored for [-2, 2] V voltage cycles and samples A, AP, and API. The double staircase step was in all cases 50 mV, while the measurements were performed under RT conditions in dark electromagnetically shielded probe station.

The I-V curves of AP and API samples are rich in negative differential resistance features within the [-2, 0] V regime and exhibit multiple resistive states compared to the A reference samples (see Fig.3.7). This is an indication that the POM layer significantly affects the transport processes most likely through regulating the current via contribution of POM-induced states [225]. These states provide intermediate energy steps for the electrons that move from the Al electrode towards overcoming the $SiO_2$ barrier.

It is already known that POMs have the ability to delocalize electron charges over several metal centers of their framework as well as over the tungsten-oxygen bonds [226, 227]. The wave functions of these electrons can partially overlap with the band gap of $SiO_2$ and tail within the band-edge discontinuities across the interface forming interface-induced gap states [225, 228] in the insulators forbidden gap. Surface modification of $SiO_2$ with APTES via covalent bonding can further facilitate the induction of such energy states of surface origin which lie, at least partly, in the $SiO_2$ band gap [229]. The existence of these intra-gap states is already confirmed via Ultraviolet Photoemission (UPS) spectroscopy in the spectroscopic characterization section (Fig.3.5).

These states imply the n-type doping of the underlying oxide which, in turn, causes the increased conductivity observed in the I-V spectra of POM-modified devices (Fig.3.7, [230]). Under reverse bias, electron

tunneling towards filling of POM molecules occurs from the Al gate (see band diagram of Fig.3.2). At zero applied voltage part of the POM molecular states are already filled with electrons, as the Al Fermi level is located above the POMs LUMO (see Fig.3.2). The application of relatively high negative gate ($> |-1.8$ V|) bias on gate raises further the Fermi level, so higher POM energy states fall below it opening available conducting pathways and increasing the measured current.

When the Si conduction band is resonant to the LUMO band of the molecule, the number of tunneling carriers across the structure reaches a maximum, resulting in the maximum current plateau observed in the [-1.7, -1.3] V region of current-voltage curve for sample P1 and in [-1.8, -1.3] V region for sample I1. Only a few carriers are able to tunnel across the structure thereafter (e.g. for $V > -1.3$ V) and the current drastically decreases with decreasing absolute bias. Therefore, the I-V curve exhibits negative differential resistance. In order to study the transport mechanisms involved in a full I-V cycle, temperature was varied from ambient conditions to 120 K. The results can be seen in Fig.3.8.

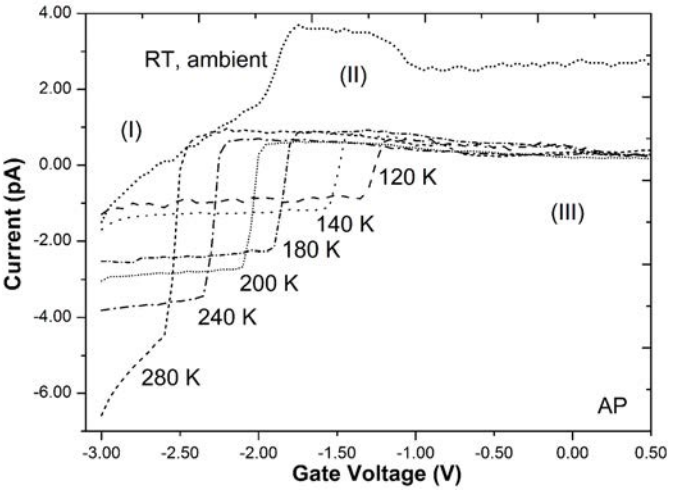


Figure 3.8: Current-voltage measurements for sample AP under selected temperatures. The double staircase step was in all cases 50 mV.

The region of high negative bias (region (I) in Fig.3.8) extends from -3 V up to approximately -1.35 V for 120 K and progressively shifts to lower voltages with increasing temperature. Within this voltage range a temperature-dependent mechanism of conduction is evident and the field dependence switches from linear to non-linear via the increase of temperature. In this case of relatively high or moderate applied fields both Poole-Frenkel (PF) and Schottky conduction mechanisms should be

considered. Both effects result from the lowering of a coulombic potential barrier by the applied electric field. The Schottky effect is associated here with the barrier at the surface of the metal and the LUMO of the POM molecules (Fig.3.2).

The Poole-Frenkel effect is normally associated with barriers in the bulk of a material. In fact donor sites, acceptor sites, and traps, as well as electrons in the valence band, experience the Poole-Frenkel effect. It is proposed here, in analogy with concepts for surface-induced intra-gap states and surface /interface-states-assisted P-F emission documented elsewhere [231, 232], that surface functionalization with APTES/POMs causes the introduction of intra-band states in the region of $SiO_2$ energy gap and facilitates P-F type charge transport across the structure there through. As indicated by the rearranged Dushman equation for the Schottky-originating current [233]:

$$ln(J_s) = \frac{\sqrt{q/4\pi\varepsilon_s}}{kT}E^{1/2} + [ln(AT^2) - \frac{q\phi_s}{kT}] \tag{3.1}$$

and by the rearranged respective Poole-Frenkel current equation [233]:

$$ln(J/E) = \frac{\sqrt{q/4\pi\varepsilon_s}}{kT}\xi E^{1/2} + [ln(C) - \frac{q\xi\phi_b}{kT}] \tag{3.2}$$

,where $\phi_b$ is the energy interval between the trap level and the bottom of the conduction band in the case of the Poole-Frenkel effect and $\phi_s$ the work function in the case of the Schottky effect. The term A in Eq.3.1 is the effective Richardson constant, characteristic of the material [228, 233], while the factor $\xi$ in Eq.3.2 is a slope parameter for the P-F effect [234]. Its value (which can vary between $\xi$=1 and $\xi$=2) depends on the acceptor compensation in the material. Both P-F and Schottky models were tested in the case of AP and API samples for region (I) data (Fig.3.9).

Quantitative analysis revealed similar slopes for the two representations (ln[J]=f[$E^{1/2}$] (Schottky relation for current density versus applied field) and ln[$\sigma$]= f[$E^{1/2}$] (P-F relation for electrical conductivity versus applied field)). The difference in slopes accounts for the amount of acceptor compensation present in the case of P-F emission [233]. In the case of traps in the POM layer we do not have compensation of the trapped charge by acceptor sites and as a result the slope of the P-F representation Ln($\sigma$) vs $E^{1/2}$ is the same as that for Schottky emission, even though the barrier lowering by the applied field is twice as that for Schottky [233, 235]. In this case the Fermi level lies near the ground state of the POM traps for P-F conduction.

This problem demonstrates the need for investigation of the temperature dependence of the slopes of the linear parts in order to uniquely

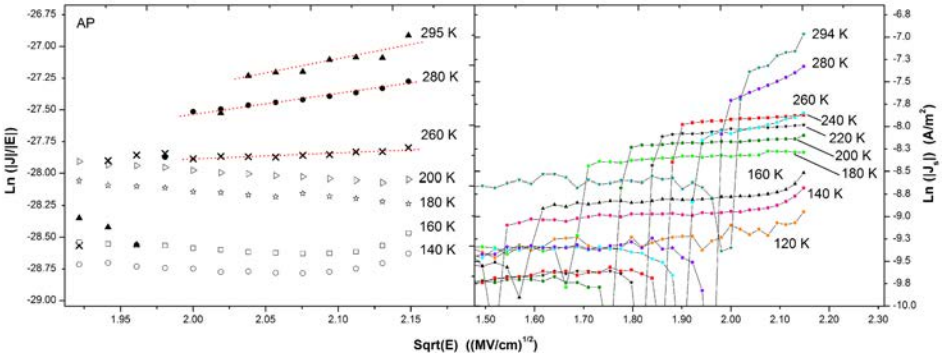


Figure 3.9: Poole Frenkel (left) and Schottky (right) representations for sample AP and negative applied voltages on gate, evincing dominance of Schottky mechanism for temperatures lower than 260 K. For higher temperatures evaluation of the slope of the fitting curves is demanded.

discriminate between the two mechanisms. For Schottky conduction the slope of Log($\sigma$) vs $E^{1/2}$ (see Eq.3.1) should remain constant (within the limits of experimental error) in the temperature region of the mechanisms prevalence, while it should have a weak field as well as a clear temperature dependence in the case of P-F conduction (as deduced from Eq.3.2 above).

Fig.3.10 represents in semi-logarithmic scale the variation of factor $\sqrt{(q/\pi\epsilon_s)}/(2k)$ as a function of temperature for POM-functionalized samples and suggests that Schottky type conduction dominates for temperatures strictly below 240 K, while for T>240 K P-F conduction is a possible candidate.

This is in agreement with the P-F representations of Fig.3.9 carried out for the same temperature range that confirms that trap assisted P-F can only be considered for temperatures within the close interval [260, 295] K. It should be noticed (see Fig.3.9, high voltage ranges) that in the case of the maximum applied voltages there is deviation from both Schottky and P-F mechanisms. For these fields we get occurrence of thermally activated hopping conduction (see Fig.3.11).

The corresponding activation energy is calculated at 25 meV, which is quite small to be attributed to charging of molecular levels and is rather assigned to hopping assisted by the sites of the $\sigma$-bonded molecular network of IPA and/or APTES organic layers. These sites constitute shallow states which become observable only at high applied voltages where the majority conduction band becomes depopulated [236]. Fig. 10 shows the difference between hopping and thermally independent QM tunneling for two applied field extremes (high (I), low (III)).

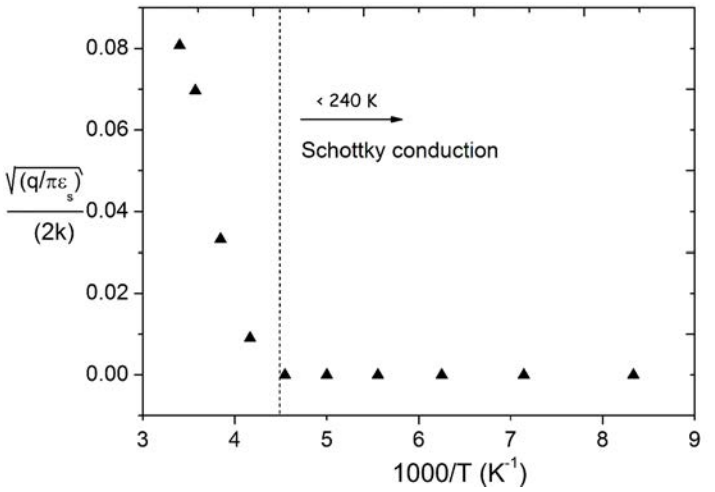


Figure 3.10: The factor Sqrt[(q/$\pi\epsilon_s$)/(2k)] determined from linear fitting of the corresponding Schottky type representations as a function of inverse temperature for sample AP.

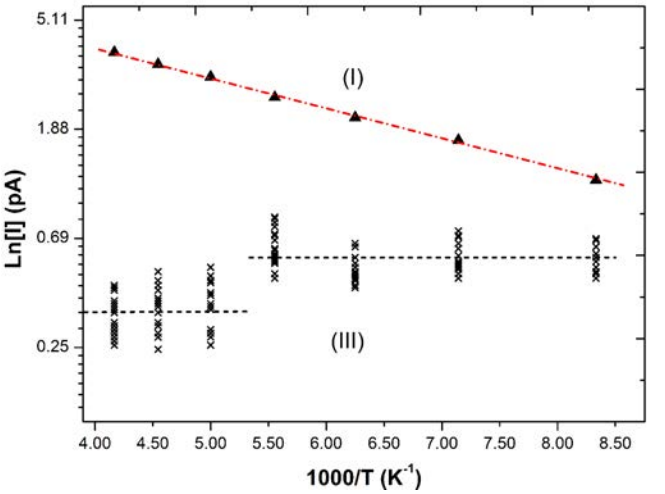


Figure 3.11: Arrhenius type plot of sample AP for various voltages. The double staircase step of I-V quasi-static measurements was in all cases 50 mV.

The region of intermediate and low applied voltages refers to regions (II) and (III) of Fig.3.8, covering absolute voltages lower than 1.35 V under reverse bias. The abrupt current magnitude decrease during transition from region (I) to region (II) (under vacuum conditions) is interpreted as the region of charging of molecular orbitals. This leads to a subsequent

screening owning to the presence of the charged POMs.

At even lower applied voltages we observe a transition to a different region (III), which is accompanied (in the ambient case) by partial screening due to the charged POM layer. For the measurements performed in vacuum conditions, this is a regime of Ohmic transport. Arrhenius type representations for a bunch of different voltages within this regime (III) reveal temperature independent conduction, which is therefore interpreted as quantum mechanical tunneling (see Fig.3.11).

In the case of positive bias there are no special features observed since transport is dominated by electrons tunneling through the $SiO_2$ barrier, making molecule regulated conduction non-observable.

### 3.4.2 Dynamic I-V measurements & electronic structure considerations

Dynamic voltage transition measurements obtained via application of a voltage ramp provide a clearer view of the response of the POM molecules to the application of electric field. The existence of special features such as peaks or humps in the I-Vs could be an indication of Coulomb blockade or resonant tunneling effects [237]. These unique features are characteristic of the molecular energy levels and can be, thus, used to probe their electronic properties.

All current-voltage measurements were performed in dark at room temperature (RT) as well as at T=80, 100, 120 and 140 K. The voltage was applied on the top electrode and was swept from -3 V to 3 V (inversion to accumulation for the n-type Si substrate) in order to investigate the charging of POM nanoislands with electrons [238]. Fig.3.12 shows typical double sweep constant ramp rate I-V curves recorded for samples A and AP for ramp rates within the range of 0.05–0.30 V/s using a fixed voltage step of 50 mV under ambient conditions.

While no pronounced features were present on the ramp rate current measured on A reference samples, the AP and API (not presented for reasons of clarity and resemblance to AP) samples exhibited rich current variations. At the beginning of the voltage ramp scan the Si substrate is in inversion state. The existence of negative current at the beginning of the measurement (i.e. at high negative voltages) suggests injection of holes into the POM layer, a fact that lowers the Fermi level (This is the equivalent of de-population of POM islands which are already populated with electrons at RT, due to the small energy difference between the Al Fermi level and the POM LUMO [239]) and opens a conducting pathway through POM states. This results in the subsequent increase of conduction current as voltage decreases.

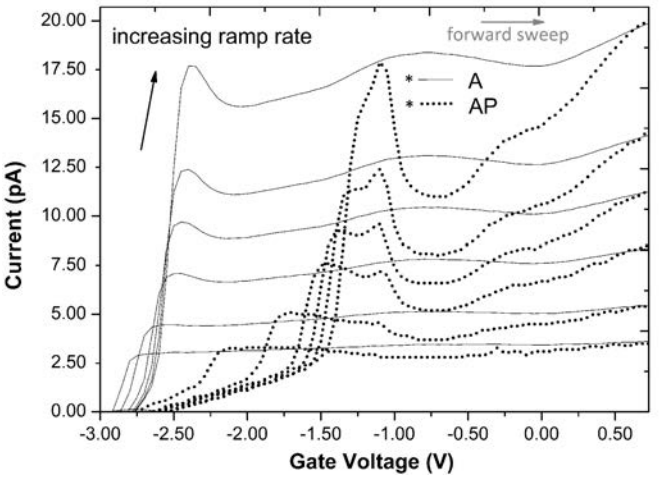


Figure 3.12: Ramp rate current-voltage characteristics in the forward sweep direction for voltage alteration rates in the range 0.05–0.30 V/s at RT conditions. The inversion to accumulation scan defines the forward sweep.

Electrons are injected from the gate into available charging states in the nanoislands, provided the proper voltages are supplied. At these voltages a single (RT case) or a double (140 K case) peak appears (around -1.1 V for AP sample at RT and -1.2 for API respectively, not shown here). The amplitude as well as the width of this current peak is strongly dependent upon the ramp rate and can be understood as an effect of the charging of POM moieties and subsequent screening. The intensity of the peak becomes higher and its width narrower upon increase of the ramp rate, maintaining the energy position of the maximum. For these voltages we get alignment of the LUMO levels of the molecule to the Al Fermi level. The double peak is the result of the contribution of the discrete LUMO levels of the molecule to the transient current. The corresponding I-V curves for both A and AP samples at T=140 K are shown in Fig.3.13. The corresponding I-V curves under optical illumination are also quoted.

The above indicate that the current screening in the inversion regime is caused by the limited availability of minority carriers in the substrate and the higher fields required for hole tunneling. The preservation of the characteristic peaks under optical illumination confirms that they are of electron origin since they are not affected by the presence of excess minority carriers within the semiconductors body. In order to clarify the nature of the transient peak, the magnitude of the current peak as a function of the ramp rate is plotted (Fig.3.14).

As observed (Fig.3.14), the current intensity in both AP and API (POM-

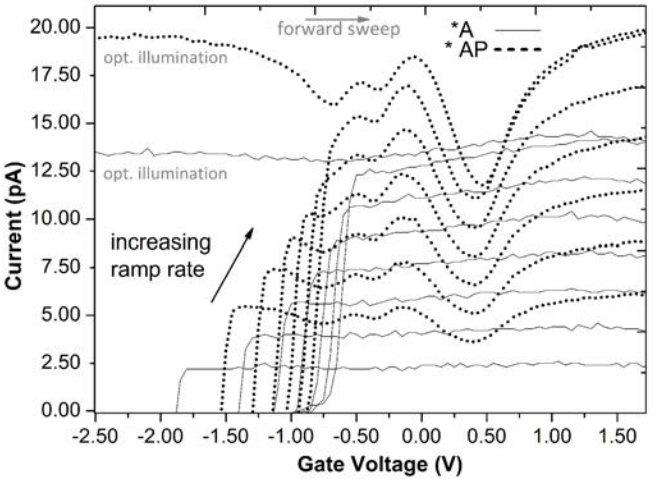


Figure 3.13: Ramp rate current-voltage characteristics in both sweep directions and range 0.05–0.30 V/s for samples A, AP. The temperature was set to 140 K.

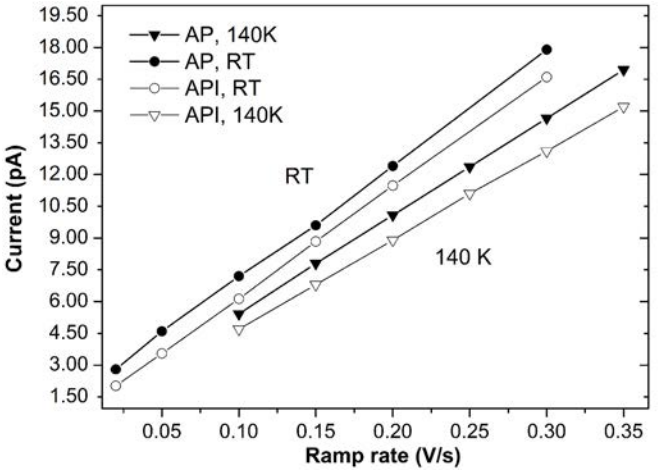


Figure 3.14: Transient current peak maximum versus ramp rate for forward sweep and samples AP, API.

containing samples) scales linearly with the ramp rate, suggesting that it originates from a displacement current [237] (within the assumption of linear dielectric medium). This, however, is not the case for the sample whose response under ramp voltage rate excitation either deviates from linearity (RT) or exhibits no current peak features at all (140 K). More thoroughly, the slope of the Ipeak current amplitude versus the ramp rate is associated with the transfer process of electrons trapped in POM states

through the tunneling medium. The corresponding tunneling-associated capacitance ($C_{tun}$) can be derived from the relation [237]:

$$I_{peak} = C_{tun} \times dV/dt \tag{3.3}$$

Since the current peaks are the charging current of the POM molecules, the area under each peak is expected to give, when divided with the ramp rate of the corresponding measurement, the amount of electrons that has tunneled into the molecular nano-islands [237, 240]. This procedure is carried out for the complex plateau-peak I-V distributions of samples AP and API after subtraction of the underlying leakage current. Calculation of the leakage current in tunneling regime was realized under the assumption of linear I (V) function and extrapolation of the low voltage linear part of leakage current in the screening regime i.e. within the (-1.0, -0.5) V interval in Fig.3.12. The charge is calculated from the integration of the area under the complex plateau-peak part of the current curve according to:

$$Q_t = \int I_c \times dt = \int I_c \times dV \times \frac{dt}{dV} = \frac{A_{peak}}{dV/dt} \tag{3.4}$$

The corresponding quantitative results for both temperatures and samples are summarized in Table3.1.

Table 3.1: Mean charge density dynamically transferred into POM nanostructures during forward sweep and various ramp rates.

| SAMPLE | T(K) | $Q_t * 10^{-7}$ $(Cb/cm^2)$ | $D_t * 10^{12}$ $(cm^{-2})$ |
|---|---|---|---|
| AP | 300 | 1.4-2.4 * | 1 |
| AP | 140 | 3.4-7.9 * | 2-5 |
| API | 300 | 1.5-2.6 * | 1 |
| API | 140 | 2.1-4.7 * | 1-3 |

** The lower $Q_t$ limit refers always to 0.35 V/s ramp rate, while the higher value refers to ramp rate 0.05 V/s.*

As observed, both trap density and trapped charge remain practically the same for AP and API samples at RT, since the IPA cap is mainly acting as a passivation layer. On the other hand trapping appears to be favored at lower temperatures, while at the same time the incorporation of IPA layer seems to reduce the density of active traps when compared to the presence of just the POM layer. This is in agreement with the information

derived from the low binding energy cut-off region of the UPS spectrum (Fig.3.5), which essentially suggests the passivation of charge-trapping oxygen vacancies in POM islands upon IPA deposition. Lowering of the temperature results in a shift of the POM-related peaks towards lower energies, while at the same time a second transient peak towards lower voltages becomes prominent. This is better demonstrated in Fig.3.15, where one can see a detail of the 140 K I-V characteristics (Fig.3.13) for scan rates ranging from 0.05 V/s up to 0.30 V/s.

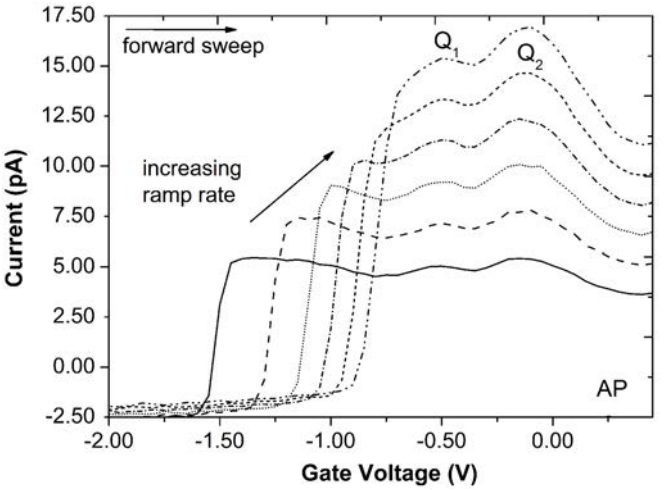


Figure 3.15: Ramp rate current-voltage characteristics in forward sweep and range 0.05–0.30 V/s for sample AP indicating both $Q_1$ and $Q_2$ transient peak observed at 140 K.

These transient peaks ($Q_1$ and $Q_2$) are attributed to the filling of the ground and first excited quantum states of POM nanoislands. The Gaussian shape of the peaks indicates their nature as resonance peaks which are broadened by disorder. Resonance naturally occurs at gate bias voltages where the Al Fermi level is aligned with an electronic state level of the POM nanoislands. The POM nanoislands electronic state levels should be determined both by quantum confinement in the occupied POM molecular orbitals and the Coulomb charging energy of the formed molecular islands [241]. For low temperatures the condition $k_BT<\Delta$ for observation of potential changes due to the sequential charging of the POM nanoislands is satisfied for a wider range of dimensions (this is important since the POM islands are not strictly mono-dispersed). As a result, the size scale limit of detectable nanostructures increases and single electron effects can be observed [242]. The energy difference corresponding to the two experimental transient current peaks of Fig.3.15

can be estimated from the following equation which connects a change in the gate voltage to a corresponding difference of sub-band energies within a quantum contact [240, 211]:

$$E_n/e = C_{tun}/C_{tot}(V_{gb} - V_{th}) \tag{3.5}$$

, where $C_{tun}$ is the capacitance associated with the tunneling barrier between the Al gate and the POM molecules (see Eq.3.3), Ctot is the composite equivalent capacitance of the structure as calculated from the high frequency C-V measurements of the structure under accumulation conditions, $V_{gb}$ is the gate voltage at each of the observed capacitance peaks and Vth the threshold voltage extracted from the high frequency C-V characteristics. The capacitance of the tunneling medium, or in other words the tunneling-associated capacitance, has been determined above via the fitting parameters of transient current peak maximum versus ramp rate measurements. The corresponding $C_{tun}$ value for the AP sample is $C_{tun} = 4.59 \times 10^{-11}$ F at 140 K. This gives a corresponding $\Delta$E= 257 meV (according to Eq.3.5) for the energy difference of the observed peaks ($Q_1$, $Q_2$) in Fig.3.15 The energy difference between the HOMO and the first excited electronic state of the $[PW_{12}O_{40}]^{3-}$ molecule was determined by means of polarographic measurements and was found to be 243 meV [243]. The deviation of the above results is less than 6% indicating that most probably these transient current peaks do originate from POM charging and can be considered a fingerprint of its unoccupied energy states.

In order now to determine the precise amount of electron charge captured by each of the available molecular states in the POM islands the complex current-voltage distribution of Fig.3.15 must be deconvoluted in elementary charging components by means of Gaussian distributions. As an example, the total charge density of sample AP at 240 K is $Q_{tot} = 2.98 \times 10^{-7} Cb/cm^2$ (Fig.3.16). This is distributed in all available molecular states in the POM islands (in case of Fig.3.16 this is a triplet of states) and absorbed in discrete charge amounts. However, the corresponding charge densities for the MIS structure reflect the total charge that is collectively trapped in the corresponding states of all molecules contained per unitary surface. The total charge trapped in each of the states (A, B, C) of the triplet is, according to the analysis in Fig.3.12: $Q_{tA} = 0.53 \times 10^{-7} Cb/cm^2$, $Q_{tB} = 1.27 \times 10^{-7} Cb/cm^2$, $Q_{tA} = 0.65 \times 10^{-7}\ Cb/cm^2$.

## 3.5 High frequency capacitance measurements

The overall charge trapped across the multilayer MIS structure under a full voltage sweep can be monitored via high frequency C-V measure-

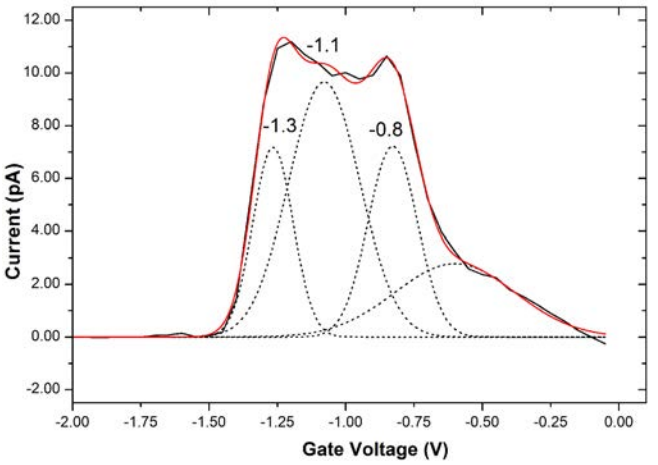


Figure 3.16: Peak analysis of the POM islands charging current at T=240 K for sample AP resulting in a state triplet. The ramp rate was set at 0.25 V/s.

ments (Fig.3.17).

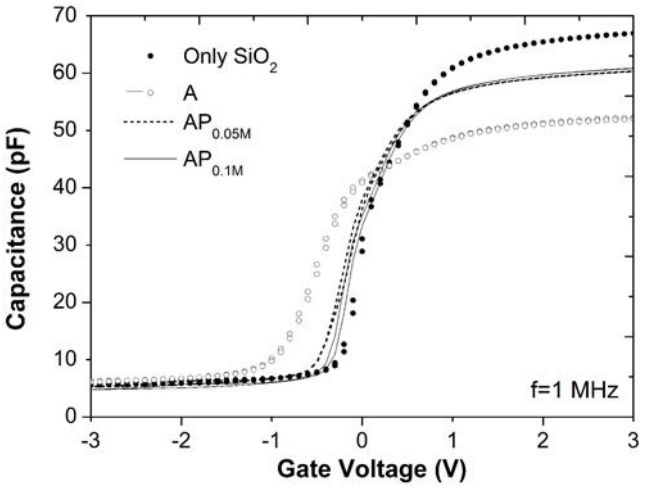


Figure 3.17: Double sweep Capacitance-Voltage characteristics at f=1MHz indicating capacitance increase upon POM molecular layer incorporation for two different concentrations of POMs. The sweep rate is 1 V/sec and voltage step 100 mV in all cases.

The functionalization of the $SiO_2$ surface with APTES results in the addition of a series capacitance and the subsequent reduction of the high frequency accumulation region capacitance $C_{acc}$ (Fig.3.17). However, af-

ter deposition of the POM molecular layers $C_{acc}$ significantly increases, indicating that the POM molecules serve as available conductivity sites for vertical conduction across the MIS structure. As a result conductivity is also increased in accumulation upon the incorporation of POMs (accumulation region IVs not included). The introduction of molecular layers on the Si/$SiO_2$ substrate induces shifts on the flatband voltage $V_{FB}$, which are related to the trapped overall charge. The flat band voltage shifts induced upon the incorporation of the molecular layers (Table3.2) indicate that the APTES layer induces significant positive charge while the POM molecules are negatively charged in equilibrium.

It can be seen that the $V_{FB}$ shift is greater in the case of sample A. The excess (non-bonded) amine groups contained within the APTES layer induce significant positive charge. Most importantly, the covalent bonding of APTES to the $SiO_2$ surface modifies the interface states and introduces positive charge that can be imaged within the semiconductor (pronounced negative $V_{FB}$ shifts). On the other hand, the POM charge is located directly under the gate and as a result its charge is mainly being imaged in the gate (poor imaging within the semiconductor leads to small $V_{FB}$ shifts). Nevertheless the small energy separation between the $E_{F,Al}$ and the POMs LUMO ($\Delta E$ ~0.1 eV) facilitates the injection of electrons into available POM molecular orbitals and results in the negative charging of POM molecular layer. Note that the $V_{FB}$ shift in the case of sample A is calculated with respect to the bare $SiO_2$ substrate, while the $V_{FB}$ shifts of $AP_1$ and $AP_2$ samples are being calculated with respect to their precursor A-type substrate.

Table 3.2: Flat band voltage shifts, induced charges (centroid weighted) and maximum trap densities under a double voltage sweep

| SAMPLE | $\Delta V_{FB}(V)$ | $Q_t \times 10^{-7}$ $(Cb/cm^2)$ | $D_t \times 10^{12}$ $(cm^{-2})$ |
|---|---|---|---|
| A | -0.52 | +2.76 | 1.7 |
| $AP_1^{(a)}$ | +0.36 | -2.20 | 1.4 |
| $AP_2^{(b)}$ | +0.4 | -2.47 | 1.5 |

*(a) POM 0.05M in precursor solution, (b) POM 0.1M in precursor solution.*

The Capacitance Equivalent Thickness (CET) derived from C-V measurements in the case of the $SiO_2$ reference substrate was 6.65 nm, in good agreement with the value derived via SE (6.5 nm). The thickness

of the grown molecular films cannot be extracted in the same way (via high-f C-V), since the dielectric constants of the self-assembled layers are generally not known.

## 3.6 Transient capacitance measurements

The technique used to characterize the fabricated MIS structures in this section is based on the method of measuring the generation lifetime $\tau_g$ in MOS capacitors [244, 245]. The capacitor is originally pulsed into deep depletion and then the evolution of the capacitance is measured over time. The generation lifetime results as the slope of the linear part of a $-d(C_{ox}/C)^2/dt$ vs $(C_f/C - 1)$ plot, where $C_{ox}$ is the oxide capacitance and $C_f$ is the final (equilibrium) capacitance value reached after relaxation. This is known as a Zerbst plot [232, 244, 245, 246]. The Heiman plot [246], which is a representation based on the integrated form of the Zerbst equation, takes into account only bulk space-charge region (scr) generation mechanisms and will be used here for the extraction of g to avoid the noise magnification, intrinsic in the Zerbst method.

In order to take advantage of the methodologies developed for the MOS capacitor and produce a theoretical relation C(t) we need to include the effect of the molecular layer. The equivalent circuit simulating the hybrid MIS capacitor is shown in Fig.3.18. The POM molecular layer is simulated as a sheet charge between the upper electrode and the oxide weakly coupled to the upper electrode and the oxide via tunneling junctions with capacitances $C_1$ and $C_2$ and resistances $R_{t1}$ and $R_{t2}$ respectively.

For the purposes of this analysis we shall treat $C_1$ and $C_2$ as ideal capacitors through which charge is slowly leaked ($R_{t1}, R_{t2} \rightarrow \infty$ in Fig.3.18). That is a reasonable approximation since the relatively thick oxide layer (6.5 nm) and the constantly applied gate voltage field (which suppresses back-tunneling) lead to very rare overall sequential tunneling events. In the general case POM discharging during the measurement is a transient phenomenon with characteristic time directly related to the $C_1$, $C_2$ quantities of the molecular layers surrounding the POM molecules and the POM molecular exciton lifetimes (which are typically of the order of nanoseconds).

Based on the configuration presented in Fig.3.18 and after some basic electrostatics we obtain a modified Zerbst equation for the POM-equipped devices (see next section for detailed derivation):

$$-\frac{d}{dt}\left(\frac{C_{ox}}{C}\right)^2 = \frac{2n_i C_o}{\tau_g N_D C_f}\left(\frac{C_f}{C} - 1\right) + \frac{2C_o^2}{N_D \epsilon_o K_s q}\frac{1}{C_1}\frac{dQ_m}{dt} \qquad (3.6)$$

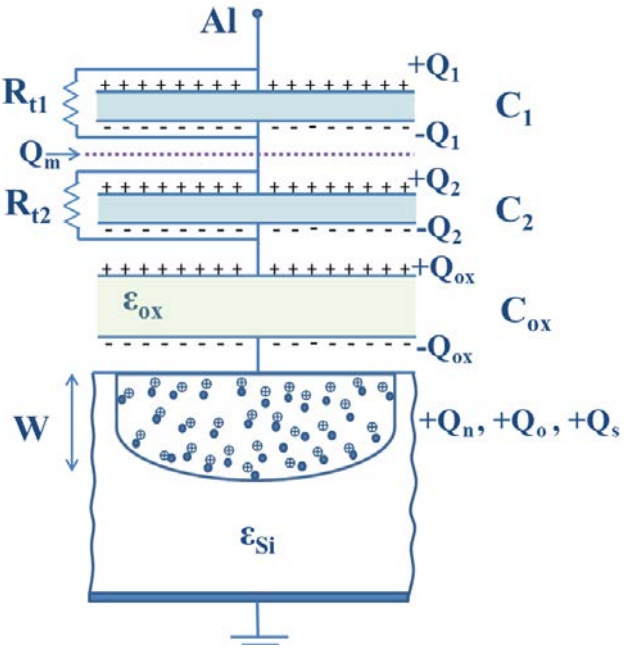


Figure 3.18: Equivalent circuit of the hybrid MIS structure in deep depletion. The molecular layer is represented as a sheet charge with a charge density of $\sigma_m$.

,where $C_o = (1/C_{ox} + 1/C_1 + 1/C_2)$ is the series capacitance of the system, ni the intrinsic carrier concentration, $N_D$ the doping density of the substrate, $\tau_g$ the generation lifetime, $C_f$ the final capacitance reached in equilibrium and $dQ_m/dt$ the rate of charge variation on the molecular layer. In deriving (Eq.3.6) the scr width-independent surface generation components, which are practically negligible for the working temperatures here, are being omitted [245].

The term $C_o$ can be experimentally derived from high frequency C-V measurement of the capacitance in accumulation. In order to estimate $\tau_g$ it is convenient to integrate (Eq.3.6) over time and use the linear part of the so called Heiman plot [246]. However, the time dependence of the term $dQ_m/dt$ is not known. Since $\tau_g$ depends merely on bulk carrier generation we proceed with the integration in the case where the molecular layer is not present. The resulting capacitance-time relation is then:

$$Ln\left(\frac{C_f/C_o - 1}{C_f/C - 1}\right) + C_f\left(\frac{1}{C_o} - \frac{1}{C}\right) = \frac{C_f n_i t}{C_o N_D \tau_g} \tag{3.7}$$

A plot of the left term vs time will allow the determination of $\tau_g$ from

the slope of the linear part. This is shown in Fig.3.19 for measurements taken at a temperature of 100 K. In the case of sample A the single-slope linear response of the graph suggests a constant $\tau_g$, characteristic of the bulk Si. The value obtained at 100 K, is $9.98\times10^{-28}$ s for A and $1.04\times10^{-29}$ s for API samples, respectively, when a negative voltage of -3.0 V is applied on the gate. In the POM functionalized cases (AP and API samples) the Heiman representation has either both a linear (characteristic of the Si bulk) and a non-linear part (POM contribution), or is nonlinear due to the dominance of POM contribution on electron-hole pair generation.

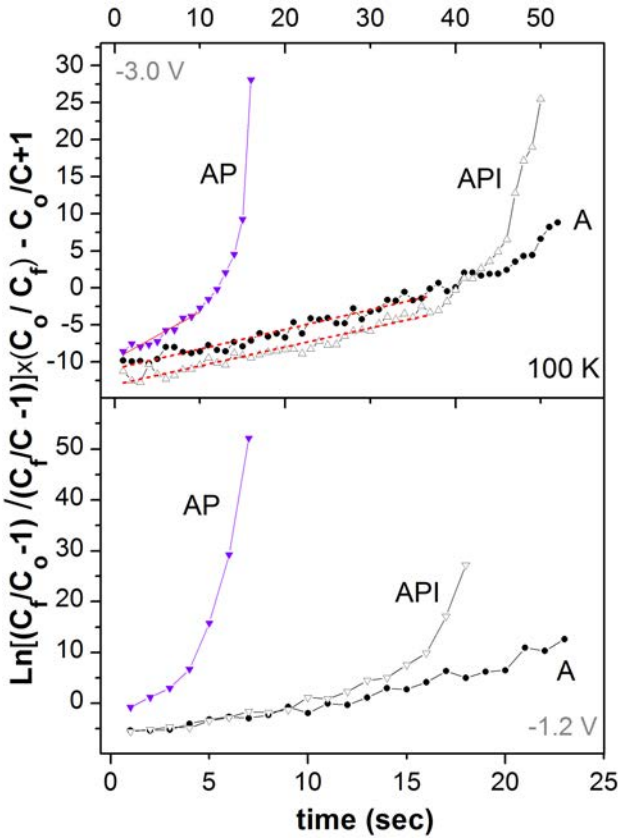


Figure 3.19: Heiman plots of samples A, AP and API at 100 K for two different gate bias favoring POM molecular layer charging.

In order to gain an insight into the function of POM molecules on the device performance, it is useful to plot the rate of change of the generated charge within the POM molecular layer. The term $1/C_1 \times dQ_m/dt$ expresses the rate of voltage drop across the molecular layer and can be deduced from rearrangement of (Eq.3.6) after experimental evaluation of the quantities $C_f$, $\tau_g$ and $C_o$, where $C_o$ is $4.118\times10^{-10}$ F in

the case of sample AP, $4.582 \times 10^{-10}$ F for API and $4.851 \times 10^{-10}$ F for sample A.

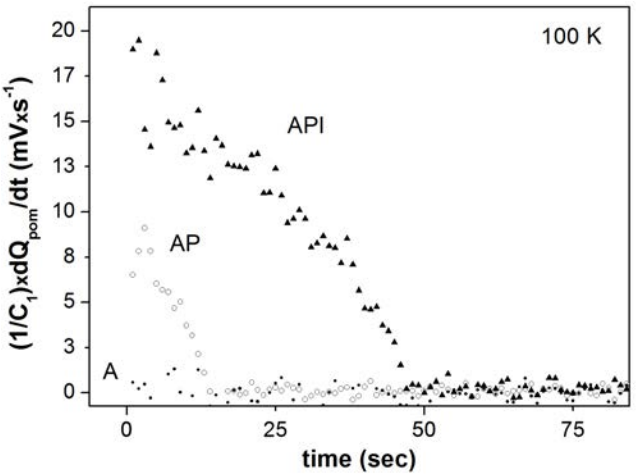


Figure 3.20: Rate of voltage drop over time due to the molecular layer-generated charge for samples A, AP and API at 100 K.

From Fig.3.20 it is evident that the incorporation of POM molecules gives rise to a pronounced current contribution across the structure that does not exist for the plain APTES layer on $SiO_2$ (curve A). In addition, the IPA capping layer (curve API of Fig.3.20) on top of POMs triples the net charging rate of the molecular layer. The total rate of change in the molecular layer charge is the algebraic sum of the trapping and detrapping rates. Since the IPA layer acts as an insulating barrier against the de-trapping (i.e. backtunneling) of electrons back to the Al gate it is expected to reduce the detrapping rate leading to the observed increase of the overall charging rate of the molecular layer.

### 3.6.1 Detailed derivation of the modified Zerbst equation

**General equation for time varying charges in a MOS capacitor in the presence of an isolated chargeable molecular interface**

In depletion (and sufficiently high modulation frequencies) the structures equivalent circuit representation (Fig.3.18) reduces to three capacitors connected in series, namely: $C_{mol}(C_1C_2/(C_1 + C_2)$, $C_{ox}$ and $C_{s,d}$.

The equivalent overall capacitance of the structure is:

$$C = \frac{C_o C_{s,d}}{(C_o + C_{s,d})}, \tag{3.8}$$

where

$$C_s = \frac{\varepsilon_{si}}{W} \tag{3.9}$$

and

$$\frac{1}{C_o} = \frac{1}{C_1} + \frac{1}{C_2} + \frac{1}{C_{ox}} \tag{3.10}$$

In the context of full depletion approximation the electrostatic field within the oxide ($|\overrightarrow{E_{ox}}|$), underlies an abrupt change at the oxide-semiconductor (o-s) interface due to the significant difference in the dielectric constant of the two media. It is further assumed that the electric field within the body of the semiconductor is a linear function of the distance from the o-s interface (assuming constant doping density ND) and is exactly zero at the edge of the depletion region (namely at x=0). Under these simplifications one can use the Gausss flux theorem $\overrightarrow{\nabla}\overrightarrow{E_{ox}} = \rho\epsilon_{Si}$ to derive the electrostatic field within the depletion region via integrating:

$$\int E_{Si}(x) = \int \frac{\rho(x)}{\epsilon_{Si}} dx \tag{3.11}$$

, where x varies between 0 and W. We, thus, get: $E_{Si} = qN_DW/\epsilon Si$. A common expression for the depletion region, W, is then obtained from the scalar surface semiconductor potential $\phi_s$ and the basic equation of electrostatics $\overrightarrow{E} = -\overrightarrow{\nabla}V$ as:

$$W = (\frac{2\varepsilon_{si}\phi_s}{qN_D})^{\frac{1}{2}}, \quad for \quad 0 \leq \phi_s \leq 2\phi_F \tag{3.12}$$

If we now incorporate the chargeable POM molecules as a sheet of homogeneously distributed charge that is weakly coupled (via junctions $C_1$, $C_2$) to the gate and oxide substrate and lies exactly at the charge centroid, the gate voltage (grounded back contact) is partially dropped across the top molecular network (IPA) with capacitance $C_1$, partially across the APTES layer with capacitance $C_2$, partially across the 6.5 nm silicon dioxide ($C_{ox}$, $\epsilon_{ox}$) and partially across the semiconductor ($C_{s,d}$, $\epsilon_{Si}$). This gives:

$$V_G = V_{FB} + \phi_s + V_{ox} + V_{mol} \tag{3.13}$$

, where $V_{FB}$ is the flatband voltage, Vox the voltage drop across the $SiO_2$, $\phi_s$ the semiconductor surface potential, $V_{mol} = V_1 + V_2$, $V_1$ being the voltage drop across the capping molecular layer (IPA) and $V_2$ the voltage drop across the bottom APTES layer. The POM trapping centers are packed between these two organics (see Fig.3.18) and their charge

is directly related to the $C_1$, $V_1$ and $C_2$, $V_2$ quantities. Note that for the purposes of this analysis we assume, as already discussed in the main text, that the POM layer influences the capacitance evolution mainly via alteration of the displacement current across the structure. The rarely-occurring tunneling events are here omitted and thus, the junctions with capacitances $C_1$ and $C_2$ behave as ideal capacitors through which charge is slowly leaked. From charge conservation across the system nodes and basic electrostatics we get:

$$V_1 = \frac{C_2}{C_1 + C_2} V_{mol} + \frac{Q_m}{C_1 + C_2} \tag{3.14}$$

$$V_2 = \frac{C_1}{C_1 + C_2} V_{mol} - \frac{Q_m}{C_1 + C_2} \tag{3.15}$$

Eq.3.15 along with the relations: $Q_2 = V_2 C_2$, $Q_{ox} = V_{ox} C_{ox}$ and $-Q_2 + Q_{ox} = 0$ (from charge conservation across the circuits nodes) is used to obtain:

$$V_G = V_{FB} + Q_n(\frac{1}{C_o}) + qN_D W(\frac{1}{C_o}) - Q_m(\frac{1}{C_1}) + \frac{qN_D W^2}{2\epsilon_{Si}} \tag{3.16}$$

‘ Let $V'_G = V_G - V_{FB}$. $Q_n$ is the overall charge (interface trap charge and inversion charge which is considered a homogeneous surface charge distribution within the context of the “sheet model) and $Q_m$ is the effective charge of the POM traps. It is assumed that the time rate of change of the interface trapped charge plays a negligible role in the capacitance transient, so the term $dQ_n/dt$ is solely the growth of the inversion charge [243]. After substituting again for convenience $V''_G = V'_G - Q_n/C_o + Q_m/C_1$ and performing the calculations involved, we obtain for W:

$$W = \frac{\varepsilon_{si}}{C_{ox}}[(1 + \frac{2V''_G C_{ox}^2}{qN_D \varepsilon_{si}})^{1/2} - 1] \tag{3.17}$$

By substituting $V_o = \frac{qN_D \varepsilon_{si}}{C_o^2}$ in Eq.3.17 we get:

$$W = \frac{\varepsilon_{si}}{C_o}[(1 + \frac{2V''_G}{V_o})^{1/2} - 1] \tag{3.18}$$

Taking Eq.3.18 and Eq.3.8 and using expression Eq.3.9 one obtains for the measured capacitance:

$$C = \frac{C_o}{1 + [(1 + \frac{2V''_G}{V_o})^{1/2} - 1]} = \frac{C_o}{(1 + \frac{2V''_G}{V_o})^{1/2}} = \frac{C_o}{(1 + \frac{2(V'_G - Q_n/C_o + Q_m/C_1)}{V_o})^{1/2}} \tag{3.19}$$

Solving Eq.3.19 for $V_G$ and differentiating with respect to t gives:

$$\frac{dV'_G}{dt} = -\frac{qK_s\varepsilon_0 N_D}{C^3}\frac{dC}{dt} - \frac{1}{C_o}\frac{dQ_n}{dt} + \frac{1}{C_1}\frac{dQ_m}{dt} \tag{3.20}$$

With $dV_{FB}/dt = 0$ and for constant $V_G$, (during the recovery from deep depletion the gate voltage is constant as imposed from the constant voltage step applied) we obtain:

$$\begin{aligned} \frac{1}{C_o}\frac{dQ_n}{dt} - \frac{1}{C_1}\frac{dQ_m}{dt} &= \frac{d}{dt}(\frac{C_o}{C})^2\frac{qK_s\varepsilon_0 N_D}{2C_o^2} \Longleftrightarrow \\ \frac{dQ_n}{dt} - (\frac{C_o}{C_1})\frac{dQ_m}{dt} &= \frac{qK_s\varepsilon_0 N_D}{2C_o}\frac{d}{dt}(\frac{C_o}{C})^2 \end{aligned} \tag{3.21}$$

, where the term $dQ_m/dt$ is the displacement current contribution from the POM molecular layer. In the general case POM charging and dis-charging is a transient phenomenon with characteristic time directly related to the $C_1$, $C_2$, $R_{t1}$, $R_{t2}$ quantities, characteristic of the molecular layers that surround the POM molecules and the POM molecular exciton lifetimes (typically of the order of nanoseconds).

### Modified Zerbst equation and the molecular-layer-controlled current

As proposed by Zerbst [243], the time variation of the overall generation charge is represented by the generation rates $Q_v/dt$ [244] (space charge region (scr)-related generation rates) and $Q_s/dt$ [244] (scr width-independent or interfacial generation rates), with:

$$\begin{aligned} Q_v/dt &= -qn_i\frac{(W - W_{inv})}{\tau_g} - qn_i s_g\frac{A_s}{A_g} \\ &= -qn_i\frac{(W - W_{inv})}{\tau_{g;eff}} \end{aligned} \tag{3.22}$$

and

$$Q_s/dt = -qn_i s'_g - \frac{qn_i^2 D_n}{N_A L'_n}, \tag{3.23}$$

where $\tau_g$ is the scr generation lifetime, $s_g$ the surface generation velocity characterizing lateral surface scr generation, As is the area of the lateral scr, Ag is the area under the gate, $s'_g$ the surface generation velocity characterizing the surface generation under the gate, $D_n$ is the electron diffusion constant and $L'_n$ an effective diffusion length that couples bulk

and back surface generation [244]. The temperature in the measurements under discussion ranges from 100 to 120 K in order to diminish any contribution from leakage current and/or mobile ions in the alteration of scr width. For these temperatures both quasi-neutral bulk generation and back surface generation rates become negligible [244] and can be safely disregarded.

Having this in mind and combining Eq.3.21, Eq.3.22, Eq.3.23 and Eq.3.9 we obtain:

$$-\frac{d}{dt}(\frac{C_o}{C})^2 = \frac{2n_i C_o}{\tau_{g;eff} N_D C_f}(\frac{C_f}{C} - 1) + (\frac{2C_o}{\epsilon_o K_s}(\frac{n_i s_{eff}}{N_D} + \frac{C_o}{C_1 N_D q}\frac{dQ_m}{dt}) \quad (3.24)$$

Estimation of $\tau_{g;eff}$ from the Zerbst-type representation of Eq.3.24 should be done with care because of the magnification of noise, intrinsic in the Zerbst method, due to the need for differentiation of the experimental data. Integration of Eq.3.24 overcomes this problem giving a general C(t) expression [245]. From the scr-related linear part of this expression, neglecting the impact of scr-independent currents on the effective generation lifetime, the value of g;eff can be easily extracted. Neglecting surface generation under the gate and in the quasi-neutral region (i.e. $s_{eff}$) we obtain Eq.3.6 in the text. Provided that all involved factors could be experimentally obtained Eq.3.24 could be solved for the rate of change of POM charge versus time. Since, though, the capacitance $C_1$ is generally not known we use Eq.3.25 instead, which provides the rate of voltage drop across the molecular layer versus time:

$$\frac{1}{C_1}\frac{dQ_m}{dt} = 2q[\frac{C_o N_D}{C^3}\frac{dC}{dt} - \frac{n_i}{\tau_{g;eff} C_f}(\frac{C_f}{C} - 1) - \frac{n_i s_{eff}}{\epsilon_o K_s}] \quad (3.25)$$

Fig.3.20 in the manuscript is then derived using Eq.3.25 and data experimentally obtained.

## 3.7 The backtunneling problem – Solution processable organic gate dielectrics

The problem of back-tunneling of electrons injected in the trapping layer (i.e. POM molecular film) towards the gate is commonly being addressed through the utilization of a gate dielectric of adequate thickness in order to prevent direct quantum mechanical tunneling and discharge due to dielectric failure. These materials should posses an appropriate insulating gap in order to hinder transport across the interfaces and should

also be defect and interface states free in order to prevent hopping conduction and leakage or energy losses during operation. An additional requirement when temperature-sensitive organics are in play is low (ideally room) temperature processing and PH-compliant solvents. In the following two polymeric solution processable candidates will be examined:

### 3.7.1 PEI

Polyethylenimine (PEI) or polyaziridine is a polymer with repeating unit composed of an amine group and a two carbon aliphatic $CH_2CH_2$ spacer.

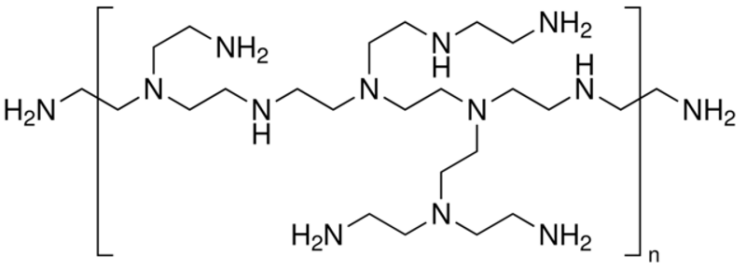


Figure 3.21: Typical branched polyethylenimine fragment.

Linear polyethyleneimines contain only primary and secondary amines, in contrast to branched PEIs which feature all primary, secondary and tertiary amino groups [247]. The latter (i.e. branched PEI) is the case used here. PEI is produced on industrial scale and finds many applications usually derived from its polycationic character [248, 247]. This is the main feature exploited here in order to benefit from its electrostatic interaction with the anionic immobilized POMs in aqueous environment and apply it via the LbL process as a gate dielectric.

#### Materials & Fabrication Details

PEI analytical standard, 50 % (w/v) in $H_2O$ (Sigma Aldrich) was used as starting material. The goal would be to create a solution-compatible process in all fabrication stages, eventually using purely molecular precursors, in order to be able to repeat the fabrication protocol on flexible substrates using injection printing techniques.

Two different fabrication methods for solution-processable dielectrics, typically used when high homogeneity and precision control on thickness is a demand, were separately evaluated. These are spin coating and the Layer-by-Layer (LbL) technique, with the first usually targeting tenths of

nm to $\mu$m-thick films, while the second $\AA$ to few tenths of nm. The viscosity of the precursor solution has to be carefully adjusted in order to meet the criteria for each method.

In the case of spin coating the success of the method is based on the dominance of intermoleculer affinity forces over the centrifugal power developed during spinning, in a way that a coherent, homogeneous film would develop. Viscosity, tuned by both PEI concentration in solution and solvent, should be higher than a critical value to ensure such results.

In the case of LbL self-assembly, on the other hand, the success of the method is based on the dominance of molecule-substrate interactions while intermoleculer affinity forces ought to play a secondary role in order to prevent early aggregation in solution, which would be pernicious for both the coherence and the homogeneity of the film. Thus, in this case viscosity should be lower than a critical value to ensure fulfillment of the above criteria.

### Spectroscopic and Structural Validation of Coating Methods & Precursor solutions

After spanning a wide range of molarities of aqueous POM an PEI precursor solutions and depositing via both spin coating and LbL techniques, the following results were obtained: Below molarities 0.1 M the PEI stereochemistry is critically disturbed. The characteristic UV-Vis band of the molecule, originating from the C-N chromophore (more specifically the $(C_2H_5)_2NH$ n to s* transition at 193 nm for secondary amines or the $(CH_5)_3N$ n to s* 199 nm transition for tertiary amino groups) is totally absent. In FTIR the molecule exhibits broad featureless areas and the main vibrational bands are either absent or shifted and deformed. Non-continuity of the film is apparent even by means of optical microscopy.

The above results are visualized in Fig.3.22, where the experimentally obtained UV spectra for a low molarity PEI film of 0.03M for slightly varying pH values (i.e. 11 and 10) are shown on the left side.

On the right, non-diluted films spanning pH values from 3.0 to 10.1 are presented (reproduced from [249]). As becomes evident, the dilution of PEI causes a vast instability on its structure resulting in total intolerance on acidification. Comparing the two diagrams it becomes evident that dilution itself has an effect equivalent to extreme acidification. Below concentrations of 0.1 M, even if the molecular structure is preserved, the continuity of the films is poor and the resulting dielectric is below the standards of a device-grade material.

In case that an extra constrain, namely the preservation of the underlying POM structure, is added the situation becomes even more compli-

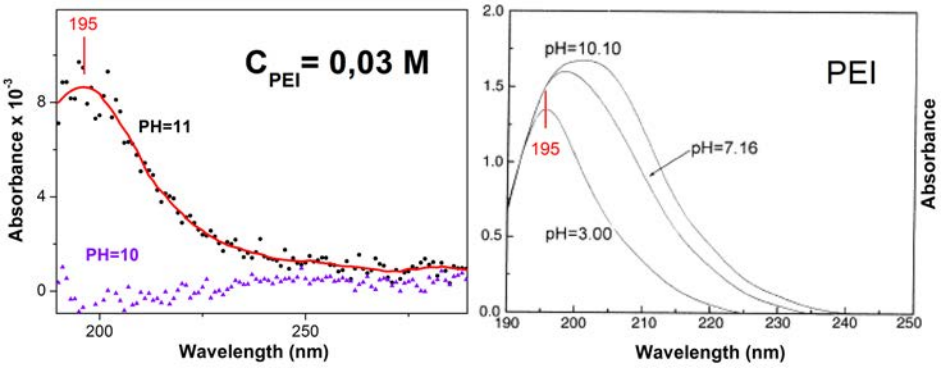


Figure 3.22: UV-Vis spectra of PEI films prepared from solutions with different PEI concentration and pH values.

cated.

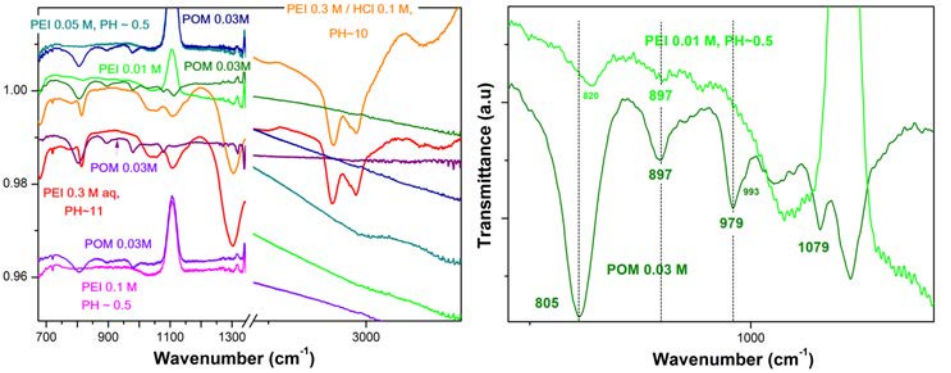


Figure 3.23: FTIR spectra of of POM molecular films before and after the deposition of PEI. PEI films are being prepared from solutions with different PEI concentration and pH values, while the underlying POM film is the same in all studied cases.

A very useful experimentally constructed diagram, clarifying this scheme is presented in Fig.3.23, where the FTIR spectra of POM molecular films before and after the deposition of PEI are collectively presented. The four characteristic asymmetric vibration peaks of POM, indicating structural integrity and preservation of the Keggin stereochemistry lie within the region 700 to 1400 $cm^{-1}$, where an intense PEI-related vibrational mode at around 1300 $cm^{-1}$ is also present. For PEI another characteristic vibrational window at 2500-3500 $cm^{-1}$ will also be of help for structural validation.

The table that follows summarizes the results concerning the safe pH and molarity ranges for each of the constituents individually as well as

when considering their interaction upon deposition.

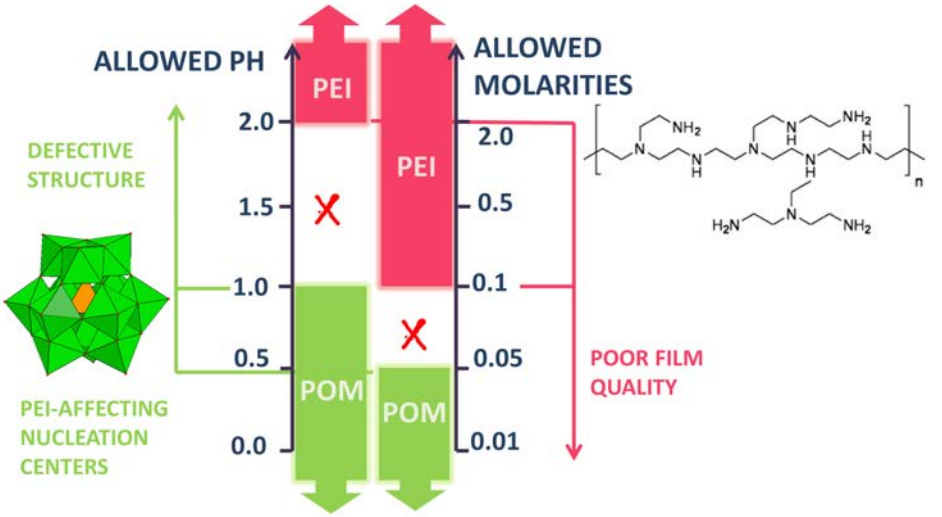


Figure 3.24: Experimentally determined regions of stability and structural integrity of POM-PEI layers as well as their quality-preserving interaction regime with varying solution PH and molarities in precursors.

It can be readily observed that the utilized aqueous precursors are not compatible, since simultaneous integrity and stability of the POM, PEI components and device-grade film quality standards cannot be met. The alternative of utilizing non-polar organic solvents, which could change the system parameters in a possibly beneficial way, is not preferable in this case.

This is because, on one hand, the necessity of a polar solvent is inherent for electrostatically-driven assembly of PEI on the underlying POM film (achievement of atomically ordered, defectless interface) and, on the other hand, because of its toxicity issues [250] in the relatively high concentrations found here to be required for good quality films.

Furthermore, the disruption of POM Keggin structure monitored for high PEI concentrations is not expected to be obviated on the molecular level via introduction of non-polar solvents. This is because crystallization water in considerable amounts is already present in the POM nanocrystalites. The later will anyway result in the dissociation of the overabundant amine groups of PEI and the concomitant disturbance of POM stereochemistry. FTIR shows that PEI interacts with POM via the passivation of its amino groups. The interaction starts on the W-Oc-W bridges (this vibrational mode is the first to be affected by gradually increasing PEI molarity) and eventually spreads throughout the whole POM structure.

The reactivity of POM-PEI interface, forces the utilization of POM

molarities higher than 0.05 M. This way the interior molecules of the thicker film are able to survive the process (confirmed via both UV-Vis and FTIR spectra). Unfortunately, higher POM concentrations, as already mentioned in Fig.3.24, introduce structural defects and inhomogeneity on the spin coated PEI through the formation of POM nucleation centers during film polymerization. This, again, results in a non-perfect film.

Therefore, PEI was abandoned as a viable molecular-friendly alternative for device-grade solution-processable gate dielectric.

### 3.7.2 PMMA

Poly methyl methacrylate (PMMA, $(C_5O_2H_8)_n$) is a transparent thermoplastic polymer often used in sheet form as a lightweight or shatter-resistant compound as well as a casting resist. It is also referred to as acrylic glass or by the trade names Plexiglas, Acrylite, Lucite, Perspex and several others. It is often preferred for its moderate properties, facile handling and processing, and low cost. The corresponding monomer methyl methacrylate ($C_5H_8O_2$), in bulk liquid form or suspended as fine droplets in water, is polymerized under the influence of free-radical initiators to form the solid PMMA. The structure of the polymer repeating unit is presented in Fig.3.25.

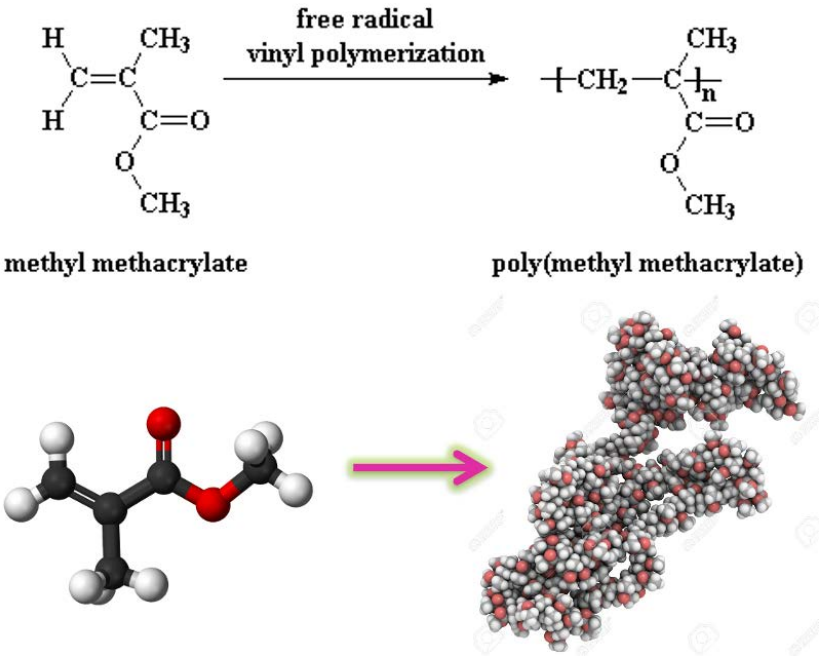


Figure 3.25: Methyl methacrylate structure and PMMA.

The presence of the pendant methyl ($CH_3$) groups prevents close packing of the polymer chains (i.e. in a crystalline fashion) as well as free rotation around the carbon-carbon bonds. As a result, PMMA is a tough and rigid polymer. In addition, it almost perfectly transmits visible light maintaining degradation tolerant under ultraviolet radiation and weather fatigue.

PMMA is essentially an organic glass at room temperature with a $T_g$ ranging from 105 $^oC$ for atactic PMMA and 85 to 165 $^oC$ for most commercial grade compounds, while its melting point $T_m$ is around 160$^oC$. Its superior stability and inertness, its good adhesion to $SiO_2$ [251] as well as its relatively high dielectric constant ($\tilde{2}$.6 at 1MHz [252]) are key factors for its investigation as gate dielectric in capacitive memory prototypes. PMMA is readily dissolved in non-polar solvents like toluene and di-chloro-methane.

For this investigation we used PMMA 350K 3% w/w in Toluene (Tol) and PMMA 350K 3% w/w in Di-chloro-methane (DCM). The two solutions were spin coated onto test $SiO_2$ on Si substrates, with the toluene-containing sol resulting in the best film quality using spinning parameters of 4000 rpm for 2 min in RT. This resulted in a 146 nm-thick (profilometer-determined thickness) homogeneous film. DCM, on the other hand, has been proven to act as a poorer solvent resulting in non-acceptable film quality. The later will not be further examined during this work.

After spin coating the film is baked at 120 $^oC$, above $T_g$, for 20 min in order for cross-linking and solvent evaporation to occur. This specific temperature is followed throughout the LbL processing and is selected due to its compatibility with the utilized organic molecules (APTES, IPA). POMs, on the other hand, remain intact even beyond 400$^oC$, so their integrity is not an issue within such processing temperatures.

The corresponding FTIR spectra along the procedure of the $SiO_2$-/APTES/POM/PMMA stack formation can be seen in Fig.3.26.

Deconvolution of the composite peaks in the spectrum of the final stack (i.e. upon PMMA deposition, light blue curve, inset) indicates that the four characteristic peaks of the POM molecular structure are retained intact after spin coating with PMMA and baking.

Having ensured structural integrity, the electronic structure of the material is the next investigation goal. The efficacy of the layer as gate dielectric (prevention of back-tunneling in the capacitive cell) depends on band alignment across the stack and the blockade of both electron and hole tunneling to and from the stack, respectively.

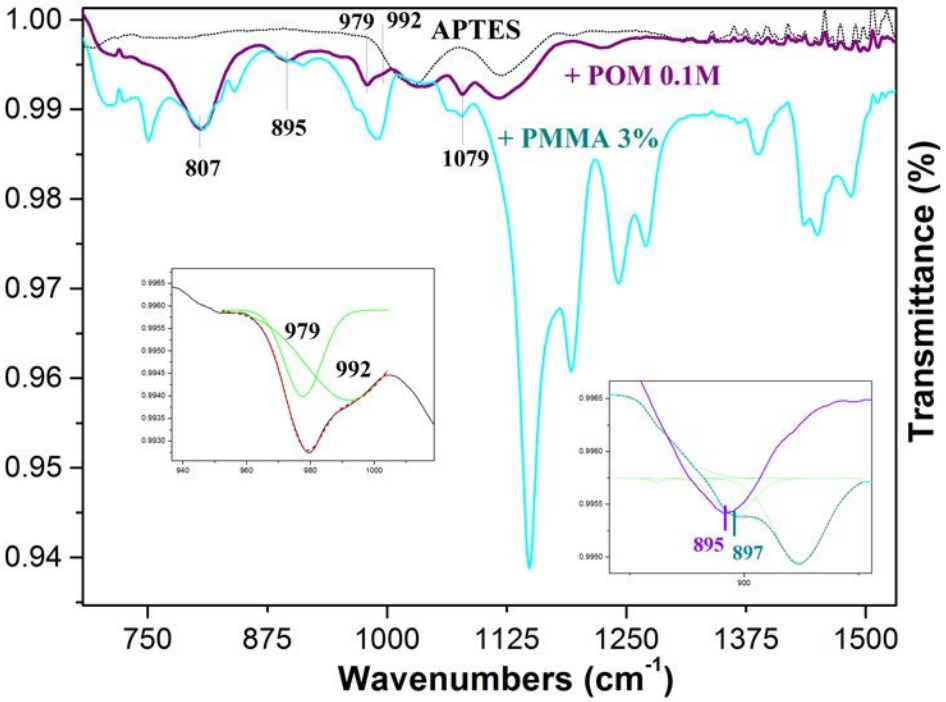


Figure 3.26: FTIR specra of PMMA-protected POM on APTES-modified $SiO_2$ on Si.

### Optical bandgap

Towards the determination of the electronic gap and the details of electronic structure the optical gap is of great value. One particular characteristic of amorphous semiconductors such as PMMA is that, unlike the crystalline ones, there exists a non-zero DOS within the mobility gap. These distinct features arise due to the presence of tail states, which are localized [253, 254] and appear due to the presence of disorders and weak bonds. This way extended states and localized states co-exist, with the latter typically appearing throughout the forbidden gap. This concept is depicted in Fig.3.27.

UV-Vis spectra of the fabricated PMMA layers have been analyzed through the Tauc model (see Eq.3.26) to acquire the optical band gap magnitude ($E_g^{opt}$). In the vicinity of the sharp absorption increase in the substance, the Tauc relation for dependence of absorbance on light photon energy applies [255].

$$\alpha(f) = \frac{A(hf - E_g^{opt})^x}{hf} \tag{3.26}$$

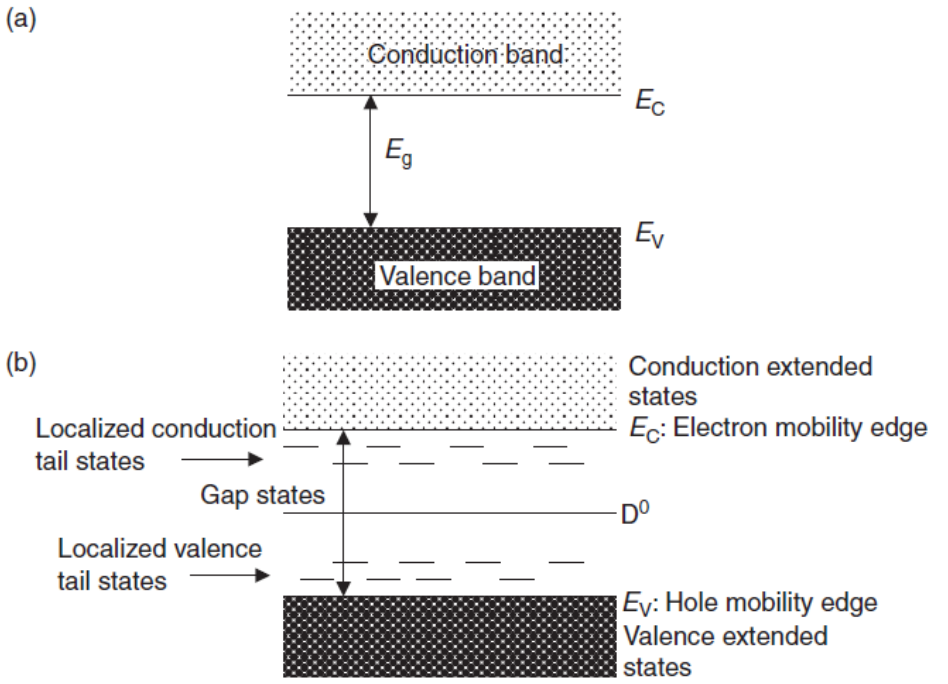


Figure 3.27: Schematic representation of DOS in crystalline (a) and amorphous (b) semiconductors (Shklovskii and Efros, 1984).

According to this model a plot of $(hf)^{1/2}$ vs hf should be linear above $E_g$ at which point a=0. Tauc plots based on UV-Vis spectra from the plot $(ahf)^{1/2}$ vs hf for PMMA layers 70nm thick are presented in Fig.3.28.

The analysis shows that $E_g^{opt}$ = 5.75 eV. The electronic bandgap is typically larger than the optical gap, especially in systems with high spatial localization of the valence and conduction states, and the difference accounts for the Coulomb energy for the system. This quite high gap value is promising for considering PMMA as gate dielectric.

Nevertheless, one should take in mind that the optical gap $E_g^{opt}$ is being estimated only for transitions from extended valence to extended conduction states, (without the involvement of any tail states), corresponding to the situation where there are no tail states, like in crystalline solids [256].

The electronic activity of these tail states, which are highly dependent upon the preparation process, is crucial for the electric performance of the material. Their activity will be mapped in the following section upon the electrical characterization of the stack.

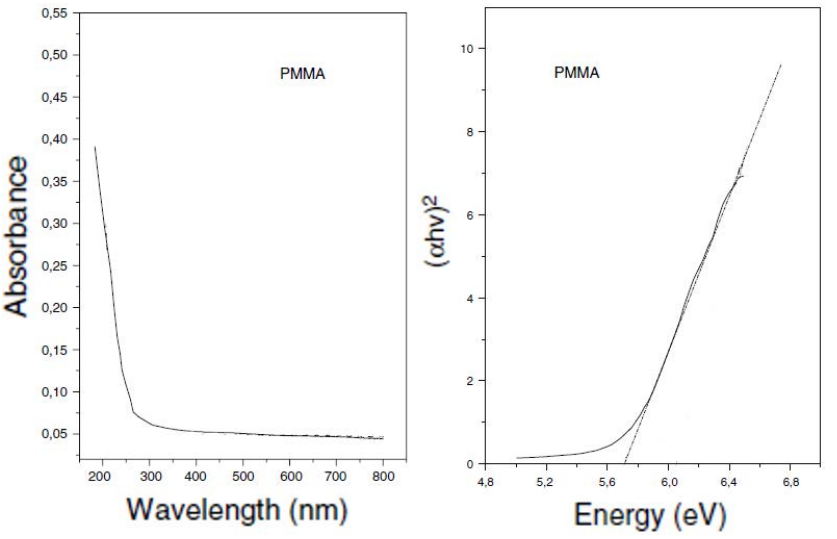


Figure 3.28: UV-Vis spectrum and Tauc plot for 70 nm-thick PMMA film.

### Electrical Characterization

The dielectric characteristics of the stack and its constituent layers can be monitored under a full voltage sweep via the high frequency C-Vs (Fig.3.29).

The deposition of PMMA on $SiO_2$ results in the addition of a series capacitance and a subsequent dramatic reduction of $C_{acc}$ (Fig.3.29). In case that a low molarity (i.e. 0.03 M) POM molecular layer is being deposited $C_{acc}$ decreases further, indicating addition of a dielectric layer in series. In the case of higher molarity (i.e. 0.1 M) molecular films, though, $C_{acc}$ increases again indicating an enhancement of the conductance across the stack caused upon the increase of POM molarity. Furthermore, the introduction of PMMA and molecular layers on the Si/$SiO_2$ substrate induces pronounced shifts on the flatband voltage $V_{FB}$, which are related to the overall trapped charge.

PMMA induces negative $\delta V_{FB}$ indicating the presence of a considerable amount of cationic centers in its volume (Table3.3). On the other hand, the positive flat band shifts induced upon the incorporation of POM layers indicate negatively charged molecular nodes. The shift is significantly greater in the case of higher POM molarity. Note that the $V_{FB}$ shift is calculated with respect to the bare $SiO_2$ substrate.

The Capacitance Equivalent Thickness (CET) derived from C-V measurements in the case of the $SiO_2$ reference substrate was 3.5 nm, in agreement with SE. The thickness of the grown molecular films cannot

be precisely extracted in the same way (via high-f C-V), due to the ambiguity in the estimation of a dielectric constant for the self-assembled layers. Thus, for the purposes of this section, thickness windows stead of specific thicknesses will be extracted for the POM assemblies.

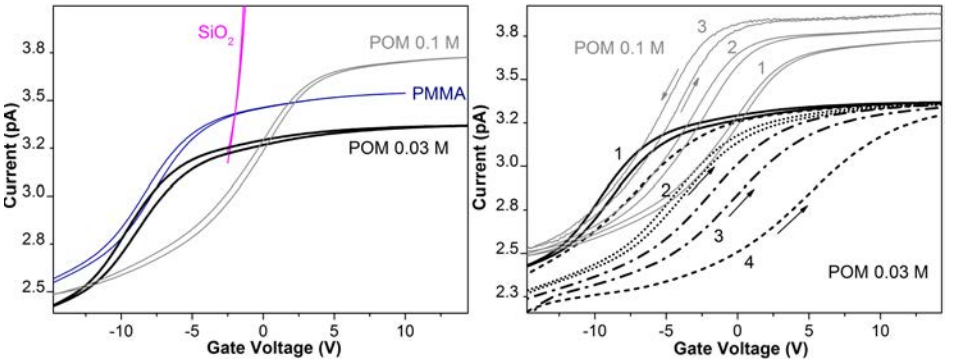


Figure 3.29: Typical high-frequency (1 MHz) C-V characteristics under bi-directional voltage sweep for the progressively built capacitive stack. $SiO_2$ represents the reference 3.5 nm tunneling oxide, PMMA the $SiO_2$/PMMA monitoring stack, POM 0.03M the final $SiO_2$/APTES/POM/IPA/PMMA stack, and POM 0.1 M the same stack with increased molecular concentration. On the right sequential cyclic sweeps for progressively extending voltage window highlight significant hole trapping, being compensated with increasing POM molarity.

Hole-originating hysteresis within a single C-V sweep is enhanced via application of progressively higher voltages. The phenomenon is attributed to the presence of PMMA volume ion trapping centers and is closely related to the concept of localized tail gap states which also contribute to the hysteretic behavior. This positive charge is partially counterbalanced through the incorporation of POM molecules (Fig.3.29) in the structure. The higher the POM concentration in film the fainter the hole contribution on a single sweep memory window. The total amount of fixed positive charge in the device is also reduced upon POM deposition.

In order to further investigate the electron injection/trapping process that constitutes the programming operation of the cell, the incremental-step-pulse programming (ISPP) method is employed. That is programming (positive) voltage pulses with constant increasing step height are being applied successively and the $V_{FB}$ is measured between two successive pulses [257, 258]. The results indicatively presented in Fig.3.30 correspond to a pulse width of 200 ns using square voltage pulses and extracted with respect to the $V_{FB}$ of a virgin device.

As the concentration of POM molecules increases from 0.03 up to 0.1 M, electron storage becomes more difficult and stronger electric fields are needed in order to achieve the same programming window. Nev-

Table 3.3: 1 MHz C-V parameters for the different constituents of the $SiO_2$/POM/PMMA stack.

| SAMPLE | EOT (nm) | d (nm) | $Q_{ox} * 10^{-8}$ $(Cb \cdot cm^{-2})$ |
|---|---|---|---|
| $SiO_2$ | - | 3.8 | +7.7 |
| +PMMA | 9.7 | 3.9 | +23.0 |
| +POM 0.03 M | 9.5 | 1.6-3.0 | +21.0 |
| +POM 0.1 M | 10.3 | 9.9-19.5 | +8.9 |

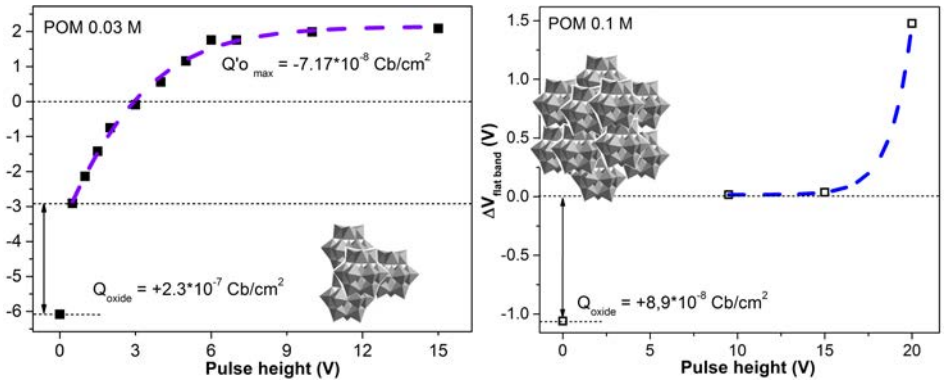


Figure 3.30: Programming windows for the fabricated MOS memory capacitive cells incorporating POM 0.03M (left) and POM 0.1 M (right) layers in a $SiO_2$/APTES/POM/IPA/PMMA stack.

ertheless, the memory windows extracted from round sweep C-V measurements in Fig.3.29 follow the typical behavior, i.e., the negative charge retained in the device increases as the POM node size increases and the fixed positive oxide charge (attributed to PMMA volume ionic charge) of the non-pulsed device is reduced by half an order of magnitude in 0.1 M films, when compared to 0.03 M films, due to the excess of negative charge in bigger POM nanocrystals.

Under pulse conditions, the reduction of the $\delta V_{FB}$ can be associated with the increased conductance in large POM nanocrystals that results in poor charge retention characteristics, as commended in the C-V characteristics of Fig.3.29. In addition, for the 0.03 M films the programming window reaches an utmost value and then remains practically constant, denoting a saturation of the molecular nodes for this case without further modification of conductance or failure.

Despite the encouraging charge trapping characteristics of the low molarity POM film (i.e. 0.03 M) the PMMA gated stack is not considered

appropriate for charge-trapping non-volatile memory cell.

When targeting reliable electron-trapping memory cells, as is the case of POM-based devices, the elimination of cationic side trapping within the structure is essential. Even though the fixed positive charge in the PMMA volume could be treated as an offset, this concept is not favorable as it would result in major reading and retention problems [66] (poor reliability). The latter is due to the progressively smaller net amount of charge carrying the information in the cell as the stored charge on the molecules becomes larger.

## 3.8 Conclusions

This chapter deals with the phenomenon of dynamic carrier exchange across the layers of a modified MIS structure via incorporation of a properly designed POM molecular layer. We demonstrated that the utilization of POM molecules can be advantageous for the realization of low power switching and/or fast writing applications as they provide multiple resistive states for low applied fields and good response to dynamic charging conditions. Moreover, their presence reduces electron-hole pair generation lifetime favoring the increase of speed in switching and writing processes.

The basic mechanisms of vertical transport are identified utilizing capacitance-voltage and current-voltage measurements, as well as transient capacitance measurements under step voltage polarization. The POM layer increases conductivity via induction of gap states (approximately 1.0 eV below Fermi level), as a result of tailing of the electron-rich orbitals of defective POM structures within the $SiO_2$ gap. Under gate injection, transport occurs through coupled processes of thermionic emission over the Schottky barrier induced by the HOMO-LUMO/ Al Fermi level mismatch and interface states assisted Poole-Frenkel transport along with resonant tunneling through molecular states at relative high and intermediate electric fields ([-1.7, -1.3] V). Hopping, coherent and incoherent tunneling also occur in the low field regime. Each mechanism dominates the current in a different bias and/or temperature regime.

Crucial parameters concerning the characteristics of the integrated molecular films can be derived from the dynamic carrier exchange between the POMs and the gate electrode. These are the active trap density of $5 \times 10^{12} cm^{-2}$ for the POM sheet and the activation energy for hopping assisted by shallow states of the σ-bonded molecular network of the IPA organic layer estimated at 25 meV. The total charge density of a POM modified sheet is of the order of $Q_{tot} = 2.9 \times 10^{-7} Cb/cm^2$ at 240 K and is distributed in all available molecular states in the POM islands (1-3 elec-

trons per molecule). The discrete charge amounts collectively occupied in the device by each one of the triplet of POM states exhibit Gaussian distribution and have been estimated as: $Q_{ta} = 0.7 \times 10^{-7} Cb/cm^2$, $Q_{tb} = 1.4 \times 10^{-7} Cb/cm^2$, $Q_{tc} = 0.8 \times 10^{-7} Cb/cm^2$ via peak deconvolution.

The structure and dimensions of the functional organic and inorganic molecular thin films were determined via a combination of methods such as electrical characterization, SE, SEM and AFM. The POM molecules are arranged in uniformly distributed nanoislands of a mean diameter of 17 nm forming a layer of mean thickness of 2.2 nm. However, the electronic structure of these nanoislands, derived via dynamic J-V measurements, remains independent of the size of the formed islands and exhibits discrete charging levels characteristic of the LUMO and LUMO+1 states of the single POM molecules. This can make the exhibition of single-electron charging effects possible even at RT.

Quantitative evaluation of the POM displacement current contribution under device operation was obtained via low temperature C(t) transient capacitance monitoring and development of a modified Zerbst-type equation. POM drastically reduces electron-hole pair generation lifetime being, thus, promising for high speed writing or switching applications.

Addressing the problem of backtunneling towards the gate via polymeric solution processable organic dielectrics was not fruitful either due to poor film quality and involved structures' stability (case of PEI) or due to the presence of significant amount of positive ionic charge (case of PMMA) in the dielectric's volume, a fact resulting in severe retention and reliability issues.

Nevertheless, the recorded ability to easily modify the POM charging threshold via selection of the top organic insulator (in this case isopentylamine) and the ability to finely tune the POM charging capacity by simply controlling the POM molarity in the precursor solution, implement multiple POM layers and/or select between different charging levels by modifying the Keggin structures heteroatom in the POM molecules, makes these materials a promising candidate for fabrication of hybrid molecular-semiconducting devices and exploitation of techniques like inject printing to modify traditional high cost doping and film growth techniques.

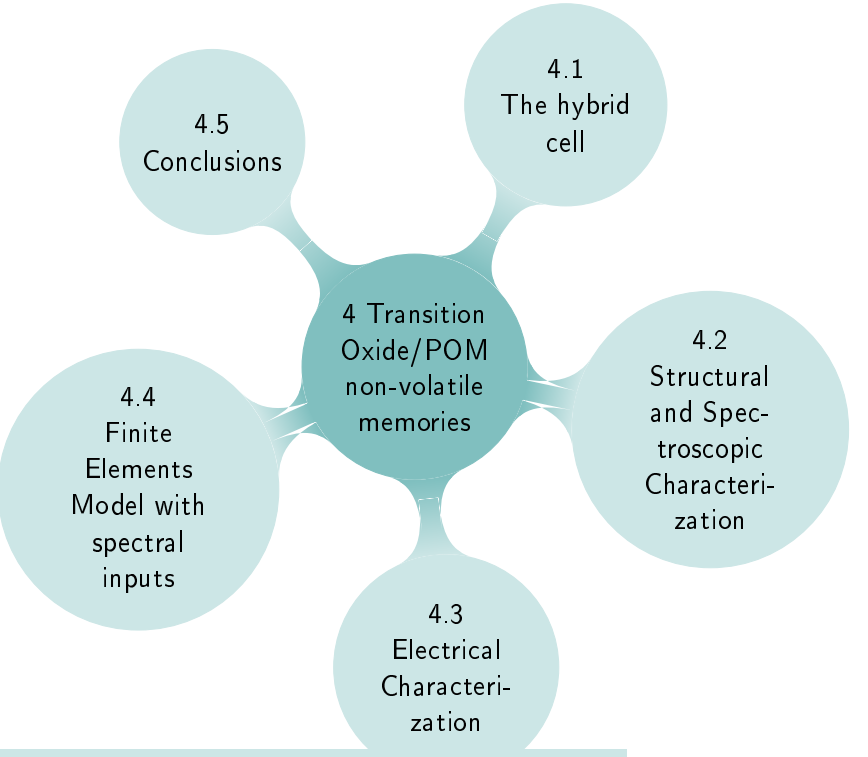


# 4

# Low dimensional polyoxometalate molecules/tantalum oxide hybrids for non-volatile capacitive memories

*Transition-metal-oxide hybrids composed of high surface-to-volume ratio $Ta_2O_5$ matrices and a molecular analogue of transition metal oxides, tungsten polyoxometalates ($[PW_{12}O40]^{3-}$), are introduced herein as a charge storage medium in molecular nonvolatile capacitive memory cells. The polyoxometalate molecules are electrostatically self-assembled on a low-dimensional $Ta_2O_5$ matrix, functionalized with an aminosilane molecule with primary amines as the anchoring moiety. The charge trapping sites are located onto the metal framework of the electron-accepting molecular entities as well as on the molecule/oxide interfaces which can immobilize negatively charged mobile oxygen vacancies. The memory characteristics of this novel nanocomposite were tested using no blocking oxide for extraction of structure-specific characteristics. The film was formed on top of the 3.1 nm-thick $SiO_2$/n-Si(001) substrates and has been found to serve as both $SiO_2$/Si interface states reducer (i.e., quality enhancer) and electron storage medium. The device with the polyoxometalates sandwiched between two $Ta_2O_5$ films results in enhanced internal scattering of carriers. Thanks to this, it exhibits a significantly larger memory window than the one containing the plain hybrid and comparable retention time, resulting in a memory window of 4.0 V for the write state and a retention time around $10^4$ s without blocking medium. Differential distance of molecular trapping centers from the cells gate and electronic coupling to the*

*space charge region of the underlying Si substrate were identified as critical parameters for enhanced electron trapping for the first time in such devices. Implementing a numerical electrostatic model incorporating structural and electronic characteristics of the molecular nodes derived from scanning probe and spectroscopic characterization, we are able to interpret the hybrids electrical response and gain some insight into the electrostatics of the trapping medium.*

## 4.1 A Hybrid Cell as Flash Memory Element

In the quest for solid state memories' downscaling approaches other than photolithographic size reduction, like the introduction of molecular components, hybrid materials and three dimensional nanostructuring are gaining ground [259]. The remarkable progress made lately in the fields of organic and molecular electronics has enabled successful fabrication of molecule-based hybrid devices, among which promising alternatives in the field of non-volatile memories [260, 261, 262, 263]. Such devices aim at exploiting the bi-stability of states either in conductance [264, 265, 266, 267], magnetic [268] and optical properties [269], polarization [270], or structure [262] upon an external stimulus to obtain binary switching functionality.

The appeal of molecular devices lies on properties that are inherent in molecules like discrete quantum states and, thus, charge localization, offering tolerance on oxide defects pretty much as with floating dots [271] and, additionally, significantly lower dimensions and multiple charging state addressing. To this end molecules with reversible redox properties seem to present an advantage [272, 273, 274, 275].

On the other hand, beyond charging efficiency, one of the most fundamental limits in speeding up memory devices is the increase of the tunneling current which follows thickness downscale of the dielectric layer and renders the device unreliable [276]. High-k oxides are now being used to reduce the leakage current while maintaining the same capacitance [277, 278].

Promising as it may seem, the combination of these two approaches is a challenging task due to constrains like the demand for low temperature growth and the precision control of the oxide/molecule interface [279]. Moreover, molecular components suffer from variability and high extraction losses at interfaces [280], facts impeding their technological competitiveness.

Therefore, the need for molecule-based devices with controlled coupling of the functional molecules to the support layer and/or the address-

ing leads and low contact resistance remains an open issue. This has triggered the research on defect-tolerant [281] CMOS-compatible processes [282] and minimization of charge injection barriers [283].

We propose here that transition metal oxides, in which bonding is intrinsically neither purely covalent nor ionic or metallic, can be a promising candidate for the formation of interfaces of low energy cost with molecular assemblies [284]. Salient features of these oxides are their potential for molecular-friendly (i.e. low temperature) growth and their typically high dielectric constant, corroborating their appeal for molecular memory applications.

### 4.1.1 Growth of near-ambient stoiciometric $Ta_2O_5$

$Ta_2O_5$ is grown via evaporative deposition of stoichiometrically pre-oxidized tantalum wire under $N_2$ atmosphere in order to preserve composition while maintaining room substrate temperature. With this method elevated substrate temperatures during growth and high-temperature post-annealing, typically used for metal oxides to optimize reactions between ionized species on the substrate [285] and obtain stoichiometry, can be avoided. With this simple method stoichiometric $Ta_2O_5$ and ambient substrate temperature can be reconciled.

However, preservation of stoichiometry is not the only objective. The grown oxide except for large scale homogeneity has to fullfill the stringent requirements for high degree of porosity in order to enable significant incrfease in the effective area of POM assembly during hybridization and, thus, increase the molecular trapping nodes' integration density. Due to low energy growth, adatom migration during deposition is suppressed. The later is essential in order to obtain locally non-flat, i.e. highly porous matrices. Moreover, low temperature processing helps maintain the mixed composition of the interfacial oxides, providing high capacitance low leakage structures [286], essential for memory applications.

#### Tuning the growth parameters

The chamber was pumped down to 1 Torr and purge filled with $N_2$ up to 4 bar. This way a clean process with no disruption of stoichiometry is ensured. As can be observed in Figures 4.1 to 4.5 except the resulting film thickness the size and density of pores is also directly affected from the applied voltage and the duration of current flow. Thus, the whole film morphology can be precisely tuned by properly choosing these two (voltage and time) growth conditions and keeping other parameters constant.

Fig.4.6 summarizes the investigated thickness versus voltage and evaporative deposition times.

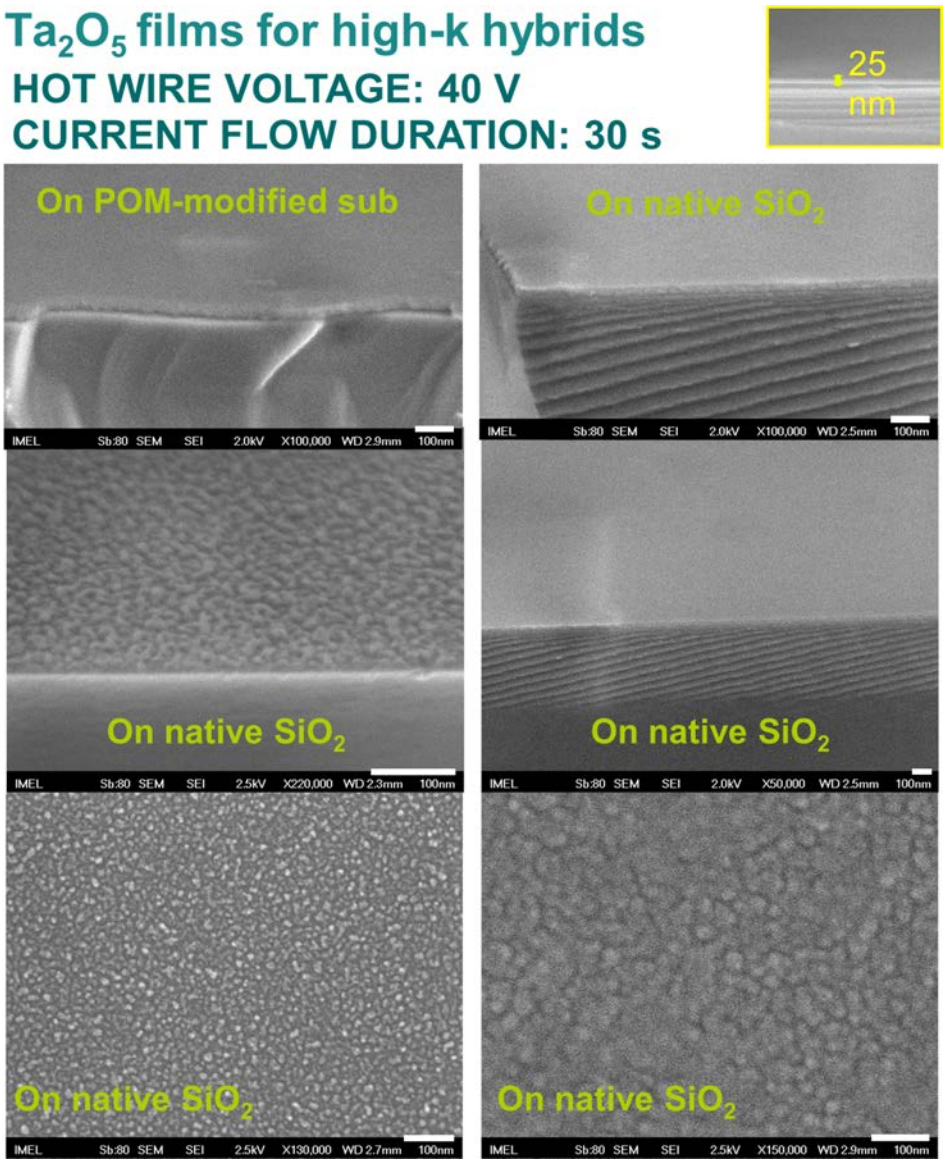


Figure 4.1: FE-SEM images of 25 nm high surface-to-volume ratio thin $Ta_2O_5$ grown on a self-assembled POM oligolayer on $SiO_2$ and plain $SiO_2$ for comparison. Tilt angle 65 degrees, 2kV energy electron beam. White bars equal 100 nm.

Based on detailed FE-SEM and AFM investigation the 25-nm-thick high surface-to-volume ratio oxide was selected. This film provides adequately thin film with the proper size of inteconnected pores so as to incorporate POM molecular nanocrystals of the order of 10 nm, a reasonable compromise between charging efficiency and localization (i.e. in-

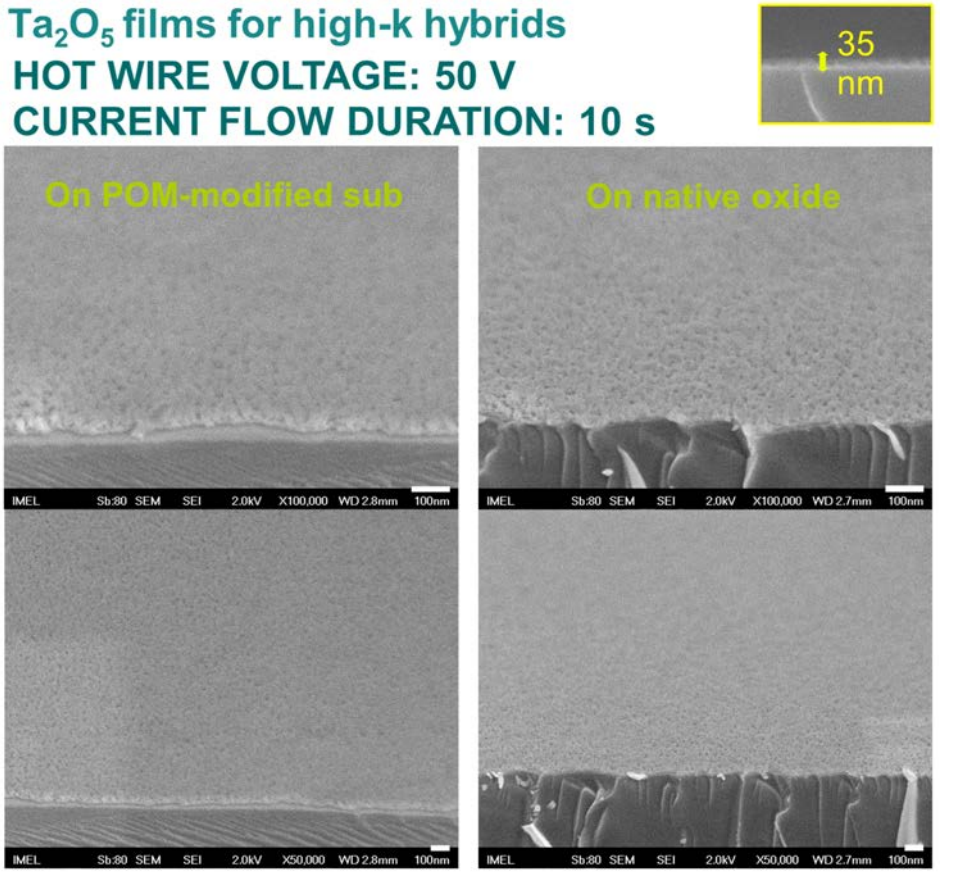


Figure 4.2: FE-SEM images of 35 nm high surface-to-volume ratio thin $Ta_2O_5$ grown on a self-assembled POM oligolayer on $SiO_2$ and plain $SiO_2$ for comparison. Tilt angle 65 degrees, 2kV energy electron beam. White bars equal 100 nm.

herent retention ability).

### Composition & stoichiometry

XPS of the 25 nm as-grown film indicates stoichiometric $Ta_2O_5$, containing a certain amount of oxygen vacancies. As seen in the right part of Figure 4.7 the O1s peak can be analyzed in two peaks, with the first located at a binding energy of $530.7 \pm 0.1eV$ corresponding to oxygen bonded to tantalum in $Ta_2O_5$, in agreement to the literature [287] and the other corresponding to oxygen related to surface contamination ($532.0 \pm 0.1eV$) [288]. The main peak of Ta4f7/2 is located at a binding energy of $26.4 \pm 0.1eV$ (Figure 4.7 left) corresponding to tantalum bonded

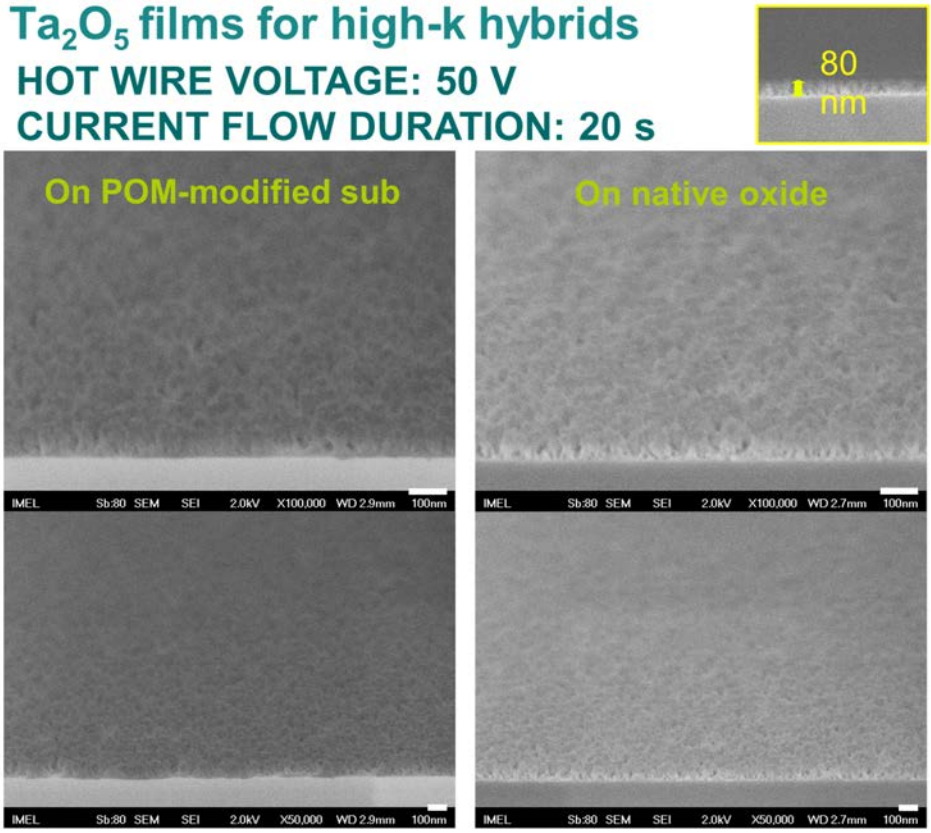


Figure 4.3: FE-SEM images of 80 nm high surface-to-volume ratio thin $Ta_2O_5$ grown on a self-assembled POM oligolayer on $SiO_2$ and plain $SiO_2$ for comparison. Tilt angle 65 degrees, 2kV energy electron beam. White bars equal 100 nm.

with oxygen in stoichiometric $Ta_2O_5$ [287, 289]. The higher binding energy peak of the 4f doublet appears at 28.4 eV and corresponds to Ta4f5/2 in $Ta_2O_5$, according to literature [289, 290].

The two peaks of the Ta4f doublet have a 4f7/2 - 4f5/2 area ratio of 4:3 and energy separation of 1.9eV, the characteristic spacing of Ta4f, in accordance to [291, 292]. The higher peak of the 4f doublet appears at 28.4 eV and corresponds to Ta4f5/2 in $Ta_2O_5$ according to the literature [293, 294, 295]. XPS analysis of the 25 nm as-grown tantalum oxide indicates stoichiometric $Ta_2O_5$, with no formation of suboxides. The film, though, contains a certain amount of oxygen vacancies detected through the 532.0 eV O1s peak contribution but, mainly, through the photoluminescence spectra that follow. This amount of vacancies in $Ta_2O_5$ is too low for the formation of detectable suboxide regions and its role is limited to the

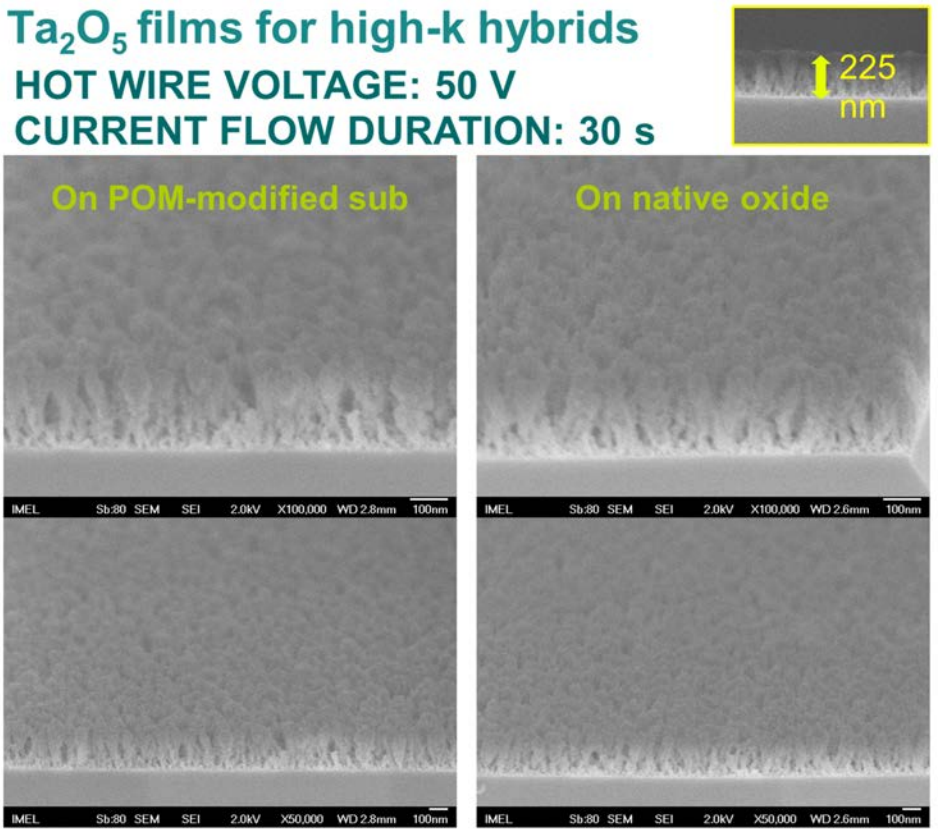


Figure 4.4: FE-SEM images of 225 nm high surface-to-volume ratio thin $Ta_2O_5$ grown on a self-assembled POM oligolayer on $SiO_2$ and plain $SiO_2$ for comparison. Tilt angle 65 degrees, 2kV energy electron beam. White bars equal 100 nm.

contribution of electrons in the form of ionized donors in the electrical conduction [296].

### 4.1.2 A hybrid high-k / molecular medium & interface dipole engineering

In all the examined cases, a thin thermal $SiO_2$ of 3.1 nm is grown on the Si surface. As a result there exists a net dipole across this high-k ($Ta_2O_5$)/low-k($SiO_2$) interface of the MOS stack. The electrostatic potential difference induced at the interface due to the dipole is : $D/(\epsilon\epsilon_0 A)$. This potential difference naturally modulates the flat band voltage of the MOS-C.

Apart from that the charge transfer between the POM molecule and the gate metal modifies the surface dipole of the Al surface strongly and

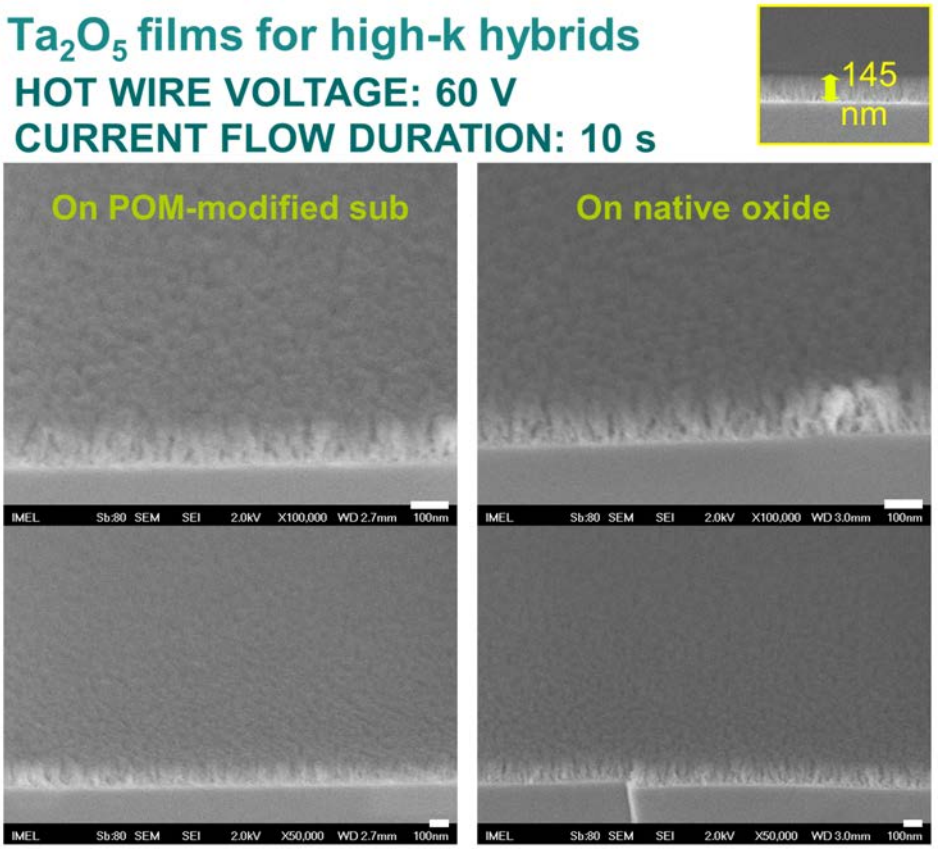


Figure 4.5: FE-SEM images of 145 nm high surface-to-volume ratio thin $Ta_2O_5$ grown on a self-assembled POM oligolayer on $SiO_2$ and plain $SiO_2$ for comparison. Tilt angle 65 degrees, 2kV energy electron beam. White bars equal 100 nm.

locally, a fact that leads to the local increase and decrease of the metal's work function.

Hybrid molecular/$Ta_2O_5$ memory cells based on self-assembled tungsten polyoxometalate molecules (POMs, $[PW_{12}O_{40}]^{3-}$) were fabricated and characterized. POMs are able to attach and delocalize electrons on their metal framework without undergoing structural damage [272, 297, 298].

The interfaces involved in this cell bear localized dipoles of molecular origin, able to influence the band alignment of the MOS stack [299, 300]. This phenomenon along with the attainment of electronic coupling of the trapped electrons to the space charge region (scr) of the Si body can be exploited to build a hybrid memory cell [301] whilst improving the properties of the high-k dielectric by mitigating fixed and/or interface

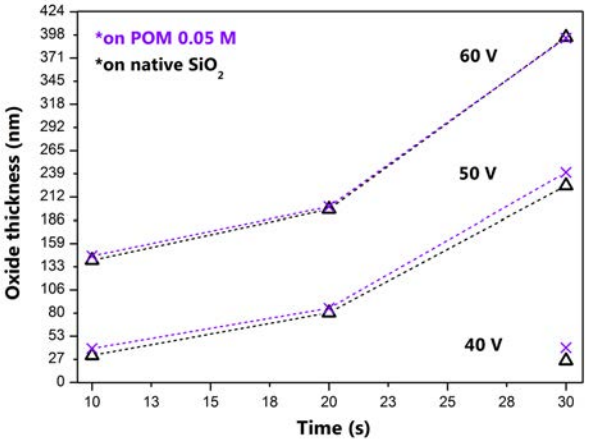


Figure 4.6: Trend lines of thickness versus voltage and evaporative deposition times for the used low temperature $Ta_2O_5$ on $SiO_2$.

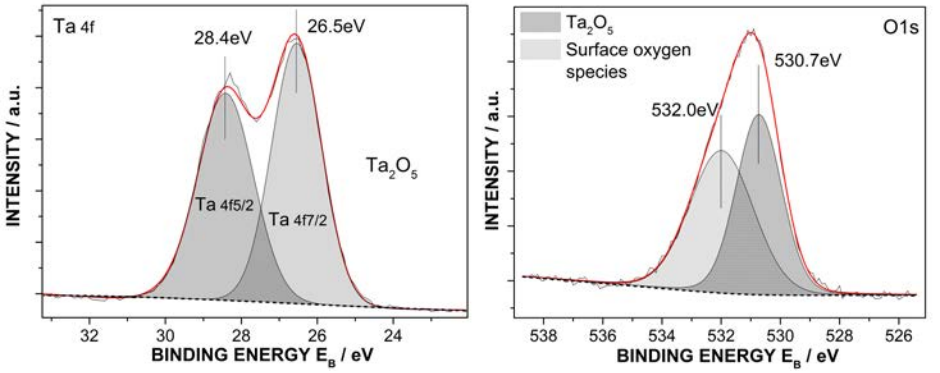


Figure 4.7: Ta4f (left) and O1s (right) XP spectra of the 25-nm-thick as-grown $Ta_2O_5$ film.

charges [302].

These capacitive memory structures extend current achievements in the field of CMOS-compatible processes for the fabrication of molecular devices [303, 304, 305], provide, similarly to [306], a way for direct access of the POM switching abilities in a MOS flash memory and introduce a new molecular hybrid of significantly improved memory window and commendable charge retention characteristics. The presented results demonstrate the suitability of this hybrid to be incorporated as high density storage node in advanced, solution-processed molecular nonvolatile flash memory arrays.

### 4.1.3 Preparation of Molecular Components

The utilized 12-Tungstophosphoric acid hydrate (POM, $HPW_{12}O_{40} \cdot xH_2O$, Aldrich), 3-aminopropyl triethoxysilane (APTES, Aldrich) and isopentylamine (IPA, Aldrich) were all of analytical grade and used without further purification. Hydrochloric acid, sulfuric acid and hydrogen peroxide (all obtained from Aldrich, analytical grade), were used for the pH adjustment of the deposition solutions and the purification and hydrophilization of the $SiO_2$ surface respectively. Deionized water with a resistivity of 15 $M\Omega cm^{-1}$ prepared from the Milli-RO plus 90 apparatus (Millipore) was used in all experiments.

The substrates used in the molecular nanostructures fabrication varied according to the characterization method applied; quartz slides were used for the UV study and silicon wafers with 3.1 nm dry oxide were used for the Fourier transform infrared spectroscopy (FTIR), scanning electron microscopy (SEM), and X-ray photoelectron spectroscopy (XPS) studies. All substrates were used after cleaning with piranha solution ($H_2O_2$:$H_2SO_4$, 1:1 v/v). The preparation of molecular nanocrystals and the subsequent self-assembly on $Ta_2O_5$ was performed according to the one-pot two-stage method analyzed in detail in Chapter 2.

### 4.1.4 Fabrication of capacitive memory cells

We fabricate memory capacitor testbeds which incorporate the material under test in the active region.

The process consists of standard photo-lithography and etching on wet-oxidized (500 nm $SiO_2$) n-type Si substrates 1-2 $\Omega cm$ defining square patterns with side dimensions of 100 $\mu$m. These constitute the active areas of the devices. A 3.1 nm-thick tunneling oxide is grown on top via dry oxidation, in order to minimize the trap density at the Si/oxide interface [307, 308]. For the assembly of the molecular traps the underlying oxide is chemically modified with APTES, a type of aminosilane molecule used for the electrostatic self-organization of POM anions via the Layer-by-layer (LBL) process [309, 29, 304]. Passivation of the immobilized POMs is attained through an IPA capping monolayer and is crucial in providing electronic decoupling from the non-injecting side of the device [303, 310]. The device is sealed with a 500-nm-thick Al gate electrode.

Three types of devices are fabricated as depicted in Figure 4.8: a) P-Ox where $Ta_2O_5$ epitaxy follows the assembly of molecular layers on $SiO_2$, b) Ox-P where $Ta_2O_5$ is grown directly on top of $SiO_2$ and the molecules follow, and c) Ox-P-Ox where the passivated POM layer is sandwiched between two $Ta_2O_5$ films. For each device type three different $Ta_2O_5$ thicknesses were tested, namely 25 nm, 80 nm and 145 nm. $Ta_2O_5$ is

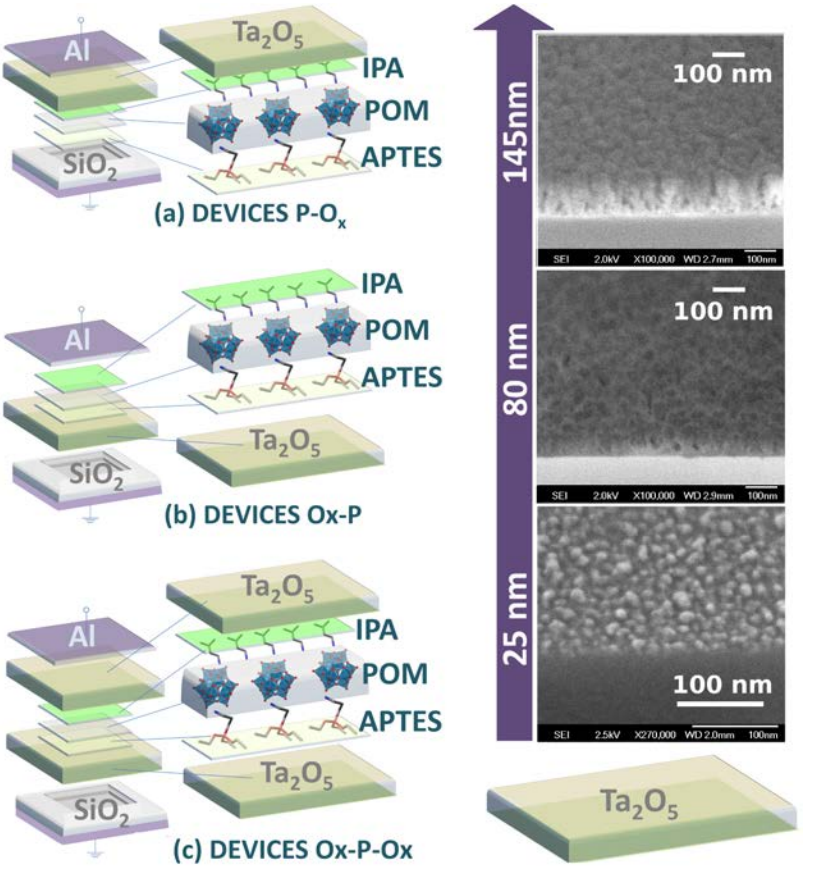


Figure 4.8: Schematics of the fabricated stacks along with three SEM snapshots depicting the growing $Ta_2O_5$ film. In figure a) $Ta_2O_5$ is grown on POM molecules self-assembled on the active region in b) $Ta_2O_5$ is directly grown on $SiO_2$ and the molecules are post assembled on top and in c) a passivated POM layer is being sandwiched between two $Ta_2O_5$ films.

grown via evaporative deposition of oxidized tantalum wire under $N_2$ environment and ambient substrate temperature.

### 4.1.5 Characterization

All electric measurements were performed in shielded probe station using a HP4041B picoammeter, a HP4284A precision LCR meter and an HP 8110A 150 MHz pulse voltage generator. For the XPS measurements unmonochromatized Mg Ka line at 1253.6 eV (12 kV with 20 mA anode current) and an analyzer (Leybold EA-11) pass energy of 100 eV were

used at 0 degree take-off angle.

For the UV photoemission spectra (UPS) the He I (21.2 eV) excitation line was used and a voltage of 12.23 eV was applied to the specimen in order to separate the high binding energy cut-off from the analyzer. UV-vis absorption spectra were obtained on a Perkin-Elmer UV-vis Lambda 40 spectrophotometer. FTIR transmittance spectra were recorded on a Bruker, Tensor 27 spectrometer using 1000 scans at 4 $cm^{-1}$ spectral resolution.

For the Photoluminescence (PL) measurements the 458 nm line of an $Ar+$ laser was used. The signal was analyzed with a Jobin Yvon SPEX HR320 monochromator and detected by a photomultiplier tube in reflection geometry. Atomic force microscopy (AFM) measurements were carried out using a TS-150 NT-MDT Solver Scanning Probe Microscope and an ultra sharp diamond-like carbon tip (curv. rad. 1-3 nm) with Au reflective side in tapping mode.

## 4.2 Investigation of the hybrid's morphology and electronic structure

The $Ta_2O_5$ matrix morphology is investigated with FE-SEM and AFM. In early deposition stages (i.e. 25 nm thickness) uniform tantalum oxide islands are being developed (Figure 4.8 right). As growth evolves we meet the cases of 80 and 145 nm, ending up with clear formation of dendrite nanocrystalline structures.

The grown oxide and the molecular nano-clusters are analyzed in 2-D (top-view) by means of AFM using a TS-150 NT-MDT Solver Scanning Probe Microscope and an ultra sharp diamond-like carbon tip (curv. rad. typically 1-3 nm) with Au reflective side in tapping mode. For the 25 nm case, a typical profile of the tantalum oxide surface before and after the modification with POM molecules is depicted in Fig.4.9 along with the roughness analysis statistics.

For the 25 nm case, the average rms roughness (Sq) obtained via AFM decreases with the addition of POM molecules from 1.7 nm to 0.3 nm. Although this indicates a surface modification, fractal analysis reveals a hidden correlation between the two structures. When analyzed with a box counting algorithm [311, 312] both surfaces are found to exhibit scale invariance with a fractal dimension (df) of 1.8 for the molecular layer and 1.7 for the $Ta_2O_5$ substrate. The AFM-derived binary images used for fractal analysis can be seen in Figure 4.10 against the original scans to enable comparison.

In the case of the molecule-modified structures this df value is consis-

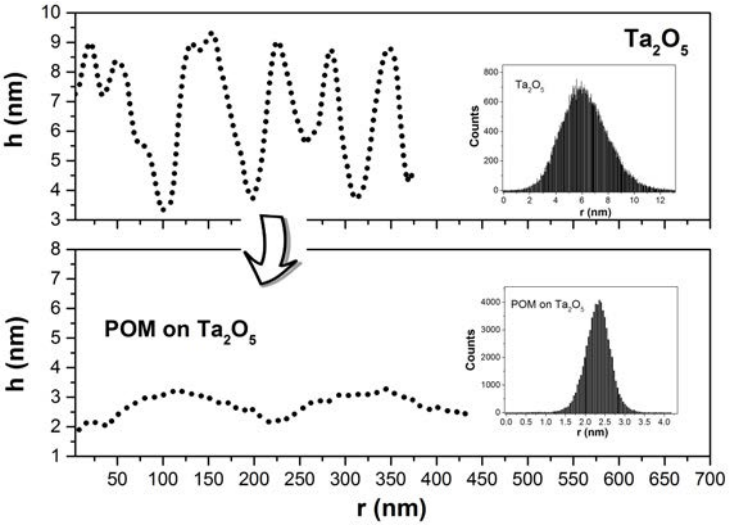


Figure 4.9: roughness analysis of AFM images and random profile of surfaces

tent with a Diffusion Limited Aggregation formation process [313]. The lower fractal dimension of $Ta_2O_5$ conveys its influence on the topology of the molecular layer [311], i.e. the electronic and structural coupling of POM molecules to the tantalum oxide matrix.

In Figure 4 UV-Vis absorption measurements indicate a shift of the $Ta_2O_5$ absorption edge towards higher wavelengths upon POM deposition, indicating an effective narrowing of the gap. The characteristic POM peaks remain intact in the absorption spectrum of the composite material, indicating the integrity of the molecular structures. Moreover, the intensity of the POM W-O transfer peak at 270 nm is tripled in the composite material, owing to its large effective surface. Along the same lines, the four FTIR bands of the Keggin structure POM [314, 315] remain unaltered upon deposition of $Ta_2O_5$ indicating no bonding disruption upon the $Ta_2O_5$-POMs interaction.

The UPS valence band spectra of sample Ox-P reveal the presence of a shallow intra-gap state centered at 1.3 eV within the $Ta_2O_5$ gap facilitating charge injection onto the states of the hybrid. The appearing gap states are attributed to the W5d band of W in the POM framework, and result from the tailing of electron-rich orbitals of reduced POM structures within the gap [303]. When POM is sandwiched between tantalum oxide films there is a sloping up tail before the high binding energy edge. This is indicative of increased inelastic scattering of the emitted valence band electrons on their way to the sample's surface.

Oxygen vacancies and oxygen interstitials have been known to emit

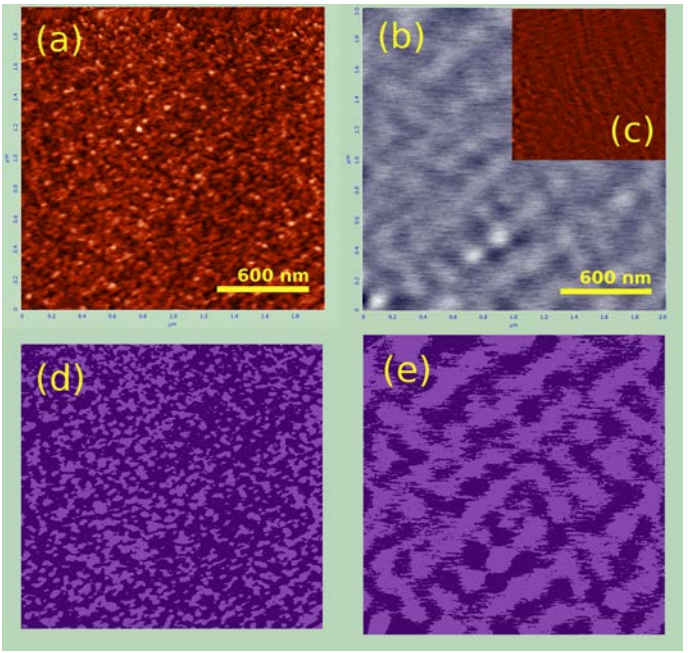


Figure 4.10: AFM images (top) and created binary images used for fractal analysis (bottom) of the 25-nm-thick $Ta_2O_5$ template before (a) and after (b) the self-assembly of the molecular clusters. Inset (c) corresponds to the morphology of the POM molecular layer when developed on a "flat" (sub-nm-roughness) $SiO_2$ surface. (e) and (f) are the binary images produced from AFM scans and used for fractal analysis after convergence of the box-counting algorithm.

in the visible part of the spectrum when excited, owning to the provision of alternate paths for the photo-induced carrier generation and recombination leaving their fingerprint on both PL and photoabsorption characteristics [316, 317, 318]. Figure 4.12 shows the PL spectra of three sample configurations, Ox, P-Ox and Ox-P excited with the 458 nm line of an $Ar+$ laser. These spectra all exhibit an asymmetric broad PL band mainly in the cyan-green region.

This band can be resolved by means of Gaussians in three discrete sub-bands attributed to specific emission centers and identified in all three cases ( Ox, P-Ox and Ox-P ). The first band, centered in green (around 500 nm for Ox-P and P-Ox, and at 517 nm for Ox), is almost identical in width and intensity for samples Ox and P-Ox, while it is slightly suppressed in sample Ox-P, where the $Ta_2O_5$ surface is post-modified, highlighting its surface origin. The intensity of the second band (located in green as well) is related to the oxygen content of the sample (the oxygen percentage is

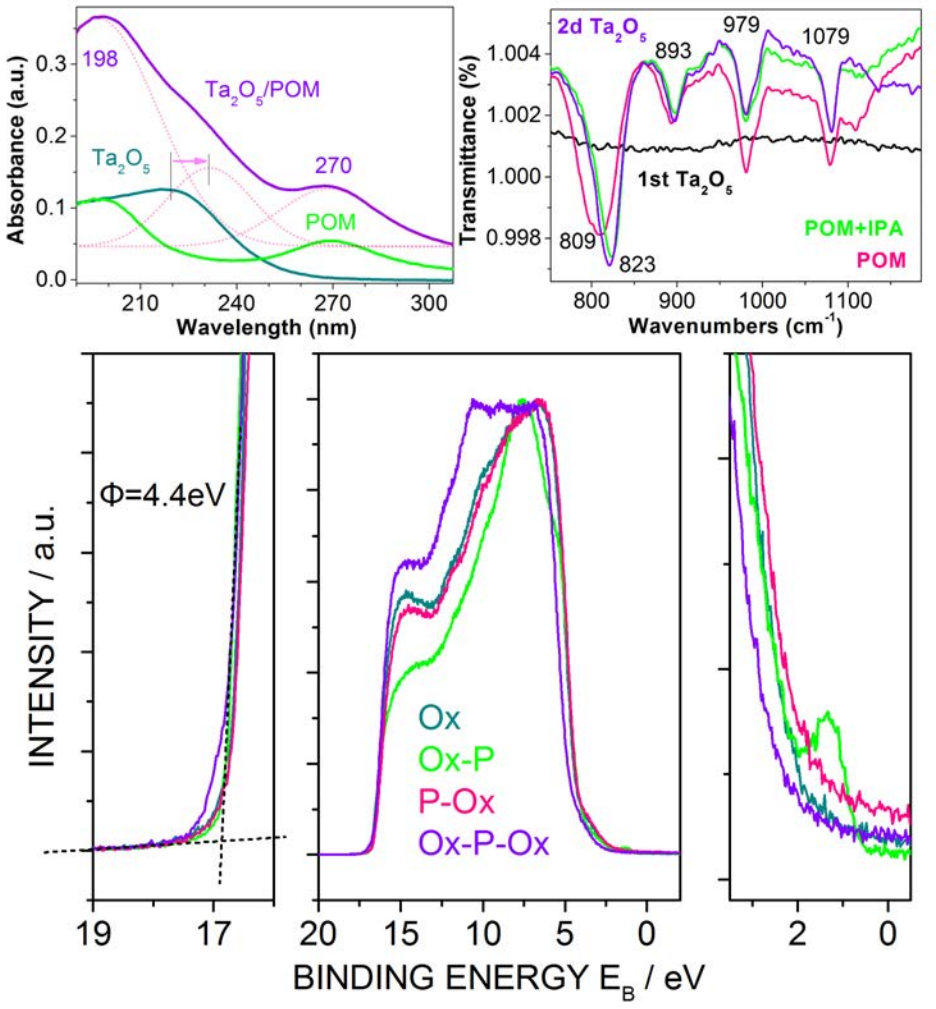


Figure 4.11: Top: UV-Vis absorbance of pure POM and $Ta_2O_5$ films along with the spectrum of the composite Ox-P type material and its spectral deconvolution next to FT-IR spectra. Down: Valence band spectra of the materials under test. On the right the region near the Fermi level is presented in magnification and on the left the high binding energy cut-off.

estimated from XPS stoichiometric analysis) pointing out its correlation to volume centers.

Interestingly this band appears centered towards yellow (576 nm) and broadened in the case the POM molecules are not present. Yellow emissions are being attributed to the presence of oxygen interstitials [319] which, in our case co-exist with oxygen vacancies (thus the broad band)

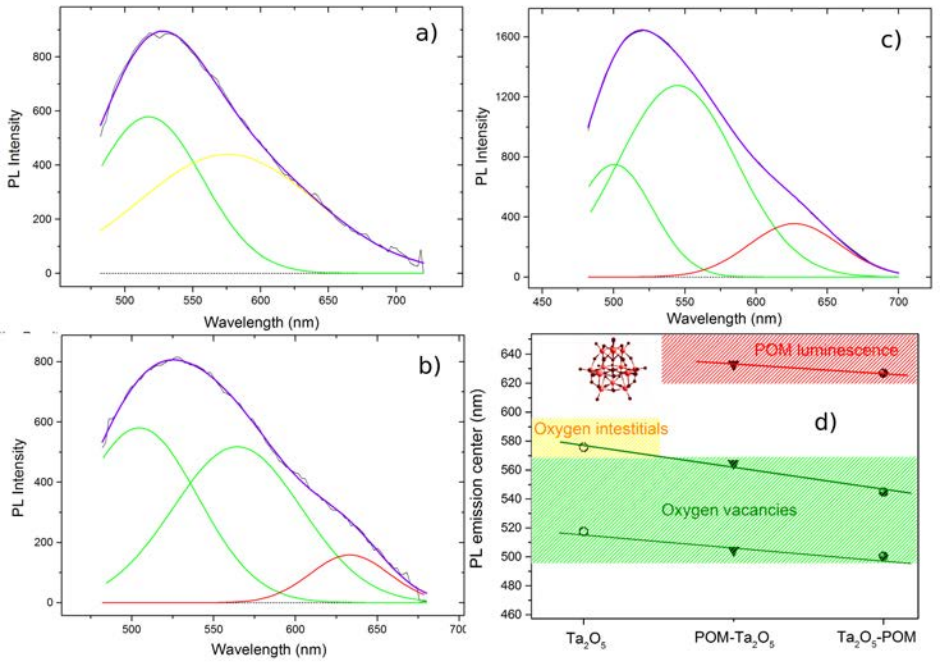


Figure 4.12: PL spectra of as-deposited $Ta_2O_5$ (Ox) (a), $Ta_2O_5$ grown on POM-modified substrate (P-Ox) (b) and POM post-functionalized $Ta_2O_5$ (Ox-P) (c). The main band is resolved by means of Gaussians in three discrete sub-bands presented in (d) and attributed to surface (lower wavelength peak) and volume emission centers, as well as to contribution from POM luminescence (red peak). In Figure (d) the lines are displayed as a guide for the eye.

in the volume of the $Ta_2O_5$, constituting its volume oxygen defects. This band shifts further to green when POM-originating oxygen vacancies [303] are entering the structure, as these vacancies tend to passivate part of the interstitials. As a result, the band is also narrowed in accordance to the suppression of the energy distribution of emissive centers.

The third contribution on the PL emission is directly related to the presence of POM molecules and is, therefore, not present in the case of Ox sample. This band centered at around 630 nm is attributed to the $O2p \rightarrow W5d$ intra-band transition in reduced POM molecules [303]. Since both the intensity and the wavelength of the green emissions are correlated to oxygen related defects in the film, these bands can be attributed to oxygen point defects in agreement with previously reported results [320].

## 4.3 Electrical characterization

Typical bidirectional capacitance-voltage (C-V) characteristics are shown in Figure 4.13.

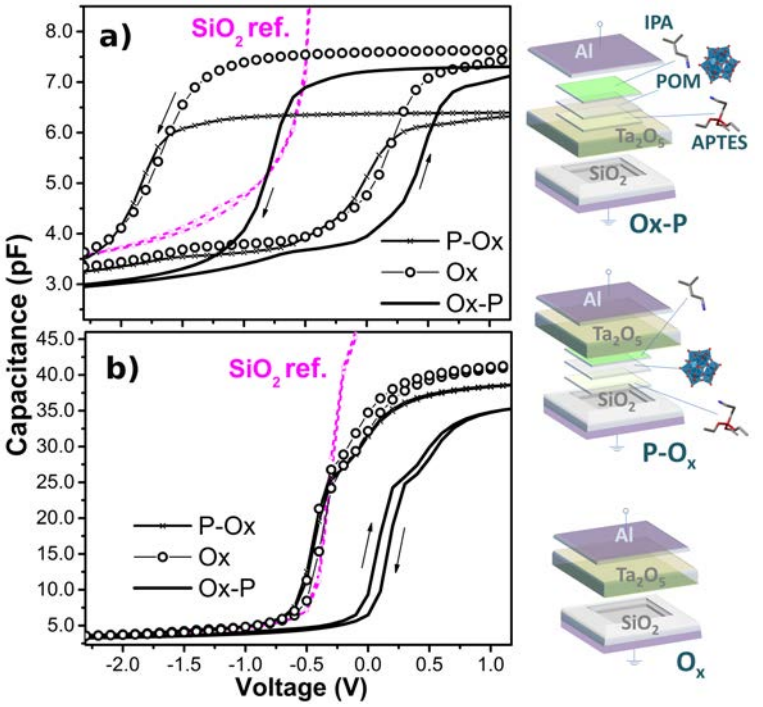


Figure 4.13: 1 MHz C-Vs under bi-directional voltage sweep for the two extreme $Ta_2O_5$ thicknesses of a) 145 and b) 25 nm. Electron trapping (positive Vfb shift) is significant only for cases Ox-P.

The voltage sweep direction was from inversion to accumulation and back to inversion. No hysteresis has been detected for the reference $SiO_2$ sample. In contrast, all $Ta_2O_5$ samples exhibit significant hysteresis that tends to increase with increasing thickness. The hysteresis width is quite large in the case of 145-nm-thick oxide (1.83 V) and reveals a favorable hole injection mechanism, a fact attributed to the presence of negatively charged oxygen vacancies in its structure.

The reference sample is suffering from the presence of fixed positive charges, with a surface density of $3.8 * 10^{-7} Cb/cm^2$ (Figure 4.13). The fact that these charges are compensated upon the deposition of thick layers of tantalum oxide is compatible with the PL results indicating the presence of negative vacancies in $Ta_2O_5$. In all cases addition of POM molecules on $Ta_2O_5$ shifts the flat band voltage to more positive values,

further compensating the fixed charge. In the case of 25nm thickness (Figure 4.13b) the hysteresis loop is mainly dependent on the presence of the POM molecules and involves pure electron storage. This is the case of interest for a memory cell and it will be further investigated.

Even though at this stage the P-Ox configuration does not seem to drastically modify the properties of the Ox layer, the comparison is essential in order to highlight the influence of the topology, and not merely the presence, of the molecular assembly on the charging efficiency of the cell. It, thus, becomes evident that intercalation of POM molecules in the $Ta_2O_5$ matrix as in the Ox-P and Ox-P-Ox cases has a striking impact on charging efficiency under a quasi-static sweep.

Figure 4.14a, b show the room temperature conductance characteristics of the control (only $SiO_2$) and Ox samples respectively for several gate voltages.

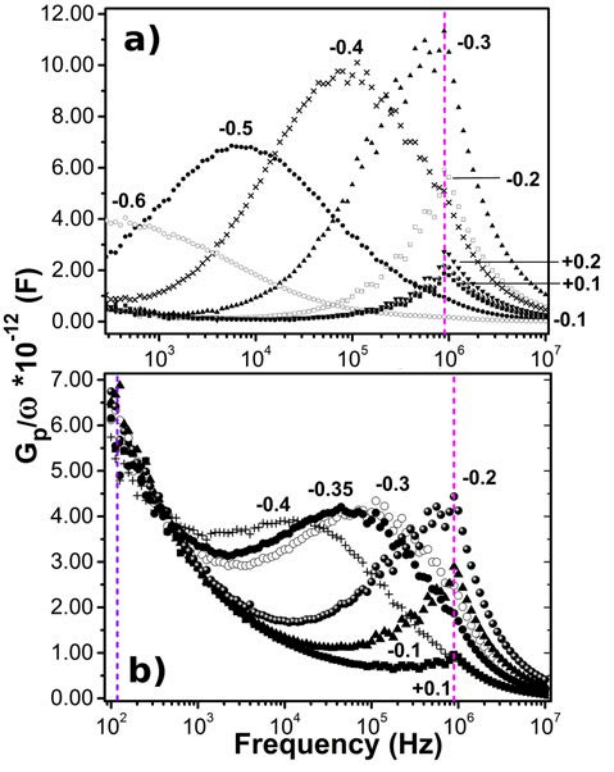


Figure 4.14: Normalized conductance vs frequency for several gate voltages for samples a) $SiO_2$ and b) Ox.

Both samples show qualitatively almost identical behavior, although the losses in sample Ox are almost two times lower than in the control $SiO_2$ sample. This provides further evidence on interface trap reduc-

tion upon $Ta_2O_5$ deposition. In weak inversion a quite narrow conductance peak dominates the normalized conductance over frequency, $G_p/\omega$, spectrum with a maximum at quite high frequencies, the same for both samples. From this value the interfacial trap density (Dit) is estimated at $7.3 * 10^{11} cm^{-2} eV^{-1}$ (time constant distributed around 1.12 $\mu sec$). The rapidly diminishing maximum as gate bias shifts the Fermi level some kT/q quanta away from the interface trap energy level, indicates a single-level interface trap [321].

Upon $Ta_2O_5$ deposition (Figure 4.14b) the existence of a significant amount of slow traps induces significant losses at low frequencies as well. As a result, there is exhibition of a second trap level with time constants distributed around 8 msec. Despite the fact that these traps are spaced away from the $SiO_2$-Si interface they are detectable in the admittance measurements, implying electronic transitions between electrons localized on $Ta_2O_5$ trapping sites and the scr. The very weak bias dependence of the amplitude of maximum loss of the latter peak suggests the presence of a whole distribution of traps with energies throughout the gap subjected to band bending variations[321].

## 4.4 Memory cell performance

In order to investigate the electron injection/trapping process under programming operation, the incremental-step-pulse programming (ISPP) method was employed [322], i.e., programming (positive) voltage pulses with constant increasing step height (1 V) were applied on the gate and the flat band voltage (Vfb) was measured between two successive pulses. Pulse widths of 100 $\mu$sec and 100 msec were tested. The results are presented in Figure 4.15 for the 25 nm-thick $Ta_2O_5$/POM hybrid which exhibited significant electron storage capacity.

The memory window is significantly affected from the duration of the applied pulse. The slopes $dV_{fb}/dV_{gate}$ of the characteristics of devices Ox-P and P-Ox (Figure 4.15) are not affected by the width of the pulse. Charge trapping, though, is more efficient (i.e. requires significantly lower voltages) at shorter pulses. On the contrary, the Ox-P-Ox sandwich cell is responsive at slow (100 msec) pulses. This is a direct consequence of the influence of the $Ta_2O_5$ slow traps discussed in the context of Figure 4.14b.

Enhanced scattering within the $Ta_2O_5$ layer (UPS discussion) prohibits short time back-tunneling, boosting the trapping ability. The process, though, is limited by the vacancy response frequency, which is of the order of msec (Figure 4.14b). Thus, the 100 msec pulse results in enhanced electron trapping onto the available POM orbitals, extending

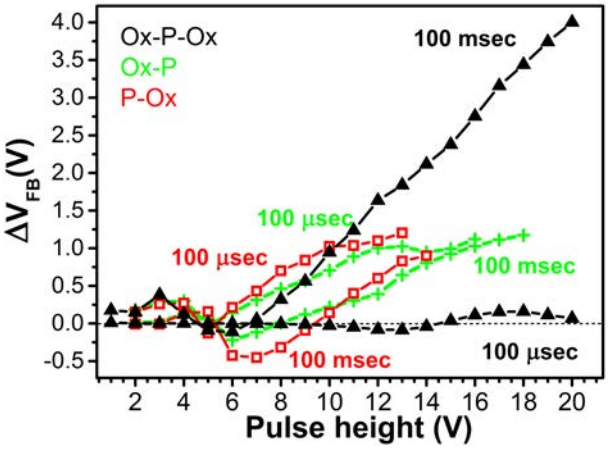


Figure 4.15: Programming windows for cells P-Ox, Ox-P and Ox-P-Ox obtained by the ISPP method (see text) utilizing two different pulse durations in order to investigate the programming speed.

the time over which charge capture can occur. Annealing of the Ox-P-Ox device at 320 $^oC$ (this temperature does not disrupt POM structure) under inert environment ($N_2$) results in a Gaussian type ISPP response (see Fig.4.16), typical for single level traps, suggesting that the distribution of trapping sites detected in the $G_p/\omega$ versus f characteristics might play a crucial role in the enhanced trapping performance of Ox-P-Ox cells.

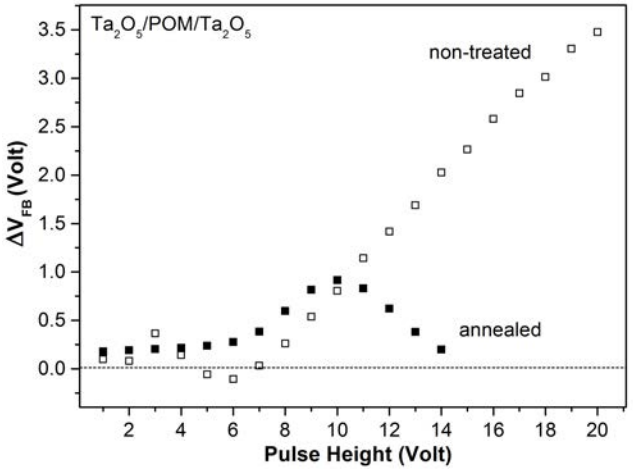


Figure 4.16: right: ISPP method results for all samples, left: Room temperature charge retention measurements for single-pulse writing programming

Note that the dynamics of charging of a POM layer on $Si/SiO_2$ are

described in detail in Chapter 3 and in [303]. Nevertheless, this configuration is not suitable for the investigation performed in the present chapter, because of the sub-femtosec charging and discharging times of POM molecular orbitals in direct contact to the gate. Therefore, the concept of pulse application and charge retention for the time scales discussed here is also not applicable.

To examine charge retention cells Ox-P, P-Ox and Ox-P-Ox were programmed via single pulses of +14 V, +10 V and +20 V (charging favorable pulses) respectively. The transient memory window (Vfb shift vs time) is shown in Figure 4.17.

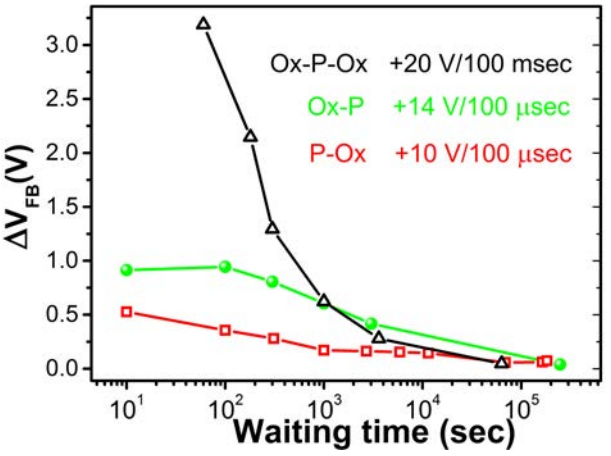


Figure 4.17: Charge retention characteristics of single-pulse programmed cells.

The device containing the POM layer buried under the tantalum oxide (P-Ox) maintains almost the half charge than the device with POM onto the porous tantalum oxide (Ox-P). This manifests the impact of the large $Ta_2O_5$ surface. In the Ox-P-Ox structures multiple inelastic scattering across the structure (see UPS) is proposed as the reason for their enhanced trapping efficiency, owing to reduced back-tunneling. For this structure we get a large amount of trapped charge constantly increasing up until 20 V. All configurations exhibited comparable retention time and did not show closing until after $10^4$ sec. In short, Ox-P cells exhibit enhanced speed, but limited charging ability due to pronounced back-tunneling, while Ox-P-Ox cells, although performing at lower programming speed, offer large memory window.

## 4.5 Finite Elements Model with spectral inputs– Electrostatics of the trapping medium

In order to quantify the distribution of charge across the $Ta_2O_5$/POM trapping medium and investigate the details of the charging mechanism we consider the simple case of a Si/$SiO_2$/$Ta_2O_5$/POM/Al stack. The alignment of all relevant electronic levels and states before and after voltage application is depicted in Figure 4.18 along with the UPS valence band spectra of the Ox-P structure.

The distribution of POM molecules across the stack is approximated with successive discrete monolayers which are embedded in the $Ta_2O_5$ film with the molecules closely packed. The hybrid exhibits sub-nm surface roughness (AFM, subsection 3.1) meaning that, most probably, the amount of POM molecules protruding from the $Ta_2O_5$ matrix and contributing mainly to the POM/Al interface are of the order of a monolayer. The LUMO of these interfacial molecules lies slightly below the Al fermi level [323], forming locally an ohmic contact (Figure 4.18). All molecular HOMOs and LUMOs are treated as continuous densities of states, rather than discrete levels [310], with characteristics derived from UV-Vis spectroscopy and UPS.

In Figure 4.18 the POM HOMOs and LUMOs, depicted as bands for simplicity, are subjected to differential energetic shift according to their distance from the Al gate and the Si scr. The LUMO shift of the top POM layer towards the Al fermi level has also been taken into account according to [323]

The POM film is discretized into layers of thickness 1nm, the diameter of POM molecules, along the growth axis of the $Ta_2O_5$/POM nanocomposite. An iterative 1-D electrostatic model is applied and the equations that involve the voltage-dependent occupancy of trapping sites in conjunction with the Poisson equation are solved across the discretized structure in a self-consistent manner. The thickness of the hybrid, $z_{max}$, is determined from cross sectional FE-SEM images.

The $Ta_2O_5$ conduction band minimum ($E_c$) and valence band maximum ($E_v$) values are derived from UV-Vis absorbance and UPS measurements while the corresponding values for Si, $SiO_2$ and the Al Fermi level are obtained bibliographically [324, 325].

Following [310] we model the HOMO as a Gaussian with its maximum and standard deviation ($\sigma$) derived from UV-Vis spectroscopy and UPS respectively. More specifically, $\sigma$ is approximated by the width of the HOMO-related feature of UPS valence band spectra (i.e. $\sigma$=0.5 eV). The bandgap value, $E_g$, is obtained via calculation of the absorption coefficient from UV-Vis spectra, linear fit of the experimental data in the vicinity

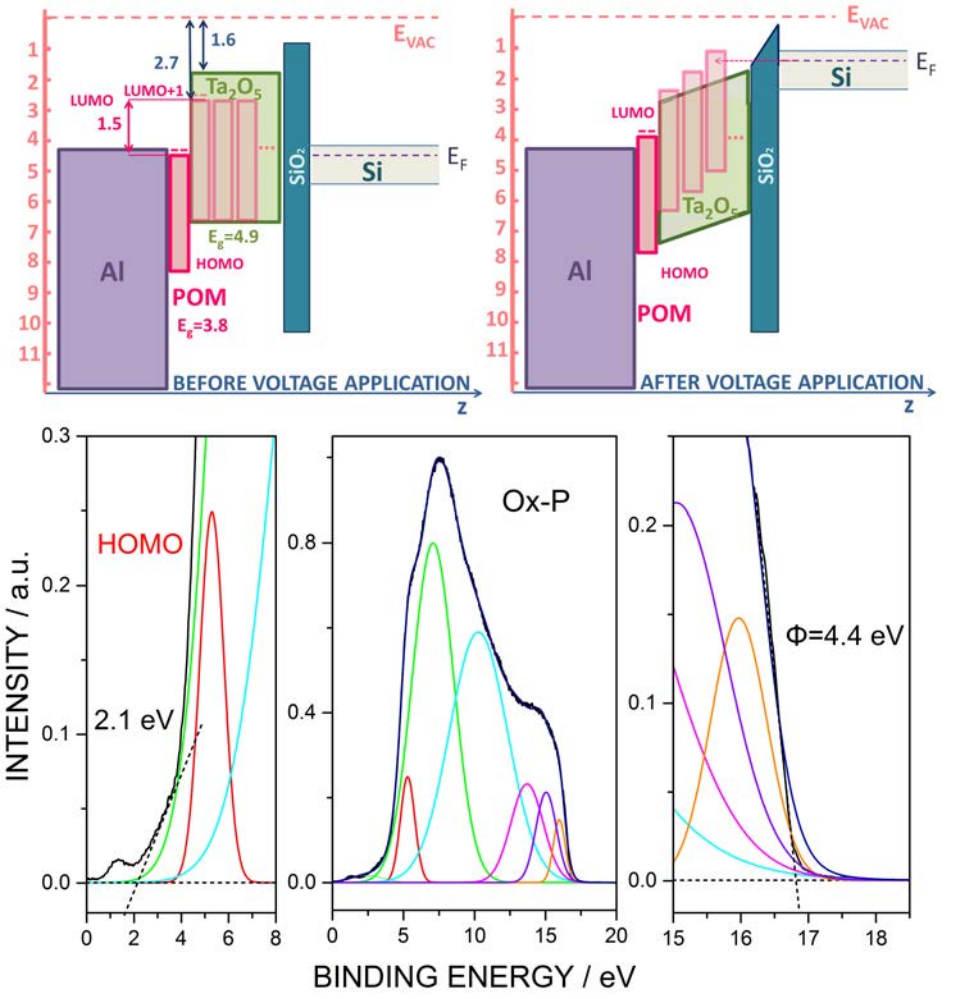


Figure 4.18: (Top): Scheme of molecular Density of States (DOS) shift due to differential distance from the scr a) Upon contact and before voltage application, b) After voltage application. (Bottom): UPS valence band spectra and deconvolution of signal by means of Gaussians for cell Ox-P. The lateral graphs depict the extracted high binding energy cut-off position and valence band onset.

of bandgap energy and calculation of the intersection point of linear fit with the abscissa (i.e. $E_g$=3.8 eV). From UPS the ionization energy, IE, is obtained (IE=6.46 for POM, 6.5 eV for $Ta_2O_5$) as the energy difference between the vacuum level and the low-binding energy onset of the UPS spectrum. The position of the HOMO maximum (peak of the Gaussian distribution) is located $2\sigma$ away from the IE onsets (i.e. $E_{HOMO}$=7.5 eV).

The LUMO maximum is obtained by shifting the onset of this distribution by $E_g + 2\sigma$ along the energy axis according to [310].

The molecular HOMO and LUMO of each monolayer are being shifted differentially, by the local electron potential energy $q \times V(z_i)$, according to their distance from the scr (Figure 4.18). This means that with increasing distance z from the accumulation region of the semiconductor, the molecular DOS shifts to progressively higher binding energy by the local electron potential energy, while the electron injection barrier becomes progressively lower [310]. The charge density $\sigma(z_i)$ on each of the POM layers is then calculated via Eq. 4.1 [310].

$$\sigma(z_i) = q \times n_{POM} \times \alpha \times$$
$$\times \left\{ \int_{-\infty}^{\infty} dE \times \frac{1}{\frac{1}{g_{HOMO}} e^{-\beta(E-E_F)}+1} \times G_{HOMO}[E + qV(z_i)] \right.$$
$$\left. - \int_{-\infty}^{\infty} dE \times \frac{1}{\frac{1}{g_{LUMO}} e^{+\beta(E-E_F)}+1} \times G_{LUMO}[E + qV(z_i)] \right\} \tag{4.1}$$

,where q is the absolute value of elementary charge, $n_{POM}$ the number of POM molecules per unit area and per discretization interval $\Delta z_i$ calculated as $7.89 \times 10^{13}/(cm^2 \Delta z)$ considering adaptation of a bcc lattice for $\alpha$-Keggin POMs [326] and a 78.9% filling factor ($\alpha$) of the hybrid with molecules (see inclusions estimation below),

$$\frac{1}{\frac{1}{g_{HOMO}} e^{-\beta(E-E_F)}+1} \tag{4.2}$$

is the Fermi-Dirac distribution for HOMO and

$$\frac{1}{\frac{1}{g_{LUMO}} e^{+\beta(E-E_F)}+1} \tag{4.3}$$

for LUMO respectively. $g_{HOMO}$, $g_{LUMO}$ are the spin degeneracies of levels both considered to be 2, $\beta = 1/k_B T$ with $k_B$ the Boltzmann constant and T the temperature, set to 300 K. The energy distributions of HOMO and LUMO levels are $G_{HOMO}[E + qV(z_i)]$ and $G_{LUMO}[E + qV(z_i)]$.

The total thickness of the hybrid, i.e. $z_{max}$ (25 nm), is determined from cross sectional FE-SEM images. The electrostatic potential across the film is initially assumed that of a parallel plate capacitor under bias (V).

The corresponding electric potential $E_{cap}z$ is fed in Eq. 4.1 to obtain an initial guess for the charge density of the first layer, $\sigma(z_0)$. The first

Al/POM interfacial layer is considered fully occupied, as indicated from UPS spectra [323], and is incorporated as a fixed charged sheet at z=0. This $\sigma(z_0)$ is plugged in as a starting value into the one dimensional Poisson equation:

$$\bigtriangledown^2 V(z_i) = -\frac{\sigma(z_i)}{\epsilon\epsilon_0} \tag{4.4}$$

to obtain the value of next layer's local potential $V(z_i)$, which is calculated via application of superposition principle as the vector sum of the capacitive electrostatic field and the fields originating from the trapped charge of all preceding layer(s). $\epsilon_0$ is the vacuum permittivity and $\epsilon$ an effective dielectric constant for the hybrid. The volume fraction of inclusions in as-grown $Ta_2O_5$ has been estimated at 78.9% via high-frequency (1MHZ) C-V and application of the Maxwell Garnett equation [327].

We assume a static dielectric constant $\epsilon$ of 25 [328, 329], typical of amorphous $Ta_2O_5$, for the nanocrystalline $Ta_2O_5$ matrix (the diameter of the nanocrystals has been determined via transmission electron microscopy (TEM) imaging and is of the order of 1 nm with no preferred orientation. The material is, thus, considered to be amorphous in terms of dielectric constant). Since POM molecular structures are expected to be highly hydrated due to crystallization water [330] a water dielectric constant is used for the POM-filled inclusions in the hybrid. This gives an effective dielectric constant of 62.7 for the composite.

The DOS of each discretization interval is then shifted in energy by the respective $q \times V(z_i)$, as shown in Figure 4.18, and the next $\sigma(z_i)$ is again calculated by occupying all states in the molecular hybrid up to the Fermi level, $E_F$. The process repeats itself iteratively by re-calculating the discrete $V(z_i)$ of the next layer every time one $\sigma(z_i)$ is obtained. We use a Dirichlet [V(0)=0] boundary condition and apply Gauss law. The result of the calculation is presented in Figure 4.19.

The plot indicates a distribution of charge density across the hybrid, owing to both differential distance of trapping levels from the accumulation layer and electronic coupling of the molecular HOMOs-LUMOs to the $Ta_2O_5$ matrix (observed energetically as $LUMO_{POM} - Ev_{Ta_2O_5}$ alignment). The existence of, essentially, a continuum of trapping states instead of a single level and the lowering of electron injection barrier for layers spaced away from the scr, are the origin of enhanced trapping efficiency in the POM/$Ta_2O_5$ hybrid.

When an additional $Ta_2O_5$ film is deposited on top of the hybrid (sandwich structure) and positive bias is applied on gate, a Schottky barrier is being formed onto the metal-oxide interface. Thus, the mobile $O^{2-}$ ions present in the $Ta_2O_5$ structure cannot migrate with the same

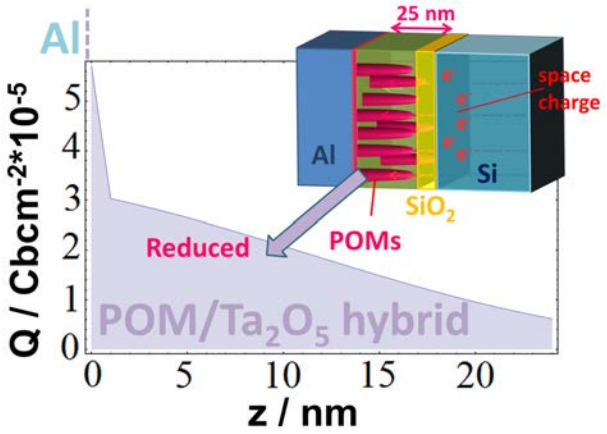


Figure 4.19: Charge density across the trapping ($Ta_2O_5$/POM) layer.

efficiency towards the gate, remaining immobilized onto the interfaces.

Driving force of this ionic charge immobilization is the lattice mismatch on the interfaces of POM-modified and non-modified transition metal oxides. Such mismatches cause modulation of the structural and electronic properties of the film, changing the local work function and resulting in adsorption of charged species [331] at the $Ta_2O_5$/POM interfaces. This results in the monitored expansion of the memory window. The process is limited by the vacancy response frequency, which corresponds to a lifetime of the order of msec, giving rise to the response enhancement of the Ox-P-Ox cell at slow pulse duration.

At the same time, enhanced scattering within the $Ta_2O_5$ layer prohibits short time back-tunneling enhancing the trapping ability.

## 4.6 Write performance (speed) and information retention ability unveiled

### Speed

As probably became clear by now, the duration of the applied pulse is directly interrelated with the trap response time. The latter is the time needed for carriers to drift and trap. Longer pulses do not necessarily result in larger quantities of trapped charge, since de-trapping can also occur during polarization.

Another issue is the existence of an amount of slow hole traps (see Fig.4.14) owing to the $Ta_2O_5$ matrix, that coexist with the fast POM electron trapping centers. For devices P-Ox, Ox-P and quicker (i.e. 100 $\mu$sec)

pulses, the slow $Ta_2O_5$ trapping centers do not have enough time to respond, so pure electron trapping is attained. You may notice, for example, that for the P-Ox and Ox-P devices positive hole trapping occurs initially for the slow 100 msec pulse (but not for the quicker 100 $\mu$sec pulse), highlighting the involvement of tantalum oxide trapping centers in the net charging process.

For Ox-P-Ox devices, though, the situation is a little bit different. The negatively charged oxygen vacancies of $Ta_2O_5$ cannot act as efficient hole traps anymore, since due to the enhanced scattering within the top $Ta_2O_5$ layer negative charge loss towards the gate, and thus, hole tunneling towards $Ta_2O_5$, is prohibited. So longer pulse duration results in enhanced electron trapping onto the POM available molecular orbitals, extending the time over which charge trapping can occur (see also last paragraph of section "Finite Elements Model with spectral inputs–Electrostatics of the trapping medium").

For shorter pulses (100 $\mu$sec) the oxide traps do not have enough time to respond and tunneling paths, due to the rearrangement of negatively charged oxygen vacancies, are quenched. For higher voltage amplitudes, though, some POM deep centers are being charged. Lower voltage drop within the molecular layer (i.e. when we have more stacked layers) results in lower tunneling current and, thus, worsens the programming speed. So Ox-P-Ox responds to slower pulses.

### Information Retention

It has been mentioned that the sandwich hybrid enhances backscattering meaning that the trapped charge monitored right after pulse application (timescale of some secs) is significantly more. Retention of charge, though, would refer to a different timescale, i.e. several hours. This, inevitably, requires different mechanism of blocking to deal with the drift of trapped charge. In Fig.4.18 we can see that $Ta_2O_5$ imposes insignificant energy barrier on the backtunneling of electrons from charged POMs and the only mechanism of blocking is the intrinsic confinement of electrons in the isolated POM quantum wells as well as the aforementioned carrier scattering within the $Ta_2O_5$ matrix. In that sense, we do not expect that this enhanced scattering will boost retention of trapped charge.

On the contrary, dVfb/dt depends on the initially trapped charge and is steeper for larger amounts of charge, as electromagnetism predicts. The point here is that, even though no blocking oxide is utilized, this hybrid is already capable of trapping and effectively retenting charge using testing methods and timescales designed for packed devices with inte-

grated blocking medium. Commercially competitive retention is going to be achieved with the utilization of the proper blocking oxide layer. In the following chapter we will be dealing with exactly this issue.

## 4.7 Conclusions

Hybrids comprising of high surface-to-volume ratio transition metal oxides (i.e. $Ta_2O_5$) and a transition metal oxide molecular analogue, Keggin type tungsten polyoxometalates, consist a novel composite material that can be fabricated using CMOS-compatible technology and serve as a memory cell based on electron trapping.

Non-volatile memory devices with commendable memory characteristics such as large memory window (4.0 Volt for the write state) and significant retention ($10^4$ sec) even without the use of blocking oxide have been fabricated utilizing a MIS capacitive cell architecture. We demonstrate for the first time that key issues for boosting the width of memory window of such devices are differential distance of trapping sites from the injection layer and effective electronic coupling to the scr of the underlying Si substrate.

The promising memory and retention characteristics of this hybrid highlight its potential as storage node for molecular nonvolatile flash memories. The fabricated memory cells are able to bring together significant figures of merit like high density of trapping sites via the combination of stable molecular components and 3-dimensional nanostructuring, electronic coupling to Si and direct accessibility of electronic levels in solid state, inherent retention of information under room temperature, bottom up fabrication logic and solution processing. They are, thus, of great potential for advanced molecule-based storage and memory technologies.

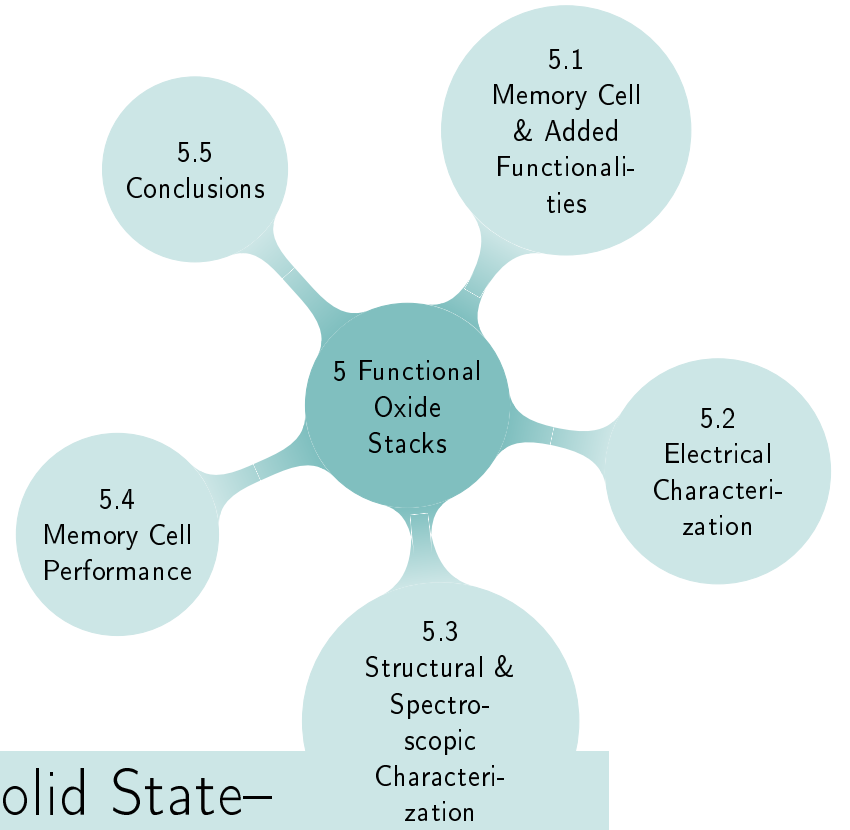


# 5

# Functional Solid State–Molecular Metal Oxide Stacks for Highly Efficient Non-Volatile Memories with Light-Boosted Electrical Storage

*As became clear from Chapter 4, one of the main factors putting the skids on the realization of silicon-competitive molecular memories, despite their promising information handling characteristics, is the difficulty in acquiring a molecular-friendly blocking oxide. This hinders long-term retention of the stored bytes and renders the cell prone to cross-talking. At the same time, even though multilevel storage is commonly highlighted as a flagship feature of molecule-based memories, an experimental realization of a multi-state capacitive memory cell still remains elusive. This stems, among others, from the difficulty of addressing discrete molecular levels at the mesoscopic scale. Ideally, high storage density, fulfillment of the current commercial threshold of 10-years-data-retention-guarantee in ambient conditions, ability of multi-state addressing, and CMOS-compatible fabrication processes should be collectively met for commercially-valuable non-volatile capacitive memory devices. An elegant way to address such a multi-aspect problem is through the incorporation of multiple functionalities in one "clever" material. Utilizing a stack of such materials and taking advantage of the power*

*of multiple interfaces, molecules and transition metal oxides it is possible to built a so-called functional oxide stack; ultimately, a complex material that meets all the aforementioned requirements, while taking advantage of photonically-addressed phononic modes to boost information storage and reach molecular states that were previously non-available. Capacitive memory cells based on this material are being fabricated with only minor modifications of the standard CMOS-line protocol. These high performance non-volatile memories are the first documented CMOS-compatible long term retention molecular capacitive cell of its kind, blazing the trail for the commercial exploitation of functional oxide and molecular hybrids as a high-end non-volatile memory product.*

---

## 5.1 Metal Oxides-Based Hybrid Memory Cell & Added Functionalities

METAL oxide semiconductors are conceptually different from the conventional Silicon, Germanium and III-V compounds. With a domain for electrical resistivity that varies over 20 orders of magnitude [332], from insulators to superconductors, these oxides are governed by quite unique rules with respect to electronic structure, charge transport mechanisms and electro-optic properties [333] providing, thus, a possibility for both conventional and completely new functions [334]. When, on top of that, transition metals are being utilized the resulting oxides, having bonds that straddle the subtle boundary between covalent ionic and metallic [335], can become, with proper engineering, the vehicle that enables a tremendous combination of advantageous properties.

Going even further, these oxides, contrarily to the established $SiO_2$ and other high temperature processed oxides typically used in the semiconductor industry, exhibit properties highly desirable for molecule-compatible devices. These include mechanical stress tolerance, compatibility with organic and photoactive materials, and high optical transparency due to their often wide energy gap [285]. Furthermore, partly due to the perceptionally different role of defects [336], high-quality electronic-grade metal oxide thin films are accessible using near-ambient conditions from both vapors and solution, widening their applicability to high-end products such as inexpensive and/or flexible optoelectronic circuits and displays [337], while exhibiting high degree of substrate tolerance.

Contradictory as it may seem from a traditional band-structure perspective [333], high conductivity and optical transparency can be com-

bined in metal oxides and their molecular analogues. In properly tuned polyoxometalate (POM) hyperstructures, the emergence of itinerant correlated electrons on the metal orbitals of the structures enhances free-electron mobility, an effect similar to doping [338]. At the same time hole conduction is suppressed by localized O2p orbitals and deep VBM levels where holes are trapped by O ions [339].

In optoelectronic applications, Metal Oxide semiconductors present clear advantages over other proposed alternatives such as organic semiconductors, carbon nanotubes (CNTs), graphene and MoS2 due to the unique combination of high carrier mobility, good optical transparency, straightforward synthetic access, large-area electrical uniformity and mechanical flexibility [285].

Organic solids on the one hand, are very much restricted by their relatively weak intermolecular interactions which confine their applicability to relatively thick films, low post-deposition temperatures and a narrow window of chemical etchers and developers. On the other hand, lack of reliable low cost production of non-defective graphene render it of limited applicability for large-scale implementation. The last non-conventional option, chalcogenides, still lack behind as uniform growth of large-area high-quality MoS2 thin films remains challenging.

At the same time complex materials and 3-D nanostructuring seem more and more like a promising way to go for devices with advanced performance and/or functionalities [67]. The growth of structurally and physicochemically different, still electronically coupled materials, on the same stack represents a bottleneck in the development of new heterostructure devices. Moreover, in the much promising field of information storage devices defect intolerance narrows the window of acceptance even further. Ability for introduction of redox molecular nodes can boost information density and provide tolerance on oxide defects in an advanced way comparing to floating dot logic [340].

Thus, the possibility of fabricating homogeneous films on large scale and the ability of incorporating non-conventional materials, like molecules, from liquid precursors in ambient conditions holds great attraction for MOs versus Si, nitride and chalcogenide semiconductors, opening possibilities for injection printing of the whole structure or parts of it. Going a step further, the successful integration of such functional oxides on silicon can offer an unlimited potential for new applications in electronics, optics and, optoelectronics [341].

### 5.1.1 Experimental Details

#### Materials-Methods

12-Tungstophosphoric acid hydrate (POM, $HPW_{12}O_{40} \cdot xH_2O$, Aldrich), 3-aminopropyl triethoxysilane (APTES, Aldrich), and isopentylamine (IPA, Aldrich) were all of analytical grade and used without further purication. Hydrochloric acid, sulfuric acid, and hydrogen peroxide (all obtained from Aldrich, analytical grade) were used for the pH adjustment of the deposition solutions and the purication and hydrophilization of the $SiO_2$ surface, respectively. Deionized water with a resistivity of 15 $M\Omega cm^{-1}$ prepared from the Milli-RO plus 90 apparatus (Millipore) was used in all experiments.

The substrates used in the molecular nanostructures fabrication varied according to the characterization method applied; quartz slides were used for the UV study and silicon wafers with 3.1 nm dry oxide were used for the Fourier transform infrared spectroscopy (FTIR), scanning electron microscopy (SEM), and X-ray photoelectron spectroscopy (XPS) studies. All substrates were used after cleaning with piranha solution ($H_2O_2 : H_2SO_4$, 1:1 v/v).

For the $Al_2O_3$ growth a Savannah-100 ALD system (Cambridge Nanotech/USA) has been used. During deposition, the substrate is maintained at $300^oC$, a temperature that has been proven not to disturb the inorganic molecular components and the molecule-saturated $Ta_2O_5$ matrix. 0.015 sec-lasting cycles of alternating $H_2O$ and trimethylaluminum (TMA) precursor pulses are being applied, interrupted by intermediate $N_2$ purging intervals of 3 sec. The average nominal growth rate is 1 Å/cycle.

#### Characterization

The stoichiometry and chemical composition of the $Al_2O_3$ films were investigated ex-situ via X-ray Photoelectron Spectroscopy (XPS). The thickness of the grown film is monitored ex-situ via both XPS and TEM analysis of samples extracted on various time instances of the growth cycle.

All electric measurements were performed in a shielded probe station using a HP4041B picoammeter, a HP4284A precision LCR meter, and an HP 8110A 150 MHz pulse voltage generator.

For the XPS measurements of the stacks, an unmonochromatized Mg $K\alpha$ line at 1253.6 eV (12 kV with 20 mA anode current) and an analyzer (Leybold EA-11) pass energy of 100 eV were used at 0 degree takeo angle. For the UV photoemission spectra (UPS), the He I (21.2 eV) excitation line was used, and a voltage of 12.23 eV was applied to the specimen in order to separate the high binding energy cuto from the analyzer.

UV–vis absorption spectra were obtained on a Perkin ElmerUVvis Lambda 40 spectrophotometer. FTIR transmittance spectra were recorded on a Bruker, Tensor 27 spectrometer using 1000 scans at $4cm^{-1}$ spectral resolution.

### 5.1.2 The cell

In this chapter a metal oxides' stack incorporating the successful findings of the previous chapters and some extra non-conventional functionalities emerging from material combination and interfacing is introduced. The stack, meant to function as a non-volatile memory element, is fabricated following a joint "solid-solution-vapor deposition" approach that overcomes major fabrication obstacles in the field of scalable molecular devices on non-standard substrates. In Fig.5.1 the stack constituents are schematically depicted.

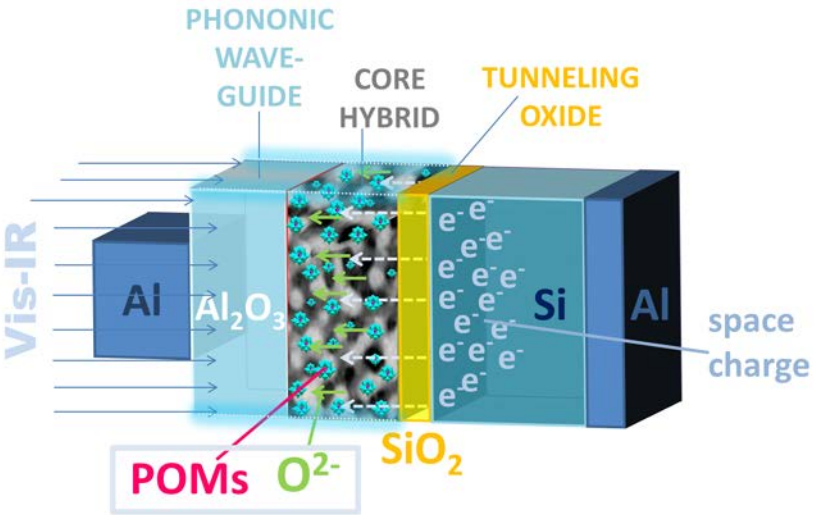


Figure 5.1: Schematics of the functional oxide stack consisting of the core molecular/solid state low dimensional transition metal oxide hybrid and the $Al_2O_3$ phononic wavequide incorporated in a capacitive memory cell. An exposed waveguide window around the Al top gate is used for optical addressing.

#### Topology & Energy Bands

The metal oxide stack encompasses two main functional components: the core and the phononic wavequide cap (Fig.5.1).

The core involves a low-dimensional transition metal oxide hybrid relying on a high surface-to-volume ratio $Ta_2O_5$ matrix with recorded fractality [61] and a molecular transition metal oxide analogue, namely the polyoxotungstate $[PW_{12}O_{40}]^{3-}$. These redox-active molecular nodes are self-assembled on the surface and pores of the underlying $Ta_2O_5$. They act by delocalizing and retaining negative charge on their metallic framework, serving as electron storage sites. Under device operation they perform in synergy with the multiple molecule/$Ta_2O_5$ interfaces; the later are responsible for immobilizing negatively charged mobile oxygen vacancies, another abundant source of negative charge available for the cell [61].

The underlying principle is that transition metal oxides naturally support low energy cost interfacing with POM transition metal oxide molecular analogues. This enables low injection barriers at interfaces, hereby reducing power consumption and expanding the memory window. Both high surface area and 3-D nanostructuring of $Ta_2O_5$ serve to enhance POM integration density. Except from write/read reliability this provides built-in charge retention.

The decreased number of stored electrons in modern nanometer-scale storage nodes leads to the intrinsic degradation of data retention times and introduces stochastic effects into the charging/discharging process [342], unacceptable for device-grade materials. Meanwhile, the matrix's fractal structure guarantees roughness-originating mismatch suppression through selection of appropriate correlation length-molecule size combination for the hybrid.

The phononic wavequide cap is a 20-nm-thick low temperature ALD-grown $Al_2O_3$, a POM-friendly gate oxide of high quality and valence-conduction band energies appropriate for blocking, i.e. interruption of the ohmic contact naturally formed between POMs and the Al gate [61].

This epitaxial layer is expected to facilitate long term retention of charge onto the molecular trapping centers in order for the device to meet the commercial standards. Moreover, having a relatively large bandgap ($\gg$3eV) it is transparent in visible and near UV light, permitting photoactivated processes in the underlying core volume when appropriate. $Al_2O_3$ is used as a vacancy-based phononic component. Interconnected $O_2$ vacancy lines in its volume create phononic waveguides through which phonons can propagate [343]. Since propagation can be stimulated and manipulated a phononic switch can be realized.

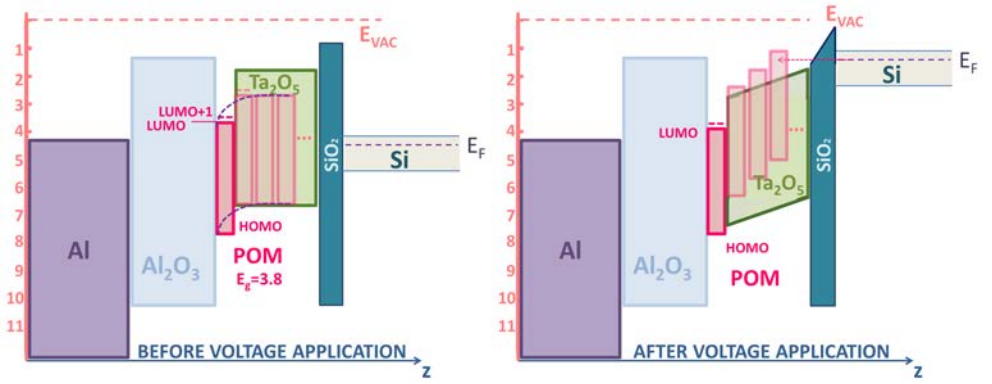


Figure 5.2: Band alignment across the stack and scheme of molecular density of states shift due to dierential distance from the scr (a) upon contact and before voltage application, (b) after voltage application.

### Addressing the Material Growth Challenges

The utilized metal oxides are grown using combined vapor- and solution-phase thin film advanced deposition techniques.

More specifically, the core transition metal oxide hybrid bearing the molecular entities is a-thermally grown, utilizing solely near-ambient conditions. DC-powered hot-wire physical vapor deposition is utilized for the growth of $Ta_2O_5$.

In pursuance of establishing an a-thermal process, the high substrate temperatures and high-temperature post-annealing, typically used for metal oxides to optimize reactions between ionized species on the substrate [285] and obtain stoichiometry, ought to be avoided. Thus, a stoichiometrically pre-oxidized tantalum wire is utilized under $N_2$ atmosphere in order to preserve composition while maintaining RT.

With this simple method stoichiometric $Ta_2O_5$ and ambient substrate temperature can be reconciled while, most importantly, due to low energy growth, adatom migration during deposition is suppressed. The later is essential in order to obtain the highly porous matrices required for high density hybridization with POM molecules. Moreover, low temperature processing helps maintain the mixed composition of the interfacial oxides, providing high capacitance low leakage structures [286], essential for memory applications.

Solution-phase processing was subsequently used for the incorporation of POM molecular entities in an ordered way. The underlying oxide matrix is chemically modified with APTES, a type of aminosilane molecule used for the electrostatic self-organization of POM anions via the layer-by-layer (LBL) process [156, 344]. POM molecular nanocrystals

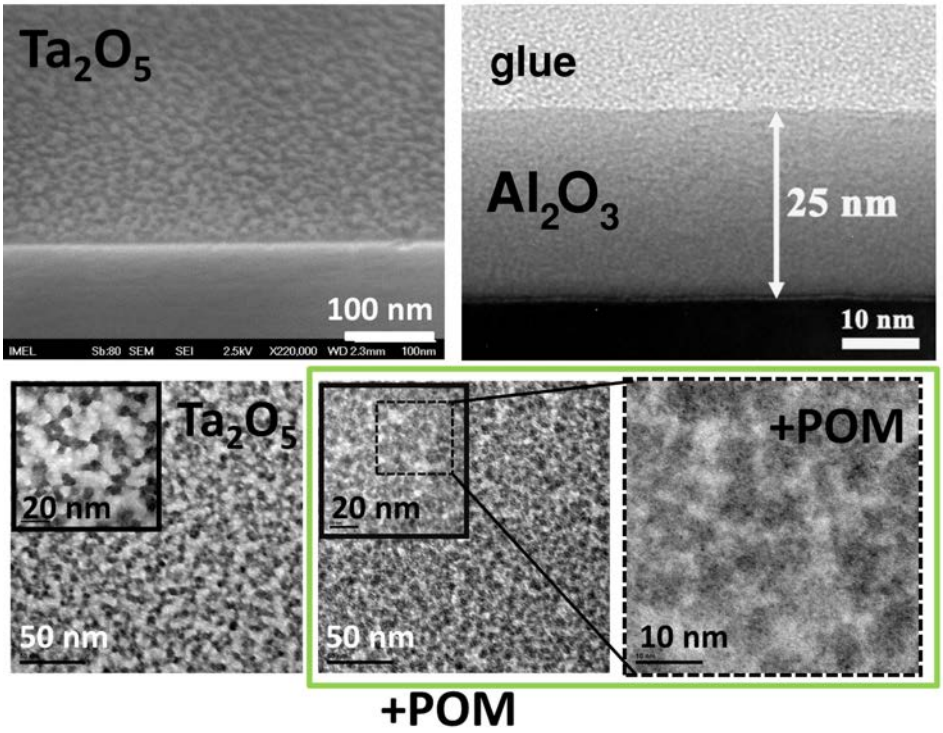


Figure 5.3: Morphology of the oxides grown with all three vapor and solution methods as obtained with FE-SEM (top) and TEM (bright field mode, bottom). The infusion of POM molecules in the $Ta_2O_5$ matrix is apparent, especially under comparison of the 20 nm scale (×210) topologies before and after POM assembly on $Ta_2O_5$.

are pre-formed in solution [338] and post-assembled on the high surface-to-volume $Ta_2O_5$ to form an electronically coupled robust hybrid [61].

For the growth of the 20 nm-thick stoichiometric $Al_2O_3$ film, serving as both gate dielectric and phononic waveguide, atomic layer deposition (ALD) was used. ALD processes are typically used to manufacture high-quality metal oxide dielectric films due to their ability for uniform growth with high precision on arbitrarily complex and large-area substrates under fully controllable conditions.

We fabricate memory capacitor testbeds which incorporate the aforementioned stack in the active region. The process consists of standard photolithography and etching on wet-oxidized (500 nm $SiO_2$) n-type Si substrates 12 Ωcm dening square patterns with side dimensions of 100 $\mu$m. These constitute the active areas of the devices. A 5 nm-thick tunneling oxide is grown on top via dry oxidation, in order to minimize the trap density at the Si/oxide interface [345, 346] and be able to test topologies

that require utilization of a tunneling oxide.

## 5.2 The Electronic Structure of the Composite

### 5.2.1 Spectroscopic Characterization

In FTIR (Fig.5.4a) the four characteristic bands of the Keggin structure POM remain unaltered upon deposition of $Ta_2O_5$ ($Ta_2O_5$/POM/ $Ta_2O_5$, $Ta_2O_5$/POM lines) indicating no bonding disruption upon the $Ta_2O_5$-POMs interaction.

For the Si wafers used as substrates, there is a strong absorption centered at 1105 $cm^{-1}$, typically attributed to the bulk Si-O-Si asymmetric stretching mode [347] and associated with interstitial oxygen in the Si bulk [286]. This vibrational mode is quite intense in several spectra presented in Fig.5.4. For example the bare $Ta_2O_5$ on $SiO_2$ (green spectrum, Fig.5.4a) exhibits this vibration on great intensity. Its detection is facile due to the high porosity and interconnected vacant space of the $Ta_2O_5$ matrix. This mode is hampered upon POM post-deposition, highlighting the saturation of the $Ta_2O_5$ bed upon POM infusion and the proportionally high absorbency of POM in this region.

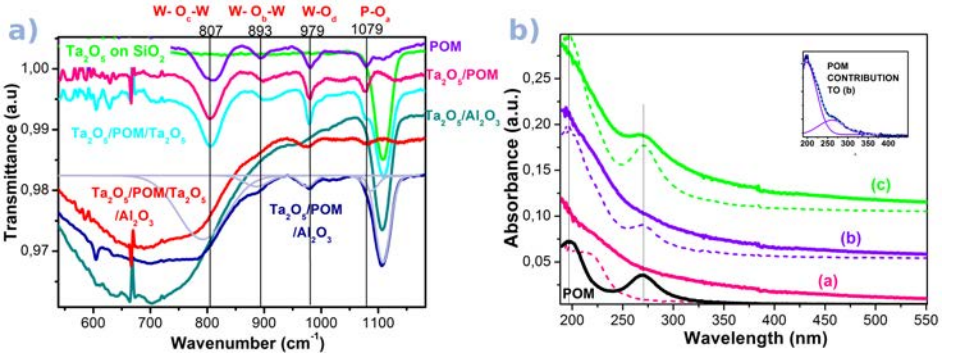


Figure 5.4: a) Monitoring of the impact of $Al_2O_3$ growth on $Ta_2O_5$ and $Ta_2O_5$/POM hybrids with FTIR spectroscopy. b) UV-Vis spectra investigation of the impact of $Al_2O_3$ growth on $Ta_2O_5$/POM hybrids utilizing various epitaxial combinations. Dotted (a): $Ta_2O_5$ on $SiO_2$, solid (a): $Ta_2O_5/Al_2O_3$ on $SiO_2$, Dotted (b): $Ta_2O_5$/POM on $SiO_2$, solid (b): $Ta_2O_5$/POM/$Al_2O_3$ on $SiO_2$, Dotted (c): $Ta_2O_5$/POM/$Ta_2O_5$ on $SiO_2$, solid (c): $Ta_2O_5$/POM/$Ta_2O_5$/$Al_2O_3$ on $SiO_2$, inset: POM contribution on the signal of solid (b).

In general, whenever $Ta_2O_5$ is the top layer, the 1105 $cm^{-1}$ stretching is easily detectable. $Al_2O_3$ is the only layer that can be deposited

on $Ta_2O_5$ without disrupting this scheme, permitting detection of the 1105 $cm^{-1}$ stretching. This implies that the $Al_2O_3$ film provides direct access to the underlying $Ta_2O_5$ states even if they were not previously available, as in the $Ta_2O_5$/POM stack. It essentially provides a route for blocked phononic excitations through wave guiding the corresponding wavelengths all the way through the stack to the POM/$Ta_2O_5$ interface.

Note that the epitaxial deposition of $Al_2O_3$ does not disturb the tantalum oxide stretching modes, and it solely introduces a broad band in lower wavenumbers extending roughly from 1000 to 500 $cm^{-1}$ (15-30 THz). These latter ionic vacancies band centered at 650 $cm^{-1}$ (19.5 THz) are high frequency phononic modes absent in the phonon DOS of the bulk $Al_2O_3$, therefore, they will be able to propagate only along the lines of $Al_2O_3$ volume defects.

According to ab-initio molecular dynamic simulations the general features of the phononic bands for amorphous aluminan are that they range from 0 to approximately 30 THz, and two bands can be distinguished, a lower one up to 15-20 THz, and a higher band from 20 to 30 THz [348]. The lower band is mainly due to Al atoms vibrations, whereas the higher band to O atoms.

Moreover, the four characteristic FTIR bands of the POM Keggin structure [349, 350] are preserved upon $Al_2O_3$ deposition, indicating the integrity of the underlying molecular structure.

TO SUM UP: The $Ta_2O_5$ layer is transparent in the investigated 13.5 to 85.6 THz region, permitting undisrupted photon exchange with the POMs infused in its structure. However, without the presence of a waveguide component on top these photons are of no impact on the molecular charging mechanism. The $Al_2O_3$ film exhibits a quite broad 27 $\mu$m band centered at about 19.5 THz, providing nanoscale phononic interconnects in THz frequencies towards the masked (in devices) POM/$Ta_2O_5$ interfaces through its interconnected vacancies. Via this frequency window the broadband incandescent bulb radiation excites lattice vibrations of specific wavelengths which are localized in the $Al_2O_3$ vacancy lines and guided to the $Al_2O_3$/POM interfaces. The peaks in the FTIR spectrum correspond to these vacancies-specific vibration modes of the $Al_2O_3$ structure.

In order to validate the phonon localization ability of the material under test, it is important to compare the intrinsic and the defect-induced vibrational properties, such as the phononic bandgap and the variation in the phonon spectra. The total phonon density of states (TPDOS) and the partial phonon density of states (PPDOS) were obtained from theoretical calculations using molecular dynamics simulations with semi-empirical potentials. A comparison of the two spectra can be seen in Fig.5.5.

The experimentally obtained band of optical phonons (bottom graph,

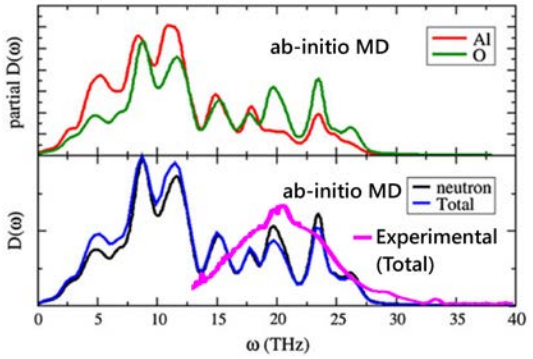


Figure 5.5: Partial, neutron, and total vibrational density of states for amorphous $Al_2O_3$. Ab-initio MD simulations from [348] and experimental (FTIR) findings for part of the total (Al and O) phononic band configuration of optical phonons.

magenta line) peaks at frequencies dominated by the O partial phonon densities (upper graph, green line) supporting its O-related nature. Moreover, the appearance of new high frequency states in the pnononic gap of the bulk $Al_2O_3$, indicates the presence of higher energy spatially localized modes, able to propagate only along the defect lines of $Al_2O_3$. An estimation of the power of thermal radiation delivered to the molecule interface through these phononic waveguides alone, considering a single state with two independent modes of oscillation corresponding to the two polarization modes of light and zero surface roughness can be calculated from Planck's formula for black body radiation and the losses accounting for light propagating above the critical angle for total confinement in $Al_2O_3$ as:

$$P = 2\frac{h\nu}{e^{h\nu/k_BT}-1}\Delta\nu \times \left\{ \arcsin\frac{1}{\sqrt{\epsilon_{Al_2O_3}}} \right\}^2 / \arcsin 90^2 \qquad (5.1)$$

where ν is the optical frequency, T is the filament's temperature, and Δν is the optical bandwidth. The dielectric constant of $Al_2O_3$ is obtained from dielectric spectroscopy (Fig.5.6c). For the used halogen bulb with 3000 K and a wavelength interval of 500 $cm^{-1}$ width around 650 $cm^{-1}$ this is translated to a power of ~20 mW. The overall phononically delivered power is of the order of 207 $\mu$W, an energy consumed for "switching on" intermolecular excitations in POM nanocrystals.

In UV-Vis (Fig.5.4) the characteristic oxygen-to-metal charge transfer peaks [152] of POM molecules at 197 and 270 nm remain intact in the absorption spectrum of the composite $Ta_2O_5$/POM material, indicating preservation of POM stereochemistry. Moreover, the intensity of the

representative 270 nm peak, which is characteristic of the Keggin structure of POM molecules and is ascribed at the O→W electron transfer, is clearly preserved in the case of the $Ta_2O_5$/POM/$Ta_2O_5$ sandwich even after $Al_2O_3$ deposition.

In the case that POM is not $Al_2O_3$-protected, as in the $Ta_2O_5$/POM case, deconvolution of the absorption signal in its elementary components can show that the 270 nm peak also exists, though greatly dumped. This could either mean that part of the POMs that are in contact with $Al_2O_3$ adopt a disturbed structure or, in conjunction with the dumped response of P-Oa vibrational mode (interior molecular oxygen) in FTIR, that O2p→W5d transfer is confined in the surface region of the integrated POM nanocrystals i.e. at the $Al_2O_3$/POM interfaces. The latter is also compatible with the commonly observed length change (weakening) of the already relatively weak bond of W to the internal oxygen [351].

### 5.2.2 Electrical Characterization

Typical bidirectional capacitance-voltage (C-V) characteristics are shown in Fig.5.6a. The voltage sweep direction was from inversion to accumulation and back to inversion. No hysteresis has been detected for the reference $SiO_2$ sample whose sum of positive charge at the interface is of $9 \times 10^{10} cm^{-2}$ (when a high-quality MOS interface has about $10^{10} cm^{-2}$ of charge).

In contrast, $Ta_2O_5$ samples exhibit significant hysteresis that tends to increase if one tries to increase their thickness (indicating a volume effect). The hysteresis reveals a favorable hole injection mechanism, introducing an amount of $3 \times 10^{11} cm^{-2}$ extra positively charged cites, a fact attributed to the presence of hole-adsorbent oxygen vacancies in its volume. $Al_2O_3$ films exhibit no hysteresis under a full sweep, confirming their suitability as gate blockage oxides. They induce, however a significant negative flatband shift due to the fixed positive charge induced by the $O_2$ deficiency.

These $O_2$-vacancies-consisting paths incorporate a density of $1.1 \times 10^{12}$ $O_2$ vacancies per $cm^2$ and are electronically interconnected to create phononic waveguides through which phonons can propagate [352]. In all cases addition of POM molecules shifts the flat band voltage to more positive values, compensating the fixed charge.

Conductance is much more sensitive to frequency than capacitance and a great tool to probe interface traps and fixed charge. Figs.5.7 show the room-temperature conductance characteristics of the control (only $SiO_2$) and subsequently grown samples, respectively, for several gate voltages.

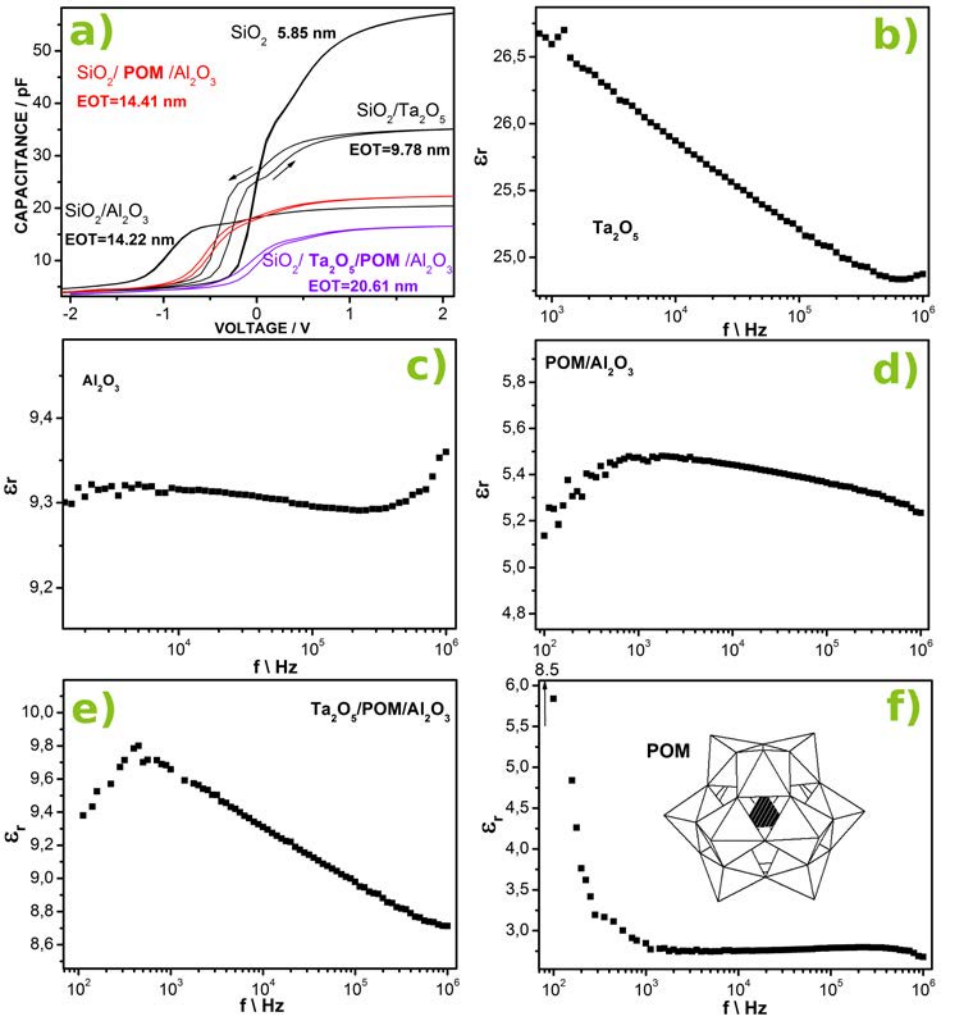


Figure 5.6: High frequency C-Vs (a), dielectric spectroscopy derived dielectric functions for the $Ta_2O_5$ matrix on $SiO_2$, (b), the $Al_2O_3$ phononic waveguide, (c), the $POM/Al_2O_3$ hybrid, (d), the composite $Ta_2O_5/POM/Al_2O_3$ stack, (e), and the POM molecular film, (f).

Both samples show qualitatively almost identical behavior, although the losses after $Ta_2O_5$ deposition are quite lower than in the control $SiO_2$ sample, providing evidence on interface trap reduction. In weak inversion, a quite narrow conductance peak dominates the normalized conductance over frequency, $G_p/\omega$, spectrum with a maximum at quite high frequencies, and time constant 1.6 $\mu$s the same for both samples. From this value, the interfacial trap density ($D_{it}$) is estimated at $7.3 \times 10^{11} cm^{-2} eV^{-1}$ (time constant distributed around 1.12 $\mu s$).

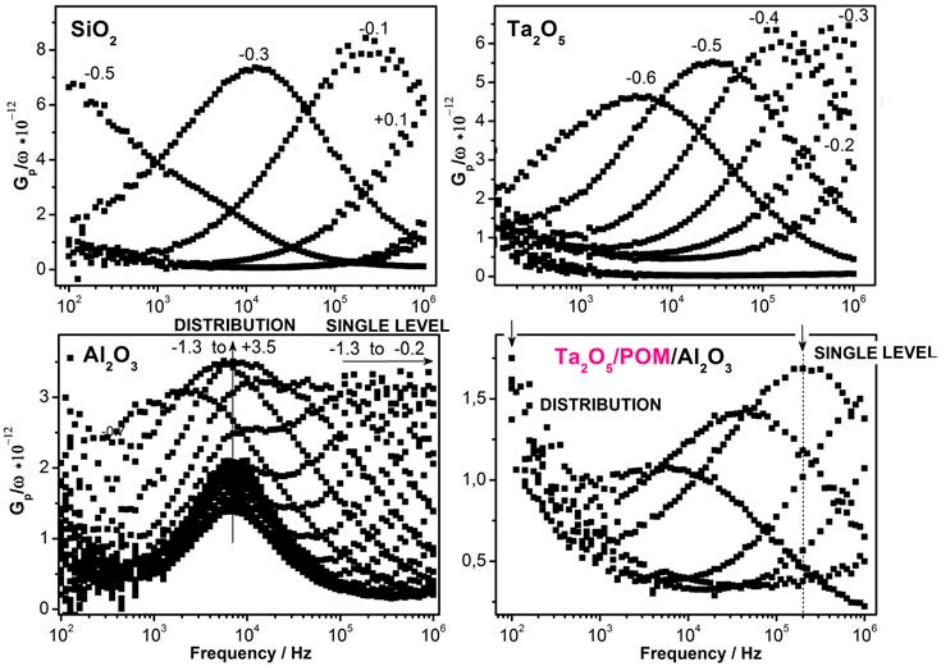


Figure 5.7: Normalized conductance vs frequency for several gate voltages for samples $SiO_2$, $Ta_2O_5$, $Al_2O_3$ and $Ta_2O_5/POM/Al_2O_3$ stacks.

The rapidly diminishing maximum as gate bias shifts the Fermi level some $k_T/q$ quanta away from the interface trap energy level, indicates a single-level interface trap [70]. Upon $Ta_2O_5$ deposition (Fig.5.7), the existence of a significant amount of slow traps induces losses at low frequencies as well. As a result, there is exhibition of a second trap level with time constants distributed around 8 ms. Despite the fact that these traps are spaced away from the $SiO_2$–Si interface, they are detectable in the admittance measurements, implying electronic transitions between electrons localized on $Ta_2O_5$ trapping sites and the scr. The very weak bias dependence of the amplitude of maximum loss of the latter peak suggests the presence of a whole distribution of traps with energies throughout the gap subjected to band bending variations [70].

In the case of $Al_2O_3$ there is an extra peak with time constant distributed around 0.15 ms whose position is totally unaffected from bias in the depletion to weak inversion region. This peak owes to fixed charge within the $Al_2O_3$ volume, and more specifically, to positively charged $O_2$ vacancies. A co-existing single level trap with time constant 2.2 $\mu$s, attributed to the shifted $SiO_2$ interface traps can be observed at higher frequencies. Losses are halved in comparison to the $Ta_2O_5$ case indi-

cating a dielectric offering improved resistance to leakage current and suppression of information loss.

In the case of POM/$Al_2O_3$ stack the $SiO_2$ interface traps are strongly electrically coupled to the POM levels causing a pronounced broadening of $SiO_2$ single constant states. POM induces fast traps resonating far below 1 $\mu$s, therefore, non-detectable with the utilized equipment. Their ultra-quick response will be spotted more accurately later on, via single pulse charging operation in the final device. Introduction of POMs also lowers losses, since trapping on POM sites lowers leakage.

Note that gate leakage along with few electronic density storage is one of the main causes of dumped retention times in non-volatile memories [342, 353].

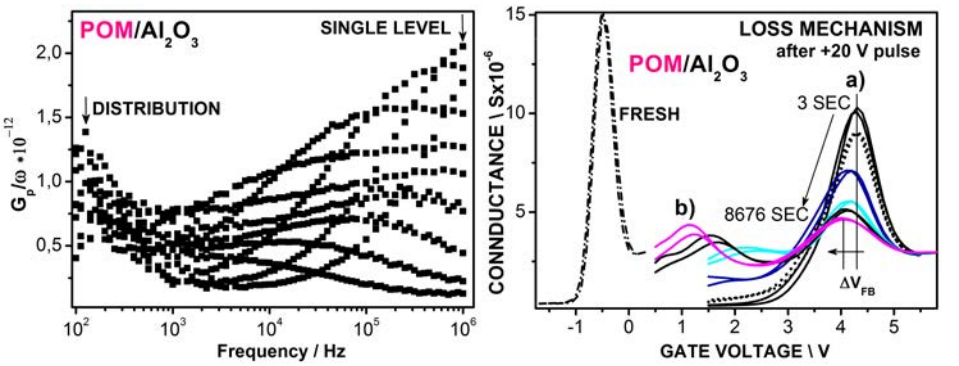


Figure 5.8: Normalized conductance vs frequency for several gate voltages and G-V characteristics for sample $POM/Al_2O_3$.

The last figure shows the charge loss mechanism after an initial charging of the POM at +20 V/100ms pulse. Once POM captures an electron, the lack of holes in its framework does not allow the electron to recombine there. If recombination can happen at some point along the stack, the traps respond to the slowly varying DC gate voltage and cause the G-V profile to peak at a different position along the gate voltage axis as trap occupancy changes with gate bias. In this case the cell starts losing information (reduction of $\Delta V_{FB}$) via the recombination of electrons at a plane of distance x from the POM centers, probably at the points where some interfacial and/or border traps reside and not through progressive diffusion to the gate. This is a direct consequence of the $POM - SiO_2$ states coupling detected in the $G_p/\omega$ vs frequency diagram of POM/$Al_2O_3$ cell.

Border traps [354, 355] are defects in the dielectric layer (but not at the semiconductor/dielectric interface), which can communicate with carriers in the underlying semiconductor. They can be accessed via carrier

tunneling through the interface into the dielectric from the semiconductor [356] and, therefore, their generation depends strongly on the quality and compositional abruptness of the semiconductor/dielectric interface. The probability of tunneling from the semiconductor into a trap falls off exponentially with increasing distance of the trap into the dielectric, so the active recombination traps necessarily reside in a few nm POM vicinity, probably inside the $SiO_2$ layer.

This is different from the case of $Ta_2O_5$/POM/$Al_2O_3$ stack, where no second conduction peak is detected and, thus, recombination centers do not play a major role to information loss (i.e. are not a major contribution to the $V_{FB}$ shifts).

## 5.3 Memory Cell Performance

In order to investigate the electron injection/trapping process under programming operation, the incremental-step-pulse programming (ISPP) method was employed [322]; that is, programming (positive) voltage pulses with constant increasing step height (1 V) were applied on the gate, and the flat-band voltage ($V_{FB}$) was measured between two successive pulses. Pulse widths of 100 ms were compared. The results are presented in Fig.5.9.

The memory window is significantly aected from the 3-D nanopatterning of $Ta_2O_5$. $Ta_2O_5$ significantly increases storage density, it slightly increases though the injection threshold by some meV as POM gets further away from $SiO_2$ injection side. The slopes $dV_{FB}/dV_{gate}$ of the characteristics of devices are also aected, being steeper for the hybrid. In overall, charge trapping is more efficient (i.e., requires signicantly lower voltages) for the hybrid. Upon combined electro-optical injection using black body radiation (on top) from an incandescent lamp and electrical pulse injection (from the bottom n-Si) , $Al_2O_3$ functions as a phononic waveguide that enables indirect (phonon-assisted) electronic transitions in the POM layer.

### 5.3.1 Turning "On" the Phononic Switch

Similarly to small-scale phononic structures the $Al_2O_3$ phononic waveguide can provide bandgaps for both phonons and light, suggesting new mechanisms with which to enhance phonon–photon interactions. As a rule of thumb, a composite made of a high dielectric solid material and air helps form photonic gaps and also promotes the likelihood of phononic gaps due to the large density contrast [357].

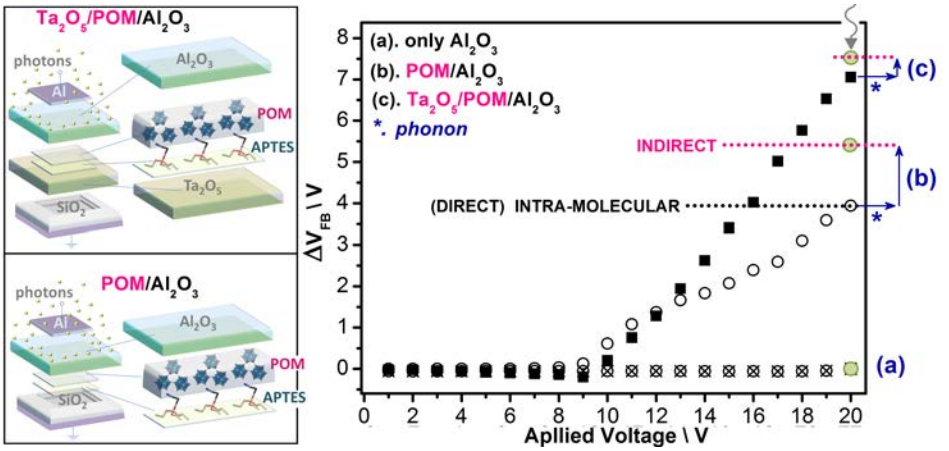


Figure 5.9: Programming windows for cells $POM/Al_2O_3$ and $Ta_2O_5/POM/Al_2O_3$ obtained by the ISPP method for pulse duration 100 msec and which has been proven beneficial for enhanced trapping efficiency for the core [61]. $Al_2O_3$-mediated optically-enhanced injection using combined optical radiation and electrical pulse application, enables indirect (phonon-assisted) electronic transitions in the POM layer (indicated by blue arrows) and boosts the flatband window (as demonstrated with the green disk symbols).

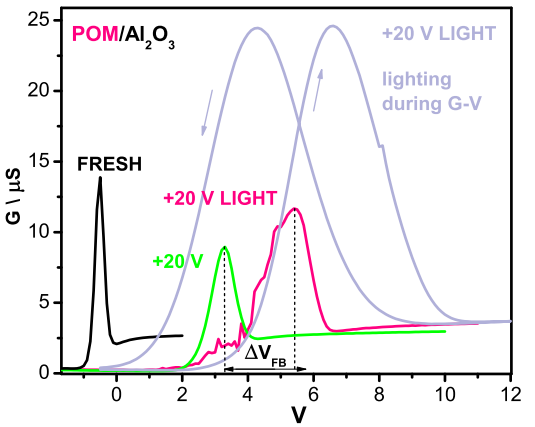


Figure 5.10: Conductance-Voltage characteristics before, after and during the opening of the phononic switch.

The phononically-assisted opening of conduction paths leading to electron transfer as well as the involvement of positively charged ionic species in the process can be confirmed in Fig.5.10. Using the monitored conductance versus voltage (G-V) characteristics of the fresh device as well

as after and during the opening of the phononic switch, the figure highlights the impact of $Al_2O_3$ phononic interconnects on the opening of electronically active channels.

### 5.3.2 Speed and Retention

In their highest recorded memory window state (20 V + Light boosting) these devices can be written with about the same efficiency with a single pulse width of 10 ns to 100 ms (see Fig.5.11). The performance of the stacks regarding to speed and phononic boost can be seen below:

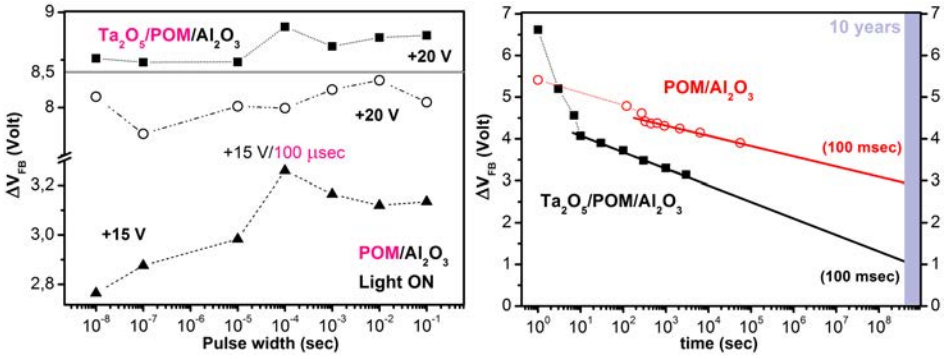


Figure 5.11: Write performance (left) and charge-retention characteristics (right) of single-pulse programmed cells in their highest recorded memory window state (20 V + light boosting).

As made clear from both Fig.5.4a and Fig.5.9 the indirect states addressing is taking part at the interface. Thus, exploitation of the memory window phononic boost is limited for the hybrid core. Indirect levels' decay is statistically rare and this favors retention in the non-hybrid case.

Moreover, phonon-assisted electron-hole recombination across the band-gap, is a relatively slow process. This lower carrier loss rate [358] towards the molecular HOMOs in the case of inter-molecularly excited POMs leads to an accumulation of electrons at the LUMO minimums. This is the origin of improved retention of indirectly charged POMs.

## 5.4 Conclusions

We have fabricated and tested capacitive memory cells based on a "clever" functional metal oxide stack, consisting of both molecular and solid state analogues. This material is being fabricated following a joint "solid-solution-vapor deposition" approach that overcomes major fabrication

obstacles in the field of scalable molecular devices on non-standard substrates with only minor modifications of the standard CMOS-line protocol. The utilized molecules are designed in a rational way in order to have pre-specified electrical properties and are incorporated using a novel two-stage one-pot self-assembly process.

Each memory element contains a 3-D-conformed hyperstructure of molecules accounting to densities of $9 \times 10^{12} cm^{-2}$ molecular NCs, corresponding to approximately $4 \times 10^{14} cm^{-2}$ storage nodes, that can store charge 65–195 $\mu Cb/cm^2$. This yields a structure that has multiple times the charge density of a typical DRAM capacitor (typically 1-2 $\mu C/cm^2$).

Using a normal incandescent lamp to take advantage of phononic pumping, we demonstrate a maximum of 37% boost on information density storage via reaching molecular states that were previously non-available. High storage density, fulfillment of the current commercial threshold of 10-years-data-retention-guarantee in ambient conditions, ability of multi-state addressing, and write speed of 10 ns are being documented for the packed cell.

The aforementioned high performance non-volatile memories are the first documented CMOS-compatible long term retention molecular capacitive cell of its kind, blazing the trail for the commercial exploitation of functional oxide and molecular hybrids as a high-end non-volatile memory product.

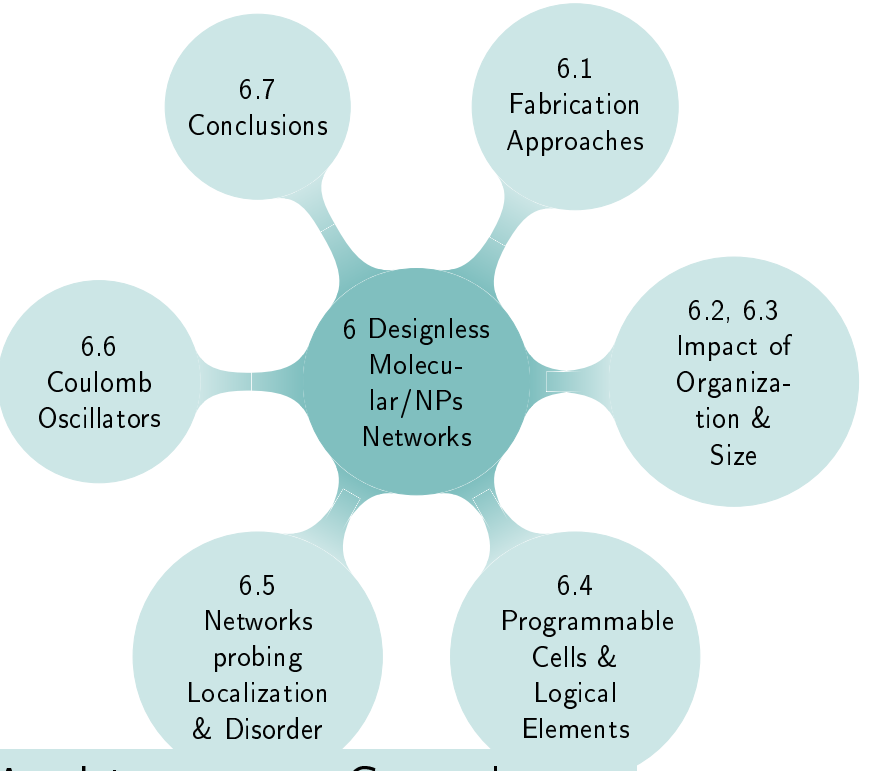


# 6

# Designless Architectures-Complex networks of Au NPs interlinked with semiconducting macro-molecules

*Contrarily to biological systems, where the emergent properties of interconnected locally active components are being used ad hoc, conventional computers are based on circuits of functional units that follow given design rules and are pre-patterned. This approach precludes potentially exploitable physical processes, such as capacitive crosstalk, on the process of problem solving.*

*This chapter is an attempt to rationalize the emergent electronic characteristics of designless multijunction networks realized through the bottom-up self-organization of hybrid metal-organic nanosize units. This includes the incorporation of disorder in the modeling of their electrical behavior and the exploitation of collective behavior of interacting nano-components.*

*We demonstrate that this way can lead to forms of computational functionality. We exploit the rich behavior of interconnected metal nanoparticles, which act as strongly nonlinear single-electron transistors and find that this nanoscale architecture can be configured on-flight to perform Boolean logic functions.*

*Precision control of charge transport is essential in providing a solid basis for the*

*design of materials with novel properties. The impact of the bottom-up fabrication processes on the functionality of the final structure is investigated and the electronic properties of molecular multi-junction networks comprising of ultra-fine gold nanoparticles (AuNPs) of diam.~1 nm, electronically linked by means of copper 3- diethylamino-1-propylsulphonamide sulfonic acid substituted phthalocyanine (CuPcSu) molecules are studied.*

*When electrons flow through the non-linked nanoparticle arrays, they experience on-site Coulomb repulsion and are strongly localized, with localization length ($\xi$=0.7 nm). Under dynamic excitation the system undergoes Coulomb oscillations, while the introduction of CuPcSu molecules results in the formation of a network of multiple molecular/Au nanojunctions and conductance increases by 5 orders of magnitude.*

*This switching behavior functions on reversible red-ox reactions and pushes carriers in a weak localization state. In this state electrons spread over several junctions and all temperature scaled current vs voltage curves, $J/T^{1+\alpha}$ vs eV/kT, collapse in one universal curve, characterizing the network and the extent of its disorder.*

*Utilizing this property we demonstrate the effect of inter-electrode distance on the conduction nodes' topological disorder. The fabricated networks consist a promising candidate for designless Au NPs-based networks with tunable properties wherever solution-based fabrication methods, such as injection printing, are envisioned.*

---

The quest for scaling down (opto)electronic devices has postulated an increasingly stronger demand for the design of new materials with desirable properties from scratch. Towards this direction the controlled formation of superstructures of binary nanoparticle/molecules mixtures opens enormous opportunities for the design of materials with unique properties.

A wide variety of organic and polymer materials with different chemical and structural characteristics have been proposed for potential use in electronics applications [359, 360, 361, 362, 363, 364]. Molecules like Copper Phthalocyanine (CuPc), have been extensively used in organic electronics owing to their controllable electronic properties and arrangement dynamics [365, 366, 367, 368, 369, 370]as well as their remarkable structural and thermal stability [371]. Their chemical doping agility [372] equips them with significant flexibility in terms of electronic properties and grants them the ability to become pre- or post-modified with functional groups of detectable electronic fingerprint.

Beyond the field of molecules, the use of metallic or semiconducting nanoparticles has been envisioned as a powerful means of attaching charge or photon localization properties in devices [373, 374, 375]. AuNPs in particular, prepared using a variety of methods from chemical reduc-

tion to laser ablation, offer a lot of choices both in size and surface properties [374, 376, 377, 378], hinting the advanced suitability of AuNPs as prototyping material for the investigation of multipurpose devices [379].

It is, however, a fact that although the performance of devices such as organic light-emitting diodes (OLEDs), organic field-effect transistors (OFETs) and solar cells has nowadays considerably improved [380, 381, 382, 383], a number of fundamental problems related to the impact and control of disorder on molecular hybrids need to be further investigated. Disorder has a pronounced influence on both optical and charge-transport properties, especially in the case of low dimensional systems. It, thus, becomes a realistic problem whenever solution-based fabrication processes, such as injection printing, are envisioned.

Aim of this work is the study of electronic transport and charge localization properties of molecular multi-junction networks that would possess tunable (opto) electronic properties and easily resolvable localization of charge. We have investigated this scheme through confinement of hybrid molecular/NP networks between high-precision nano-leads utilizing sulfur functional groups (in the form of CuPcSu), one of the most robust [384] and archetypal ways of grafting organic molecules on gold. The results demonstrate the feasibility of this concept and render this system and the corresponding analysis promising candidates for the fabrication of novel devices.

The fabricated nano-dimensional platforms can be used as a testbed monitoring the electronic properties and disorder of the hybrid networks under test, or could be directly used as biosensors. Gaps naturally occurring in these nanofabricated networks could be functionalized to adsorb certain specimens. Changes in the current flowing through the structure are potentially usable to detect or even quantify this adsorption. Yet, before high precision nanogap biosensing can be accomplished, charge carrier transport in hybrid nanojunction networks of various topologies needs to be modeled and understood.

## 6.1 Fabrication approaches for the formation of complex Au NPs/semiconducting linker networks

There are a great many ways of preparing noble metal NPs, depending mainly on the desirable properties/application and/or the restrictions imposed by the involved materials. For the purposes of the formation of networks of Au NPs/semiconducting linkers Au NPs were prepared following the subsequent three approaches:

### 6.1.1 Chemical synthesis

One of the most frequent routes to prepare noble metal NPs in liquid media (colloids) is chemical reduction. This method is based on the controlled reduction of a metallic salt in the presence of a suitable reducing agent and a certain amount of stabilizing molecules.

In this work citrate stabilized Au NPs were prepared via reduction of $HAuCl_4$ with sodium citrate according to the procedure of Lee and Meisel [13]. 125 ml of 1.2 mM solution of $HAuCl_4$ was brought to boiling under vigorous stirring. To this solution 12.5 ml of 1% sodium citrate solution was added rapidly. The reaction mixture quickly changed the color from pale yellow to dark red. The boiling continued for 10 min and then the hydrosol was cooled down under stirring for another 45 min.

The concentration of gold in the resulting hydrosol was $1.1 \times 10^{-3}$ M. In this process sodium citrate plays the dual role of reducing as well as stabilizing agent, through the repulsive surface action of citrate anions, so no additional stabilizer is used. TEM images of Au NPs as deposited from the corresponding colloids on carbon-coated copper grids are shown in Fig.6.1 and indicate a mean NP diameter of 17.9±0.2 nm.

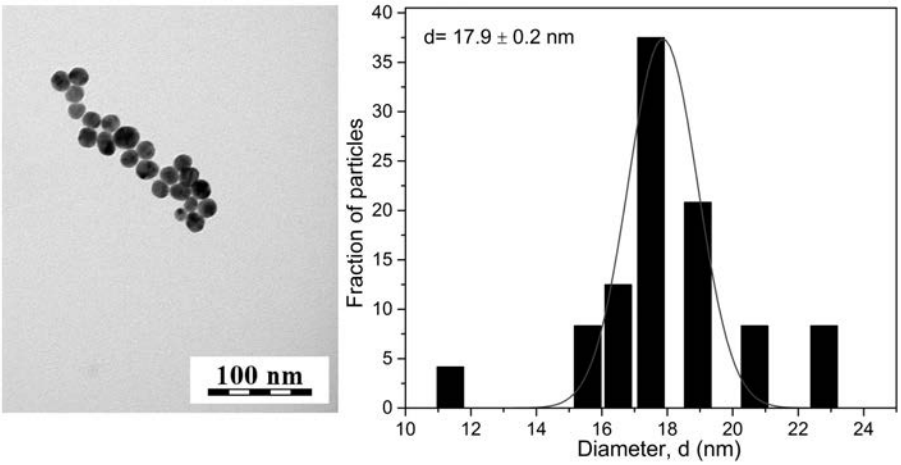


Figure 6.1: TEM image of chemically synthesized AuNP colloids (a) and histograms of number distribution of AuNPs (b). The estimated average diameter was 17.9±0.2 nm.

The colloidal stability of the produced AuNPs in the water ambient was inspected via measuring the zeta potential. The resulting value for citrate stabilized AuNPs was -42.7 mV, indicating a stable colloid [14]. Taking advantage of the relatively large surface area of these 17.9 nm chemically synthesized NPs it is possible to investigate phenomena like the evolution

of Surface Plasmon Resonance (SPR) peaks for different extent of surface functionalization with CuPcSu linker molecules.

### 6.1.2 Laser Ablation

During laser ablation a bulk material target is irradiated via a pulsed laser, typically in the ns or fs frequency regime, in order to detach nanosized parts.

In case of fs pulses used in this work, the pulse duration is significantly shorter than the time required for electron-phonon energy transfer, which is of the order of few ps [385, 386]. This results in a negligible heat transfer to the irradiated material and a direct solid-vapor or solid-plasma transition for the ablated NPs for frequencies above the ablation threshold. This rapid vaporization is essential in order to obtain small particles with sufficiently narrow size distribution. In the case of longer (i.e. ns) pulses, the laser heating-produced thermal wave has adequate time to spread through the bulk material within the pulse duration and, as a result, the material evaporates from the molten phase of the metal's surface.

In order to facilitate liquid phase self-assembly in the subsequent process of network formation we performed laser ablation in liquid (i.e. ultra pure $H_2O$) ambient. This imposes some extra constrains regarding the pulse energy of the laser. For fluencies lower than 100 $J/cm^2$ Kabashin and Meunier [387] reported occurrence of rapid vaporization, resulting in relatively small particles of narrow size distribution. On the contrary, for higher fluencies the heating of the surface of the bulk material by the solvent-confined plasma produces NP sizes and distributions assimilating the case of longer (i.e. ns) pulses.

Following these guidelines, Au NPs were prepared by ablation of a high purity Au foil immersed in ultra pure $H_2O$, using the fundamental harmonic of a Nd:YAG laser operating at frequency-doubled, 532 nm low power pulses (few $J/cm^2$) with pulse width of 100 fs and 10 Hz repetition rate. Height of water on the gold target was 5-7 mm. Laser beam diameter was 6 mm before lens and is calculated to be 30 mm on the surface of the target. The used setup is schematically presented in Fig.6.2.

The produced NPs were characterized by UV-vis optical extinction, transmission electron microscopy (TEM) and Dynamic Light Scattering (DLS). UV-Vis absorption spectra were recorded in the spectral range 200-800 nm using a double beam Perkin Elmer Lambda 950 UV-Vis spectrophotometer. The sols were measured in a 1 cm quartz cuvette, layered thin films were deposited and scanned on quartz substrates. TEM images of Ag and Au colloids were obtained with a JEOL JEM 200 CX trans-

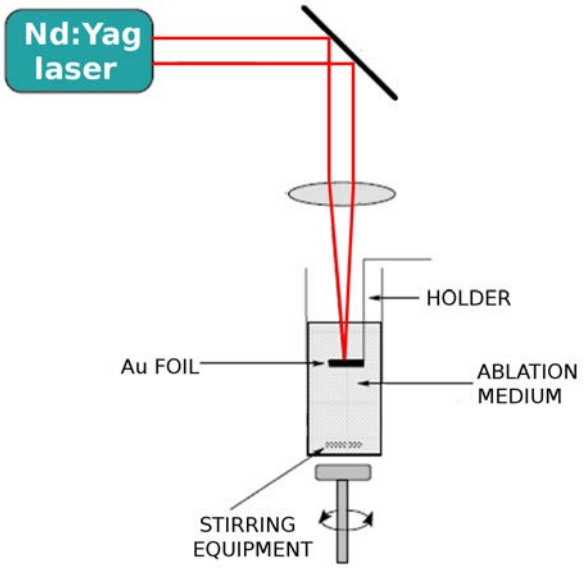


Figure 6.2: Schematics of the used liquid-operating laser ablation setup.

mission electron microscope. The colloid exhibited a good stability, i.e. repeatable UV-vis spectrum after sediment filtering even after 6 months, and a mean NP size below 10 nm. DLS measurements for the study of the hydrodynamic size distribution of the NPs in water, were done using the Nano ZS (red badge) ZEN 3600 Malvern Zetasizer.

The possibility to reduce NP size via ablation offers several advantages for the realization of realization of novel electronic platforms. These include enhanced localization of carriers onto the NP nodes and, thus, reduction of thermal noise and exhibition of single-electron transport phenomena when electrically addressed in devices.

There is, however, a stability trade-off in this case. Directly after the ablation various species like clusters, fragments and ions are collectively present in solution. These can re-arrange and crystallize over time, forming new NPs, increasing size dispersion and affecting the plasmonic peak. Thus, proper filtering before usage of stock solutions is essential to assure mono-dispersed NPs.

### 6.1.3 Physical Vapor Deposition

Au NPs of 1.4 nm diameter were prepared directly from solid state via evaporative deposition in high vacuum ($P \leq 1 \times 10^{-6}$ Torr). The evaporation rate was kept constant at 0.1 nm/sec and was monitored in situ via a quartz crystal placed symmetrically to the substrates under deposition

with respect to the Au source. Due to the weak chemical reaction of the deposited Au with the $SiO_2$ substrate and the low deposition temperature (i.e. room temperature), an abrupt interface is formed. Low temperature growth suppresses migration, implying that Au is deposited as discrete NPs at the nucleation centers before an appreciable material thickness is reached [388].

With this method the size of grown Au NPs can be controlled down to a single nanometer, making size- and surface/interface-related effects of increased importance. In this case the NP nodes are deposited homogeneously in solid state, a fact simplifying the modeling of the system and the interpretation of its electrical response. Moreover, due to the high surface-to-volume ratio of NPs, surface adhesion forces dominate over electromagnetic field induced stresses rendering the system a robust platform that yields reproducible results.

## 6.2 Impact of NP preparation method & polarizability of solvent on the organization of NPs under electric field & Localized Surface Plasmons

In order to understand the mechanisms governing conduction in complex NP/linker molecule arrays a reasonable approach is to start by studying conduction in pure Au NP assemblies. The monitoring of the formation of such an assembly by means of in-situ electrical and optical characterization would provide information about the kinetics and the physical mechanisms that govern the arrangement of metallic NPs from liquid. Understanding these interactions is crucial in order to gain control over the structure and electrical properties of the formed networks. At first stage the assembly of AuNPs on plane is attempted via AC field electrophoretic deposition.

For the in-situ monitoring of the assembly process under electric field application an optical microscope with a DSLR camera attached on the ocular lens was used. The NPs were manipulated and addressed on platforms equipped with Au $\mu$m-spaced electrodes patterned on barium borosilicate glass substrates by standard photolithography and lift-off. These serve as a visible-light-transparent electrical testing and assembly platforms. Pairs of interconnected electrodes with parallel overlapping fingers and gap size of 50 $\mu$m were used. The electrode overlap was 4.4 mm and their thickness 40 nm (see Fig.6.5). All electrode gaps on the sample can be contacted in parallel.

For the formation of AuNP assemblies three types of solutions were used:

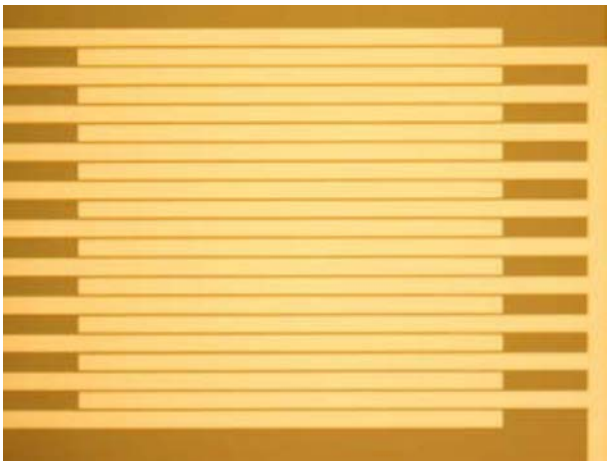

Figure 6.3: High quality interdigital 30 nm-thick Au with 10 nm high work function adhesion layer (ITO) electrodes (structured by lift-off) on 230 nm $SiO_2$ on n-doped Si. The same structures were patterned on barium borosilicate glass to assist optical addressing during electrical measurements.

(a) Pure colloid of citrate stabilized AuNPs in aqueous solution ($1.1 \times 10^{-3}$ M) with mean diameters of 17.9 nm (see subsection 6.1.1).
(b) Au NPs with a mean diameters of 4-5 nm prepared by laser ablation in polar solvent (i.e. deionized water) (see subsection 6.1.2) and
(c) Ablated Au NPs with mean diameters of 4-5 nm in non-polar solvent (i.e. butanol).

In order to create the assembly field we utilize a HP 3310B function generator and provide a sinus type voltage waveform of 2.0 or 5.0 V (4 and 10 Vpp respectively at open circuit) and frequency 1MHz. This quite high frequency value is selected in order to avoid any electrolytic reactions during the assembly process (the ionic species do not have adequate time to respond to the alteration of the field) and to ensure that there will be no net movement of the NPs due to their surface charge.

The colloidal solution is injected with a micro-pipette inside an electro-deposition cell placed onto the active area of the chip under test. As soon as voltage is applied to the electrodes, the assembly procedure is monitored in real-time via impedance and relative face recording over time with a HP4284A precision LCR meter. At the same time sequential frames in light transmission mode are recorded every 10 sec using a DSLR camera adapted onto the ocular lens of an optical microscope.

The voltage was successively increased from 2.0, where no evidence (recordable with the tools used) of assembly occurred after 60 min, to 5.0

V. At this latter voltage the first indications of assembly were observed after several minutes (40 min) to one hour. Assembly was realized via the formation of micrometer size dendritic structures and/or chains in the close vicinity of the electrodes. Nevertheless, even for very high NP concentration and electrodeposition time no gap closure was reported by means of in-situ electrical measurements.

### ABLATED NPs + BUTANOL

In the case of high NP concentration and ablated Au NPs in non-polar solvent aggregates and/or dendrimers are first formed in solution and are then post-attracted in the close vicinity of the electrodes.

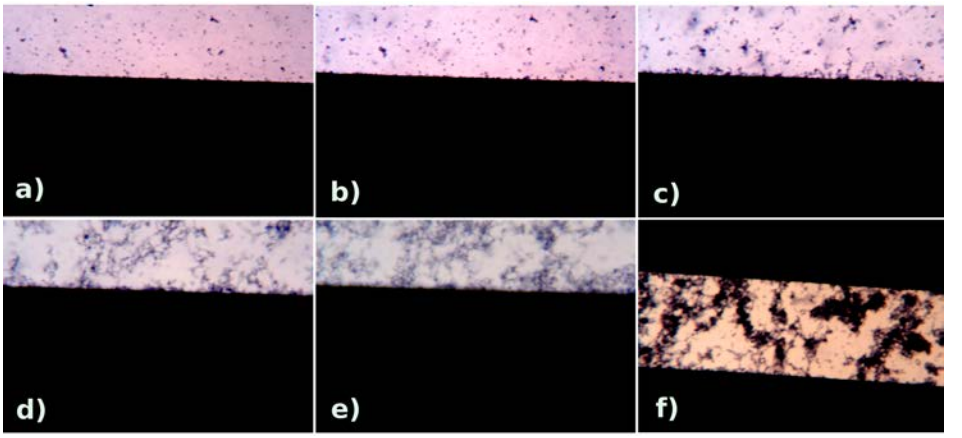


Figure 6.4: Instances of the electrophoretic assembly process for laser-ablated Au NPs in 1-butanol.

During electro deposition there is a net Au NP movement across the area between the electrodes. The particles are suspended in a spatially non-uniform electric field (the field is stronger in the vicinity of the electrode edges). The applied field induces a dipole in the Au particles [389]. The interaction of the induced dipole with the electric field generates a force. Due to the presence of the field gradient, these forces are not equal and there is a net movement captured in the frames recorded by the camera (Fig.6.5) in real time.

The formed dipoles tend to align with the field and the generated force acts up the field gradient towards the region of highest electric field (electrode edges). This force is dependent on the induced dipole, and is unaffected by the direction of the electric field, responding only to the field gradient. The enhanced dipole momentum of the aggregates (vector sum of isolated dipoles) with respect to isolated NPs explains the

fact that they are more effectively attracted towards highest electric field regions when they overcome a critical size by aggregation in solution. This is most probably the reason of the observed aggregates attraction on the electrode edges when they exceed a critical size.

As reported in [390] the growth of the NP superstructure is expected to begin as an elongated dipole. At first some few dipolar NPs fuse and build up an initial seed. Due to the oriented attachment, the seed grows in length and thus the electric field based on generated accumulated dipoles, increases. At a later growth stage, further parallel attachment of the particles is replaced by branching. This may be rationalized by the alignment of dipolar NPs according to the electric field lines and hence, branching of the seed is initiated where the field strength is largest, i.e. at the poles.

### ABLATED NPs + D.I. WATER

Not evident chain, branch or aggregate formation in the vicinity of the electrodes.

### CITRATE STABILIZED NPs + D.I. $H_2O$

In the case of high NP concentration and chemically prepared Au NPs in D.I. water there was not evident chain, branch or aggregate formation in the vicinity of the electrodes. In the case of diluted aqueous sol (1:10 v/v) There were evident (micrometer scale) indications of NP and chain and/or dendritic structure formation approximately 40 min after voltage application. The formation of these structures was primarily realized at the edges of the electrodes.

### Comments

In the case of citrate stabilized NPs mobile citrate ions can cause electric field screening in the vicinity of the electrodes. This can greatly affect the kinetics of NPs under field, since it neutralizes their charge and homogenizes the local distribution of overall charge prohibiting, thus, attraction and arrangement of the NP dipoles.

This argument is valid for all aqueous solutions, on one hand due to the autodissociation of water and on the other hand due to the presence of other counterbalancing ions in sol. The concept explains the lack of chain, branch or aggregate formation in the vicinity of the electrodes when mere D.I. water was used. This fact is further supported by the observed rapid accumulation of NPs in the case that $H_2O$ is replaced with butanol.

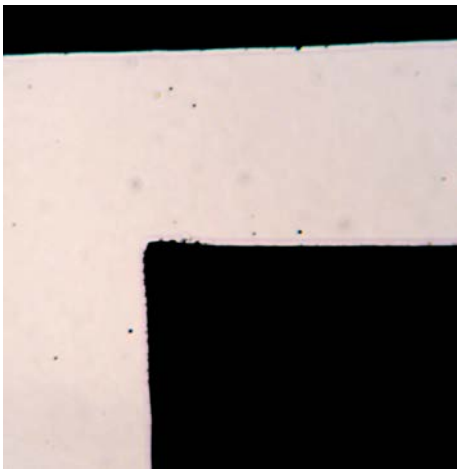

Figure 6.5: Instance of the electrophoretic assembly process for citrate-stabilized chemically prepared Au NPs in DI water.

In other words, the polarity of solvent can become the vehicle of tuning the strength of interaction between NPs in sol.

**Localized Surface Plasmon Resonance – A comparative study**

Interaction of AuNPs with light is strongly dictated by the dielectric constant of the surrounding medium, shape and physical dimensions of NPs. Oscillating electric fields of a light ray propagating near a colloidal NP interact with the free electrons in its volume causing a concerted oscillation of electron charge that is in resonance with the frequency of visible light. These resonant oscillations are known as surface plasmons (SP). SP strongly confined on the surface of metallic NPs is termed localized surface plasmon resonance (LSPR) [391].

For small (~ 30nm) monodisperse AuNPs the SPR phenomenon causes an absorption of light in the blue-green portion of the spectrum (~ 450 nm) while red light (~ 700 nm) is reflected, yielding a rich red color. As particle size increases, the wavelength of surface plasmon resonance-related absorption shifts to longer, redder wavelengths. Red light is then absorbed, and blue light is reflected, yielding solutions with a pale blue or purple color. As particle size continues to increase toward the bulk limit, surface plasmon resonance wavelengths move into the IR portion of the spectrum and most visible wavelengths are reflected, giving the NPs clear or translucent color. Thus, besides the enhancement of optical absorption of NP surface adsorbates [392], the LSPRs consist a tool of determining the mean NP size by solely optical means.

Fig.6.6 provides a comparative overview of Au NP systems prepared

by all three fabrication methods examined in this work. In case of the self-assembled network, the presence of the NPs is confirmed via the characteristic SPR peak in the UV-vis absorption spectrum. The resonance wavelength is significantly shifted towards longer wavelengths in comparison to the Au NPs in hydrosol.

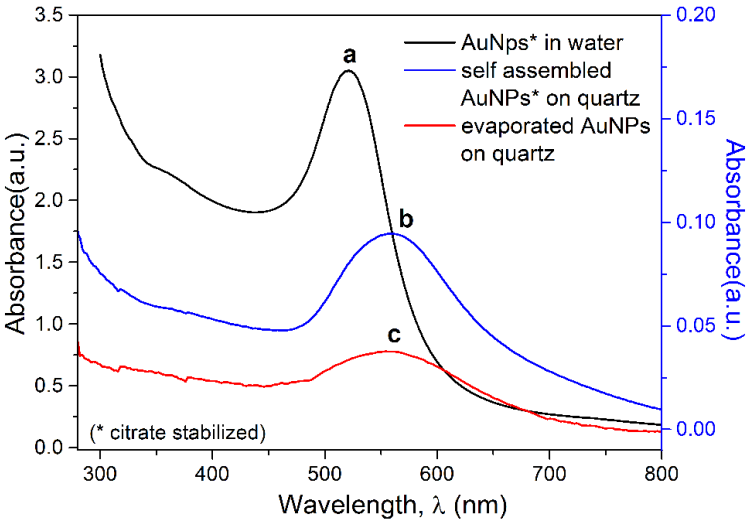


Figure 6.6: UV-Vis absorption spectra of Au NPs on quartz prepared by different techniques. The solid state systems scale is displayed on the right. The graphs from the higher to the lower absorption structures show: (a) citrate stabilized AuNPs in aqueous solution, (b) citrate stabilized AuNPs self-assembled on APTES-modified quartz substrate via the LbL technique and (c) fine Au NPs grown on clean quartz slide via physical vapor deposition.

This is to be expected due to the significant change in the refractive index of the medium surrounding the particles (i.e. from water in the liquid phase to a complex medium composed of CuPcSu molecules and air (case of self-assembled NPs) or just air (case of evaporated NPs) in the solid state. Note that the resonant frequency has been reported to be red shifted with the increase of the mediums refractive index [393].

Concerning the system of evaporated NPs the reduction of the NP diameter by almost a factor of 10 comparing to the citrate stabilized NPs pushes the surface plasmon resonance band towards shorter wavelengths [394]. At the same time, the drastic decrease of the inter particle distance with the evaporative deposition causes a counteracting red shift along with a broadening of the peak [395]. The observed red curve in Fig.6.6 is the resulting interplay between the two trends.

## 6.3 Hybrid AuNPs/CuPcSu networks-Impact of NP organization on the electronic & electrical characteristics

### Preparation of the organic linkers

For the functionalization of Au nanoparticles a low-molecular weight organic semiconductor was used, namely copper 3-diethylamino-1-propylsulphonamide sulfonic acid phthalocyanine (CuPcSu). The material was directly prepared from copper phthalocyanine (CuPc) via a two-step reaction, according to Ciba Geigy Corporation Patent [396] slightly modified in that N-diethylaminopropylamine (instead of N-dimethylaminopropylamine) was used as a starting material.

In the first step CuPc sulfochloride, containing 11.2 % sulphur S and 11.5 % hydrolyzable Cl, was prepared via the reaction of CuPc with chlorosulfonic acid and thionylchloride. The CuPc sulfochloride contained 2.8 $SO_2Cl$ and 0.2 $SO_3H$ groups per molecule. Subsequently, CuPc sulfonamide was synthesized from the CuPc sulfochloride via reaction with N-diethylaminopropylamine in water medium. After termination of the reaction, the product was filtered and rinsed off with distilled water up to the point that no detectable traces of N-diethylaminopropylamine were present. Finally, it was dried at $105^oC$. The product average formula is:

$$CuPc(SO_2NHCH_2CH_2CH_2N(C_2H_5)_2)_{2.8}(SO_3H)_{0.2}$$

, with its chemical structure presented in Fig.6.9. Stock solutions (both of concentration $5 \times 10^{-5}$ M), were prepared by dissolving CuPcSu in butanol (spectroscopic grade, Aldrich). APTES (obtained from Aldrich) was of analytical grade and was used without further purification for the chemical treatment (silanization) of $SiO_2$ surfaces during the self-assembly layer-by layer (LbL) process. Deionized water with a resistivity of 15 $M\Omega \cdot cm^{-1}$ prepared from a Milli-RO plus 90 apparatus (Millipore) was used in all the experiments.

In order to evaluate the impact of complex network formation on the surface plasmon resonance (SPR) bands of the deposited AuNPs, the changes induced on the SPs of pure NPs after arrangement and changes of their dielectric environment ought to be monitored. In this subsection we provide a comparative overview of Au NP systems after addition of surface linkers both in solution and in solid state, where NPs are assembled via three different methods:

**Substrate-Linker driven network formation (self-assembly)**

These networks were fabricated via application of the layer by layer self assembly process (LbL) on the exposed $SiO_2$ surface of the nanoelectrode-equipped substrate. The process consists of hydrophilization of the oxide surface via the creation of -OH surface groups using mild oxygen plasma treatment (Power (Watt)=800, Pressure (Pa)=1.33, $O_2$ (sccm)=100, Bias (V)=0 for 2.5 min).

The resulting highly hydrophilic surface is subsequently chemically modified via the silanization of the exposed O atoms resulting in the covalent bonding of the silane group of 3-aminopropyl-triethoxysilane (APTES) molecule with the deprotonated -OH groups. APTES aqueous solution (2% v/v, pH 7) was deposited on the surface at full coverage and room temperature (RT) for 20 min, rinsed cautiously with de-ionized water, and dried under low pressure (2 bar) $N_2$ steam.

Silanization of the $SiO_2$ substrate was obtained during thermal treatment at 120 $^oC$ for 20 min through the reaction between the silane groups of strongly physisorbed APTES molecules and deprotonated surface -OH groups. The exposed amine groups are protonated in solution, forming a positively charge molecular template on the $SiO_2$ surface.

Au NPs were prepared as described in Subsection 6.1.1. Having negative surface charge, the NPs are adsorbed on the aminosilane functionalized $SiO_2$ surface driven by electrostatic-type forces (i.e. nucleophilic reaction of exposed amino groups of APTES with carbonyl groups of functional AuNPs [15]) in aqueous environment [16].

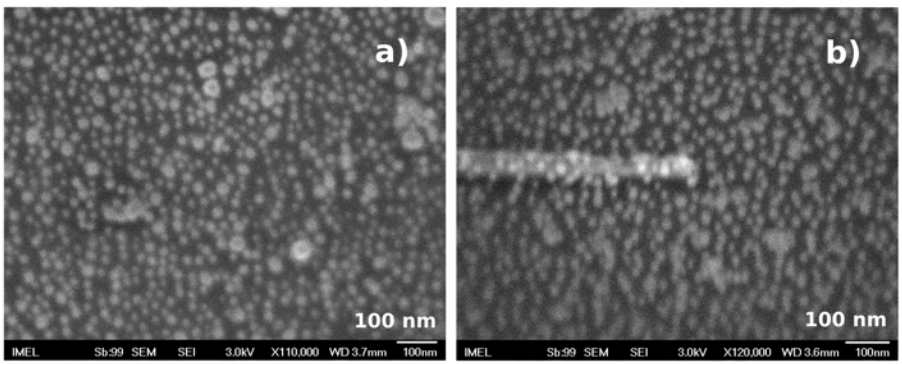


Figure 6.7: FE-SEM image of the network of chemically prepared citrate stabilized Au NPs self-assembled on the nanoelectrode equipped $SiO_2$ substrate.

This way the self-assembly emerges as an interplay between repulsive forces among the negative surface charge of the functionalized NPs (quantified by measuring their negative zeta potential) and attractive elec-

trostatic forces between the positively charged amino-end groups of the APTES and the NPs. What follows is the electrostatic assembly of the composite NPs/molecular linkers in solution. The resulting assembly is the uniform dense network of weakly coupled Au nodes presented in Fig.6.7, Fig.6.8.

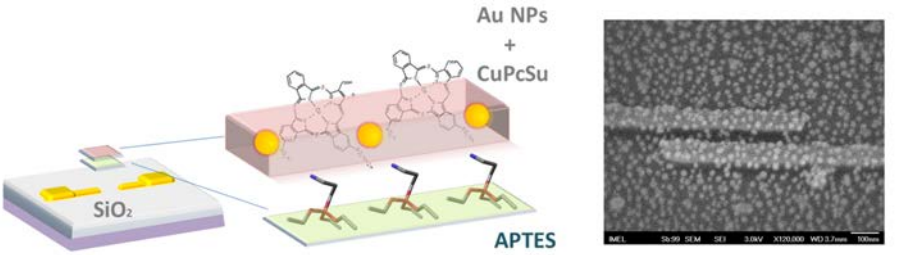


Figure 6.8: Hybrid molecular/NP network based on self-assembly.

The formed thin CuPcSu layer surrounding the NP nodes is expected to have a significantly reduced band gap when compared to that of the "bulk" CuPcSu [397]. This results in enhanced surface conductivity, providing good electronic coupling to the nanoelectrodes is established.

However, The NP coupling to the Au leads is weak. In the case of opposing electrodes the junctions hardly exhibit any conduction current, due to increased difficulty in obtaining a nearest neighbor for conduction across the full lead-to-lead distance and the intense fringing effects in the vicinity of the contacts.

On the other hand, pronounced conduction occurs in overlapping parallel nanoleads, due to the addressing of a large array and the existence of a homogeneous field between contacts. Transport involves collective electronic activity through 2-d pathways, such that any few electron effects are smeared out. Conduction currents are of the order of $2 \times 10^{-8}$ A for applied fields of the order of 0.24 MV/cm, while no significant hysteresis is observed. The charging process, where any, is of stochastic nature.

**Interparticle/interlinker-driven network formation (Deposition via Drop-casting)**

These networks were fabricated via drop casting the composite NPs/molecular linkers sol on the nanoelectrode-equipped test platform. This case is of special interest, due to its direct applicability on injection printing technology. The produced assemblies are expected to form 3-dimensional hybrid networks due to the pre-functionalization of the full NPs surface with the molecular linkers. In particular, the 3-diethylamino-1-

propylsulphonamide and sulfonic acid groups serve as cross linkers between NPs in all three dimensions, while all degrees of freedom are still available in the liquid state. The resulting colloid of molecularly functionalized NPs is stable with no precipitation tendency, as indicated from its strongly negative zeta potential value (-40.2 V).

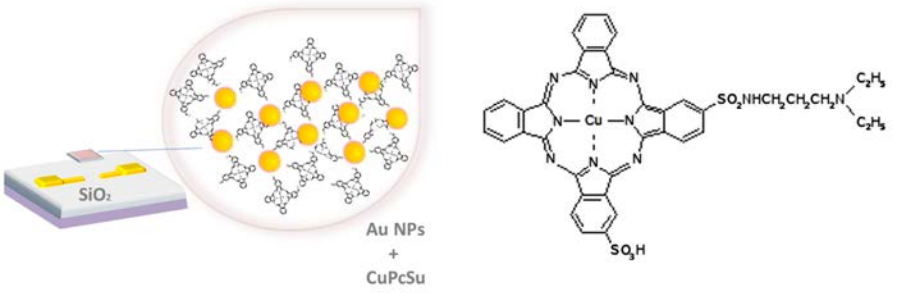


Figure 6.9: Left: Hybrid molecular/NP network based on drop-casting. On the right: Stereochemical structure of the Copper 3-diethylamino-1-propylsulphonamide sulfonic acid phthalocyanine molecule in two dimensions.

During reaction time the AuNPs interact with the S groups of the thiol-substituted sites of the organic oligomers [398]. In general, though, the functionalized NPs of the drop-cast network are only weakly interacting between them, i.e. with Wan der Waals and dipole-dipole forces and not covalently bonded to the linkers. This is in accordance with the case of self-assembled networks and is evident from XPS analysis of the characteristic peaks of CuPcSu upon network formation and interaction with the Au NPs (see Fig.6.10).

More specifically, the Au 4f doublet appear at the binding energy of 84.2 eV and 87.5 eV, as expected for metallic Au NPs. No change in shape or binding energy was observed after CuPc film deposition which indicates absence of strong chemical interaction between molecules and NPs.

The main C1s peak appears in all the cases at a binding energy of 284.7 eV with no change upon CuPc deposition on Au. The peak is asymmetric towards higher binding energies due the contribution of two more peaks, as shown in the C1s core level peak deconvolution. In this figure the CuPc film is analyzed in three components: A peak at 284.7 eV, attributed to aromatic carbon of the benzene rings, a peak at a 286.1 eV, corresponding to pyrrole carbon bonded to nitrogen and a third due to a $\pi - \pi*$ satellite [399].

The N1s XPS peak for the CuPc film and AuNPs/CuPc composite appears as one single peak at a binding energy of 398.9 eV attributed to non-equivalent N in the pyrrole rings and the bridge position in the

chemical structure of the CuPc, not separated enough energetically to give rise to resolved peaks, in agreement with previous observations [400]. Again no shift or change in the peak was observed due to the presence of AuNPs.

The Cu2p3/2 core level spectra for both the CuPc film and the hybrid appears at a binding energy of 395.5 eV, in agreement with the literature. It is consistent with copper in the Cu(II) oxidation state observed in the molecular solid phase without changes upon hybridization with Au.

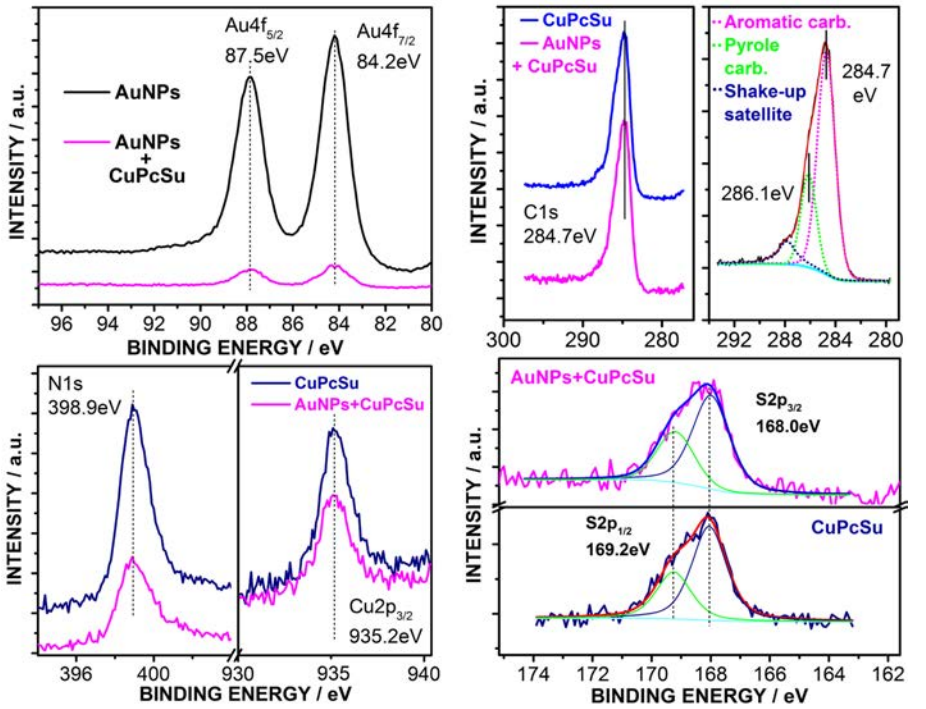


Figure 6.10: XPS spectra of: Au 4f for bare AuNPs and after deposition of CuPcSu (top left) and C1s, N1s, Cu2p and Su2p Characteristic peaks of CuPcSu and AuNPs+CuPcSu films. The lack of alteration in the shape and positions of all characteristic peaks of AuNPs and CuPcSu framework, indicate the absence of strong chemical interaction between AuNPs and CuPcSu.

It, thus, becomes evident that, though electronically coupled (as revealed upon FTIR spectra in Appendix Section 8.5 and electrical measurements in the following sections), the NPs are not covalently bonded (Fig.6.10) to the organic linkers, preserving the electronic identity of the CuPc molecule [401, 402]. As a result of their non-covalent adhesion onto the substrate the NPs are susceptible to movement upon application of dc field in the case they possess non-zero net charge.

For the drop-cast network the precursor solution was investigated by

means of measuring its zeta potential, which was found to be -40.4 mV. This value is indicative of the negative surface charge of functionalized NPs, ensuring its colloidal stability. It is worth mentioning that, contrarily to the self-assembly method where we obtain sheet conduction, the drop-casting deposition results in a CuPcSu medium that exhibits bulk-like band formation [403, 404] facilitating electronic transitions to and from the AuNPs.

The arrangement of nanoelectrodes addressing the network is directly related to the emerging transport phenomena. As an example, in the case of opposing contacts the dynamic lines of the field created under voltage application are strongly non-uniform. Their density and curvature is pronounced in the close vicinity of the electrodes' tips, while they tend to linearize and space out further away.

This non-uniformity of the field has as consequence the occurrence of conformation changes during the first voltage cycles, due to differential electric force intensity on the network. This results in non-reproducible hysteresis loops for the first approximately 5 cycles. However, after some sequentially repeated [0, Vmax] and [0, Vmin] voltage cycles we obtain stabilization of conformation and we are able to get reproducible I-V curves. The following results have been taken after realization of conformation stabilization with this method.

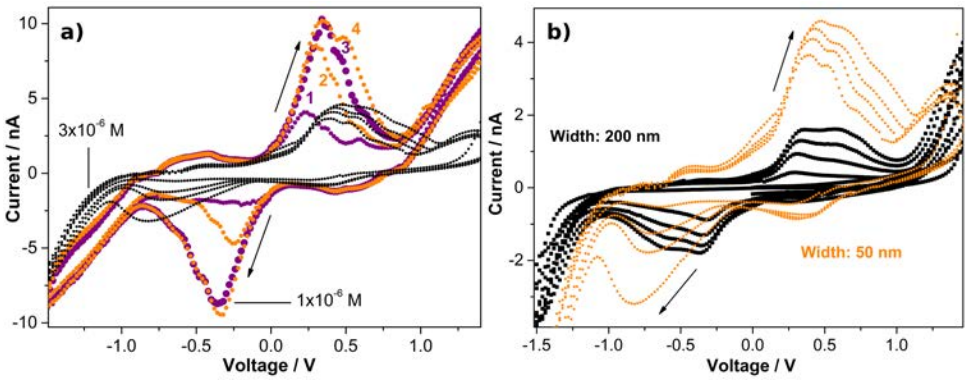


Figure 6.11: Sequential current-voltage cycles for 75 nm distant junctions and opposing nanoelectrodes. All voltage cycles are performed from -1.5 to 1.5 V and back. In a) the color curves were performed at a relatively low CuPc concentration ($1 \times 10^{-6}$ M), while the black ones at a bigger concentration of $3 \times 10^{-6}$ M. The intensity of the current peaks increases upon repetition of measurement cycles for both cases. In b) high CuPc concentration of $3 \times 10^{-6}$ M is addressed. The orange curves were performed at the 50 nm width junctions, while the black ones at the junctions with 200 nm width. The intensity of the current peaks increases upon repetition of measurement cycles for both cases.

In Fig.6.11a we can see the effect of increasing concentration of molecular linker on the network for 75 nm wide multi-junction networks. Two characteristic charging peaks emerge for both cases. Strange as it may initially seem, the current peak intensity and the area under each peak (i.e. the injected charge at each available level) is approximately halved for subtriple CuPcSu concentration in the precursor sol. This points out to the relative delocalization of the charge on the network via the increase of the linker portion. Smearing out (broadening) of the charging peaks is also observed, especially for reverse scans (-1.5 to +1.5 V), where part of the already charged AuNPs are not available for charging in early energies.

Thus, wherever NDR features are desirable, i.e. logic gates' function, low CuPcSu concentrations are the most effective. In Fig.6.11b two different electrode widths are inspected with the narrower electrodes resulting in more defined charging paths and, hence, narrower and more intense current peaks corresponding to more efficient charging and current injection.

On the other hand, for overlapping contacts a more uniform electric field is attained. Complexity in this case arises from the fact that multiple transport paths are addressed at the same time, in parallel. Electrical measurements were performed in overlapping junctions with 0.5 $\mu$m overlap width and 75nm interelectrode distance. Sequential voltage cycles are presented in the following figure.

From Fig.6.12 we see that in the case of parallel overlapping electrodes the changes in hysteresis are most probably due to charging of the NPs and/or the linker molecules, while conformation changes do not alter drastically the response. At the 1st cycle of Fig.6.12 current injection in the NP structures begins at about 0.2 V as we increase the voltage from 0V to 1V. By decreasing the voltage again towards 0V the charged NPs lower the conduction current, as now we get partial screening and less available conductivity sites for transport. At 2d cycle the remaining charged sites screen the current and as a result significant current injection starts later, at 0.4 V. For the 2d cycle the overall current is lower, as expected, due to the first cycle's charging.

Upon a 3d voltage cycle we get more or less the same current response with slightly lower current intensity for the 0V to 1V scanning direction. That means that some of the carriers trapped in the previous cycle had enough time to discharge between the voltage cycles. During the returning 1V to 0V scanning direction of the 3d cycle we have an instability occurrence that results in sudden discharge of the NPs, giving rise at the observed peak at 0.1V. The relatively broad width of the peak is attributed to the size distribution of the NPs (which are not monodis-

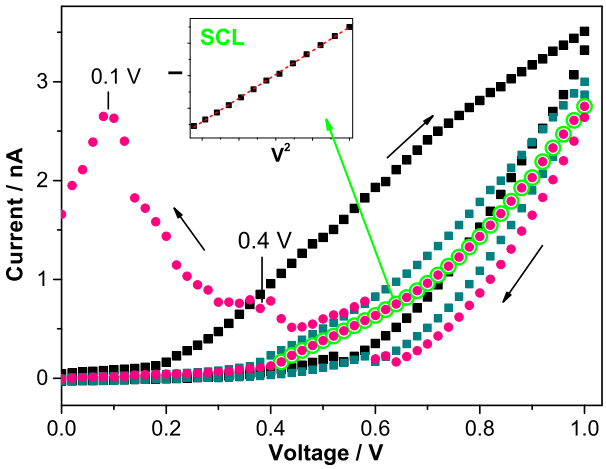


Figure 6.12: Sequential voltage cycles for 75 nm distant junctions of overlapping electrodes and high CuPc concentration (3E-6 M). All voltage cycles are performed from 0 to 1 V and back. The number on the curves denotes the serial number of the measurement. The inset is a space-charge limited current representation of the non-linear part of the current (starting from about 0.4 V) for 0 -> 1 voltage polarity.

persed).

When one plots the injection part of the I-V characteristic in space charge limited representation gets the response presented in the inset of Fig.6.12, which is in excellent agreement with the presence of an injection mechanism. At the next (4th) cycle the initial current is higher, as expected, due to the discharge of the NPs that occurred at the end of the previous cycle. When we return back (1V to 0V direction) again, we have significant hysteresis and a major charging effect.

## 6.4 Programmable Cells and Logical Elements

In the previous section I-V characteristics for the case of opposing as well as parallel and overlapping electrodes of drop-cast networks are interpreted as cases of addressing discrete charging levels, injecting electrons into available energy levels and exhibiting negative differential resistance over a significant area of low voltages around 0V.

As observed in Figs. 6.13 to 6.15 the mechanism of charge transport through the hybrid network is strongly dependent on its dimensionality. In the case of self-assembled single-NP-layer network transport is confined in a sheet parallel to the plane and there is no hysteresis upon a full voltage cycle. Electrons move through sequential tunneling between

adjacent NPs forming a spatially uniform conductive medium.

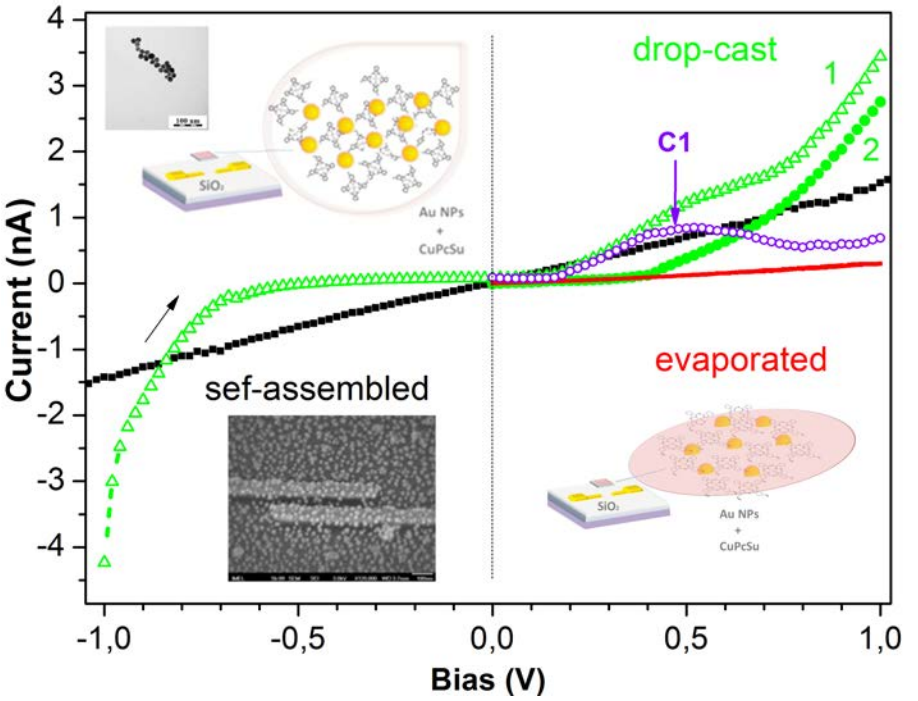


Figure 6.13: Low voltage quasi-static current-voltage characteristics

Driven by the external potential, the charges are entering the system from the higher voltage electrode. For low voltages the NP-trapped electrons screen the external potential prohibiting current flow. Above a threshold value $V_{TH}$ current-voltage characteristics follow a non-linear dependence according to the law: $I \sim (V - V_{TH})/V_{TH})^{\zeta}$.

The conduction threshold ($V_{TH}$) is significantly lower in the self-assembled layer (sheet conductance) than in the evaporated case (Figs.6.13, 6.14). For drop cast NP networks the collective conduction threshold is by far the lowest among the three cases (Fig.6.13), while the low voltage I-V characteristics exhibit a highly non-ohmic behavior (Fig.6.14).

In Fig.6.13 the difference between the first and second voltage sweep in drop-cast networks (green curves) is the charging peak C1. In other words curve 2 is deconvoluted in curve 1 and peak C1. The response highlights the charging nature of the hysteresis observed in Fig.6.14. The importance of history of charging-discharging on the I-V characteristics of three dimensional drop-cast networks, contrarily to the 2-dimensional self-assembly case where sequential I-V curves coincide is also demonstrated.

The charging energy for the ultra-fine evaporated NPs is Ec=1.029

eV. The corresponding value for the chemically prepared NPs is 85 meV. So, since both Ec and number of NPs required to gap the interelectrode distance decrease significantly in the case of chemically prepared NPs, the condition V/(# of NPs)<Ec for exhibition of non-linear co-tunneling regime [405] is satisfied for significantly lower voltage values. This is translated in lower power consumption for exhibition of non-linear effects in drop-cast networks. Non-linear I-V characteristics are highly desirable since they can be directly exploited to demonstrate logic functions by the networks [406].

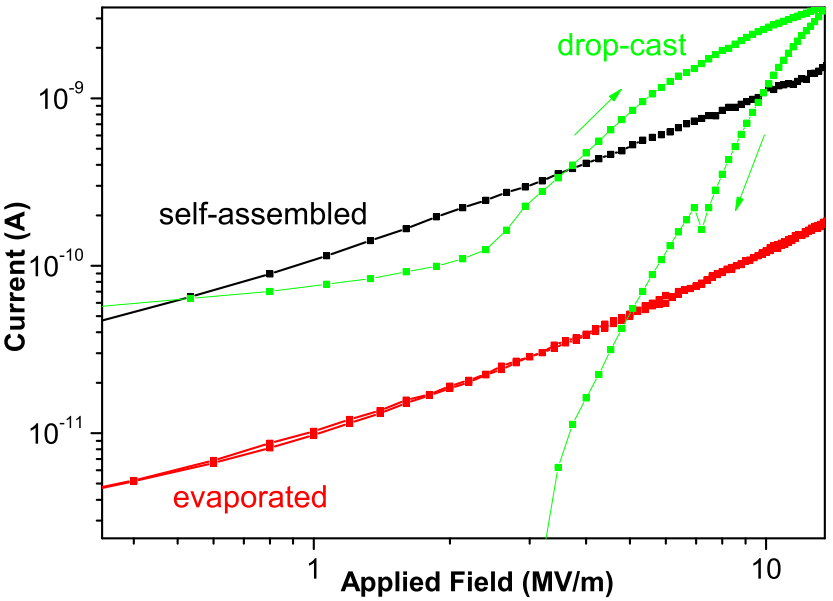


Figure 6.14: Low voltage quasi-static current-voltage characteristics

The diagram of Fig.6.14 emphasizes on the hysteresis effect. Note that in the 3-d case the I-V curves are not symmetric with respect to the origin (i.e. 0 V) a fact highlighting the rectifying properties of the film. Moreover, conductivity in three dimensions is enhanced suggesting the involvement of multiple conduction channels in parallel.

The NP nodes are only weakly coupled and randomly dispersed in all 3 dimensions favoring thus, charge trapping, conformational changes and exhibition of hysteresis. The conduction thresholds as well as the conductivity of the array depend upon the stochastic process of charging of the NP nodes.

Transport for the drop cast networks is characterized by a collective percolation threshold, below which collective Coulomb blockade phenomena dominate, impeding electronic conduction across the complex

array (see Fig.6.15).

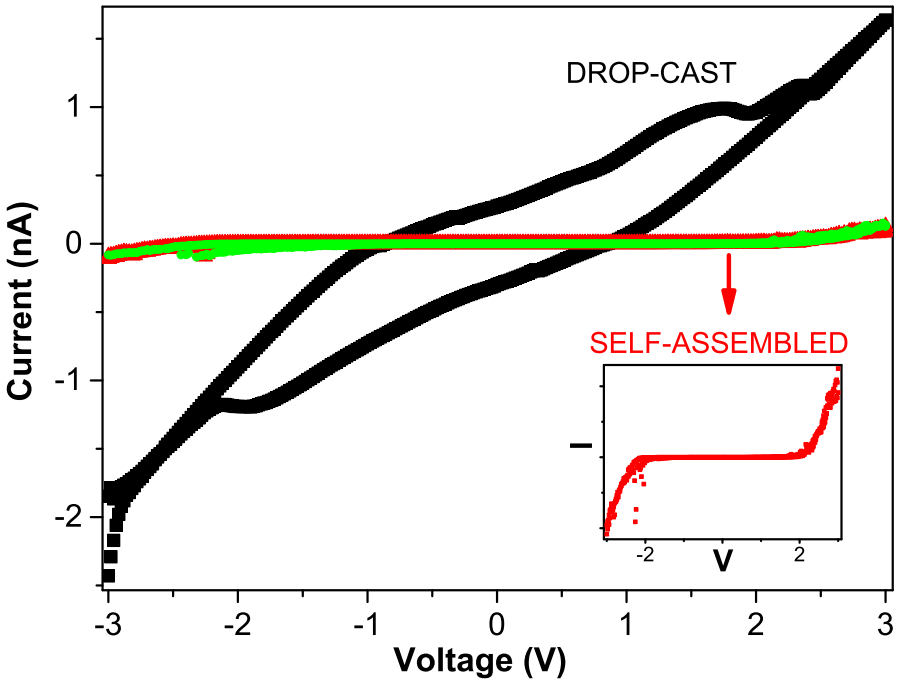


Figure 6.15: Current-voltage characteristics

For those cases, at large bias, above the Coulomb blockade threshold $V_{TH}$, the I-V characteristics follow a power-law dependence on V-$V_{TH}$ (more specifically: $(V - V_{TH})/V_{TH})^{\zeta}$ with a temperature independent exponent $\zeta$ close to 3 (2.93) , which emerges as a consequence of branching [407].

Based on the exhibited: a) the strongly nonlinear (switching) behavior of SETs presented in Fig.6.14 and b) their mutual interactions yielding $V_{TH}$=0.42 V and $\zeta = 2.93 \pm 0.02$ Fig.6.15 one can now set the goal to find logic gates.

In order, though, to investigate the suitability of the above networks as a logic element a more appropriate electrode topology should be selected. Thus, the networks were confined and addressed with crossing nanoelectrodes contouring an area of 30 × 200 nm. With such a configuration of electrodes information can be written and addressed at the same time. Conventional e-beam lithography on PMMA and lift-off where utilized for their fabrication as for the other nanoelectrode topologies.

Scanning now the system over larger applied voltages using the aforementioned crossing electrodes of 35 and 435 nm pair distance respectively we obtained the characteristics of Fig.6.14.

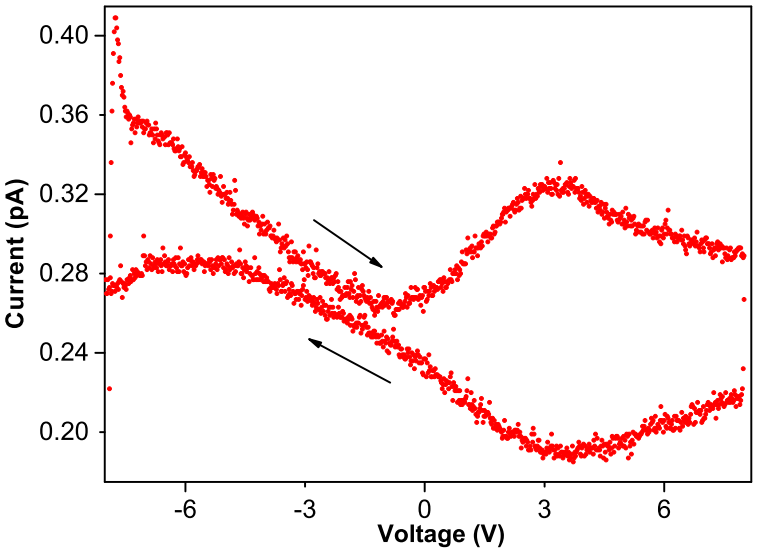


Figure 6.16: I-V characteristics under quasi-static excitation. The measurement has been carried out on a network confined in the active region of a crossing electrode configuration 30 × 200 nm in ambient. The concentration of CuPcSu linkers in here $3 \times 10^{-6}$ M.

Notably, the hybrid exhibits excellent stability and results reproducibility even at such high energy regime. We argue that the pronounced NDR effect can be utilized towards the construction of logical elements, while the multiple resistive levels and hysteretic effects can be of use in memories and switches. NDR phenomena are amphipolar and are observed for both scanning directions. NDR response is a prerequisite for logical element functionality from the cell.

For the construction of a functional nanocell the hybrid NP/molecular network has to be accessed via lithographically patterned nanoprobes in order to assure reliable programming and reading of the cell. The cross electrode configuration utilized here is ideal for this purpose. High quality, low variability electrodes patterned via e-beam lithography confine a network within a nano-dimensional active region. The network itself has an internal structure emerging from self-assembly and with this topology a chaotic nanostructured network becomes accessible for standard mesoscopic electrical addressing.

This is an entirely different approach than the one encountered in conventional integrated circuits. The resulting nanocell can be programmed, erased and reprogrammed dynamically, through collective switching of the constituent nodes between on and off resistive states. The cell functions real time with a response time of merely 10 ns. As can

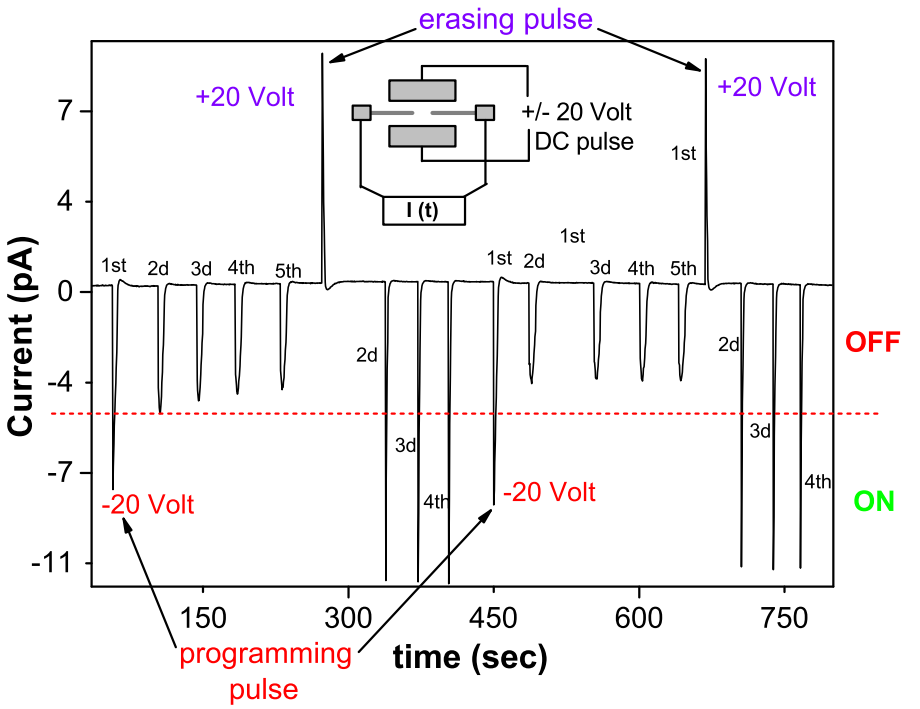


Figure 6.17: Room temperature logic cell function for hybrid AuNPs/CuPcSu ($3 \times 10^{-6}$ M networks drop-cast on a planar transistor structure.

be seen in Fig.6.17 the cell "remembers" the given information sequence and functions accordingly.

More specifically, when -20 V 10 ns pulses are applied on the cell after an initial -20 V 10 ns the system is set in a low resistance (ON) state. +20 V 10 ns pulses applied after an initial +20 V "switching" pulse address the corresponding OFF state (i.e. a state of higher resistance). The network changes polarization state during the +20 V switching pulse and thereafter it conducts negative current, as is also the case for negative pulses. The network is trained to transport carriers collectively always in the same direction, independently of the voltage polarity. Moreover, it collectively "learns" to discriminate between two resistive levels according to the polarity of the "switching" pulse. Both states can be read real time with one of the two couples of crossing electrodes (see inset of Fig.6.17) defining the cell using a low reading voltage of 500 mV.

The pulse sequence response of the network as depicted in Fig.6.17 can be further quantified by means of input and output signals as depicted in Fig.6.18, where the $V_{IN}$ and $I_{OUT}$ versus time (t) plots that correspond to a two-input "then-if" logical gate are depicted.

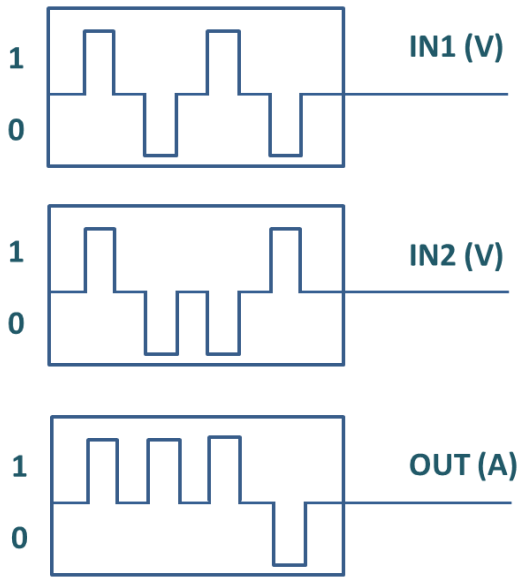


Figure 6.18: Truth table of logical "(then)-if" function as realized on-flight from the NP network.

The local properties modification of the network (i.e. charging, resistive switching, etc.) has a strong influence on the output signal, a fact attributed to capacitive coupling to the full area of the NP network. The resulting concept of a logical element realization is entirely based upon locally active interacting components following a non-conventional designless approach based on self-regulation.

## 6.5 Benefits from network functionality. A platform that probes the localization of charge and the extent of disorder

Precision control of charge transport can provide a solid basis for the design of materials with novel properties. We report on the bottom-up fabrication and study of the electronic properties of molecular multi-junction networks comprising of ultra-fine gold nanoparticles (AuNPs) of diam. 1.4 nm, electronically linked by means of copper 3-diethylamino-1-propylsulphonamide sulfonic acid substituted phthalocyanine (CuPcSu) molecules. When electrons flow through the non-linked NP arrays, they experience on-site Coulomb repulsion and are strongly localized, with localization length ($\xi$=0.7 nm).

Under dynamic excitation the system functions as a single electron

transport regulator, undergoing Coulomb oscillations, while the introduction of CuPcSu molecules results in the formation of a network of multiple molecular/Au nanojunctions and conductance increases by 5 orders of magnitude. This switching behavior functions on reversible red-ox reactions and pushes carriers in a state of weaker localization. In this state electrons spread over several junctions and all temperature scaled current vs voltage curves, $J/T^{1+\alpha}$ vs eV/kT, collapse in one universal curve, characterizing the network and the extent of its disorder.

Utilizing this property we demonstrate the effect of inter-electrode distance on the conduction nodes topological disorder. The system consists a promising candidate for Au NPs-based thin films with tunable properties wherever solution-based fabrication methods, such as injection printing, are envisioned.

In order to address small dimensional systems and reduce variability we confined the networks between standardized, high-precision leads manufactured via e-beam lithography. Au nanoelectrodes (of edge roughness $\pm$ 3 nm) were patterned using e-beam lithography and lift-off on $Si/SiO_2$ (80 nm thick) substrates. The electrodes were parallel and overlapping for a length of $2\mu m$. Different pairs where prepared with distances 25 and 50 nm.

Ultra-fine AuNPs of av. diam. 1.4 nm were thermally evaporated (PVD) on this template, forming a network of fixed inter-particle gaps, which can be functionalized with CuPcSu oligomers in a subsequent drop-casting step, under $N_2$ environment and balanced deposition surface. AuNPs strongly interact with the Sulphur (S) groups of the thiol-substituted sites of CuPcSu [384, 408], resulting in the formation of a quasi-3D multi-junction network with topology dictated from the NP nodes. The ultra-fine size of NPs makes size- and surface/interface-related effects of increased importance, rendering the metal-semiconductor interface an intrinsic feature of the nanosystem rather than an external contact to the macroscopic leads [379, 409].

The drop casting of linkers ensures the formation of extended band structure [410] in the close vicinity of the NPs, promoting electronic coupling among the Au nodes. The band alignment of constituents and the device schematics can be seen in Fig.6.19.

In order to evaluate the AuNPs-CuPcSu coupling and the electronic exchange reactions between the ligand and the Au nodes, we monitor the evolution of Surface Plasmon Resonance (SPR) peaks for different extent of surface modification of the AuNP nodes with CuPcSu molecules. Fig.6.20 demonstrates (a): the UV-Vis absorption spectra of citrate-stabilized AuNPs in water, (b), (c): AuNPs functionalized with CuPcSu ligands of progressively greater quantity, and (d): pure CuPcSu, and

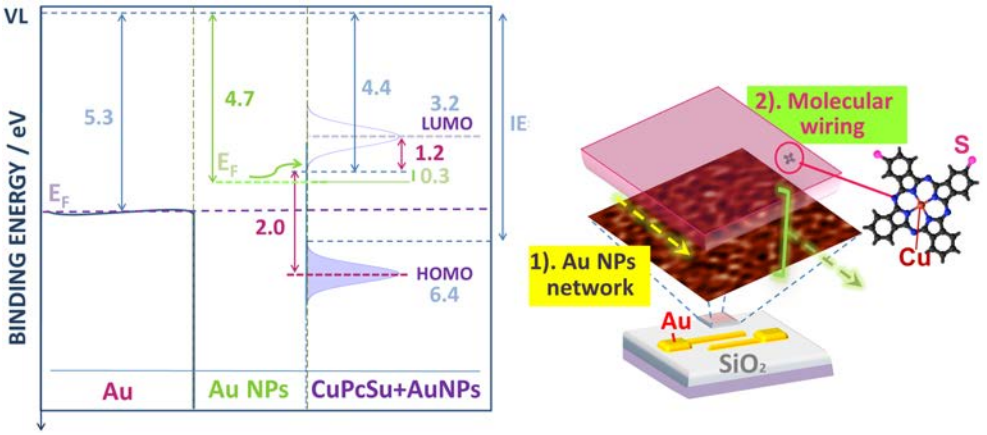


Figure 6.19: Energy levels at equilibrium (left) and schematics of the hybrid AuNPs/CuPcSu networks confined between nanodistant Au electrodes (right). The numbering indicates the sequence of formation of each layer. Arrows depict the net current direction across the structure.

provides evidence on the nature of electronic interactions between the molecular ligand and the AuNPs.

Citrate stabilized AuNPs hydrosol exhibits an absorption band around 520 nm, the characteristic peak of the SPR band of isolated spherical NPs. By increasing CuPcSu concentration in the Au hydrosol, the intensity of the first SPR band decreases along with the evolution of a second SPR band at longer wavelength (curves b and c). This broad second SPR band is indicative of aggregation of the NPs [411] due to the adsorption of CuPcSu on their surface. This band is generally broader and dumped with increasing ligand concentration.

Such changes have been related to the reduction of CuPcSu from the electron-rich AuNPs, most likely concerning reduction of the ligand part of the molecule [412, 413]. Curve (d) shows the absorption spectra of CuPcSu in butanol. Similarly to other metallophthalocyanines, its spectra in near UV and visible consists of two main bands: the Soret or B-band maximum at about 332 nm and a broader band in the visible region (Q band) at 600-700 nm, both related to the $\pi - \pi*$ transition [414].

Phthalocyanine itself is known to form aggregates in both aqueous solution and organic solvent with the extent of aggregation highly solvent and concentration-dependent [415]. Indeed, the Q band is split into a doublet, with a main peak at 665 nm, attributed to the CuPcSu monomer, and a satellite peak at lower intensity (621 nm). The peak at 621 nm is formed due to aggregation or dimerization, and results in the weakening of the main absorption band [416, 417, 418].

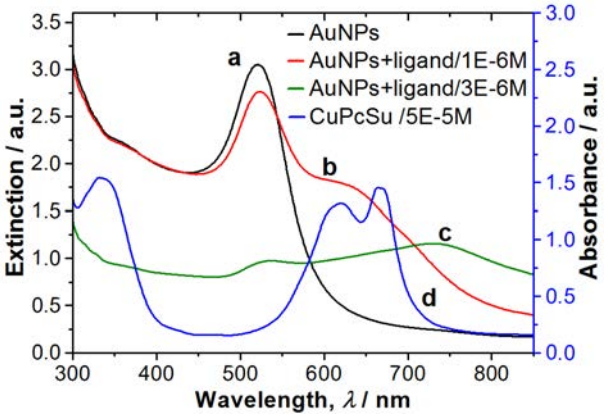


Figure 6.20: UV-Vis absorption spectra of (a) citrate stabilized AuNPs hydrosol, (b) AuNPs/CuPcSu ($1 \times 10^{-6}$M) sol, (c) AuNPs/CuPcSu ($3 \times 10^{-6}$M) sol, (d) pure CuPcSu ($5 \times 10^{-5}$M) sol in butanol.

In solid state the UV-vis spectra of CuPcSu films ($5 \times 10^{-5}$M) (Fig.6.21 Up) show a Q-band doublet consisting of two peaks centered at 620 and 678 nm, with the short wavelength peak being of high relative intensity comparing to the 678 nm main absorption band. The absorption arising from dimer and/or aggregate formation (620 nm) exhibits no significant energy shift when going from liquid to the solid state, indicating that some aggregates are already formed in solution. This agglomeration is what grants CuPcSu bulk-like properties (i.e. band structure formation) [399].

On the right part of Fig.6.21 deconvolution of the absorption band of AuNPs/CuPcSu composite provides retrieval of the CuPcSu Q-band doublet absorption peaks at 621 and 681 nm, enhanced via surface plasmon excitation in the nanoparticles [419], as well as the contribution of the AuNPs SPR peak. The latter is red shifted in comparison to the non-modified NPs resonance peak, indicating an enhancement of the interparticle coupling upon deposition of the CuPcSu molecular film [420].

Fine details regarding the nature of physical and chemical interactions as well as the electronic structure of both the hybrid network and its constituents can be resolved by means of XPS and UPS. XPS revealed no changes in the shapes and binding energies of the characteristic core level peaks of the composite comparing to the peaks of their isolated constituents. This involves the Au 4f doublet (84.2 eV and 87.5 eV), the C1s core level peak of CuPcSu (284.7 eV), the N1s peak of N in the pyrrole rings and the bridge positions of the molecule (398.9 eV) as well as the Cu2p3/2 core level spectra of the central Cu atom in its Cu(II) oxidation state (395.5 eV) and the S2p peak (168.0 eV).

This indicates absence of significant chemical interaction between the CuPcSu oligomers and the AuNPs and suggests that the AuNP nodes are only weakly interlinked (i.e. without the formation of covalent bonds).

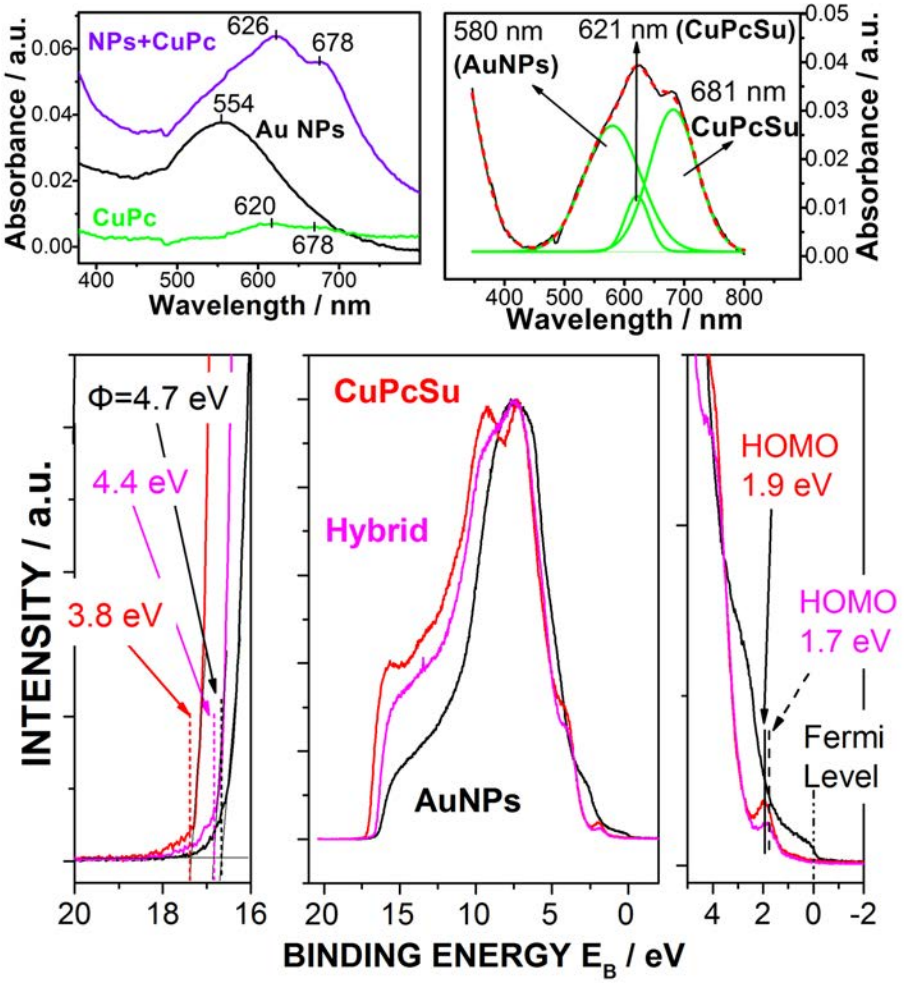


Figure 6.21: (Left): UV-Vis absorption spectra of PVD grown AuNPs on quartz, CuPcSu on quartz (from CuPcSu $5 \times 10^{-5}$ M butanol sol) and composite AuNPs/CuPcSu network. (Right): UV-Vis absorption of AuNPs/CuPcSu network and its deconvolution in elementary spectral absorptions. With dashed red curve: the result of fitting. (Down): Valence band spectra of CuPcSu molecular film (in red), AuNP-equipped $SiO_2$ (in black) as well as the hybrid (in pink). On the right: the region near the Fermi level in magnification and on the left: the high binding energy cut-off.

The main contribution on the Au valence band is the oxygen 2p peak at about 6 eV, indicating the strong coupling of the AuNPs to the under-

lying $SiO_2$. Near the Fermi region the 5s states at the Fermi level of Au are clearly visible. The work function of the AuNPs is measured at 4.7 eV, as expected for contaminated Au and taking into account that it concerns nanoparticles on silicon oxide a fact that reduces the work function [421] (The work function of bulk clean Au is typically 5.1-5.5 eV [422, 423, 424]).

Upon deposition of CuPcSu the work function of Au NPs is further reduced by 0.3 eV. This reduction applies on the CuPcSu-modified Au leads as well and enhances the electrode-network coupling via the creation of intermediate energy steps within the part of metal NPs and Au leads that touch the CuPcSu semiconducting ligand [425, 426]. The HOMO peak of CuPcSu, located at 1.9 eV, with an onset at 1.3 eV, is broadened and shifted by 0.2 eV towards lower binding energies upon interaction with the deposited AuNPs, while there is an increase of the work function value by 0.6 eV (see high binding energy cut-off).

Despite the fact that the main characteristics of the valence band of the molecular layer remain the same in the complex network, the above mentioned observables confirm the electronic interaction between AuNPs and CuPcSu. This interaction disrupts the initially isolated states of the molecule and it manifests itself as an interface dipole at the NP-CuPcSu interfaces and a system-specific charge modification [427, 428], resulting in an overall 0.3 eV change of the electrostatic potential. The distribution of the evaporated NPs on the substrate ($SiO_2$ - 80 nm) is depicted in the following AFM topographies (Fig.6.22).

The images show the formation of a dense network of discrete ultrafine AuNPs with a mean diameter of 1.4 nm. The scaling of the NPs with scanning area size confirms that they are not an artifact of the measurement [429].

## 6.6 Electron Transport through AuNPs/CuPcSu multi-junction networks

The Current-Voltage-Temperature (I-V-T) response of references containing i) only the linker molecules and ii) the bare AuNPs network, without addition of linker, under quasi-static (voltage staircase) field application is presented in Fig.6.23. In case i) the current flow through the system was insignificant with conductance below 0.07 pS for the 50 nm case and below 0.2 pS for the 25 nm electrode separation for all T.

CuPc is typically a wide bandgap semiconductor [430, 431] with carrier mobility strongly depended upon the amount of external doping, the presence of crystallinity and the amount of -stacking between monomers [432, 433]. Low zero gate voltage current in CuPc channel OFETs has al-

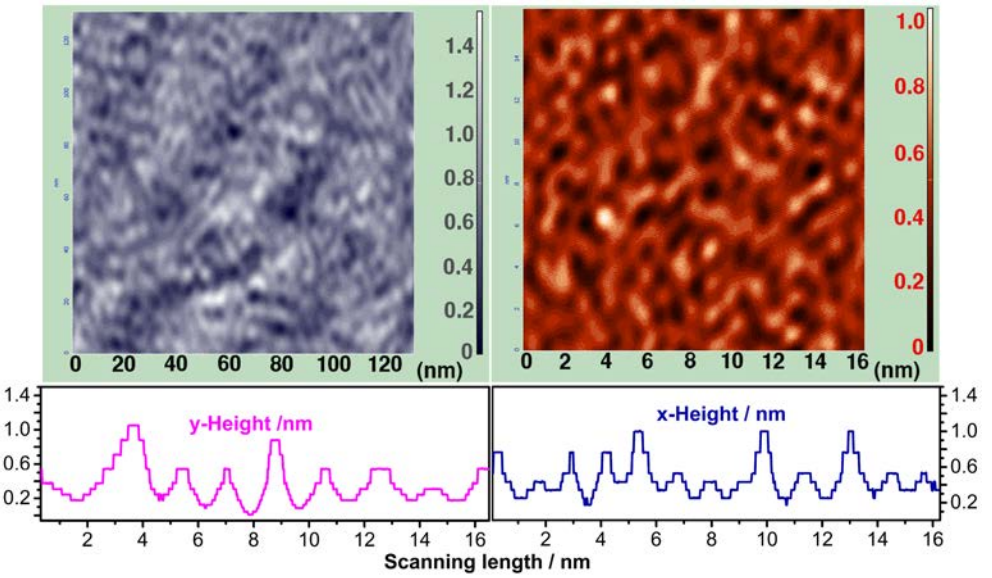


Figure 6.22: (Top): Representative AFM scans of AuNPs evaporated on the device active region in tapping mode. (Bottom): Cross section profiles of the higher magnification AFM image, highlighting the topography.

ready been established by several authors [432, 434]. In the present study the solution-processing-induced disorder of the film[435] and the rather loose van der Waals bonds among molecules prohibit effective overlap of the molecular orbitals and result in the localization of electrons in the phthalocyanine framework [436] and the observed poor conductivity of the plain CuPcSu molecular film.

The electric response of the network depends strongly upon the electrode distance. This happens because certain physical properties like the overall contact resistance, the percolation threshold, the static energetic disorder of hopping sites [437, 438] and the coupling to the environment [439, 440] change dramatically with array size.

For 50 nm (Fig.6.23a) transport is characterized by a T-dependent percolation threshold. The presence of this threshold is characteristic for disordered systems of NPs in the presence of collective Coulomb blockade effects [441, 442]. In this case the charging energy for an isolated AuNP is 1.029 eV, i.e. far above the thermal energy even at RT, therefore the exhibition of Coulomb gap is rather expected.

The mean energy level spacing ($\delta$) of a single NP node is 0.047 eV, so quantum charge fluctuations are suppressed up to RT. The Thouless energy for intragrain electron motion is 2.418 eV with electron life time within a single grain of 0.27 femtosec in RT. The dimensionless intragrain

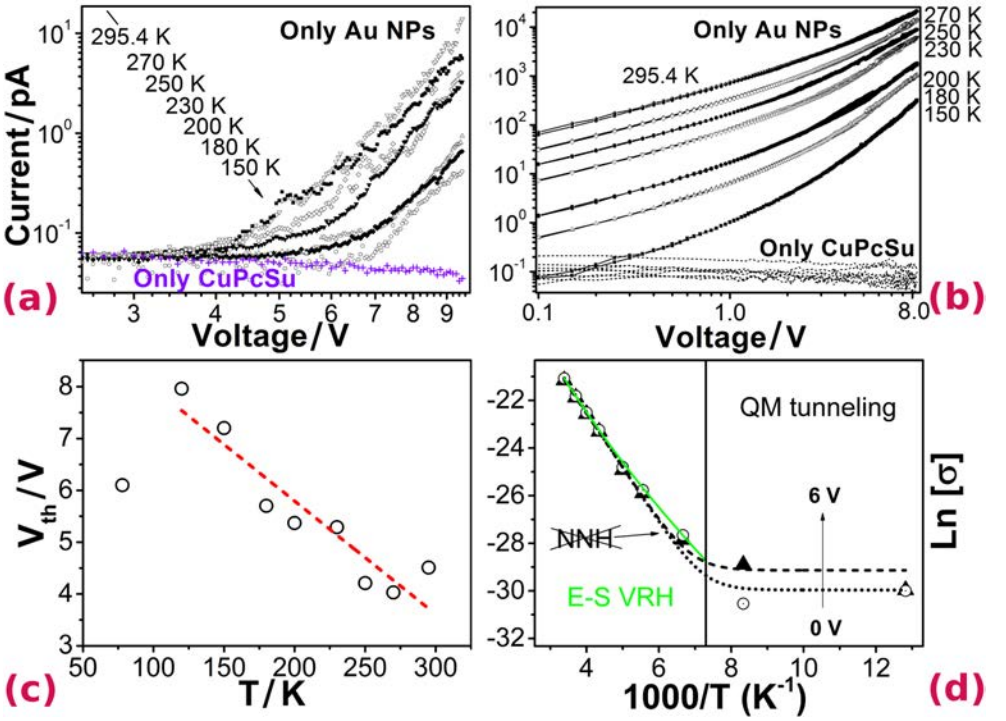


Figure 6.23: Double logarithmic plot of I-V characteristics for planar nanoelectrodes of (a): 50 nm and (b): 25 nm inter-electrode distance. Picture (c) depicts a tendency for linear increase of the conduction threshold as T recedes for the 50 nm case. (d) Arrhenius representation of I-V-T data concerning 25 nm-distant nanoelectrodes depicting the dominant transport mechanisms for low and intermediate voltages.

conductance, $g_0$, is 51.31>1 while the tunneling (intergrain) conductance is much smaller ($g_0 >> g_T$) for all samples. Indicatively, for the non-linked networks $g_T$ is of the order of 0.02 and $4.25 \times 10^{-9}$ for the 25 and 50 nm respectively, both <<1.

The conductance of the system is given by $g_T^{-1} + g_0^{-1} \simeq g_T^{-1}$, thus, the electrons are always localized and the main contribution to macroscopic resistivity comes from the tunneling barriers between NPs [443].

The I-V curves of Fig.6.23b scale according to $((V - V_{th})/V_{th})^{\zeta}$, where $V_{th}$ is the voltage threshold above which conduction occurs [444]. $V_{th}$ decreases linearly with increasing T, in accordance to [445], except a deviating behavior at 78 K (Fig.6.23c). This power law is understood in the framework of collective charge transport in arrays of metal quantum dots, proposed by Middleton and Wingreen [446], and is related to the progressive opening of conduction channels or, when talking for low voltages and T>0, to sequential tunneling along branching paths [447].

The exponent $\zeta$ is related to the dimensionality of the NP array. In our case $\zeta$ has been found to have a temperature-independent value of 6.8±0.6, suggesting that transport takes place in all 3 dimensions [441].

According to Tran et. al. $\zeta$ can be used to derive the number of junctions, j, participating in the cotunneling events via $\zeta$=2j1 [447]. So here j=4. A typical Arrhenius representation in the region below the voltage threshold (i.e. within the Coulomb blockade regime) shows T-independent conduction below 150 K, indicative of quantum mechanical (QM) tunneling (see Fig.6.24).

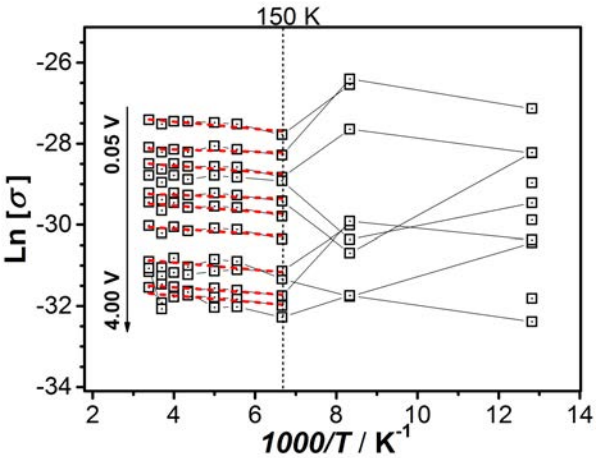


Figure 6.24: Arrhenius plot of I-V-T data concerning parallel overlapping 50 nm-distant nanoelectrodes.

A thermal trend for T≥150 K corresponds to activation energy of solely 8 meV, a value much smaller than the energy expected for hopping conduction (NNH, $\sigma = \sigma_o exp[(_a/(k_B T))]$ [448]). This suggests that dominant electronic processes occur in a very narrow energy band, around the Fermi level [449].

The evident lack of significant temperature dependence for long arrays can be associated with very weak interparticle coupling [450]. The electronic wave functions of the involved states reside in the close vicinity of the Fermi level, localized near the NP surface [451] and are essentially acting as traps.

When the interelectrode distance decreases to 25nm the threshold disappears and conductance is significantly enhanced (Fig.6.23b). Non-linearity of I is increased with decreasing T, while the T dependence at low bias tends to merge into a less T-dependent high bias. The behavior seen in Fig.6.23b resembles that of short parallel conduction paths, each retaining a strongly temperature-dependent prefactor in conductivity as opposed to the weaker linear T dependence of Vth for 50 nm [447].

A typical Arrhenius representation (Fig.6.23d) shows that experimental data can be well described in terms of inelastic cotunneling, having the same functional form for temperature dependence as Efros-Shklovskii (E-S) type Variable Range Hopping (VRH) [445], for intermediate T and QM tunneling for even lower T values.

More specifically, for T below 150 K suppression of temperature-activated mechanisms facilitates observation of the underlying QM tunneling current (right part of black lines). In the region [RT, 150K] conductivity falls in the case of E-S law $\sigma(T) \sim exp(T_0/T)^{1/2}$, corresponding to strong electron interactions and formation of a Coulomb gap [452]. The characteristic temperature, $T_0$, is a parameter related to the localization length $\xi$ when only long-range Coulomb interactions are present [452] and is calculated as $T_0$=64516 K.

Using this value of $T_0$, $\epsilon$=1 (considering vacuum as interparticle medium) and the relation $\xi = 2.8e^2/(k_B T_0 \dot{4}\pi\epsilon_0\epsilon)$ [453], we obtain $\xi$=0.7 nm. This lower-than-the-NP-size localization length points to the importance of strong on-site Coulomb repulsion [454]. Coulomb repulsion strongly localizes conduction electrons, causing the observed insulating behavior below 150 K [454]. Under such temperatures conduction is essentially carried out via QM tunneling. The electron hopping length explicitly depends on temperature, with the co-tunneling distance approaching that of a single junction at sufficiently high temperatures [455].

This point, indicating the crossover to simple activated Arrhenius behavior, is suppressed up to ~400K for our structure, in contrast to the commonly encountered thermally activated electron transport at RT for such systems [456]. After the incorporation of CuPcSu linkers V was kept below 3 Volt in order to avoid local overheating and/or overstressing of the organic bridges and to ensure smooth functioning of the linker under multiple I-V cycles. Fig.6.25 shows the I-V-T data after the addition of CuPcSu linker molecules.

The addition of CuPcSu linkers caused a dramatic increase of approximately 5 orders of magnitude on the amplitude of conduction current, demonstratingprobing an excellent n-type semiconducting linker. Charge is transferred from the AuNP dopant to the CuPcSu layer, since the Fermi level of Au NPs in contact to the molecular film is spaced only 1.2 eV below the CB distribution maximum (in contrast to the 2.0 eV spacing from the VB maximum), which is equivalent to say we have an extrinsic n-type semiconductor.

The concept of n-type doping of originally p-type semiconducting linkers through the utilization of metal NPs (metal NP doping-induced Fermi level shift) has been reported before [457, 458]. The mixing of the $\pi$ molecular orbitals with NP states [459] are believed to be responsible

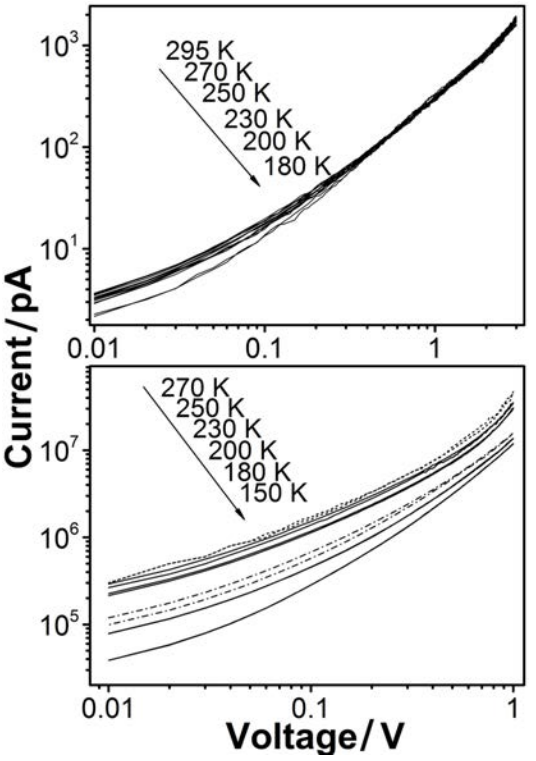


Figure 6.25: I-V characteristics for contacts with inter-electrode distance of (Top): 50 nm and (Bottom): 25 nm. The I-Vs concern networks of evaporated NPs post-functionalized with CuPcSu linkers drop cast ($5 \times 10^{-5}$ M) under $N_2$ conditions.

for this electronic coupling. In fact, the electronic interaction of CuPcSu oligomers with Au atoms can lead to the formation of conduction pathways with many different ways, depending mainly on the strength and nature of their coupling [448, 460, 461] as well as the existence of disorder due to kinks, cross-links and impurities [462].

For in-plane transport across the 50 nm arrays all I-V traces are approaching the same power-law behavior with exponent close to 2, merging onto a single trace for high V. This later dependency is typical of sequential tunneling along branching conduction paths [446]. Thermally activated conduction occurs only well above 2 V with the thermal range of occurrence expanding with increasing voltage (see Fig.6.26).

As with the non-linked NPs, the deduced mean activation energy is of the order of 8 meV, a value witnessing the lack of significant temperature dependence for the long arrays. Transport is being carried out via sequential tunneling around the level of chemical potential for all examined temperatures, a fact associated with the still weak (as in the bare

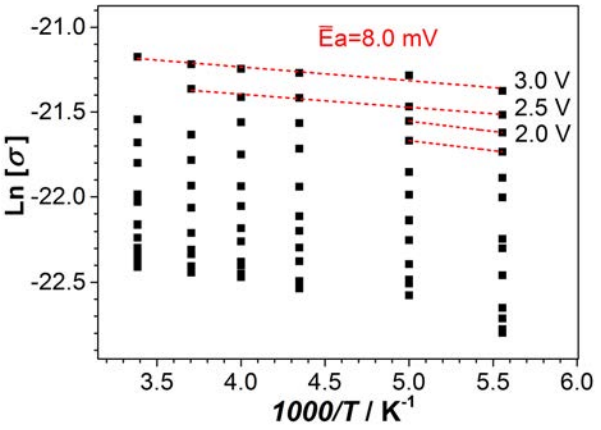


Figure 6.26: Failure of the Arrhenius scheme for the CuPcSu-modified networks of 50 nm distance.

networks) interparticle coupling.

Moving to the 25-nm arrays (Fig.6.25 bottom) the decrease of temperature results in lower J and an increasing deviation from Ohmic behavior. Again, T-dependent behavior at small bias merges into a less T-dependent high bias. Interestingly, for both distances, the transport current yields power-law relations with both T and V. A generalized temperature dependence model of the form [463, 464]:

$$J = J_o \dot{T}^{1+\alpha} \dot{s}inh(\gamma \frac{eV}{kT}) |\Gamma(1 + \frac{\alpha}{2} + i\gamma \frac{eV}{\pi kT})|^2 \qquad (6.1)$$

, which was originally derived for dissipative tunneling in a biased double-well quantum system [463], is found to predict the current response of the composite networks. The parameter $\alpha$ is the dimensionless friction coefficient of the system, related to energy dissipation during transport; while , originally equal to 1 in the model problem[463], functions here as a weight function. It accounts for the percent of voltage drop on each tunnel junction [464] and is, thus, related to the number of tunneling barriers. [85]

When the scaled density $J/T^{1+\alpha}$ is plotted against the dimensionless parameter eV/kT, a universal curve is obtained (see Fig.6.27) described by Eq.6.1 [463, 465].

More specifically, the region of low V (kT>> eV), yields a $J \sim T^{\alpha}$ dependence with $\alpha$=0.7 for the 50 nm spacing and $\alpha$=3 for the 25 nm; while for higher V and/or low T (kT<<eV) the T dependence becomes weaker and there is a $J \sim V^{\beta}$ dependence from voltage. With these fixed values of $\alpha$, the scaled current density $J/T^{1+\alpha}$ is calculated for each T. All scaled $J/T^{1+\alpha}$ vs eV/kT curves collapse in one universal curve,

characteristic of the network.

In this picture, the system is in a state of weaker localization [466] (than in the case of non-linked AuNPs). Indeed, the dimensionless tunneling conductance is $g_T = 3.90 \times 10^{-7} - 1.34 \times 10^{-6} << 1$ for the 50 nm sample and $g_T$=0.033-0.099<1 for the 25 nm sample, indicating that the systems are still in a weak coupling state.

The value of $\alpha$ is essentially a measure of the coupling strength of the system of quantum wells to a bath of oscillators assumed to have an Ohmic spectrum (representing the dissipation of leads) [463], and can be used as a measure of disorder [463, 466]. The fact that $\alpha$ increases when the interelectrode spacing becomes smaller can be associated with the opening of extra conduction channels leading to a more complex thermal interaction with the electrodes.

Similar to the non-linked 25-nm array this can be interpreted in terms of short independent channels acting in parallel [447]. Fig.6.27 shows the scaled current density as a function of the dimensionless parameter eV/kT exhibiting universal behavior for all T. Nonlinear regression analysis of the normalized (i.e. scaled) graphs results in a value of $\gamma$=0.077 for the 50 nm spacing and $\gamma$=0.050 for the 25 nm. The resulting best fit is quoted in green together with the scaled data.

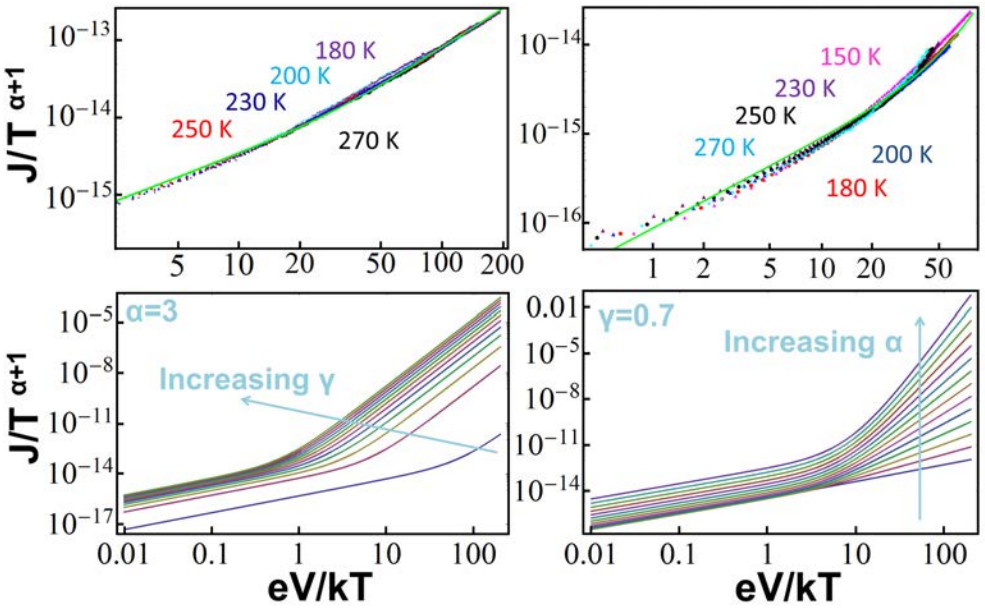


Figure 6.27: Scaled $J/T^{1+\alpha}$ curves with $\alpha$=0.7 for 50 nm arrays (Left) and $\alpha$=3 for 25 nm arrays (Right) vs eV/kT, collapsing in one universal curve. The green line is the generated $J/T^{1+\alpha}$(eV/kT) curve. At the bottom: Influence of the and parameters on the $J/T^{1+\alpha}$ vs eV/kT universal scaling curve.

The inverse of $\gamma$ is related to the number of tunneling barriers involved in sequential tunneling between the contacts [464, 467]. In our case $1/\gamma$=13 for the 50-nm-long networks and is increased to $1/\gamma$=20 for the 25-nm-long networks, indicating opening of more independent conduction channels [468] or branching of existing channels [446, 447] (contributing extra tunneling junctions) for the shorter distance. This is in accordance to the results for the values of $\alpha$. Field-driven behavior for larger applied bias [469] for the 25- nm spaced electrodes is discussed in Subsection 6.6.1.

The influence of $\alpha$ and $\gamma$ parameters on transport is clarified at the bottom of Fig.6.27. Decrease of the number of involved molecular junctions (i.e. increase of the value of $\gamma$) results in increased current, moving the inflection point towards progressively lower energies. Increase of the value of $\alpha$, i.e. increase of the disorder [463, 466], results in enhancement of the non-linear response and the overall current density.

### 6.6.1 Electron Transport under high fields

It can be observed that, under high field application, the universal scaling scheme begins to falter. As already seen in Fig.6.27, there is a deviation of the experimental I-V data above 200 K and high voltage from the universal scaling law curve in the case of 25 nm spaced nanoelectrodes. Under high fields the most-common conduction mechanism through insulating mediums is tunneling [73].

It can be confirmed from Fig.6.28 that this is exactly the regime (i.e. above 200 K) in which we have occurrence of F-N tunneling (linear negative slope part of graph). The observed weak temperature dependence of the amplitude of FN tunneling current is consistent with the change of the Fermi level of the Au cathode with temperature [470].

Both CuPcSu-linked and plain AuNPs are quoted in Fig.6.28 to enable comparison of the mean potential barrier and thickness of these effective barriers for tunneling between the NP nodes. The temperature of 230 K is selected as the lowest temperature of F-N exhibition for the interlinked networks.

The fitting curve depicted in Fig.6.28 is the result of non-linear regression fitting of a three voltage region model function, that incorporates low voltage (Ohmic), intermediate (tunneling through a trapezoidal barrier) and high voltage (F-N tunneling through a triangular barrier) tunneling according to the corresponding Simmons's formulas [52]. The total current is expressed as a linear combination of weighted functions each representing one of the above conduction mechanisms via the equation:

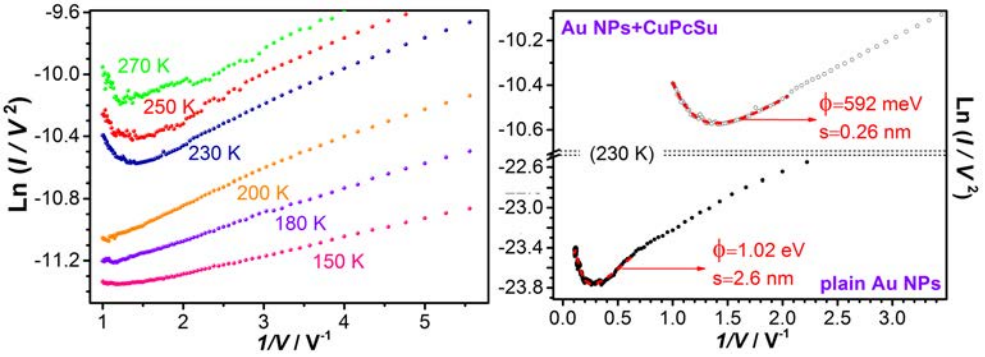


Figure 6.28: F-N representation for overlapping contacts configuration with a distance of 25 nm for the samples with evaporated NPs after addition of CuPcSu linker molecules ($5 \times 10^{-5}$ M) drop cast under $N_2$ ambient.

$$
\begin{aligned}
J_{total} = C_1 \cdot J_{L1} \cdot \bar{\phi}^{1/2} \cdot V \cdot exp\left[ -A\bar{\phi}^{1/2}) \right] + \\
+C_2 \cdot J_{L2} \cdot \left\{ (\bar{\phi} - \frac{eV}{2}) \cdot exp\left[ -A(\bar{\phi} - \frac{eV}{2})^{1/2} \right] - \right. \\
\left. -(\bar{\phi} + \frac{eV}{2}) \cdot exp\left[ -A(\bar{\phi} + \frac{eV}{2})^{1/2} \right] \right\} + \\
+C_3 \cdot J_{L3} \cdot V^2 \cdot exp\left[ \frac{-2A \cdot \bar{\phi}^{3/2}}{3e} \cdot \frac{1}{V} \right] + J_o
\end{aligned}
\tag{6.2}
$$

, with $J_{L1} = [3 \cdot (2m)^{1/2}/(2s)] \cdot (e/h)^2$, $A = (4\pi s/h) \cdot (2m)^{1/2}$, $J_{L2} = [e/(2hs^2)]$, $J_{L3} = (2.2 \cdot e^3)/(8h\bar{\phi}s^2)$ and $J_o$ any leakage current contributing as offset. The $C_1$, $C_2$, $C_3$ constants are the weight factors of each electronic transport mechanism contribution.

Graphical investigation of the above equations pointed out that the value of the parameter a=10.235 $\cdot\sqrt{\bar{\phi}}\cdot$s incorporating the values of inter-electrode material thickness, s, and mean potential barrier, $\bar{\phi}$, where $\bar{\phi}$ is expressed in eV and s in nm, should be >2 for physically meaningful current response at low and intermediate fields. The generated I(V) curve is a smooth function that reproduces the experimental data in the region within and close the F-N regime ensuring compatibility of the mean potential barrier height and width across the transition regions.

On the basis of the conventional tunneling picture the inflection in the F-N plot is attributed to the transition from a direct to F-N tunneling transport. However, materials containing weakly coupled nanostructures, such as these hybrid networks, display large insulating gaps and

flat bands, and the effective mass approximation often fails when moving away from the band edges. An alternative explanation is given by the resonant molecular model [471].

On this basis, the entering of the NP charging level peak or the entering of the HOMO peak of the AuNPs-modified molecular linker into the bias window at the turning point sharply enhances the magnitude of electric current, resulting in the inflection. Thus, the potential barrier obtained in Fig.6.28 for the non-linked NPs network corresponds to the charging energy of the NPs increased by a factor owing to the poor coupling coefficient with the nanoelectrodes.

In the case of NPs interlinked with CuPcSu oligomers this barrier value drops by ~0.4 eV. This is in agreement with the work function reduction of the hybrid network when compared to the NPs template, which is estimated at 0.3 eV from the high binding energy cut-off of UPS spectra (Fig.6.21). Regarding the effective thickness of the interparticle barrier for resonant tunneling, this is estimated to 2.6 nm for the non-linked nanoparticles and is significantly reduced down to 0.25 nm when the nanoislands are molecularly wired.

### 6.6.2 On the nature of the universal scaling of temperature-normalized I-V characteristics

The scaling collapse observed in the hybrid AuNPs/CuPcSu networks is commonly advocated as evidence for tunneling in Luttinger liquid, a theoretical model describing interacting electrons in semi-infinite one-dimensional systems. Nevertheless, the fact that the I-V-T characteristics are described by Eq.6.1 is not sufficient condition for the existence of Luttinger liquid. Moreover, in our case the fabricated networks are not really 1-D since, as the encountered E-S law shows, conduction occurs via 2 or even 3 dimensional pathways.

In fact, since tunneling current is the convolution of the tunneling probability and the density of states, the observed scaling could as well originate from a power-law scaling of the first [472]. Indeed, in the original derivation of Eq.6.1power-law scaling was assigned to tunnel probability, due to coupling of the system with an (unspecified) environment [463].

### 6.6.3 Coulomb oscillation on the NP nodes

In the bare NP networks the discreteness of charge transfer within the Coulomb blockade regime causes the oscillating behavior of tunneling current [473]. Conduction proceeds via tunneling through the interparticle barriers. The dominant I-V oscillations have a well-defined periodicity

(Fig.6.29b), indicating that a single NP limits the conductance. Nevertheless, the presence of additional NPs gives rise to beating effects present as a shoulder on the main sawtooth signal [474].

In principle, due to the very small size of the evaporated AuNPs (diameter of 1.4 nm), with $E_c$=1.026 eV and $\delta$=0.047 eV, it would be possible to observe Coulomb-blockade-related effects and quantum fluctuations of charge even at RT. The V where Coulomb blockade effects should be expected are below 1.4 V for an electrically gated single metallic dot of this radius, but can become orders of magnitude larger in the case we have a system of many capacitive structures in series.

When the NP array is biased through a voltage ramp of constant rate (dV/dt) then at Q≥e/2 tunneling will be allowed in the available states of a non-charged NP, resulting in an observable increase of the current flowing through the structure. Q will now fall to e/2, resulting in the descent of I till a new charging cycle begins. This leads to the oscillation of the current in a saw-tooth manner, with fundamental frequency equal to (dV/dt)C/e, i.e. directly proportional to the V alteration rate. This is demonstrated in the I-Vs of Fig.6.29.

These oscillations are not evident when the system is biased in a quasi-static manner, but can emerge when a voltage ramp dV/dt is used. The voltage variation causes oscillations which are due to sequential tunneling events in a similar manner as those observed when electrons travel through a series of quantum dots. The effect is known as single-electron turnstile pumping and has been demonstrated by applying alternative voltage on a side gate [475, 476, 477].

As expected, the oscillation frequency, owning to single NPs, remains practically the same if one doubles the length of the array from 25 to 50 nm. From Fig.6.29 the oscillation period, expressed as a voltage interval, is estimated to be $\Delta$V=380 mV, corresponding to an oscillation frequency of f=0.26 Hz for the a=0.1 V/s ramping rate. Thus, the self-capacitance of a single NP is estimated at $2.11 \times 10^{-19}$ F. This corresponds to a diameter of 1.9 nm, close to the AFM estimation of 1.4 nm for the AuNP size (Fig.6.22) and points to the electrical isolation of as-grown NPs. As seen in Fig.6.29 this oscillating behavior is superimposed onto a collective Coulomb blockade behavior, in accordance to the quasi-static case depicted in Fig.6.23a.

Transport is again characterized by the presence of a percolation threshold, indicative of a collective Coulomb blockade behavior. For relatively low applied V the tunnel multi-junction is pinched off, while for high V values the conductance approaches its ohmic value. In between these two extreme cases oscillations are observed [478]. Current is higher for smaller distance leads since the transmission probability through the

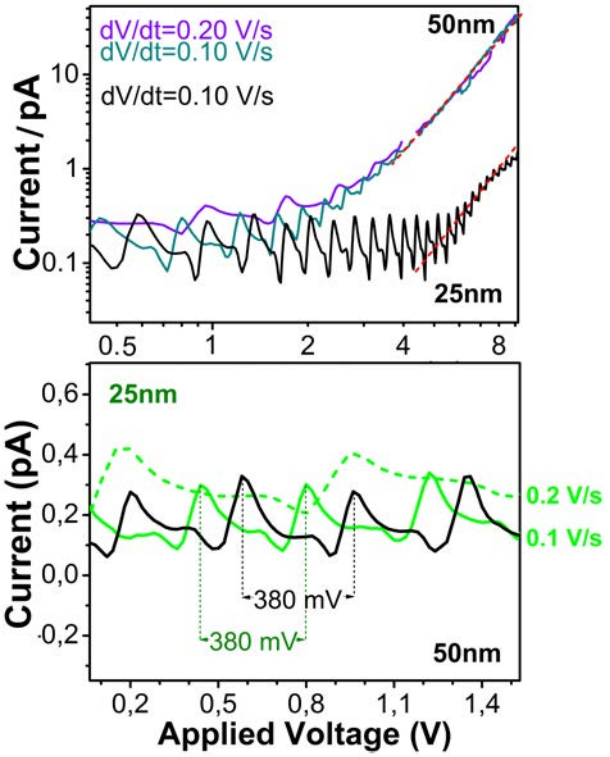


Figure 6.29: Ramp rate I-V characteristics at 78 K for NP arrays without addition of CuPcSu linkers, exhibiting Coulombic oscillations. The lower panel highlights in double linear axis the independence of the oscillation frequency from the size of the array and the possibility of probing higher energy charging levels upon increasing the voltage alteration rate to 0.2 V/s.

array decreases inversely with length [479].

### 6.6.4 The role of the molecular linker

Although XPS analysis revealed absence of significant chemical interaction between the CuPcSu oligomers and the AuNPs (Fig.6.10), suggesting that AuNPs are only weakly (i.e. not covalently) interlinked, a 0.3 eV work function reduction was detected in the Au UPS spectrum (Fig.6.21). This means that, upon deposition of CuPcSu, the work function of Au NPs is further reduced by 0.3 eV and that, naturally,this reduction also applies on the CuPcSu-modified Au leads.

On one hand, lower work function is equivalent to the increase of the overall conductivity of the network while, on the other hand, it enhances the electrode-network coupling via the creation of intermediate energy steps that couple bulk Au inside the electrodes to the electronic states of

Au NPs that are not in direct contact to the drop cast CuPcSu linkers. The result is a boost in carrier injection efficiency from the Au leads towards the complex network or, equivalently, electrode-network coupling enhancement.

Accordingly, the broadening and shifting of CuPcSu HOMO towards lower binding energies along with the increased value of its work function indicate the electronic interaction between AuNPs and CuPcSu, monitored as an interface dipole at the NP-CuPcSu interfaces and a system-specific charge modification, resulting in an overall 0.3 eV change of the electrostatic potential. This suggests that the molecule is electrostatically coupled to the NPs, presumably due to dipole-dipole interactions.

These interactions are strong enough to result in the electronic linkage of NPs and in the relative delocalization observed through the enhanced conductivity of the electrical measurements. The dramatic increase of approximately 5 orders of magnitude on the amplitude of conduction current points to an excellent n-type semiconducting linker.

Charge is transferred from the AuNP dopant to the CuPcSu layer rendering the molecule an extrinsic n-type semiconductor. This concept of n-type doping of originally p-type semiconducting linkers through the utilization of metal NPs (metal NP doping-induced Fermi level shift) has been reported before [457, 458] and is attributed to the mixing of the $\pi$ molecular orbitals with NP states [459].

Furthermore, FTIR investigation (see Appendix Section 8.5) also indicated evidence of electronic interaction affecting certain CuPcSu vibrational modes between linkers and NPs.

Regarding the issue of non-detection of disruption in the core level peaks via XPS this does by no means imply absence of electronic exchange between the molecules and the AuNPs. Indeed, it has been shown via ab-initio calculations [428] that the metal atom of phthalocyanines is able to act as an electron provider to the ligand, exhibiting minimal influence in the molecular orbitals.

Moreover, it has been confirmed from UV-Vis measurements that CuPcSu molecules couple to the Au nodes by means of reversible red-ox reactions. Under voltage application, the AuNP nodes play essentially the double role of both donor and acceptor. They accept electrons that are removed from the charge-bearing orbitals of CuPcSu under the generated field force, acting as an electron sink, and they donate electrons to available charging states (i.e. the Cu(II) states of the metal center) of the molecular linkers promoting, thus, electron transport.

This scheme is straight forwardly deduced from Fig.6.19, where the UPS observables are schematically depicted. Due to the high CuPcSu density in the drop cast film this mechanism is quite efficient, leading to

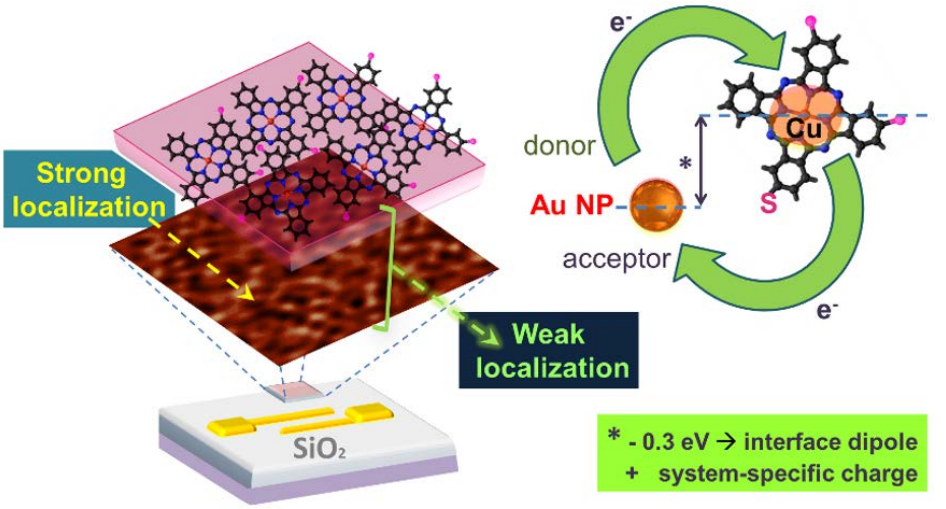


Figure 6.30: Weak localization through CuPcSu addition. The scheme of bi-modal functionality of Au NPs in the hybrid Au NPs/CuPcSu network as both donor to the Cu(II) states of the CuPcSu metal center and acceptor (i.e. electron sink).

the recorded 5-orders-of-magnitude increase of conduction current.

Going further, one should take in mind that current carrying molecular junctions have both electron and phonon contributions to the current flux and that thermal electronic excitation and local electrical heating of molecules drastically influence transport mechanisms [480, 481] even at low applied voltages. Therefore, higher-than-ambient I-V characteristics of the molecular linker are a useful way of probing thermally-activated processes involved in conduction.

This investigation is performed on barium borosilicate glass substrate (obtained from Corning) equipped with interdigitated overlapping Au electrodes of 4.4 mm overlap and 50 $\mu$m separation in order to maximize the probed area.

Double staircase I-V characteristics for temperatures ranging from 0 to 30 °C for a thin CuPcSu layer spin coated on the barium borosilicate substrate is presented in Fig.6.31a. The black curve is obtained after I-V-T stress cycles at temperatures up to 60 °C.

In Fig.6.31b Double staircase I-V characteristics of the same film and substrate for temperatures from 20 to 60 °C can be observed. Again, the black curve is obtained after I-V-T stress cycles at temperatures up to 60 °C.

Ahhrenius type representation of the above characteristics indicates the presence of two different thermally activated conduction processes

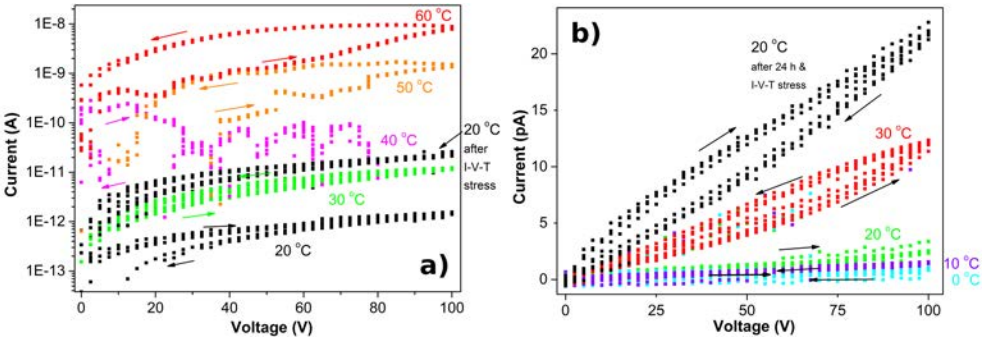


Figure 6.31: Double staircase I-V characteristics for a spin coated thin CuPcSu film on interdigitated overlapping Au electrodes.

with activation energies 1.7 eV and 243 meV respectively. As can be observed in Fig.6.32 the temperature of 20°C is the crossover temperature between the two conduction regimes. As discussed by Nakada et al in [482] such a change in the slope of the Ahhrenius diagrams pointing to such differences in activation energy stems from a change from extrinsic to intrinsic conduction. This implies existence of additional carriers with electronic states within the gap which may be easily excited and act as impurity.

The presence of filled electronic states localized in the band gap has already been predicted theoretically by Hamann and Lehmann [483, 484] for thin films as well as for the crystalline surface of copper phthalocyanine (CuPc). These states are attributed to surface lattice defects of high concentration.

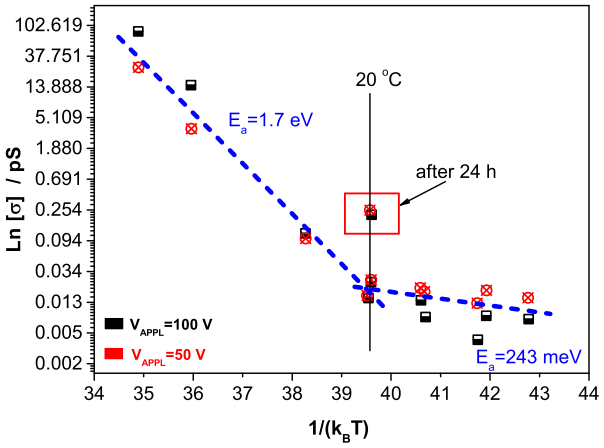


Figure 6.32: Ahhrenius type representation for a spin coated thin CuPcSu film on interdigitated overlapping Au electrodes.

Sussman [485] has reported that the distribution of trapping sites in CuPc is altered by annealing. Oxygen causes distribution of trap levels altered by annealing, giving two distinct activation energies. The role of adsorbed oxygen is to create carriers and to act as impurity in the extrinsic conduction region. In the case of phthalocyanines, oxygen is bound much more tenaciously with the binding energies being unequal in the two conduction regimes. Notice that heat treatment in air or vacuum does not remove oxygen completely.

### 6.6.5 Impact of linkers on the electronic lifetime & the electron localization within NPs

#### 25-nm Electrode Spacing

Even at 294.5 K the mean conductance of the 25 nm sample in the low voltage [0,1] regime is $1.03 \times 10^{-5}$ S and, therefore, lower than the quantum conductance ($R_Q = 2e^2/h = 7.7 \times 10^{-5}$ S). Thus, in general exhibition of Coulomb blockade for low T and V is expected for these contacts. The value of special conductivity is 412.36 S/m (note that the special conductivity of bulk Gold is $4.10 \times 10^7$ S/m). From this value the dimensionless tunneling conductance: $g_T$=0.021176 <<1. This value is indicative of weak coupling between the grains and insulating behavior.

In general, the grain (intragrain) conductance is much larger than the tunneling (intergrain) one ( $g_o >> g_T$). Indeed, in our case $g_o$=51.31>>-$g_T$=0.02.

The conductance of the entire system is given by $g_T^{-1} + g_o^{-1} \approx g_T^{-1}$, that is equivalent to say that the drop of applied electric potential occurs only inside the tunnel barrier. The ratio of the grain conductance and the tunneling conductance is 2566. Thus, the main contribution to macroscopic resistivity comes from the contacts between the grains.

The localization length, $\xi$, has already been found to be 0.7 nm < $d_{NP}$=1.4 nm (see (Fig.6.23d)) indicating strong onsite Coulomb repulsion. The width of the smearing of the energy levels in the grains $\Gamma = g_T\delta$= 0.998 meV. The mean electronic lifetime within the granule (i.e. inside a NP) is given from $\hbar/(g_T\delta)$=$L^2/D_{eff}$ = 0.66 psec.

After CuPcSu addition at 294.5 K the minimum conductance of the 25 nm sample in the [0, 1] V is $1.6 \times 10^{-5}$ S, so still lower than $R_Q$. The special conductivity is 640 S/m. Regarding the dimensionless tunneling conductance we get : $g_T$= 0.032865887<<1. The value is again indicative of weak coupling between the grains and insulating behavior for all temperatures. $\Gamma = g_T\delta$= 1.548916 meV.

The mean electronic lifetime within the granule (NP) is given from $\hbar/\Gamma$=0.42495 psec. The ratio of the grain conductance and the tunneling

conductance is $1.56 \times 10^3$. Thus, the main contribution to macroscopic resistivity comes from the contacts between the grains.

### 50-nm Electrode Spacing

At 294.5 K the mean conductance of the 50 nm sample in the [1, 8] V regime is $1.7 \times 10^{-13}$ S $<<$ $R_Q$, thus we have exhibition of Coulomb blockade for all T and low V. The special conductivity is 3.4 $\mu$S/m. The dimensionless tunneling conductance is: $g_T = 4.25 \times 10^{-9} << 1$ and is indicative of very weak coupling between NPs and insulating behavior for all temperatures. $\Gamma = g_T\delta = 2.00 \times 10^{-7}$ meV. The mean electronic lifetime within the granule (NP) is given from $\hbar/\Gamma = L^2/D_{eff}$=3.29 $\mu$sec. In this case$g_o = 51.31 >> g_T = 4.25 \times 10^{-9}$.

The ratio of the grain conductance and the tunneling conductance is $1.21 \times 10^{10}$. So again, as for the 25 nm case, the main contribution to macroscopic resistivity comes from the contacts between the grains. Since for all cases g$<<$1, electrons remain localized inside the grains.

After CuPcSu addition at 294.5 K the min conductance of the 50 nm sample in the [0, 1] V is $1.9 \times 10^{-10}$ S $<<R_Q$. The special conductivity is 3.8 mS/m. For the dimensionless tunneling conductance we obtain: $g_T = 3.90282 \times 10^{-7} << 1$. This value indicates perseverance of weak coupling between the grains after deposition of linker and insulating behavior for all examined temperatures.$\Gamma = g_T\delta = 1.839 \times 10^{-5}$ meV. The mean electronic lifetime within the granule (NP) is given from $\hbar/\Gamma$=35.785 nsec. The ratio of the grain conductance and the tunneling conductance is $1.56 \times 10^3$. Thus, the main contribution to macroscopic resistivity comes from the contacts between the grains.

In short, electron states within single NP grains are always localized, even at RT. For both the wide (w = 50 nm) and narrow (w =25nm) contacts the tunneling resistance is quite high $R_T > R_Q$ and samples exhibit charge localization and Coulomb Blockade regime.

For the highest $R_T$ (50 nm) Coulomb blockade is displayed at all temperatures, while for the lower $R_T$ (25 nm and linker-modified arrays), samples exhibit a proper Coulomb Blockade regime only for temperatures equal to or below 150K. The observation of discrete energy levels requires that both quantum charge fluctuations and thermal fluctuations be suppressed. The elimination of quantum charge fluctuations requires that the total device resistance (R) be large compared to the quantum resistance of a single charge $R_Q$.

### 6.6.6 Transport in the limit of weak coupling-sequential tunneling & electron co-tunneling

The dominant transport mechanism in the system is greatly influenced by the size of the array which affects the overall coupling strength and percolation threshold:

#### 25-nm Electrode Spacing-no Linkers

Transport is carried out via QM tunneling at low temperatures (T-independent transport), and inelastic co-tunneling (with the same functional form for temperature dependence as ES VRH) in the intermediate temperature regime up to RT. The crossover temperature between QM tunneling and inelastic co-tunneling is $T_{C1}$=180 K.

According to the emerging law for the temperature dependence of the E-S hopping distance [486] NNH is expected to be taking over as the dominant transport mechanism after approximately $T_{C2}$=400 $^oC$ (2d crossover temperature, not experimentally reached). To conclude, transport across the full array at temperature higher than 180 K occurs via a sequence of co-tunneling events, each involving a few particles, up to 4, depending on temperature.

#### 50-nm Electrode Spacing-no Linkers

We get a Coulomb blockade regime for low/intermediate voltages followed by non-linear transport above the conduction threshold. Within the Coulomb gap there is a transition from T-independent (QM tunneling) for low temperatures to T-dependent (phonon-assisted) conduction for intermediate temperatures. The crossover temperature is $T_{C1}$=150 K.

The conductivity above 150 K has a simple thermally activated Arrhenius behavior with $\sigma = \sigma o \cdot exp[-(Ea/kT)]$ but with a very small activation energy ($\sim$ 8 meV) indicating very weak temperature dependence and transport around the Fermi level. This lack of temperature dependence (or significant temperature dependence) can be associated with the very weak interparticle coupling [450] in long arrays.

Tunneling current is well-known to exhibit little or no dependence on temperature and is consistent with interparticle tunneling. In other words, due to the extremely weak interparticle coupling no temperature-dependent transport, such as co-tunneling, is observed at low bias.

At large bias, above the Coulomb blockade threshold $V_{TH}$(T), the I-V characteristics follow a power-law dependence on V-$V_{TH}$ (more specifically :$(V - V_{TH})/V_{TH})^{\zeta}$ with a temperature independent exponent $\zeta$ close

to 7 (6.77), which emerges as a consequence of branching [446]. The conduction threshold, $V_{TH}$(T), is temperature dependent with linear dependence on temperature. This behavior is characteristic of sequential tunneling along branching paths that navigate local Coulomb blockade thresholds and optimize the overall charging energy cost [191].

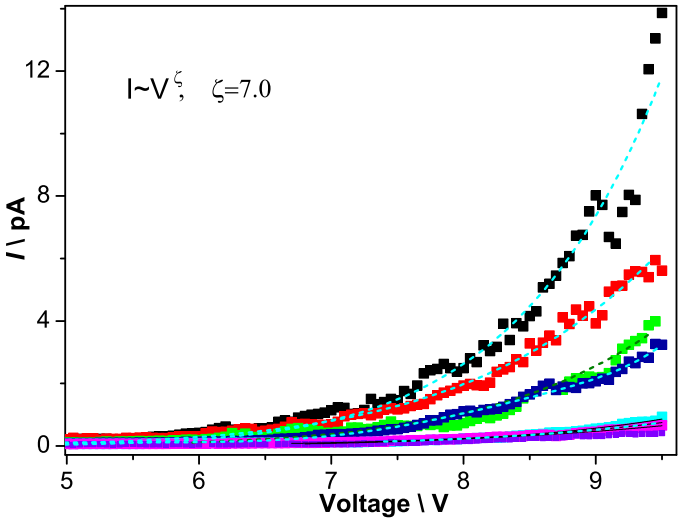


Figure 6.33: Power-law dependence of current from applied voltage above the threshold $V_{TH}$ for 50 nm spaced nanoelectrodes without addition of linkker molecules.

The charging energy is Ec=1.029 eV. So in the range V/(number of NPs)<1.029 Volt we should lie in the non-linear cotunneling regime. The exponent $\zeta$ can be related to the # of junctions, j, participating in the co-tunnel events via $\zeta$=2j1 [191]. So here j=4.

### 25-nm Electrode Spacing with Linkers

There is an apparent increase in nonlinearity with decreasing temperature. The highly nonlinear and strongly temperature-dependent behavior at finite but small bias merges into a much less temperature-dependent high bias. For high voltages and/or low temperatures (kT<<eV) all I-V traces approach the same power-law behavior $J \sim V^{\beta}$ with a temperature independent exponent close to 2 [465].

This later dependency is typical of sequential tunneling along branching conduction paths [446]. The region of low voltages (kT>> eV), yields a $J \sim T^{a}$ dependence with a=3.0. This behavior resembles that of short parallel paths [191], since I-Vs for the 25 nm have a strongly temperature-dependent prefactor a=3.0, in contrast to the weaker a=0.7 for the 50 nm.

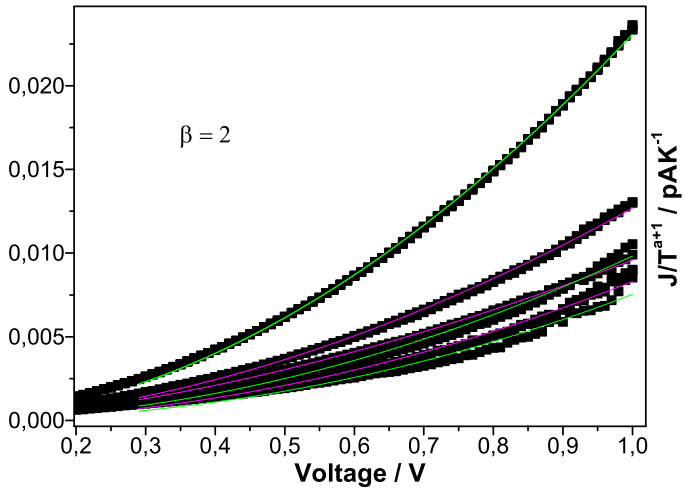


Figure 6.34: Power-law dependence of current from applied voltage with a temperature independent exponent ($J \sim V^{\beta}$) for 25 nm spaced nanoelectrodes with CuPcSu linker molecules.

No purely temperature dependent (and voltage independent) behavior has been detected for low voltages.

### 50-nm Electrode Spacing with Linkers

There is an apparent increase in nonlinearity with decreasing temperature. The nonlinear and temperature-dependent behavior at finite but small bias merges into a much less temperature-dependent high bias.

More specifically, the region of low voltages (kT>> eV), yields a $J \sim T^{a}$ dependence with a=0.7, while for higher voltages and/or low temperatures (kT<<eV) the temperature dependence becomes weaker and there is a $J \sim V^{\beta}$ dependence from voltage with $\beta$ close to 2. All I-V traces approach the same power-law behavior with with a temperature independent exponent close to 2, merging onto this asymptote at different temperatures. This later dependency emerges as a consequence of branching of conduction paths [446].

Again, as with the non-linked NPs, we have lack of significant temperature dependence for the long arrays with transport being carried out via sequential tunneling for all examined temperatures. This can be associated with the still weak (as in the bare networks) interparticle coupling.

The temperature dependence of the ES hopping (inelastic co-tunneling) distance [486] for the 25 nm case is quoted in Fig.6.35

As stated in [486], at sufficiently high temperatures the co-tunnel dis-

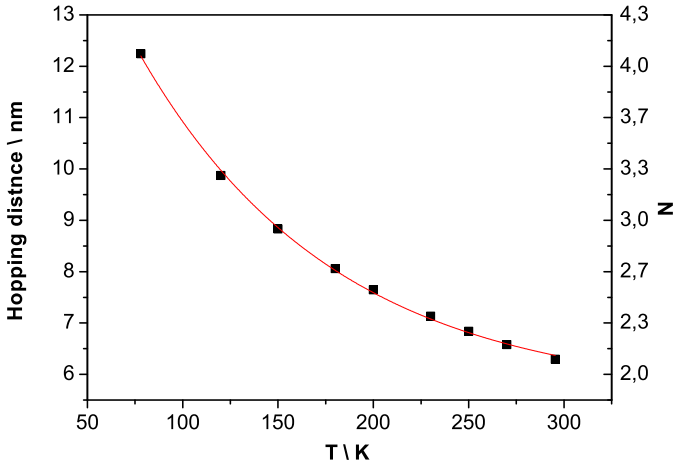


Figure 6.35: Temperature dependence of the E-S hopping distance as well as involved number of junctions.

tance should approach that of a single junction. At this point $g_T$ crosses over to simple activated, Arrhenius behavior. As can be seen there is no crossover from E-S to simple activated transport with N=1 up to RT.

On the contrary, according to the trend dictated by the fitting curve this should occur at ~400 K. So, as already demonstrated in Fig.6.23d, there are only two regimes present; namely, the E-S VRH and QM tunneling with a crossover temperature of $T_{C2}$=180 K.

For larger applied bias, the Coulomb blockade regime is exceeded and the I-V characteristics will cross over from co-tunneling to field-driven behavior. This is expected for V>>Vt, where Vt is the threshold for the Coulomb blockade regime. At low temperatures, Vt $=0.23 \cdot N \cdot E_C$ for an array of N×N grains [487], leading to values around 6 V for the 25 nm spaced multijunctions of Fig.6.23b.

## 6.7 Conclusions

We discussed the fabrication and study of molecular multi-junction networks comprising of ultrafine AuNPs and soluble CuPcSu oligomers. The impact of fabrication-induced disorder and localization on charge-transport are also addressed.

We demonstrate that specific preparation methods can lead to forms of low power computational functionality. We exploit interconnected metal NPs of diam. 17.9 nm, which act as strongly nonlinear single-electron transistors and find that this nanoscale architecture can be configured on-flight to perform Boolean logic functions.

The resulting nanocell can be programmed, erased and reprogrammed dynamically, through collective switching of the constituent nodes between on and off resistive states. It collectively "learns" to discriminate between two resistive levels according to the polarity of the "switching" pulse and the history of addressing (i.e. sequence of pulses and their polarity). The cell functions real time as a two-input "then-if" logical gate with a response time of merely 10 ns and can be read real time using a low reading voltage of 500 mV.

We further report on the study of the electronic properties of molecular multi-junction networks comprising of ultra-fine AuNPs of diam. 1.4 nm, electronically linked by means of copper 3-diethylamino-1-propyl-sulphonamide sulfonic acid substituted phthalocyanine molecules. When electrons flow through the non-linked NP arrays, they experience on-site Coulomb repulsion and are strongly localized, with localization length ($\xi$=0.7 nm). Under dynamic excitation the system functions as a single electron-transport regulator, undergoing Coulomb oscillations, whereas the introduction of CuPcSu molecules results in the formation of a network of multiple molecular/Au nanojunctions and conductance increases by 5 orders of magnitude.

This switching behavior functions on reversible red-ox reactions and pushes carriers in a state of weaker localization. In this state electrons spread over several junctions and all temperature scaled current vs voltage curves, $J/T^{1+\alpha}$ vs $eV/kT$, collapse in one universal curve, characterizing the network and the extent of its disorder. Utilizing this property we demonstrate the effect of inter-electrode distance on the conduction nodes topological disorder.

We demonstrate that reduction of inter-electrode distance is a means of increasing the systems disorder via the opening of multiple conduction pathways in parallel. Carrier injection in the hybrid is boosted via band formation in the molecular volume and transport is promoted via enhancement of both interparticle and electrode-network coupling. AuNP nodes play now the double role of both donor and acceptor, accepting electrons that are removed from the charge-bearing orbitals of CuPcSu and donating electrons to the available Cu(II) states of the CuPcSu metal center.

Bearing in mind that the electronic structure (i.e. doping levels) of CuPcSu is extremely sensitive to the presence of a wide variety of gases [434, 488, 489, 490] this mechanism can be directly exploited in detectors or gas-aware switches. The system consists a promising candidate for Au NPs-based thin films with tunable properties wherever solution-based fabrication methods, such as injection printing, are envisioned.

# 7

# General Conclusions & Perspectives

The findings of this work suggest that the two-stage bottom-up self-assembly of tungsten polyoxometalates in ambient conditions represents an alternative approach to produce nanodevices with consistently tunable performance characteristics, bridging the gap between disorder and scaling-up in solution-derived films.

A nested one-pot self-assembly process is applied in two stages, in order to separately address intermolecular and molecule-substrate interactions. This way molecular hyperstructures of controllable building blocks' crystallization and spatial correlation length are being fabricated.

Owing to the weak inter-crystal as well as inter-layer coupling, the produced structures largely preserve their original single-NC properties on plane, modified only by long range Coulomb interactions between neighbors. This feature is beneficial for applications related to information storage, where intergrain tunneling and, thus, bit loss should be efficiently suppressed.

By extending the crystallization extent the intra-grain electron-electron interactions are enhanced to the point where itinerary correlated electrons appear in previously strongly localized electronic states and a dimensional crossover driven SMIT is enforced under vertical transport. The extreme electronic bandgap modification for transport through the PtIr/POM/APTES/$SiO_2$/Si stack stems from both intragrain electron-electron interactions and PtIr/POM coupling. This is translated in extreme tunability of the coupling coefficient of POM molecules to the in-

jecting leads by solely dimensional means. Thus, interface alignment and stack performance can be directly tuned via the extent of crystallization in the molecular film.

Careful control over POM crystallization can yield solution-printed molecular hyperstructures with transport properties of extreme tunability and selectivity and figures of merit on par with their single-NC counterparts. Precision control over crystallization is a major asset for devices, since the electronic coupling between adjacent molecules and the intrinsic mobility are primarily governed by the molecular packing arrangement [148, 149].

For low molecular densities, STM revealed the existence of electronic states strongly localized on plane, owing to very weak inter-crystal coupling. As aggregation proceeds, the increasing influence of intermolecular interactions pushes the system towards a state of progressively increasing correlation under vertical transport. This transformation amplifies the free-carrier concentration and manifests itself as a two-orders-of-magnitude vertical current amplification in the low ($< 2$ V) voltage regime and four orders of magnitude at 4 V between the $1 \times 10^{-1}$ and $1 \times 10^{-4}$ M films.

This addresses a significant challenge, namely the problem of contact formation to molecular components [184, 185] through the simple solution of tunable highest occupied molecular orbitals (HOMOs)-lowest unoccupied molecular orbitals (LUMOs) of POM assemblies. Being able to transport or confine charge at will, these hyperstructures constitute better candidates for circuitry components and transistor channels.

In plane, on the other hand, electronic states are always strongly localized, owing to weak inter-crystal as well as inter-layer coupling. Thus, electrons in POM NCs are always localized on plane, even at RT, implying impeded transport and enhanced Coulomb interactions for a wide range of T and V.

This is beneficial for information-storage applications where preservation and retention of information is a key feature. Selection between 1-D and 2-D planar transport is possible as well and depends on the choice of addressing leads. This later property can be directly exploited for new efficient bit addressing and reading configurations, paving the way to potentially novel information addressing architectures.

Moreover, the structures realized this way have properties particularly tolerant in disorder. Due to their highly symmetric Keggin structure [150, 151] they are able to form self-assembled films with building blocks of controlled crystallization extent and collective electronic properties on par with their molecular building blocks. They are, thus, promising for solution-printed molecular semiconductor films with electronic proper-

ties of noticeable tunability, high stability and predictability.

Next the phenomenon of dynamic carrier exchange across the layers of a modified MIS structure via incorporation of a properly designed POM molecular layer is investigated. We demonstrate that the utilization of POM molecules can be advantageous for the realization of low power switching and/or fast writing applications as they provide multiple resistive states for low applied fields and good response to dynamic charging conditions. Moreover, their presence reduces electron-hole pair generation lifetime favoring the increase of speed in switching and writing processes.

The basic mechanisms of vertical transport are identified utilizing capacitance-voltage and current-voltage measurements, as well as transient capacitance measurements under step voltage polarization. The POM layer increases conductivity via induction of gap states (approximately 1.0 eV below Fermi level), as a result of tailing of the electron-rich orbitals of defective POM structures within the $SiO_2$ gap. Under gate injection, transport occurs through coupled processes of thermionic emission over the Schottky barrier induced by the HOMO-LUMO/ Al Fermi level mismatch and interface states assisted Poole-Frenkel transport along with resonant tunneling through molecular states at relative high and intermediate electric fields ([-1.7, -1.3] V). Hopping, coherent and incoherent tunneling also occur in the low field regime. Each mechanism dominates the current in a different bias and/or temperature regime.

Crucial parameters concerning the characteristics of the integrated molecular films can be derived from the dynamic carrier exchange between the POMs and the gate electrode. These are the active trap density of $5 \times 10^{12} cm^{-2}$ for the POM sheet and the activation energy for hopping assisted by shallow states of the σ-bonded molecular network of the IPA organic layer estimated at 25 meV. The total charge density of a POM modified sheet is of the order of $Q_{tot} = 2.9 \times 10^{-7} Cb/cm^2$ at 240 K and is distributed in all available molecular states in the POM islands (1-3 electrons per molecule). The discrete charge amounts collectively occupied in the device by each one of the triplet of POM states exhibit Gaussian distribution and have been estimated as: $Q_{ta} = 0.7 \times 10^{-7} Cb/cm^2$, $Q_{tb} = 1.4 \times 10^{-7} Cb/cm^2$, $Q_{tc} = 0.8 \times 10^{-7} Cb/cm^2$ via peak deconvolution.

The structure and dimensions of the functional organic and inorganic molecular thin films were determined via a combination of methods such as electrical characterization, SE, SEM and AFM. The POM molecules are arranged in uniformly distributed nano-islands of a mean diameter of 17 nm forming a layer of mean thickness of 2.2 nm. However, the electronic structure of these nanoislands, derived via dynamic J-V measurements, remains independent of the size of the formed islands and exhibits discrete

charging levels characteristic of the LUMO and LUMO+1 states of the single POM molecules. This can make the exhibition of single-electron charging effects possible even at RT.

Quantitative evaluation of the POM displacement current contribution under device operation was obtained via low temperature C(t) transient capacitance monitoring and development of a modified Zerbst-type equation. POM drastically reduces electron-hole pair generation lifetime being, thus, promising for high speed writing or switching applications.

Addressing the problem of backtunneling towards the gate via polymeric solution processable organic dielectrics was not fruitful either due to poor film quality and involved structures' stability (case of PEI) or due to the presence of significant amount of positive ionic charge (case of PMMA) in the dielectric's volume, a fact resulting in severe retention and reliability issues.

Nevertheless, the recorded ability to easily modify the POM charging threshold via selection of the top organic insulator (in this case isopentylamine) and the ability to finely tune the POM charging capacity by simply controlling the POM molarity in the precursor solution, implement multiple POM layers and/or select between different charging levels by modifying the Keggin structures heteroatom in the POM molecules, makes these materials a promising candidate for fabrication of hybrid molecular-semiconducting devices and exploitation of techniques like inject printing to modify traditional high cost doping and film growth techniques.

In an effort to enhance trapping times and information density a 3-d integration scheme is proposed. Hybrids comprising of high surface-to-volume ratio transition metal oxides (i.e. $Ta_2O_5$) and a transition metal oxide molecular analogue, Keggin type tungsten polyoxometalates, consist a novel composite material that can be fabricated using CMOS-compatible technology and serve as a memory cell based on electron trapping.

Non-volatile memory devices with commendable memory characteristics such as large memory window (4.0 Volt for the write state) and significant retention ($10^4$ sec) even without the use of blocking oxide have been fabricated utilizing a MIS capacitive cell architecture. We demonstrate for the first time that key issues for boosting the width of memory window of such devices are differential distance of trapping sites from the injection layer and effective electronic coupling to the space charge region of the underlying Si substrate.

The promising memory and retention characteristics of this hybrid highlight its potential as storage node for molecular nonvolatile flash memories. The fabricated memory cells are able to bring together significant figures of merit like high density of trapping sites via the combina-

tion of stable molecular components and 3-dimensional nanostructuring, electronic coupling to Si and direct accessibility of electronic levels in solid state, inherent retention of information under room temperature, bottom up fabrication logic and solution processing. They are, thus, of great potential for advanced molecule-based storage and memory technologies.

Despite maintaining information for several hours the hybrid molecular-low dimensional transition metal oxide core is not able to meet the 10-years information retention criterion for commercially exploitable non-volatile memories. In order to elegantly address this issue we fabricate and test capacitive memory cells based on a "clever" functional metal oxide stack, consisting of both molecular and solid state analogues. This material is being fabricated following a joint "solid-solution-vapor deposition" approach that overcomes major fabrication obstacles in the field of scalable molecular devices on non-standard substrates with only minor modifications of the standard CMOS-line protocol. The utilized molecules are designed in a rational way in order to have pre-specified electrical properties and are incorporated using a novel two-stage one-pot self-assembly process.

Each such memory element contains a 3-d-conformed hyperstructure of molecules accounting to densities of $9 \times 10^{12} cm^{-2}$ molecular NCs, corresponding to approximately $4 \times 10^{14} cm^{-2}$ storage nodes, that can store charge 65–195 $\mu Cb/cm^2$. This yields a structure that has multiple times the charge density of a typical DRAM capacitor (typically 1-2 $\mu C/cm^2$).

Using a normal incandescent lamp to take advantage of phononic pumping, we demonstrate a maximum of 37% boost on information density storage via reaching molecular states that were previously non-available. High storage density, fulfillment of the current commercial threshold of 10-years-data-retention-guarantee in ambient conditions, ability of multi-state addressing, and write speed of 10 ns are being documented for the packed cell.

The aforementioned high performance non-volatile memories are the first documented CMOS-compatible long term retention molecular capacitive cell of its kind, blazing the trail for the commercial exploitation of functional oxide and molecular hybrids as a high-end non-volatile memory product.

Following an approach different than the fabrication of fully prepatterned circuits, brain-inspired, neural systems performing in networks and "data-centric" non-Von Neumann processing are among the latest trends for non-conventional approaches in the semiconductor industry race.

We demonstrate that specific preparation methods can lead to forms

of low power computational functionality. More specifically, drop-cast weakly interconnected (i.e. not covalently bonded) metal NPs, adopting a 3-d conformation are shown to act as strongly nonlinear single-electron transistors. In such cases charge trapping and localization as well as conformational changes under stress result in hysteretic response. Both the collective conduction threshold (percolation) for the network and the system's conductance depend upon the stochastic NP charging and discharging process.

In such cases of strongly interacting network nodes and for voltages well above the Coulomb blockade threshold the characteristic I-Vs follow a $((VV_{TH})/V_{TH})^{\alpha}$ rule, where $\alpha = 2.93$. The later is emerging as a consequence of the presence of multiple conduction paths.

Based on this strong non-linearity, the impact of local component properties' alteration on the collective properties and the exhibition of negative differential resistance regions we set the goal to perform logic functions. The drop-cast nanojunction 3-d arrays exhibit a collective conduction threshold of 0.42 V and $\alpha$=2.93 a fact that makes them suitable platforms for logic function exhibition.

The networks can be configured on-flight to modify their resistance between two discrete levels depending on the "write" pulse. Both levels can be addressed real time utilizing nano-electrode pairs and reading voltage of the order of 500 mV.

In terms of input -output signals ($V_{IN}$ (t) and $I_{OUT}$ (t)) the network performs as a two-input "then-if" logic gate.

The resulting nano-cell can be programmed, erased and reprogrammed dynamically, through collective switching of the constituent nodes between on and off resistive states. It collectively "learns" to discriminate between two resistive levels according to the polarity of the "switching" pulse and the history of addressing (i.e. the sequence of pulses and their polarity). The cell functions real time as a two-input "then-if" logical gate with a response time of merely 10 ns and can be read real time using a low reading voltage of 500 mV. We have thus, obtained a nanoscale architecture can be configured on-flight to perform certain quick and energetically efficient Boolean logic functions.

We further report on the study of the electronic properties of molecular multi-junction networks comprising of ultra-fine AuNPs of diam. 1.4 nm, electronically linked by means of copper 3-diethylamino-1-propyl-sulphonamide sulfonic acid substituted phthalocyanine molecules. When electrons flow through the non-linked NP arrays, they experience on-site Coulomb repulsion and are strongly localized, with localization length ($\xi$=0.7 nm). Under dynamic excitation the system functions as a single electron-transport regulator, undergoing Coulomb oscillations, whereas

the introduction of CuPcSu molecules results in the formation of a network of multiple molecular/Au nanojunctions and conductance increases by 5 orders of magnitude.

This switching behavior functions on reversible red-ox reactions and pushes carriers in a state of weaker localization. In this state electrons spread over several junctions and all temperature scaled current vs voltage curves, $J/T^{1+\alpha}$ vs $eV/kT$, collapse in one universal curve, characterizing the network and the extent of its disorder. Utilizing this property we demonstrate the effect of inter-electrode distance on the conduction nodes topological disorder.

Utilizing this property we demonstrate that reduction of inter-electrode distance is a means of increasing the systems disorder via the opening of multiple conduction pathways in parallel. Carrier injection in the hybrid is boosted via band formation in the molecular volume and transport is promoted via enhancement of both interparticle and electrode-network coupling. AuNP nodes play now the double role of both donor and acceptor, accepting electrons that are removed from the charge-bearing orbitals of CuPcSu and donating electrons to the available Cu(II) states of the CuPcSu metal center.

Bearing in mind that the electronic structure (i.e. doping levels) of CuPcSu is extremely sensitive to the presence of a wide variety of gases [434, 488, 489, 490] this mechanism can be directly exploited in detectors or gas-aware switches. The system consists a promising candidate for Au NPs-based thin films with tunable properties wherever solution-based fabrication methods, such as injection printing, are envisioned.

Regarding the POM-based memory cells the write/red speed could be greatly optimized through reduction of gate oxide & tunneling oxide thickness. Accordingly, the power consumption can be minimized through the reduction of gate oxide thickness and differential POM concentrations along the z axis to reduce injection threshold.

The memory window can be further optimized through fine tuning the $Al_2O_3$ phonon coupling to the oxide/POM interfacial charge transfer states.

Finally, exploiting this weak coupling of POM nanocrystals in hyperstructures, one could explore the possibility of fabricating POM-based Van der Waals heterostructures [491] (designer heterostructures made layer by layer in a precisely chosen sequence ) where exotic phenomena, typically requiring very low temperatures, can be explored.

# 8

# Appendix

## 8.1 Post-processing of AFM images

AFM digital images were obtained in non-conduct, tapping mode and post-processed via appropriate low pass filtering in 2-D Fourier space [492]. More specifically, the spatial intensity topographic images were first analyzed via a 2-D Fast Fourier Transform. The resulting patterns were distributed along a main axis indicating the anisotropic arrangement of the deposited NPs. Subsequently, the higher frequencies, corresponding to the minimal wavelengths (i.e. random single pixel noise), were filtered out in the FFT image via a low pass filter and the resulting image was subjected to an inverse Fourier transform. In the final images the deposited NP structures are well-observable proving that this method is adequate for the achievement of sub-nm resolution even in ambient conditions.

## 8.2 Calculation of $\zeta$ exponent and $V_{TH}$ from I-V data

To deduce $\zeta$ and $V_{TH}$ values from the I-V data, we first plot the function I·dV/dI versus V, which is linear above $V_{TH}$ and allows one to determine $\zeta$. Then, we obtain the $V_{TH}$ value from fitting I-V data to the scaling law [493] in a classical least-square fit of the I (V) using $\zeta$ as a fixed parameter. The mean statistical error in the estimation of $V_{TH}$ is equal to: $\delta V_{TH} = \pm 0.011 V$

## 8.3 Fractal Analysis of AFM images–Raw curves

The raw curves used to determine the fractal dimension are provided in Fig.8.1.

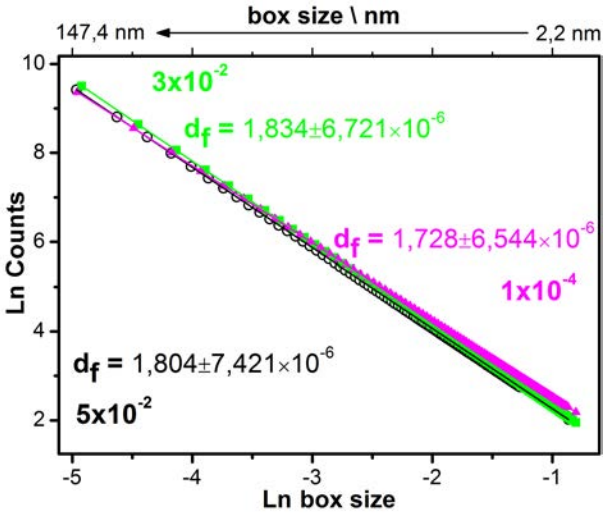


Figure 8.1: Obtained logarithmic regression lines for counts vs box size used to determine the fractal dimension of POM hyperstructures.

The standard error of the mean value of fractal dimension in the high molarity regimes (where intra grain information is filtered), i.e. in the cases $3 \times 10^{-2}$ and $5 \times 10^{-2}$ of the graph, is of the order of 0.015. For the $1 \times 10^{-4}$ M case is even less. Therefore, discussion of differences of the order of 0.1 in fractal dimensions is meaningful and is enough to highlight the difference between the presence of intra and inter-grain structure.

More importantly, even though they remain experimentally resolvable, these two dimensions are close enough in values in order to be both consistent with an off-lattice diffusion limited aggregation process of molecular cluster formation. This highlights the correct utilization of a powerful post-processing evaluation tool for the crystallization/aggregation mechanism of POMs and other molecules of fractal arrangement in solution.

## 8.4 ALD cycle instances and setup topology

For the $Al_2O_3$ growth a Savannah-100 ALD system (Cambridge Nanotech/USA) has been used. During deposition, the substrate is maintained

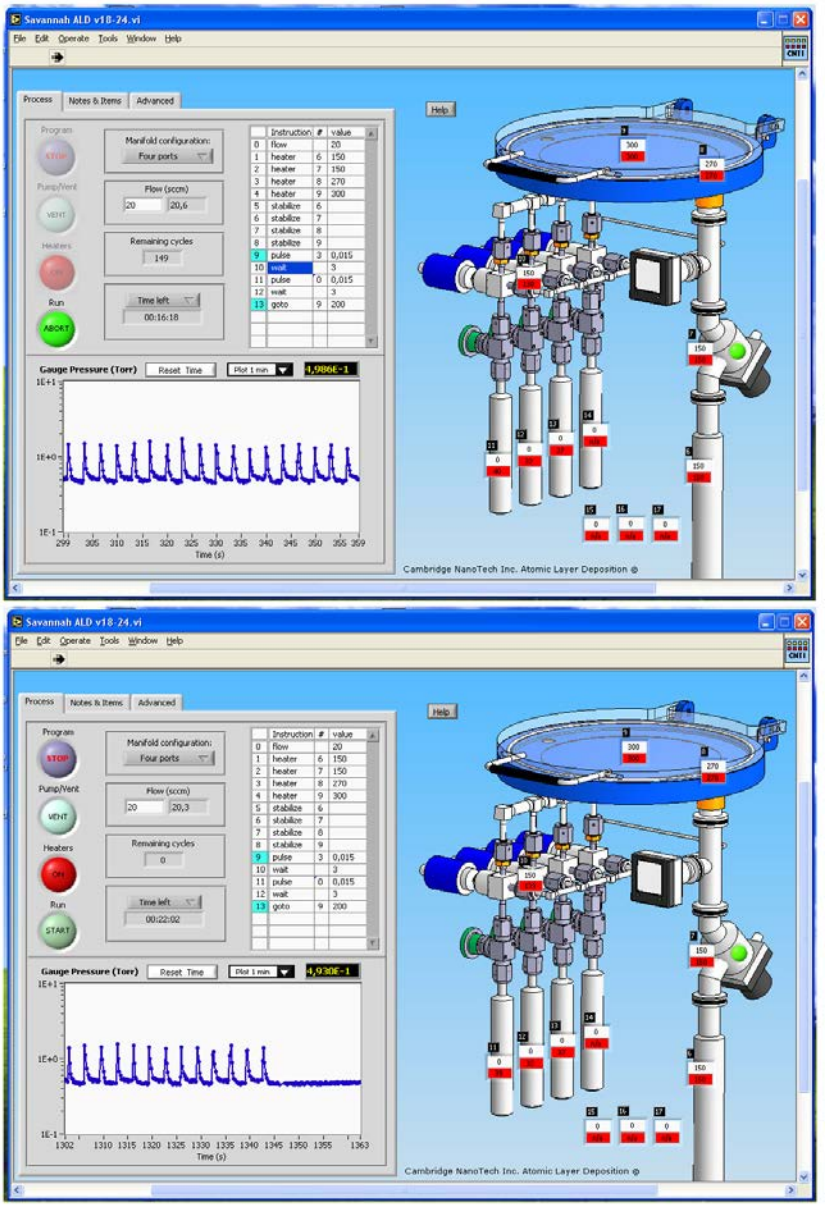


Figure 8.2: Savannah Atomic Layer Deposition System user interface. Instances captured during (top) and after (bottom) ALD deposition of $Al_2O_3$. The indication of the reactor chamber pressure gauge and the topology of the setup along with thermocouple indications on several points including the sample holder are provided.

at 300°C. Temperatures can be set by typing values into the light blue areas (dialogue boxes) in Fig.8.2. The current temperature readings are

indicated in the red area of each heater under the set point.

0.015 sec-lasting cycles of alternating $H_2O$ and trimethylaluminum (TMA) precursor pulses are being applied, interrupted by intermediate $N_2$ purging intervals of 3 sec. The pulses are monitored in-situ in the Reactor Pressure Plot Area interface (see Fig.8.2). ALD is a self-limiting process so each cycle produces exactly a monolayer. The average nominal growth rate for the applied conditions is 1 Å/cycle.

## 8.5 FTIR Spectra

The FTIR specta were taken after CuPc absorption on the surface of Au NPs. The composite is deposited on Au nanoelectrode-patterned $SiO_2$ on n-Si substrates. Two thousand co-added scans were collected at 4 $cm^{-1}$ resolution in the mid-IR region (3999-371 $cm^{-1}$) with a mirror velocity corresponding to a data collection rate of 20 kHz. The interferograms were Fourier transformed with triangular apodization and zero-filling. The spectral intensities are reported as reflectivity in transmittance (1-absorbance , -log(R/Ro)) units, where Ro is the reflectivity of a reference sample (evaporated Au NPs on nanoelectrode equipted $SiO_2$ substrate on n-Si).

In Fig.8.3 the characteristic CuPcSu peaks are shifted in the case of the hybrid Au NPs/CuPcSu network, electronic interaction between CuPcSu molecules and Au. This is a complementary evidence of the electronic coupling between molecules and NPs, as monitored in the electrical characterization of the hybrids, despite the absence of strong chemical interaction monitored in XPS core level spectra.

## 8.6 Coulomb blockade oscillations

Conduction at low temperatures proceeds via tunneling through the interparticle barriers. The dominant I-V oscillations have a well-defined periodicity, indicating that a single NP limits the conductance. Nevertheless, the presence of additional NPs gives rise to multiple periodicities and to beating effects [494] present as a shoulder overlapping the main sawtooth signal. The tunneling current through the array changes periodically as a function of applied gate voltage in a saw tooth-like manner with a period of $V = e/C_{max}$, where $C_{max}$ is the smallest clusters surface capacitance [495].

However, this is not a quasi-static measurement and, since voltage is changing dynamically in time with a constant rate dV/dt, the tunneling array can be viewed as a kind of a turnstile clocking device [496, 497, 498]

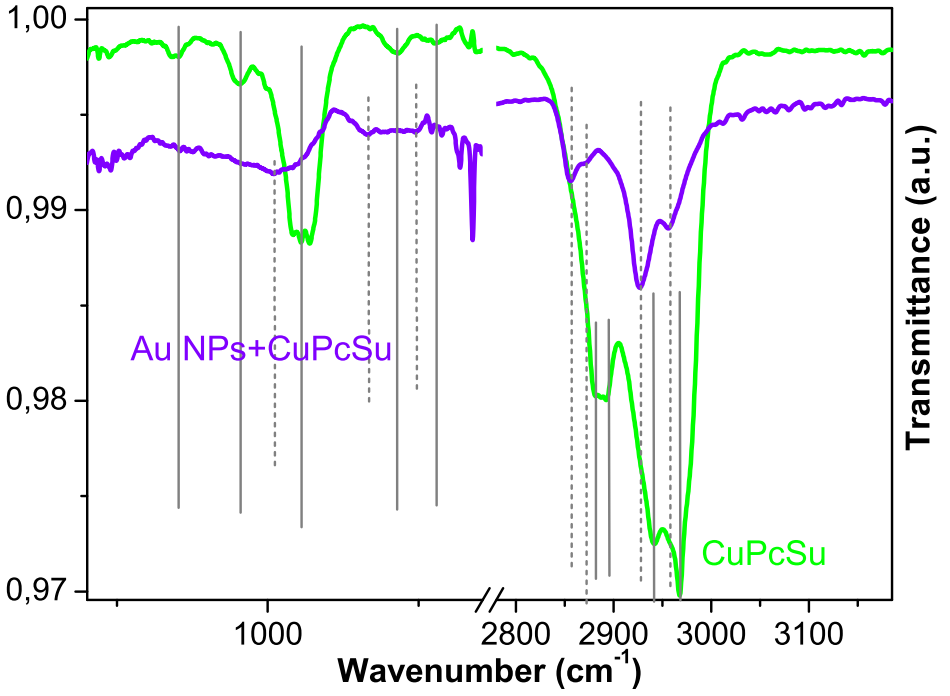


Figure 8.3: FTIR specta of CuPcSu on Au nanoelectrode-patterned $SiO_2$ on n-Si substrates without (green line) and with (purple line) evaporated Au NPs.

with oscillation of charge/current across the junctions with a fundamental frequency : $_{SET}$= I/e [496] and a tunneling current proportional to the frequency of the modulation of the voltage on the lead or, in our case, to the frequency dictated from the applied ramp rate. The curves tend to oscillate between consecutive multiples of e·$v_{SET}$. This shows that the device can also pass several electrons per cycle in a controlled way. At higher current amplitude it is possible to fill the central island with more than one electron [499]. The differential conductance of the system is given as:

$$\frac{dI}{dV} = \frac{1}{NR} + \frac{dI_{SET}}{dV} = \frac{1}{NR} + \frac{dI_{SET}/dt}{dV/dt} \tag{8.1}$$

,where NR is the series resistance of sequential NPs and $I_{SET}$ the sequential tunneling current. In a periods time $dI_{SET}/dt$ is the same for both ramp rates (see Fig.6.29), as expected for SET. In other words, if we go from I (V) to I (t) through the transformation dV/dt=0.10 and 0.20 respectively, we will end up with the same graph. 1/NR is constant, and $dI_{total}$ is also the same for both ramp rates. From these observations and Eq.8.1, it follows that the ΔV corresponding to a SET event is directly

proportional to the ramp rate dV/dt.

Regarding the period of $e/2C_{max}$ this should be used for the quasi-static case. With a recharging time of 3.8 sec the 100 mV/sec implies a period dV of 380 mV. Correspondingly, the 200 mV/sec implies a dV of 760 mV, but the recharging time remains the same, i.e. 3.8 sec.

The doubling of current amplitude for double ramp rate emerges as a consequence of the relation for displacement current I=dQ/dt=C·dV/dt. The # of tunneling electrons dQ/dt is doubled for double dV/dt. Since the recharging time $\tau_R$ is of the order of 3.8 sec for our system, for higher dV/dt a second, higher energy charging level is being probed with energy separation $2e^2/2C_{max}$.

# Bibliography


[1] M. Liehr, "Aim photonics tomorrows technology at the speed of light," *Defense AT&L*, September-October 2016.

[2] C. Hu, *Modern semiconductor devices for integrated circuits*. Prentice Hall, 2010.

[3] S. Association *et al.*, "International technology roadmap for semiconductors 2.0: 2015," *Austin, TX, Executive Summary*, 2015.

[4] D. K. Ferry, J. Bird, and S. M. Goodnick, "Transport in nanostructures," 2009.

[5] A. Chen, J. Hutchby, V. Zhirnov, and G. Bourianoff, *Emerging nanoelectronic devices*. John Wiley & Sons, 2014.

[6] G. A. T. Jung H. Yoon, Hillery C. Hunter, "Flash & dram si scaling challenges, emerging non-volatile memory technology enablement – implications to enterprise storage and server compute systems," in *2013 IBM International Flash Memory Summit*, pp. 1–19, - IBM Corporation, 2013.

[7] E. Zhang, W. Wang, C. Zhang, Y. Jin, G. Zhu, Q. Sun, D. W. Zhang, P. Zhou, and F. Xiu, "Tunable charge-trap memory based on few-layer mos2," *ACS nano*, vol. 9, no. 1, pp. 612–619, 2014.

[8] Y. Nishi, *Advances in non-volatile memory and storage technology*. Elsevier, 2014.

[9] "Ibm research builds functional 7nm processor," July 2015.

[10] "International technology roadmap for semiconductors," 2015.

[11] D. Vasileska, S. Goodnick, and G. Klimeck, *Computational Electronics: Semiclassical and Quantum Device Modeling and Simulation*. CRC Press, 2016.

[12] J. S. Meena, S. M. Sze, U. Chand, and T.-Y. Tseng, "Overview of emerging nonvolatile memory technologies," *Nanoscale research letters*, vol. 9, no. 1, p. 1, 2014.

[13] P. Lee and D. Meisel, "Adsorption and surface-enhanced raman of dyes on silver and gold sols," *The Journal of Physical Chemistry*, vol. 86, no. 17, pp. 3391–3395, 1982.

[14] R. J. Hunter, *Introduction to modern colloid science*. Oxford University Press, 1993.

[15] M.-C. Daniel and D. Astruc, "Gold nanoparticles: assembly, supramolecular chemistry, quantum-size-related properties, and applications toward biology, catalysis, and nanotechnology," *Chemical reviews*, vol. 104, no. 1, pp. 293–346, 2004.

[16] A. M. Douvas, E. Makarona, N. Glezos, P. Argitis, J. A. Mielczarski, and E. Mielczarski, "Polyoxometalate-based layered structures for charge transport control in molecular devices," *ACS nano*, vol. 2, no. 4, pp. 733–742, 2008.

[17] S. K. Ghosh and T. Pal, "Interparticle coupling effect on the surface plasmon resonance of gold nanoparticles: from theory to applications," *Chemical Reviews*, vol. 107, no. 11, pp. 4797–4862, 2007.

[18] D. B. Pedersen and E. Duncan, "Surface plasmon resonance spectroscopy of gold nanoparticle-coated substrates: Use as an indicator of exposure to chemical warfare simulants," tech. rep., DTIC Document, 2005.

[19] K. L. Kelly, E. Coronado, L. L. Zhao, and G. C. Schatz, "The optical properties of metal nanoparticles: the influence of size, shape, and dielectric environment," *The Journal of Physical Chemistry B*, vol. 107, no. 3, pp. 668–677, 2003.

[20] T. Ung, L. M. Liz-Marzan, and P. Mulvaney, "Optical properties of thin films of au@ sio2 particles," *The Journal of Physical Chemistry B*, vol. 105, no. 17, pp. 3441–3452, 2001.

[21] M. T. Pope and A. Müller, "Polyoxometalate chemistry: An old field with new dimensions in several disciplines," *Angewandte Chemie International Edition in English*, vol. 30, no. 1, pp. 34–48, 1991.

[22] C. Mack, *Fundamental principles of optical lithography: the science of microfabrication*. John Wiley & Sons, 2008.

[23] G. Wiederrecht, *Handbook of nanofabrication*. Academic Press, 2010.

[24] A. Broers, A. Hoole, and J. Ryan, "Electron beam lithographyresolution limits," *Microelectronic Engineering*, vol. 32, no. 1, pp. 131–142, 1996.

[25] J. Torok, R. D. Re, H. Herbol, S. Das, I. Bocharova, A. Paolucci, L. E. Ocola, C. Ventrice Jr, E. Lifshin, G. Denbeaux, *et al.*, "Secondary electrons in euv lithography," *Journal of Photopolymer Science and Technology*, vol. 26, no. 5, pp. 625–634, 2013.

[26] W. F. Smith, "Organic electronics: Self-assembly is ready to roll," *Nature nanotechnology*, vol. 2, no. 2, pp. 77–78, 2007.

[27] W. F. Smith, "Organic electronics: Self-assembly is ready to roll," *Nature nanotechnology*, vol. 2, no. 2, pp. 77–78, 2007.

[28] N. Glezos, A. M. Douvas, P. Argitis, F. Saurenbach, J. Chrost, and C. Livitsanos, "Electrical characterization of molecular monolayers containing tungsten polyoxometalates," *Microelectronic Engineering*, vol. 83, no. 49, pp. 1757 – 1760, 2006. Micro- and Nano-Engineering {MNE} 2005 Proceedings of the 31st International Conference on Micro- and Nano-Engineering.

[29] M. Pope and A. Müller, "Introduction to polyoxometalate chemistry : From topology via self-assembly to applications," in *Polyoxometalate Chemistry From Topology via Self-Assembly to Applications* (M. Pope and A. Mueller, eds.), pp. 1–6, Springer Netherlands, 2001.

[30] L.-H. Lee, *Fundamentals of adhesion*. Springer Science & Business Media, 2013.

[31] C. P. Pradeep, D.-L. Long, and L. Cronin, "Cations in control: crystal engineering polyoxometalate clusters using cation directed self-assembly," *Dalton Transactions*, vol. 39, no. 40, pp. 9443–9457, 2010.

[32] H.-H. Perkampus, H.-C. Grinter, and T. Threlfall, *UV-VIS Spectroscopy and its Applications*. Springer, 1992.

[33] R. Desai, V. Mankad, S. K. Gupta, and P. K. Jha, "Size distribution of silver nanoparticles: Uv-visible spectroscopic assessment," *Nanoscience and Nanotechnology Letters*, vol. 4, no. 1, pp. 30–34, 2012.

[34] R. Levinson, *More modern chemical techniques*. Royal Society of Chemistry, 2001.

[35] S. Link and M. A. El-Sayed, "Shape and size dependence of radiative, non-radiative and photothermal properties of gold nanocrystals," *International Reviews in Physical Chemistry*, vol. 19, no. 3, pp. 409–453, 2000.

[36] P. Paula and J. d. Atkins, "Elements of physical chemistry," 2009.

[37] B. C. Smith, *Fundamentals of Fourier transform infrared spectroscopy*. CRC press, 2011.

[38] M. Dresselhaus, "Solid state physics part ii optical properties of solids," 1999.

[39] T. Nguyen, S. Mackowski, H. Rho, H. Jackson, L. Smith, J. Wrobel, K. Fronc, J. Kossut, G. Karczewski, M. Dobrowolska, *et al.*, "Resonant photoluminescence and excitation spectroscopy of cdse/znse and cdte/znte self-assembled quantum dots," in *MRS Proceedings*, vol. 737, pp. E9–2, Cambridge Univ Press, 2002.

[40] J. Ohara and S. Yamamoto, "Nonlinear lattice relaxation of photoexcited diplatinum-halide chain compounds," *Physical Review B*, vol. 73, no. 4, p. 045122, 2006.

[41] S. Eaton-Magaña and C. M. Breeding, "An introduction to photoluminescence spectroscopy for diamond and its applications in gemology.," *Gems & Gemology*, vol. 52, no. 1, pp. 2–17, 2016.

[42] J.-w. Cai, J.-p. Xu, X.-s. Zhang, X.-p. Niu, T.-y. Xing, T. Ji, and L. Li, "Defect-related visible luminescence of zno nanorods annealed in oxygen ambient," *Optoelectronics Letters*, vol. 8, pp. 4–8, 2012.

[43] N. Miriyala, K. Prashanthi, and T. Thundat, "Oxygen vacancy dominant strong visible photoluminescence from bifeo3 nanotubes," *physica status solidi (RRL)-Rapid Research Letters*, vol. 7, no. 9, pp. 668–671, 2013.

[44] M. Zhu, Z. Zhang, and W. Miao, "Intense photoluminescence from amorphous tantalum oxide films," *sensors*, vol. 5, p. 7, 2006.

[45] H. Arwin and D. E. Aspnes, "Unambiguous determination of thickness and dielectric function of thin films by spectroscopic ellipsometry," *Thin Solid Films*, vol. 113, no. 2, pp. 101–113, 1984.

[46] W. A. McGahan, B. Johs, and J. A. Woollam, "Techniques for ellipsometric measurement of the thickness and optical constants of thin absorbing films," *Thin Solid Films*, vol. 234, no. 1-2, pp. 443–446, 1993.

[47] P. Van der Heide, *X-ray photoelectron spectroscopy: an introduction to principles and practices*. John Wiley & Sons, 2011.

[48] M. Yoshitake and W. Song, "Interface potential measurement with electron spectroscopic method," *Journal of Surface Analysis*, vol. 13, no. 2, p. 185, 2006.

[49] R. Schlaf, H. Murata, and Z. Kafafi, "Work function measurements on indium tin oxide films," *Journal of Electron Spectroscopy and Related Phenomena*, vol. 120, no. 1, pp. 149–154, 2001.

[50] R. Wiesendanger and H.-J. Güntherodt, *Scanning tunneling microscopy III: theory of STM and related scanning probe methods*, vol. 29. Springer Science & Business Media, 2013.

[51] J. Bardeen, "Tunnelling from a many-particle point of view," *Physical Review Letters*, vol. 6, no. 2, p. 57, 1961.

[52] J. G. Simmons, "Electric tunnel effect between dissimilar electrodes separated by a thin insulating film," *Journal of applied physics*, vol. 34, no. 9, pp. 2581–2590, 1963.

[53] P. Klapetek, *Quantitative Data Processing in Scanning Probe Microscopy: SPM Applications for Nanometrology*. William Andrew, 2012.

[54] P. Klapetek, *Quantitative Data Processing in Scanning Probe Microscopy: SPM Applications for Nanometrology*. William Andrew, 2012.

[55] M. H. van Es and H. Sadeghian, "Euv blank defect and particle inspection with high-throughput immersion afm with 1nm 3d resolution," in *SPIE Advanced Lithography*, pp. 97782Z–97782Z, International Society for Optics and Photonics, 2016.

[56] V. Constantoudis, E. Gogolides, A. Tserepi, C. D. Diakoumakos, and E. S. Valamontes, "Roughness characterization in positive and negative resists," *Microelectronic engineering*, vol. 61, pp. 793–801, 2002.

[57] J. C. Russ, "Fractal surfaces. 1994."

[58] V. Constantoudis, G. Patsis, and E. Gogolides, "Fractals and device performance variability: The key role of roughness in micro and nanofabrication," *Microelectronic Engineering*, vol. 90, no. 0, pp. 121 – 125, 2012.

[59] N. Sahoo, S. Thakur, R. Tokas, A. Biswas, and N. Kamble, "Morphological, microstructural and optical properties supremacy of binary composite filmsa study based on gd 2 o 3/sio 2 system," *Applied Surface Science*, vol. 253, no. 7, pp. 3455–3463, 2007.

[60] V. Constantoudis, G. Patsis, and E. Gogolides, "Fractals and device performance variability: The key role of roughness in micro and nanofabrication," *Microelectronic Engineering*, vol. 90, pp. 121–125, 2012.

[61] A. Balliou, G. Papadimitropoulos, G. Skoulatakis, S. Kennou, D. Davazoglou, S. Gardelis, and N. Glezos, "Low-dimensional polyoxometalate molecules/tantalum oxide hybrids for non-volatile capacitive memories," *ACS applied materials & interfaces*, vol. 8, no. 11, pp. 7212–7220, 2016.

[62] S. Seal, *Functional nanostructures: processing, characterization, and applications*. Springer Science & Business Media, 2010.

[63] N. Eichenlaub, *Design, Characterization and Modeling of Charge Trapping Nonvolatile Semiconductor Memory Devices*. ProQuest, 2009.

[64] A. Balliou, G. Papadimitropoulos, G. Skoulatakis, S. Kennou, D. Davazoglou, S. Gardelis, and N. Glezos, "Low-dimensional polyoxometalate molecules/tantalum oxide hybrids for non-volatile capacitive memories," *ACS applied materials & interfaces*, vol. 8, no. 11, pp. 7212–7220, 2016.

[65] P. Dimitrakis, P. Normand, C. Bonafos, E. Papadomanolaki, and E. Iliopoulos, "Gan quantum-dots integrated in the gate dielectric of metal-oxide-semiconductor structures for charge-storage applications," *Applied Physics Letters*, vol. 102, no. 5, pp. –, 2013.

[66] S. Aritome, *NAND Flash Memory Technologies*. John Wiley & Sons, 2015.

[67] S. I. Association, "International technology roadmap for semiconductors: 2014 itrs white papers," *ITRS*, vol. 2.0., no. 2.0., 2014.

[68] J. Hilibrand and R. Gold, "Determination of the impurity distribution in junction diodes from capacitance-voltage measurements," *RCA review*, vol. 21, no. 2, pp. 245–252, 1960.

[69] A. C. Diebold, *Handbook of silicon semiconductor metrology*. CRC Press, 2001.

[70] E. H. Nicollian and J. R. Brews, *MOS (metal oxide semiconductor) physics and technology*, vol. 1987. Wiley New York et al., 1982.

[71] A. Jakubowski, W. Marciniak, and H. Przewlocki, *Diagnostic measurements in LSI/VLSI integrated circuits production*, vol. 7. World Scientific, 1991.

[72] D. K. Schroder, *Semiconductor material and device characterization, Second edition*. John Wiley & Sons, inc., 1998.

[73] S. Sze and K. Ng Kwok, *Physics of semiconductor devices 3rd Edition*. Wiley Online Library, 2007.

[74] A. Jakubowski, W. Marciniak, and H. Przewlocki, *Diagnostic measurements in LSI/VLSI integrated circuits production*. World Scientific Publishing Company, 1991.

[75] J. S. Huang *Proc. IEEE*, vol. 58, p. 1849, 1970.

[76] R. Ertuğrul and A. Tataroğlu, "Influence of temperature and frequency on dielectric permittivity and ac conductivity of au/sno2/n-si (mos) structures," *Chinese Physics Letters*, vol. 29, no. 7, p. 077304, 2012.

[77] A. Yacoby, U. Sivan, C. Umbach, and J. Hong, "Interference and dephasing by electron-electron interaction on length scales shorter than the elastic mean free path," *Physical review letters*, vol. 66, no. 14, p. 1938, 1991.

[78] G. Fiori, F. Bonaccorso, G. Iannaccone, T. Palacios, D. Neumaier, A. Seabaugh, S. K. Banerjee, and L. Colombo, "Electronics based on two-dimensional materials," *Nature nanotechnology*, vol. 9, no. 10, pp. 768–779, 2014.

[79] C. Author, "Themed collection of articles, profile: Emerging investigators 2016: novel design strategies for new functional materials," *Journal of Materials Chemistry A*, vol. 4, no. 18, pp. 6670–6679, 2016.

[80] H. Zhu and Q. Li, "Novel molecular non-volatile memory: Application of redox-active molecules," *Applied Sciences*, vol. 6, no. 1, p. 7, 2015.

[81] C. Busche, L. Vilà-Nadal, J. Yan, H. N. Miras, D.-L. Long, V. P. Georgiev, A. Asenov, R. H. Pedersen, N. Gadegaard, M. M. Mirza, *et al.*, "Design and fabrication of memory devices based on nanoscale polyoxometalate clusters," *Nature*, vol. 515, no. 7528, pp. 545–549, 2014.

[82] S. R. Forrest, "The path to ubiquitous and low-cost organic electronic appliances on plastic," *Nature*, vol. 428, no. 6986, pp. 911–918, 2004.

[83] A. M. Hiszpanski and Y.-L. Loo, "Directing the film structure of organic semiconductors via post-deposition processing for transistor and solar cell applications," *Energy & Environmental Science*, vol. 7, no. 2, pp. 592–608, 2014.

[84] N. R. Tummala, Z. Zheng, S. G. Aziz, V. Coropceanu, and J.-L. Bredas, "Static and dynamic energetic disorders in the c60, pc61bm, c70, and pc71bm fullerenes," *The journal of physical chemistry letters*, vol. 6, no. 18, pp. 3657–3662, 2015.

[85] K. Efetov, *Supersymmetry in disorder and chaos*. Cambridge University Press, 1999.

[86] Y. Ji, D. F. Zeigler, D. S. Lee, H. Choi, A. K.-Y. Jen, H. C. Ko, and T.-W. Kim, "Flexible and twistable non-volatile memory cell array with all-organic one diode–one resistor architecture," *Nature communications*, vol. 4, 2013.

[87] K. J. Thorley and C. Risko, "Mapping the configuration dependence of electronic coupling in organic semiconductors," *Journal of Materials Chemistry C*, vol. 4, no. 17, pp. 3825–3832, 2016.

[88] G. Schull, T. Frederiksen, A. Arnau, D. Sánchez-Portal, and R. Berndt, "Atomic-scale engineering of electrodes for single-molecule contacts," *Nature nanotechnology*, vol. 6, no. 1, pp. 23–27, 2011.

[89] M. Iwamoto, Y.-S. Kwon, and T. Lee, *Nanoscale interface for organic electronics*. World Scientific, 2011.

[90] M. Stanisavljević, A. Schmid, and Y. Leblebici, *Reliability of Nanoscale Circuits and Systems: Methodologies and Circuit Architectures*. Springer Science & Business Media, 2010.

[91] D.-L. Long, R. Tsunashima, and L. Cronin, "Polyoxometalates: building blocks for functional nanoscale systems," *Angewandte Chemie International Edition*, vol. 49, no. 10, pp. 1736–1758, 2010.

[92] M. T. Pope and U. Kortz, "Polyoxometalates," *Encyclopedia of Inorganic and Bioinorganic Chemistry*, 2012.

[93] J. Keggin, "The structure and formula of 12-phosphotungstic acid," in *Proceedings of the Royal Society of London A: Mathematical, Physical and Engineering Sciences*, vol. 144, pp. 75–100, The Royal Society, 1934.

[94] Y.-R. Guo, Q.-J. Pan, Y.-D. Wei, Z.-H. Li, and X. Li, "Theoretical studies on the electronic and spectroscopic properties of keggin-structure polyoxometalates /-[xm12o40]n (x=si, p; m=mo, w)," *Journal of Molecular Structure: {THEOCHEM}*, vol. 676, no. 13, pp. 55 – 64, 2004.

[95] J. M. Poblet, X. López, and C. Bo, "Ab initio and dft modelling of complex materials: towards the understanding of electronic and magnetic properties of polyoxometalates," *Chemical Society Reviews*, vol. 32, no. 5, pp. 297–308, 2003.

[96] B. Nohra, H. El Moll, L. M. Rodriguez Albelo, P. Mialane, J. Marrot, C. Mellot-Draznieks, M. OKeeffe, R. Ngo Biboum, J. Lemaire, B. Keita, *et al.*, "Polyoxometalate-based metal organic frameworks (pomofs): structural trends, energetics, and high electrocatalytic efficiency for hydrogen evolution reaction," *Journal of the American Chemical Society*, vol. 133, no. 34, pp. 13363–13374, 2011.

[97] C. Allain, D. Schaming, N. Karakostas, M. Erard, J.-P. Gisselbrecht, S. Sorgues, I. Lampre, L. Ruhlmann, and B. Hasenknopf, "Synthesis, electrochemical and photophysical properties of covalently linked porphyrin–polyoxometalates," *Dalton Transactions*, vol. 42, no. 8, pp. 2745–2754, 2013.

[98] C. Busche, L. Vilà-Nadal, J. Yan, H. N. Miras, D.-L. Long, V. P. Georgiev, A. Asenov, R. H. Pedersen, N. Gadegaard, M. M. Mirza, *et al.*, "Design and fabrication of memory devices based on nanoscale polyoxometalate clusters," *Nature*, vol. 515, no. 7528, pp. 545–549, 2014.

[99] Z. Sun, L. Xu, W. Guo, B. Xu, S. Liu, and F. Li, "Enhanced photoelectrochemical performance of nanocomposite film fabricated by self-assembly of titanium dioxide and polyoxometalates," *The Journal of Physical Chemistry C*, vol. 114, no. 11, pp. 5211–5216, 2010.

[100] A. Flütsch, T. Schroeder, M. G. Grütter, and G. R. Patzke, "Hiv-1 protease inhibition potential of functionalized polyoxometalates," *Bioorganic & medicinal chemistry letters*, vol. 21, no. 4, pp. 1162–1166, 2011.

[101] A. Salomon, D. Cahen, S. Lindsay, J. Tomfohr, V. Engelkes, and C. Frisbie, "Comparison of electronic transport measurements on organic molecules," *Advanced Materials*, vol. 15, no. 22, pp. 1881–1890, 2003.

[102] A. Patel and S. Pathan, *Polyoxomolybdates as Green Catalysts for Aerobic Oxidation*. Springer, 2015.

[103] J. M. Maestre, X. Lopez, C. Bo, J.-M. Poblet, and N. Casan-Pastor, "Electronic and magnetic properties of $\alpha$-keggin anions: A dft study of [xm12o40] n-,(m= w, mo; x= aliii, siiv, pv, feiii, coii, coiii) and [sim11vo40] m-(m= mo and w)," *Journal of the American Chemical Society*, vol. 123, no. 16, pp. 3749–3758, 2001.

[104] J. M. Maestre, X. Lopez, C. Bo, J.-M. Poblet, and N. Casan-Pastor, "Electronic and magnetic properties of $\alpha$-keggin anions: A dft study of [xm12o40] n-,(m= w, mo; x= aliii, siiv, pv, feiii, coii, coiii) and [sim11vo40] m-(m= mo and w)," *Journal of the American Chemical Society*, vol. 123, no. 16, pp. 3749–3758, 2001.

[105] M. Sadakane and E. Steckhan, "Electrochemical properties of polyoxometalates as electrocatalysts," *Chemical Reviews*, vol. 98, no. 1, pp. 219–238, 1998.

[106] M. Kozik, C. F. Hammer, and L. C. Baker, "Nmr of phosphorus-31 heteroatoms in paramagnetic 1-electron heteropoly blues. rates of intra-and intercomplex electron transfers. factors affecting line widths," *Journal of the American Chemical Society*, vol. 108, no. 24, pp. 7627–7630, 1986.

[107] N. Suaud, A. Gaita-Arino, J. M. Clemente-Juan, J. Sánchez-Marín, and E. Coronado, "Electron delocalization in mixed-valence keggin polyoxometalates. ab initio calculation of the local effective transfer integrals and its consequences on the spin coupling," *Journal of the American Chemical Society*, vol. 124, no. 50, pp. 15134–15140, 2002.

[108] E. I. Solomon, R. A. Scott, and R. B. King, *Computational inorganic and bioinorganic chemistry*. John Wiley & Sons, 2013.

[109] M. Pope *et al.*, *Polyoxometalates: From Platonic Solids to Anti-Retroviral Activity: From Platonic Solids to Anti-Retroviral Activity*, vol. 10. Springer Science & Business Media, 1994.

[110] M. T. Pope and G. M. Varga Jr, "Heteropoly blues. i. reduction stoichiometries and reduction potentials of some 12-tungstates," *Inorganic Chemistry*, vol. 5, no. 7, pp. 1249–1254, 1966.

[111] B. Bujanovic, S. Ralph, R. Reiner, K. Hirth, and R. Atalla, "Polyoxometalates in oxidative delignification of chemical pulps: Effect on lignin," *Materials*, vol. 3, no. 3, pp. 1888–1903, 2010.

[112] M. J. Janik, B. B. Bardin, R. J. Davis, and M. Neurock, "A quantum chemical study of the decomposition of keggin-structured heteropolyacids," *The Journal of Physical Chemistry B*, vol. 110, no. 9, pp. 4170–4178, 2006.

[113] M. Ammam, "Polyoxometalates: formation, structures, principal properties, main deposition methods and application in sensing," *Journal of Materials Chemistry A*, vol. 1, no. 21, pp. 6291–6312, 2013.

[114] R. Contant, "Relations entre les tungstophosphates apparentés à l'anion pw12o403-. synthèse et propriétés d'un nouveau polyoxotungstophosphate lacunaire k10p2w20o7024h2o," *Canadian journal of chemistry*, vol. 65, no. 3, pp. 568–573, 1987.

[115] A. Hiskia, A. Mylonas, and E. Papaconstantinou, "Comparison of the photoredox properties of polyoxometallates and semiconducting particles," *Chemical Society Reviews*, vol. 30, no. 1, pp. 62–69, 2001.

[116] X. Lopez, J. M. Maestre, C. Bo, and J.-M. Poblet, "Electronic properties of polyoxometalates: A dft study of $\alpha/\beta$-[xm12o40] n-relative stability (m= w, mo and x a main group element)," *Journal of the American Chemical Society*, vol. 123, no. 39, pp. 9571–9576, 2001.

[117] I.-M. Mbomekallé, X. López, J. M. Poblet, F. Sécheresse, B. Keita, and L. Nadjo, "Influence of the heteroatom size on the redox potentials of selected polyoxoanions," *Inorganic chemistry*, vol. 49, no. 15, pp. 7001–7006, 2010.

[118] H. H. Kung, *Transition metal oxides: surface chemistry and catalysis*, vol. 45. Elsevier, 1989.

[119] I. B. Bersuker, *Electronic structure and properties of transition metal compounds: introduction to the theory*. John Wiley & Sons, 2010.

[120] H. H. Kung, *Transition metal oxides: surface chemistry and catalysis*, vol. 45. Elsevier, 1989.

[121] A. Author, "Profile: Emerging investigators 2016: novel design strategies for new functional materials," *Journal of Materials Chemistry A*, vol. 4, no. 18, pp. 6670–6679, 2016.

[122] P. Ruffieux, J. Cai, N. C. Plumb, L. Patthey, D. Prezzi, A. Ferretti, E. Molinari, X. Feng, K. Mullen, C. A. Pignedoli, *et al.*, "Electronic structure of atomically precise graphene nanoribbons," *Acs Nano*, vol. 6, no. 8, pp. 6930–6935, 2012.

[123] Z. Sun, T. Liao, Y. Dou, S. M. Hwang, M.-S. Park, L. Jiang, J. H. Kim, and S. X. Dou, "Generalized self-assembly of scalable two-dimensional transition metal oxide nanosheets," *Nature communications*, vol. 5, 2014.

[124] G. Fiori, F. Bonaccorso, G. Iannaccone, T. Palacios, D. Neumaier, A. Seabaugh, S. K. Banerjee, and L. Colombo, "Electronics based on two-dimensional materials," *Nature nanotechnology*, vol. 9, no. 10, pp. 768–779, 2014.

[125] B. Sun, W. Hong, Z. Yan, H. Aziz, and Y. Li, "Record high electron mobility of 6.3 cm2v- 1s- 1 achieved for polymer semiconductors using a new building block," *Advanced Materials*, vol. 26, no. 17, pp. 2636–2642, 2014.

[126] B. Capozzi, J. Xia, O. Adak, E. J. Dell, Z.-F. Liu, J. C. Taylor, J. B. Neaton, L. M. Campos, and L. Venkataraman, "Single-molecule diodes with high rectification ratios through environmental control," *Nature nanotechnology*, vol. 10, no. 6, pp. 522–527, 2015.

[127] H. Zhu and Q. Li, "Novel molecular non-volatile memory: Application of redox-active molecules," *Applied Sciences*, vol. 6, no. 1, p. 7, 2015.

[128] C. Busche, L. Vilà-Nadal, J. Yan, H. N. Miras, D.-L. Long, V. P. Georgiev, A. Asenov, R. H. Pedersen, N. Gadegaard, M. M. Mirza, *et al.*, "Design and fabrication of memory devices based on nanoscale polyoxometalate clusters," *Nature*, vol. 515, no. 7528, pp. 545–549, 2014.

[129] S. R. Forrest, "The path to ubiquitous and low-cost organic electronic appliances on plastic," *Nature*, vol. 428, no. 6986, pp. 911–918, 2004.

[130] A. M. Hiszpanski and Y.-L. Loo, "Directing the film structure of organic semiconductors via post-deposition processing for transistor and solar cell applications," *Energy & Environmental Science*, vol. 7, no. 2, pp. 592–608, 2014.

[131] N. R. Tummala, Z. Zheng, S. G. Aziz, V. Coropceanu, and J.-L. Bredas, "Static and dynamic energetic disorders in the c60, pc61bm, c70, and pc71bm fullerenes," *The journal of physical chemistry letters*, vol. 6, no. 18, pp. 3657–3662, 2015.

[132] K. Efetov, *Supersymmetry in disorder and chaos*. Cambridge University Press, 1999.

[133] Y. Ji, D. F. Zeigler, D. S. Lee, H. Choi, A. K.-Y. Jen, H. C. Ko, and T.-W. Kim, "Flexible and twistable non-volatile memory cell array with all-organic one diode–one resistor architecture," *Nature communications*, vol. 4, 2013.

[134] K. J. Thorley and C. Risko, "Mapping the configuration dependence of electronic coupling in organic semiconductors," *Journal of Materials Chemistry C*, vol. 4, no. 17, pp. 3825–3832, 2016.

[135] G. Schull, T. Frederiksen, A. Arnau, D. Sánchez-Portal, and R. Berndt, "Atomic-scale engineering of electrodes for single-molecule contacts," *Nature nanotechnology*, vol. 6, no. 1, pp. 23–27, 2011.

[136] M. Iwamoto, Y.-S. Kwon, and T. Lee, *Nanoscale interface for organic electronics*. World Scientific, 2011.

[137] M. Stanisavljević, A. Schmid, and Y. Leblebici, *Reliability of Nanoscale Circuits and Systems: Methodologies and Circuit Architectures*. Springer Science & Business Media, 2010.

[138] D.-L. Long, R. Tsunashima, and L. Cronin, "Polyoxometalates: building blocks for functional nanoscale systems," *Angewandte Chemie International Edition*, vol. 49, no. 10, pp. 1736–1758, 2010.

[139] H. B. Akkerman, P. W. Blom, D. M. De Leeuw, and B. De Boer, "Towards molecular electronics with large-area molecular junctions," *Nature*, vol. 441, no. 7089, pp. 69–72, 2006.

[140] S. Park, G. Wang, B. Cho, Y. Kim, S. Song, Y. Ji, M.-H. Yoon, and T. Lee, "Flexible molecular-scale electronic devices," *Nature nanotechnology*, vol. 7, no. 7, pp. 438–442, 2012.

[141] C. P. Pradeep, D.-L. Long, G. N. Newton, Y.-F. Song, and L. Cronin, "Supramolecular metal oxides: Programmed hierarchical assembly of a protein-sized 21 kda [(c16h36n) 19 {H2NC (CH2O) 3P2V3W15O59} 4] 5- polyoxometalate assembly," *Angewandte Chemie*, vol. 120, no. 23, pp. 4460–4463, 2008.

[142] J.-M. Lehn and J. Sanders, "Supramolecular chemistry. concepts and perspectives," *Angewandte Chemie-English Edition*, vol. 34, no. 22, p. 2563, 1995.

[143] N. Glezos, A. M. Douvas, P. Argitis, F. Saurenbach, J. Chrost, and C. Livitsanos, "Electrical characterization of molecular monolayers containing tungsten polyoxometalates," *Microelectronic engineering*, vol. 83, no. 4, pp. 1757–1760, 2006.

[144] N. Glezos, A. M. Douvas, P. Argitis, F. Saurenbach, J. Chrost, and C. Livitsanos, "Electrical characterization of molecular monolayers containing tungsten polyoxometalates," *Microelectronic engineering*, vol. 83, no. 4, pp. 1757–1760, 2006.

[145] D. Velessiotis, A. Douvas, S. Athanasiou, B. Nilsson, G. Petersson, U. Södervall, G. Alestig, P. Argitis, and N. Glezos, "Molecular junctions made of tungsten-polyoxometalate self-assembled monolayers: Towards polyoxometalate-based molecular electronics devices," *Microelectronic Engineering*, vol. 88, no. 8, pp. 2775–2777, 2011.

[146] N. Tsuda, K. Nasu, A. Fujimori, and K. Siratori, *Electronic conduction in oxides*, vol. 94. Springer Science & Business Media, 2013.

[147] J. Meyer, S. Hamwi, M. Kröger, W. Kowalsky, T. Riedl, and A. Kahn, "Transition metal oxides for organic electronics: energetics, device physics and applications," *Advanced Materials*, vol. 24, no. 40, pp. 5408–5427, 2012.

[148] J.-L. Brédas, J. P. Calbert, D. da Silva Filho, and J. Cornil, "Organic semiconductors: A theoretical characterization of the basic parameters governing charge transport," *Proceedings of the National Academy of Sciences*, vol. 99, no. 9, pp. 5804–5809, 2002.

[149] G. Giri, E. Verploegen, S. C. Mannsfeld, S. Atahan-Evrenk, D. H. Kim, S. Y. Lee, H. A. Becerril, A. Aspuru-Guzik, M. F. Toney, and Z. Bao, "Tuning charge transport in solution-sheared organic semiconductors using lattice strain," *Nature*, vol. 480, no. 7378, pp. 504–508, 2011.

[150] M. T. Pope, *Heteropoly and isopoly oxometalates*, vol. 8. Springer Verlag, 1983.

[151] J. J. Borrás-Almenar, E. Coronado, A. Müller, and M. Pope, *Polyoxometalate molecular science*, vol. 98. Springer Science & Business Media, 2003.

[152] M. Pope and A. Müller, *Polyoxometalates: from platonic solids to anti-retroviral activity*, vol. 10. Springer Science & Business Media, 2012.

[153] N. Koch, N. Ueno, and A. T. S. Wee, *The molecule-metal interface*. John Wiley & Sons, 2013.

[154] F. Secheresse, *Polyoxometalate Chemistry: Some Recent Trends*, vol. 8. World Scientific, 2013.

[155] M. Lonfat, B. Marsen, and K. Sattler, "The energy gap of carbon clusters studied by scanning tunneling spectroscopy," *Chemical physics letters*, vol. 313, no. 3, pp. 539–543, 1999.

[156] M. Pope and A. Müller, *Polyoxometalate chemistry from topology via self-assembly to applications*. Springer Science & Business Media, 2001.

[157] J. M. Pigga, M. L. Kistler, C.-Y. Shew, M. R. Antonio, and T. Liu, "Counterion distribution around hydrophilic molecular macroanions: The source of the attractive force in self-assembly," *Angewandte Chemie International Edition*, vol. 48, no. 35, pp. 6538–6542, 2009.

[158] Z. Zhang, T. Murayama, M. Sadakane, H. Ariga, N. Yasuda, N. Sakaguchi, K. Asakura, and W. Ueda, "Ultrathin inorganic molecular nanowire based on polyoxometalates," *Nature communications*, vol. 6, 2015.

[159] H. Li, S. Pang, S. Wu, X. Feng, K. Mullen, and C. Bubeck, "Layer-by-layer assembly and uv photoreduction of graphene–polyoxometalate composite films for electronics," *Journal of the American Chemical Society*, vol. 133, no. 24, pp. 9423–9429, 2011.

[160] A. M. Douvas, E. Makarona, N. Glezos, P. Argitis, J. A. Mielczarski, and E. Mielczarski, "Polyoxometalate-based layered structures for charge transport control in molecular devices," *ACS nano*, vol. 2, no. 4, pp. 733–742, 2008.

[161] J. M. Poblet, X. López, and C. Bo, "Ab initio and dft modelling of complex materials: towards the understanding of electronic and magnetic properties of polyoxometalates," *Chemical Society Reviews*, vol. 32, no. 5, pp. 297–308, 2003.

[162] M. Vasilopoulou, A. M. Douvas, L. C. Palilis, S. Kennou, and P. Argitis, "Old metal oxide clusters in new applications: spontaneous reduction of keggin and dawson polyoxometalate layers by a metallic

electrode for improving efficiency in organic optoelectronics," *Journal of the American Chemical Society*, vol. 137, no. 21, pp. 6844–6856, 2015.

[163] E. Davis and N. Mott, "Conduction in non-crystalline systems v. conductivity, optical absorption and photoconductivity in amorphous semiconductors," *Philosophical Magazine*, vol. 22, no. 179, pp. 0903–0922, 1970.

[164] J. Tauc, "Optical properties and electronic structure of amorphous ge and si," *Materials Research Bulletin*, vol. 3, no. 1, pp. 37–46, 1968.

[165] N. Suaud, A. Gaita-Arino, J. M. Clemente-Juan, J. Sánchez-Marín, and E. Coronado, "Electron delocalization in mixed-valence keggin polyoxometalates. ab initio calculation of the local effective transfer integrals and its consequences on the spin coupling," *Journal of the American Chemical Society*, vol. 124, no. 50, pp. 15134–15140, 2002.

[166] M. Sadakane and E. Steckhan, "Electrochemical properties of polyoxometalates as electrocatalysts," *Chemical Reviews*, vol. 98, no. 1, pp. 219–238, 1998.

[167] R. Thouvenot, M. Fournier, R. Franck, and C. Rocchiccioli-Deltcheff, "Vibrational investigations of polyoxometalates. 3. isomerism in molybdenum (vi) and tungsten (vi) compounds related to the keggin structure," *Inorganic Chemistry*, vol. 23, no. 5, pp. 598–605, 1984.

[168] X. Zhang, C. Zhang, H. Guo, W. Huang, T. Polenova, L. C. Francesconi, and D. L. Akins, "Optical spectra of a novel polyoxometalate occluded within modified mcm-41," *The Journal of Physical Chemistry B*, vol. 109, no. 41, pp. 19156–19160, 2005.

[169] J. Yarwood, R. Douthwaite, and S. Duckett, *Spectroscopic properties of inorganic and organometallic compounds*, vol. 40. Royal Society of Chemistry, 2009.

[170] B. Stuart, *Infrared spectroscopy*. Wiley Online Library, 2005.

[171] C. Tsai, K.-H. Li, J. Campbell, B. Hance, M. Arendt, J. White, S.-L. Yau, and A. Bard, "Effects of illumination during anodization of porous silicon," *Journal of electronic materials*, vol. 21, no. 10, pp. 995–1000, 1992.

[172] D. K. Ferry, S. M. Goodnick, and J. Bird, *Transport in nanostructures*. Cambridge University Press, 2009.

[173] A.-L. Barabási and H. E. Stanley, *Fractal concepts in surface growth*. Cambridge university press, 1995.

[174] T. A. Witten and L. M. Sander, "Diffusion-limited aggregation," *Physical Review B*, vol. 27, no. 9, p. 5686, 1983.

[175] L. Leonat, G. Sbârcea, and I. V. Branzoi, "Cyclic voltammetry for energy levels estimation of organic materials," *UPB Sci Bull Ser B*, vol. 75, pp. 111–118, 2013.

[176] M. Nishioka, *Transport properties of carbon based devices*. ProQuest, 2008.

[177] V. M. Agranovich and G. C. La Rocca, *Organic nanostructures: science and applications*, vol. 149. IOS Press, 2002.

[178] D. Skoog, S. Crouch, and F. Holler, "Analytical methods," *Principles of Instrumental Analysis. California Cengage Learning Inc.,*, pp. 6–19, 2006.

[179] E. Katelhon, C. Batchelor-McAuley, and R. G. Compton, "Voltammetric peak heights of the proton–hydrogen redox couple: A comprehensive analysis," *The Journal of Physical Chemistry C*, vol. 119, no. 40, pp. 23203–23210, 2015.

[180] M. W. Reeks, "Stokes-einstein equation,"

[181] M. Smoluchowski, "Contribution à la théorie de l'endosmose électrique et de quelques phénomènes corrélatifs," *Pisma Mariana Smoluchowskiego*, vol. 1, no. 1, pp. 403–420, 1924.

[182] N. F. Atta, A. Galal, and S. M. Ali, "Determination of the diffusion coefficients for charge transfer through homo-, bilayered-and copolymers of 3-methyl-thiophene and n-methylpyrrole.," *Int. J. Electrochem. Sci*, vol. 7, pp. 785–805, 2012.

[183] A. Balliou, A. Douvas, P. Normand, D. Tsikritzis, S. Kennou, P. Argitis, and N. Glezos, "Tungsten polyoxometalate molecules as active nodes for dynamic carrier exchange in hybrid molecular/semiconductor capacitors," *Journal of Applied Physics*, vol. 116, no. 14, p. 143703, 2014.

[184] Y. Komoto, S. Fujii, H. Nakamura, T. Tada, T. Nishino, and M. Kiguchi, "Resolving metal-molecule interfaces at single-molecule junctions," *Scientific reports*, vol. 6, 2016.

[185] H. Basch, R. Cohen, and M. A. Ratner, "Interface geometry and molecular junction conductance: Geometric fluctuation and stochastic switching," *Nano letters*, vol. 5, no. 9, pp. 1668–1675, 2005.

[186] S. D. Kevan, *Angle-resolved photoemission: theory and current applications*, vol. 74. Elsevier, 1992.

[187] D. Barreca, G. Carta, A. Gasparotto, G. Rossetto, E. Tondello, and P. Zanella, "A study of nanophase tungsten oxides thin films by xps," *Surface Science Spectra*, vol. 8, no. 4, pp. 258–267, 2001.

[188] C. Carbone, M. Veronese, P. Moras, S. Gardonio, C. Grazioli, P. Zhou, O. Rader, A. Varykhalov, C. Krull, T. Balashov, *et al.*, "Correlated electrons step by step: itinerant-to-localized transition of fe impurities in free-electron metal hosts," *Physical review letters*, vol. 104, no. 11, p. 117601, 2010.

[189] M. J. Son, S. Kim, S. Kwon, and J. W. Kim, "Interface electronic structures of organic light-emitting diodes with wo 3 interlayer: a study by photoelectron spectroscopy," *Organic Electronics*, vol. 10, no. 4, pp. 637–642, 2009.

[190] L. Fleming, C. Fulton, G. Lucovsky, J. Rowe, M. Ulrich, and J. Lüning, "Local bonding analysis of the valence and conduction band features of tio2," *Journal of Applied Physics*, vol. 102, no. 3, p. 033707, 2007.

[191] T. Tran, I. Beloborodov, J. Hu, X. Lin, T. Rosenbaum, and H. Jaeger, "Sequential tunneling and inelastic cotunneling in nanoparticle arrays," *Physical Review B*, vol. 78, no. 7, p. 075437, 2008.

[192] I. Beloborodov, A. Lopatin, V. Vinokur, and K. Efetov, "Granular electronic systems," *Reviews of Modern Physics*, vol. 79, no. 2, p. 469, 2007.

[193] D. C. Cabra, A. Honecker, and P. Pujol, *Modern theories of many-particle systems in condensed matter physics*, vol. 843. Springer Science & Business Media, 2012.

[194] H. Tompkins and E. A. Irene, *Handbook of ellipsometry*. William Andrew, 2005.

[195] N. Ravindra, P. Ganapathy, and J. Choi, "Energy gap–refractive index relations in semiconductors–an overview," *Infrared physics & technology*, vol. 50, no. 1, pp. 21–29, 2007.

[196] T. Moss, "Relations between the refractive index and energy gap of semiconductors," *Physica status solidi (b)*, vol. 131, no. 2, pp. 415–427, 1985.

[197] A. Balliou, A. Douvas, P. Normand, D. Tsikritzis, S. Kennou, P. Argitis, and N. Glezos, "Tungsten polyoxometalate molecules as active nodes for dynamic carrier exchange in hybrid molecular/semiconductor capacitors," *Journal of Applied Physics*, vol. 116, no. 14, p. 143703, 2014.

[198] S. Baskoutas and A. F. Terzis, "Size-dependent band gap of colloidal quantum dots," *Journal of applied physics*, vol. 99, no. 1, p. 013708, 2006.

[199] C. Dekker *et al.*, "Carbon nanotubes as molecular quantum wires," *Physics today*, vol. 52, pp. 22–30, 1999.

[200] W. Yan, L. Meng, M. Liu, J.-B. Qiao, Z.-D. Chu, R.-F. Dou, Z. Liu, J.-C. Nie, D. G. Naugle, and L. He, "Angle-dependent van hove singularities and their breakdown in twisted graphene bilayers," *Physical Review B*, vol. 90, no. 11, p. 115402, 2014.

[201] P. Bhadrachalam, R. Subramanian, V. Ray, L.-C. Ma, W. Wang, J. Kim, K. Cho, and S. J. Koh, "Energy-filtered cold electron transport at room temperature," *Nature communications*, vol. 5, 2014.

[202] I. Zacharia, D. Goldhaber-Gordon, G. Granger, M. Kastner, Y. B. Khavin, H. Shtrikman, D. Mahalu, and U. Meirav, "Temperature dependence of fano line shapes in a weakly coupled single-electron transistor," *Physical Review B*, vol. 64, no. 15, p. 155311, 2001.

[203] H. Grabert, G.-L. Ingold, M. H. Devoret, D. Estève, H. Pothier, and C. Urbina, "Single electron tunneling rates in multijunction circuits," *Zeitschrift für Physik B Condensed Matter*, vol. 84, no. 1, pp. 143–155, 1991.

[204] L. L. Sohn, L. P. Kouwenhoven, and G. Schön, *Mesoscopic electron transport*, vol. 345. Springer Science & Business Media, 2013.

[205] L. Jdira, P. Liljeroth, E. Stoffels, D. Vanmaekelbergh, and S. Speller, "Size-dependent single-particle energy levels and interparticle coulomb interactions in cdse quantum dots measured by scanning tunneling spectroscopy," *Physical Review B*, vol. 73, no. 11, p. 115305, 2006.

[206] A. Carvalho, R. Ribeiro, and A. C. Neto, "Band nesting and the optical response of two-dimensional semiconducting transition metal dichalcogenides," *Physical Review B*, vol. 88, no. 11, p. 115205, 2013.

[207] A. V. Kolobov and J. Tominaga, *Two-Dimensional Transition-Metal Dichalcogenides*, vol. 239. Springer, 2016.

[208] J. Brewer and M. Gill, *Nonvolatile memory technologies with emphasis on flash: a comprehensive guide to understanding and using flash memory devices*. Wiley-IEEE Press, 2008.

[209] M. Ratner, "A brief history of molecular electronics," *Nature nanotechnology*, vol. 8, no. 6, pp. 378–381, 2013.

[210] W. F. Smith, "Organic electronics: Self-assembly is ready to roll," *Nature nanotechnology*, vol. 2, no. 2, pp. 77–78, 2007.

[211] D. Xiang, X. Wang, C. Jia, T. Lee, and X. Guo, "Molecular-scale electronics: from concept to function," *Chemical reviews*, vol. 116, no. 7, pp. 4318–4440, 2016.

[212] H. B. Akkerman, P. W. Blom, D. M. De Leeuw, and B. De Boer, "Towards molecular electronics with large-area molecular junctions," *Nature*, vol. 441, no. 7089, pp. 69–72, 2006.

[213] S. P. Cummings, J. Savchenko, and T. Ren, "Functionalization of flat si surfaces with inorganic compoundstowards molecular cmos hybrid devices," *Coordination Chemistry Reviews*, vol. 255, no. 15, pp. 1587–1602, 2011.

[214] D. Velessiotis, A. Douvas, S. Athanasiou, B. Nilsson, G. Petersson, U. Södervall, G. Alestig, P. Argitis, and N. Glezos, "Molecular junctions made of tungsten-polyoxometalate self-assembled monolayers: Towards polyoxometalate-based molecular electronics devices," *Microelectronic Engineering*, vol. 88, no. 8, pp. 2775–2777, 2011.

[215] A. M. Douvas, E. Makarona, N. Glezos, P. Argitis, J. A. Mielczarski, and E. Mielczarski, "Polyoxometalate-based layered structures for charge transport control in molecular devices," *ACS nano*, vol. 2, no. 4, pp. 733–742, 2008.

[216] E. Makarona, E. Kapetanakis, D. Velessiotis, A. Douvas, P. Argitis, P. Normand, T. Gotszalk, M. Woszczyna, and N. Glezos, "Vertical devices of self-assembled hybrid organic/inorganic monolayers based on tungsten polyoxometalates," *Microelectronic Engineering*, vol. 85, no. 5, pp. 1399–1402, 2008.

[217] J. Hong, K. Lowack, J. Schmitt, and G. Decher, "Layer-by-layer deposited multilayer assemblies of polyelectrolytes and proteins: from ultrathin films to protein arrays," in *Trends in Colloid and Interface Science VII*, pp. 98–102, Springer, 1993.

[218] A. Hiskia, A. Mylonas, and E. Papaconstantinou, "Comparison of the photoredox properties of polyoxometallates and semiconducting particles," *Chemical Society Reviews*, vol. 30, no. 1, pp. 62–69, 2001.

[219] H. Fujiwara, *Spectroscopic ellipsometry: principles and applications*. John Wiley & Sons, 2007.

[220] F. Bussolotti, L. Lozzi, M. Passacantando, S. La Rosa, S. Santucci, and L. Ottaviano, "Surface electronic properties of polycrystalline wo 3 thin films: a study by core level and valence band photoemission," *Surface Science*, vol. 538, no. 1, pp. 113–123, 2003.

[221] H. Taketa, S. Katsuki, K. Eguchi, T. Seiyama, and N. Yamazoe, "Electronic structure and redox mechanism of dodecamolybdophosphate," *The Journal of Physical Chemistry*, vol. 90, no. 13, pp. 2959–2962, 1986.

[222] K. Eguchi, Y. Toyozawa, N. Yamazoe, and T. Seiyama, "An infrared study on the reduction processes of dodecamolybdophosphates," *Journal of Catalysis*, vol. 83, no. 1, pp. 32–41, 1983.

[223] Y. Baer, "The natural energy scale for xps spectra of metals," *Solid State Communications*, vol. 19, no. 7, pp. 669–671, 1976.

[224] N.-M. Park, S. H. Kim, S. Maeng, and S.-J. Park, "High negative differential resistance in silicon quantum dot metal-insulator-semiconductor structure," *Applied physics letters*, vol. 89, no. 15, p. 153117, 2006.

[225] W. Mönch, "Role of virtual gap states and defects in metal-semiconductor contacts," in *Electronic Structure of Metal-Semiconductor Contacts*, pp. 224–227, Springer, 1990.

[226] V. Mosser, D. Weiss, K. Klitzing, K. Ploog, and G. Weimann, "Density of states of gaas-algaas-heterostructures deduced from temperature dependent magnetocapacitance measurements," *Solid state communications*, vol. 58, no. 1, pp. 5–7, 1986.

[227] K. Tytko, J. Mehmke, and S. Fischer, "Bonding and charge distribution in isopolyoxometalate ions and relevant oxidesa bond valence

approach," in *Bonding and Charge Distribution in Polyoxometalates: A Bond Valence Approach*, pp. 129–321, Springer, 1999.

[228] W. Mönch, *Electronic properties of semiconductor interfaces*, vol. 43. Springer Science & Business Media, 2013.

[229] Y. Peter and M. Cardona, *Fundamentals of semiconductors: physics and materials properties*. Springer Science & Business Media, 2010.

[230] N. Glezos, P. Argitis, D. Velessiotis, and C. Diakoumakos, "Tunneling transport in polyoxometalate based composite materials," *Applied physics letters*, vol. 83, no. 3, pp. 488–490, 2003.

[231] P. Nagpal and V. I. Klimov, "Role of mid-gap states in charge transport and photoconductivity in semiconductor nanocrystal films," *Nature communications*, vol. 2, p. 486, 2011.

[232] S. Pandey, D. Cavalcoli, B. Fraboni, A. Cavallini, T. Brazzini, and F. Calle, "Role of surface trap states on two-dimensional electron gas density in inaln/aln/gan heterostructures," *Applied Physics Letters*, vol. 100, no. 15, p. 152116, 2012.

[233] S. M. Sze and K. K. Ng, *Physics of semiconductor devices*. John wiley & sons, 2006.

[234] W. R. Harrell and J. Frey, "Observation of poole–frenkel effect saturation in sio 2 and other insulating films," *Thin solid films*, vol. 352, no. 1, pp. 195–204, 1999.

[235] J. Sparkes, *Semiconductor devices*. CRC Press, 1994.

[236] V. Butko, J. Lashley, and A. Ramirez, "Low-temperature field effect in a crystalline organic material," *Physical Review B*, vol. 72, no. 8, p. 081312, 2005.

[237] V. Ioannou-Sougleridis and A. Nassiopoulou, "Dynamic charge transfer effects in two-dimensional silicon nanocrystal layers embedded within sio2," *Journal of Applied Physics*, vol. 106, no. 5, p. 054508, 2009.

[238] C. Busseret, S. Ferraton, L. Montès, and J. Zimmermann, "A three charge-states model for silicon nanocrystals nonvolatile memories," *IEEE transactions on electron devices*, vol. 53, no. 1, pp. 14–22, 2006.

[239] L. C. Palilis, M. Vasilopoulou, A. M. Douvas, D. G. Georgiadou, S. Kennou, N. A. Stathopoulos, V. Constantoudis, and P. Argitis, "Solution processable tungsten polyoxometalate as highly effective cathode interlayer for improved efficiency and stability polymer solar cells," *Solar Energy Materials and Solar Cells*, vol. 114, pp. 205–213, 2013.

[240] Y. Shi, X. Yuan, J. Wu, H. Bu, H. Yang, P. Han, Y. Zheng, and T. Hiramoto, "Dynamics of tunneling into charge-tunable si quantum dots," *Superlattices and Microstructures*, vol. 28, no. 5, pp. 387–392, 2000.

[241] J. A. Fernández, P. Miró, J. Bonet-Ávalos, C. Bo, and J. M. Poblet, "Electronic structure and surface properties of the mixed-valence doughnut shaped polyoxomolybdate nanocapsule mo 57 v 6," *Inorganica Chimica Acta*, vol. 363, no. 15, pp. 4368–4373, 2010.

[242] D. K. Ferry, S. M. Goodnick, and J. Bird, *Transport in nanostructures*. Cambridge University Press, 2009.

[243] M. T. Pope and G. M. Varga Jr, "Heteropoly blues. i. reduction stoichiometries and reduction potentials of some 12-tungstates," *Inorganic Chemistry*, vol. 5, no. 7, pp. 1249–1254, 1966.

[244] M. Zerbst, "Relaxation effects at semiconductor-insulator interfaces," *NASA STI/Recon Technical Report N*, vol. 78, 1977.

[245] D. K. Schroder, *Semiconductor material and device characterization*. John Wiley & Sons, 2006.

[246] J. Kang and D. Schroder, "The pulsed mis capacitor. a critical review," *Physica status solidi (a)*, vol. 89, no. 1, pp. 13–43, 1985.

[247] P. Dubruel, *Cationic Polymers in Regenerative Medicine*. Royal Society of Chemistry, 2014.

[248] R. L. Davidson and M. Sittig, *Water-soluble resins*. Reinhold New York, 1962.

[249] B. Gao, P. Jiang, F. An, S. Zhao, and Z. Ge, "Studies on the surface modification of diatomite with polyethyleneimine and trapping effect of the modified diatomite for phenol," *Applied surface science*, vol. 250, no. 1, pp. 273–279, 2005.

[250] V. Ajith, G. Suman, P. Kishore, J. Madhuri, G.-G. Maribel, and B. Rafael, "Use of polyethyleneimine polymer in cell culture as attachment factor and lipofection enhancer," 2004.

[251] M. J. Madou, *Fundamentals of microfabrication: the science of miniaturization*. CRC press, 2002.

[252] I. Mejia and M. Estrada, "Characterization of polymethyl methacrylate (pmma) layers for otfts gate dielectric," in *Devices, Circuits and Systems, Proceedings of the 6th International Caribbean Conference on*, pp. 375–377, IEEE, 2006.

[253] N. F. Mott and E. A. Davis, *Electronic processes in non-crystalline materials*. OUP Oxford, 2012.

[254] K. Morigaki, *Physics of amorphous semiconductors*. World Scientific, 1999.

[255] D. Adler, B. Schwartz, and M. C. Steele, *Physical properties of amorphous materials*. Springer Science & Business Media, 2013.

[256] J. Singh and K. Shimakawa, *Advances in amorphous semiconductors*. CRC Press, 2003.

[257] P. Dimitrakis, P. Normand, C. Bonafos, E. Papadomanolaki, and E. Iliopoulos, "Gan quantum-dots integrated in the gate dielectric of metal-oxide-semiconductor structures for charge-storage applications," *Applied Physics Letters*, vol. 102, no. 5, p. 053117, 2013.

[258] K.-D. Suh, B.-H. Suh, Y.-H. Lim, J.-K. Kim, Y.-J. Choi, Y.-N. Koh, S.-S. Lee, S.-C. Kwon, B.-S. Choi, J.-S. Yum, *et al.*, "A 3.3 v 32 mb nand flash memory with incremental step pulse programming scheme," *IEEE Journal of Solid-State Circuits*, vol. 30, no. 11, pp. 1149–1156, 1995.

[259] Executive, "International technology roadmap for semiconductors: 2013 edition executive summary," *Semiconductor Industry Association, San Francisco, CA*, 2013.

[260] C.-W. Tseng, D.-C. Huang, and Y.-T. Tao, "Organic transistor memory with a charge storage molecular double-floating-gate monolayer," *ACS applied materials & interfaces*, vol. 7, no. 18, pp. 9767–9775, 2015.

[261] H.-Y. Chi, H.-W. Hsu, S.-H. Tung, and C.-L. Liu, "Nonvolatile organic field-effect transistors memory devices using supramolecular block copolymer/functional small molecule nanocomposite electret," *ACS applied materials & interfaces*, vol. 7, no. 10, pp. 5663–5673, 2015.

[262] B. Radha, A. A. Sagade, and G. U. Kulkarni, "Metal-organic molecular device for non-volatile memory storage," *Applied Physics Letters*, vol. 105, no. 8, 2014.

[263] J. Shaw, Y.-W. Zhong, K. J. Hughes, T.-H. Hou, H. Raza, S. Rajwade, J. Bellfy, J. R. Engstrom, H. D. Abruña, and E. C. Kan, "Integration of self-assembled redox molecules in flash memory devices," *Electron Devices, IEEE Transactions on*, vol. 58, no. 3, pp. 826–834, 2011.

[264] W. Tang, H. Shi, G. Xu, B. S. Ong, Z. D. Popovic, J. Deng, J. Zhao, and G. Rao, "Memory effect and negative differential resistance by electrode-induced two-dimensional single-electron tunneling in molecular and organic electronic devices," *Advanced Materials*, vol. 17, no. 19, pp. 2307–2311, 2005.

[265] J. E. Green, J. W. Choi, A. Boukai, Y. Bunimovich, E. Johnston-Halperin, E. DeIonno, Y. Luo, B. A. Sheriff, K. Xu, Y. Shin, and Shik, "A 160-kilobit molecular electronic memory patterned at 1011 bits per square centimetre," *Nature*, vol. 445, no. 7126, pp. 414–417, 2007.

[266] C. Wang, P. Gu, B. Hu, and Q. Zhang, "Recent progress in organic resistance memory with small molecules and inorganic–organic hybrid polymers as active elements," *J. Mater. Chem. C*, vol. 3, no. 39, pp. 10055–10065, 2015.

[267] P.-Y. Gu, F. Zhou, J. Gao, G. Li, C. Wang, Q.-F. Xu, Q. Zhang, and J.-M. Lu, "Synthesis, characterization, and nonvolatile ternary memory behavior of a larger heteroacene with nine linearly fused rings and two different heteroatoms," *Journal of the American Chemical Society*, vol. 135, no. 38, pp. 14086–14089, 2013.

[268] M. Khan, U. S. Bhansali, and H. Alshareef, "High-performance nonvolatile organic ferroelectric memory on banknotes," *Advanced Materials*, vol. 24, no. 16, pp. 2165–2170, 2012.

[269] C. Simão, M. Mas-Torrent, N. Crivillers, V. Lloveras, J. M. Artés, P. Gorostiza, J. Veciana, and C. Rovira, "A robust molecular platform for non-volatile memory devices with optical and magnetic responses," *Nature Chemistry*, vol. 3, no. 5, pp. 359–364, 2011.

[270] D. A. Ryndyk, P. DAmico, and K. Richter, "Single-spin polaron memory effect in quantum dots and single molecules," *Physical Review B*, vol. 81, no. 11, p. 115333, 2010.

[271] S. Lai, "Flash memories: Successes and challenges," *IBM Journal of Research and Development*, vol. 52, pp. 529–535, July 2008.

[272] F. Volatron, J.-M. Noël, C. Rinfray, P. Decorse, C. Combellas, F. Kanoufi, and A. Proust, "Electron transfer properties of a monolayer of hybrid polyoxometalates on silicon," *Journal of Materials Chemistry C*, 2015.

[273] A. H. Flood, E. W. Wong, and J. F. Stoddart, "Models of charge transport and transfer in molecular switch tunnel junctions of bistable catenanes and rotaxanes," *Chemical physics*, vol. 324, no. 1, pp. 280–290, 2006.

[274] H. Zhu, C. A. Hacker, S. J. Pookpanratana, C. A. Richter, H. Yuan, H. Li, O. Kirillov, D. E. Ioannou, and Q. Li, "Non-volatile memory with self-assembled ferrocene charge trapping layer," *Applied Physics Letters*, vol. 103, no. 5, 2013.

[275] B. Hu, C. Wang, J. Wang, J. Gao, K. Wang, J. Wu, G. Zhang, W. Cheng, B. Venkateswarlu, M. Wang, P. S. Lee, and Q. Zhang, "Inorganic–organic hybrid polymer with multiple redox for high-density data storage," *Chemical Science*, vol. 5, no. 9, pp. 3404–3408, 2014.

[276] D. A. Buchanan, "Scaling the gate dielectric: materials, integration, and reliability," *IBM Journal of Research and Development*, vol. 43, no. 3, pp. 245–264, 1999.

[277] M. Groner and S. George, "High-k dielectrics grown by atomic layer deposition: Capacitor and gate applications," *Interlayer Dielectrics for Semiconductor Technologies*, vol. 1, p. 327, 2003.

[278] M. Bohr, R. Chau, T. Ghani, and K. Mistry, "The high-k solution," *IEEE Spectrum*, vol. 44, no. 10, pp. 23–29, 2007.

[279] A. H. Flood, J. F. Stoddart, D. W. Steuerman, and J. R. Heath, "Whence molecular electronics?," *Science*, vol. 306, no. 5704, pp. 2055–2056, 2004.

[280] E. Lörtscher, "Wiring molecules into circuits," *Nature nanotechnology*, vol. 8, no. 6, pp. 381–384, 2013.

[281] J. R. Heath, P. J. Kuekes, G. S. Snider, and R. S. Williams, "A defect-tolerant computer architecture: Opportunities for nanotechnology," *Science*, vol. 280, no. 5370, pp. 1716–1721, 1998.

[282] G. S. Rose, A. C. Cabe, N. Gergel-Hackett, N. Majumdar, M. R. Stan, J. C. Bean, L. R. Harriott, Y. Yao, and J. M. Tour, "Design approaches for hybrid cmos/molecular memory based on experimental device data," in *Proceedings of the 16th ACM Great Lakes symposium on VLSI*, pp. 2–7, ACM, 2006.

[283] J. Niederhausen, P. Amsalem, J. Frisch, A. Wilke, A. Vollmer, R. Rieger, K. Müllen, J. Rabe, and N. Koch, "Tuning hole-injection barriers at organic/metal interfaces exploiting the orientation of a molecular acceptor interlayer," *Physical Review B*, vol. 84, no. 16, p. 165302, 2011.

[284] A. A. Demkov and A. B. Posadas, *Integration of functional oxides with semiconductors*. Springer, 2014.

[285] X. Yu, T. J. Marks, and A. Facchetti, "Metal oxides for optoelectronic applications," *Nature materials*, vol. 15, no. 4, pp. 383–396, 2016.

[286] G. Alers, D. Werder, Y. Chabal, H. Lu, E. Gusev, E. Garfunkel, T. Gustafsson, and R. Urdahl, "Intermixing at the tantalum oxide/silicon interface in gate dielectric structures," *Applied Physics Letters*, vol. 73, no. 11, pp. 1517–1519, 1998.

[287] D. S. E. Atanassova, "X-ray photoelectron spectroscopy of thermal thin $ta_2o_5$ films on si," *Applied Surface Science*, vol. 135, pp. 71–82, 1998.

[288] Y. S. Kim and Y. Shimogaki, "X-ray photoelectron spectroscopic characterization of the adhesion behavior of chemical vapor deposited copper films," *Journal of Vacuum Science and Technology A*, vol. 19, no. 5, pp. 2642–2651, 2001.

[289] W. Song, J. Ying, W. He, V.-Q. Zhuo, R. Ji, H. Xie, S. Ng, S. L. Ng, and Y. Jiang, "Nano suboxide layer generated in ta2o5 by ar+ ion irradiation," *Applied Physics Letters*, vol. 106, no. 3, p. 031602, 2015.

[290] G. Dhanaraj, K. Byrappa, V. Prasad, and M. Dudley, *Springer handbook of crystal growth*. Springer Science & Business Media, 2010.

[291] R. Nyholm, A. Berndtsson, and N. Martensson, "Core level binding energies for the elements hf to bi (z= 72-83)," *Journal of Physics C: Solid State Physics*, vol. 13, no. 36, p. L1091, 1980.

[292] D. M. Riffe and G. Wertheim, "Ta (110) surface and subsurface core-level shifts and 4 f 7/2 line shapes," *Physical Review B*, vol. 47, p. 6672, 1993.

[293] W. Song, J. Ying, W. He, Y.-Q. Zhuo, R. Ji, H. Xie, S. Ng, S. L. Ng, and Y. Jiang, "Nano suboxide layer generated in ta2o5 by ar+ ion irradiation," *Applied Physics Letters*, vol. 106, no. 3, p. 031602, 2015.

[294] G. Dhanaraj, K. Byrappa, V. V. Prasad, and M. Dudley, "Crystal growth techniques and characterization: An overview," in *Springer Handbook of Crystal Growth*, p. 955, Springer, 2010.

[295] A. Muto, F. Yano, Y. Sugawara, and S. Iijima, "The study of ultrathin tantalum oxide films before and after annealing with x-ray photoelectron spectroscopy," *Japanese journal of applied physics*, vol. 33, no. 5R, p. 2699, 1994.

[296] R. Eason, *Pulsed laser deposition of thin films: applications-led growth of functional materials*. John Wiley & Sons, 2007.

[297] M. T. Pope and A. Müller, "Polyoxometalate chemistry: An old field with new dimensions in several disciplines," *Angewandte Chemie International Edition in English*, vol. 30, no. 1, pp. 34–48, 1991.

[298] M. Ammam, "Polyoxometalates: formation, structures, principal properties, main deposition methods and application in sensing," *Journal of Materials Chemistry A*, vol. 1, no. 21, pp. 6291–6312, 2013.

[299] A. Huang, X. Zheng, Z. Xiao, M. Wang, Z. Di, and P. Chu, "Interface dipole engineering in metal gate/high-k stacks," *Chinese Science Bulletin*, vol. 57, no. 22, pp. 2872–2878, 2012.

[300] O. Yaffe, S. Pujari, O. Sinai, A. Vilan, H. Zuilhof, A. Kahn, L. Kronik, H. Cohen, and D. Cahen, "Effect of doping density on the charge rearrangement and interface dipole at the molecule-silicon interface," *The Journal of Physical Chemistry C*, vol. 117, no. 43, pp. 22422–22427, 2013.

[301] A.-J. Lim, J. Hou, D.-L. Kwong, and Y.-C. Yeo, "Manipulating interface dipoles of opposing polarity for work function engineering within a single metal gate stack," in *Electron Devices Meeting, 2008. IEDM 2008. IEEE International*, pp. 1–4, Dec 2008.

[302] N. Miyata, "Study of direct-contact hfo2/si interfaces," *Materials*, vol. 5, no. 3, pp. 512–527, 2012.

[303] A. Balliou, A. Douvas, P. Normand, D. Tsikritzis, S. Kennou, P. Argitis, and N. Glezos, "Tungsten polyoxometalate molecules

as active nodes for dynamic carrier exchange in hybrid molecular/semiconductor capacitors," *Journal of Applied Physics*, vol. 116, no. 14, p. 143703, 2014.

[304] A. M. Douvas, E. Makarona, N. Glezos, P. Argitis, J. A. Mielczarski, and E. Mielczarski, "Polyoxometalate-based layered structures for charge transport control in molecular devices," *ACS Nano*, vol. 2, no. 4, pp. 733–742, 2008.

[305] T. He, J. He, M. Lu, B. Chen, H. Pang, W. F. Reus, W. M. Nolte, D. P. Nackashi, P. D. Franzon, and J. M. Tour, "Controlled modulation of conductance in silicon devices by molecular monolayers," *Journal of the American Chemical Society*, vol. 128, no. 45, pp. 14537–14541, 2006.

[306] C. Busche, L. Vilà-Nadal, J. Yan, H. N. Miras, D.-L. Long, V. P. Georgiev, A. Asenov, R. H. Pedersen, N. Gadegaard, M. M. Mirza, D. J. Paul, J. M. Poblet, and L. Cronin, "Design and fabrication of memory devices based on nanoscale polyoxometalate clusters," *Nature*, vol. 515, no. 7528, pp. 545–549, 2014.

[307] C. Mahata, I.-K. Oh, C. M. Yoon, C. W. Lee, J. Seo, H. Algadi, M.-H. Sheen, Y.-W. Kim, H. Kim, and T. Lee, "The impact of atomic layer deposited sio 2 passivation for high-k ta 1- x zr x o on the inp substrate," *Journal of Materials Chemistry C*, vol. 3, no. 39, pp. 10293–10301, 2015.

[308] S. K. Zhang, Z. W. Fu, L. Ke, F. Lu, Q. Z. Qin, and X. Wang, "Properties of interface states at ta2o5/n-si interfaces," *Journal of Applied Physics*, vol. 84, no. 1, pp. 335–338, 1998.

[309] P. Broekmann, K. H. Doetz, and C. A. Schalley, eds., *Templates in Chemistry III*, vol. 287. Springer Berlin Heidelberg, 2009.

[310] H. G. Oehzelt Martin, Koch Norbert, "Organic semiconductor density of states controls the energy level alignment at electrode interfaces," *Nat Commun*, vol. 5, no. 4174, 2014.

[311] V. Constantoudis, G. Patsis, and E. Gogolides, "Fractals and device performance variability: The key role of roughness in micro and nanofabrication," *Microelectronic Engineering*, vol. 90, no. 0, pp. 121 – 125, 2012.

[312] A.-L. Barabási, *Fractal concepts in surface growth*. Cambridge university press, 1995.

[313] T. A. Witten and L. M. Sander, "Diffusion-limited aggregation," *Phys. Rev. B*, vol. 27, pp. 5686–5697, May 1983.

[314] C. Rocchiccioli-Deltcheff, M. Fournier, R. Franck, and R. Thouvenot, "Vibrational investigations of polyoxometalates. 2. evidence for anion-anion interactions in molybdenum(vi) and tungsten(vi) compounds related to the keggin structure," *Inorganic Chemistry*, vol. 22, no. 2, pp. 207–216, 1983.

[315] J. F. Keggin, "Structure of the molecule of 12-phosphotungstic acid," *Nature, Letters to Editor*, vol. 132, no. 351, 1933.

[316] J.-w. Cai, J.-p. Xu, X.-s. Zhang, X.-p. Niu, T.-y. Xing, T. Ji, and L. Li, "Defect-related visible luminescence of zno nanorods annealed in oxygen ambient," *Optoelectronics Letters*, vol. 8, no. 1, pp. 4–8, 2012.

[317] N. Miriyala, K. Prashanthi, and T. Thundat, "Oxygen vacancy dominant strong visible photoluminescence from bifeo3 nanotubes," *physica status solidi (RRL) Rapid Research Letters*, vol. 7, no. 9, pp. 668–671, 2013.

[318] M. Zhu, Z. Zhang, and W. Miao, "Intense photoluminescence from amorphous tantalum oxide films," *Applied Physics Letters*, vol. 89, no. 2, 2006.

[319] F. Hai-Bo, Y. Shao-Yan, Z. Pan-Feng, W. Hong-Yuan, L. Xiang-Lin, J. Chun-Mei, Z. Qin-Sheng, C. Yong-Hai, and W. Zhan-Guo, "Investigation of oxygen vacancy and interstitial oxygen defects in zno films by photoluminescence and x-ray photoelectron spectroscopy," *Chinese Physics Letters*, vol. 24, no. 7, p. 2108, 2007.

[320] M. Zhu, Z. Zhang, and W. Miao, "Intense photoluminescence from amorphous tantalum oxide films," *Applied Physics Letters*, vol. 89, no. 2, 2006.

[321] E.H.Nicolian and J.R.Brews, *MOS (Metal Oxide Semiconductor) Physics and Technology*. Wiley, New York, 1982.

[322] P. Dimitrakis, P. Normand, C. Bonafos, E. Papadomanolaki, and E. Iliopoulos, "Gan quantum-dots integrated in the gate dielectric of metal-oxide-semiconductor structures for charge-storage applications," *Applied Physics Letters*, vol. 102, no. 5, 2013.

[323] M. Vasilopoulou, A. M. Douvas, L. Palilis, S. Kennou, and P. Argitis, "Old metal oxide clusters in new applications: Spontaneous reduction of keggin and dawson polyoxometalate layers by a metallic

electrode for improving efficiency in organic optoelectronics," *Journal of the American Chemical Society*, 2015.

[324] E. D. Palik, *Handbook of optical constants of solids*, vol. 3. Academic press, 1998.

[325] H. S. Nalwa, *Handbook of Surfaces and Interfaces of Materials: Surface and interface phenomena*, vol. 1. Academic Press, 2001.

[326] J. Keggin, "The structure and formula of 12-phosphotungstic acid," in *Proceedings of the Royal Society of London A: Mathematical, Physical and Engineering Sciences*, vol. 144, pp. 75–100, The Royal Society, 1934.

[327] O. Levy and D. Stroud, "Maxwell garnett theory for mixtures of anisotropic inclusions: Application to conducting polymers," *Physical Review B*, vol. 56, no. 13, p. 8035, 1997.

[328] C. Chaneliere, S. Four, J. Autran, and R. Devine, "Dielectric permittivity of amorphous and hexagonal electron cyclotron resonance plasma deposited $ta_2o_5$ thin films," *Electrochemical and solid-state letters*, vol. 2, no. 6, pp. 291–293, 1999.

[329] C. Chaneliere, S. Four, J. Autran, R. Devine, and N. Sandler, "Properties of amorphous and crystalline $ta_2o_5$ thin films deposited on si from a $ta(oc_2h_5)_5$ precursor," *Journal of applied physics*, vol. 83, pp. 4823–4829, 1998.

[330] M. Pope and A. Müller, *Polyoxometalate chemistry from topology via self-assembly to applications*. Springer Science & Business Media, 2001.

[331] F. P. Netzer, F. Allegretti, and S. Surnev, "Low-dimensional oxide nanostructures on metals: Hybrid systems with novel properties," *Journal of Vacuum Science & Technology B*, vol. 28, no. 1, pp. 1–16, 2010.

[332] H. Schaumburg, "Keramik, bd. 5 der reihe werkstoffe und bauelemente der elektrotechnik," 1994.

[333] V. Henrich, P. Cox, and U. Diebold, "The surface science of metal oxides," *Physics Today*, vol. 48, p. 58, 1995.

[334] X. Yu, T. J. Marks, and A. Facchetti, "Metal oxides for optoelectronic applications," *Nature materials*, vol. 15, no. 4, pp. 383–396, 2016.

[335] C. Rao and B. Raveau, "Transition metal oxides," *Annual Review of Physical Chemistry*, vol. 40, no. 1, pp. 291–326, 1989.

[336] J. A. Schwarz, C. I. Contescu, and K. Putyera, *Dekker encyclopedia of nanoscience and nanotechnology*, vol. 3. CRC press, 2004.

[337] K. Nomura, H. Ohta, A. Takagi, T. Kamiya, M. Hirano, and H. Hosono, "Room-temperature fabrication of transparent flexible thin-film transistors using amorphous oxide semiconductors," *Nature*, vol. 432, no. 7016, pp. 488–492, 2004.

[338] A. Balliou, M. Bouroushian, A. Douvas, G. Skoulatakis, S. Kennou, and N. Glezos, "Extreme electronic structure modification and low-dimensional transport tuning via the controllable crystallization of self-assembled polyoxometalate nanoclusters," *Submitted*, vol. x, no. x, pp. xx–xx, 2016.

[339] T. Kamiya and H. Hosono, "Electronic structures and device applications of transparent oxide semiconductors: What is the real merit of oxide semiconductors?," *International Journal of Applied Ceramic Technology*, vol. 2, no. 4, pp. 285–294, 2005.

[340] S. S. Gowda, *Investigation of multi-state charge-storage properties of redox-active organic molecules in silicon-molecular hybrid devices for DRAM and Flash applications*. ProQuest, 2007.

[341] J. M. Vila-Fungueiriño, R. Bachelet, G. Saint-Girons, M. Gendry, M. Gich, J. Gazquez, E. Ferain, F. Rivadulla, J. Rodriguez-Carvajal, N. Mestres, *et al.*, "Integration of functional complex oxide nanomaterials on silicon," *Frontiers in Physics*, vol. 3, p. 38, 2015.

[342] S. Aritome, *NAND Flash Memory Technologies*. IEEE Press Series on Microelectronic Systems, Wiley, 2015.

[343] A. P. Sgouros, M. R. Neupane, M. Sigalas, N. Aravantinos-Zafiris, and R. K. Lake, "Nanoscale phononic interconnects in thz frequencies," *Physical Chemistry Chemical Physics*, vol. 16, no. 42, pp. 23355–23364, 2014.

[344] P. Broekmann, K. H. Dötz, and C. A. Schalley, *Templates in Chemistry III*, vol. 287. Springer, 2009.

[345] C. Mahata, I.-K. Oh, C. M. Yoon, C. W. Lee, J. Seo, H. Algadi, M.-H. Sheen, Y.-W. Kim, H. Kim, and T. Lee, "The impact of atomic layer deposited sio 2 passivation for high-k ta 1- x zr x o on the inp substrate," *Journal of Materials Chemistry C*, vol. 3, no. 39, pp. 10293–10301, 2015.

[346] S. Zhang, Z. Fu, L. Ke, F. Lu, Q. Qin, and X. Wang, "Properties of interface states at ta2o5/n-si interfaces," *Journal of applied physics*, vol. 84, pp. 335–338, 1998.

[347] Z. C. Feng and R. Tsu, *Porous silicon*, vol. 35. World Scientific, 1994.

[348] G. Gutiérrez, E. Menéndez-Proupin, C. Loyola, J. Peralta, and S. Davis, "Computer simulation study of amorphous compounds: structural and vibrational properties," *Journal of materials science*, vol. 45, no. 18, pp. 5124–5134, 2010.

[349] J. F. Keggin, "Structure of the crystals of 12-phosphotungstic acid," *Nature, Letters to Editor*, vol. 132, pp. 351–351, Sept 1933.

[350] C. Rocchiccioli-Deltcheff, M. Fournier, R. Franck, and R. Thouvenot, "Vibrational investigations of polyoxometalates. 2. evidence for anion-anion interactions in molybdenum(vi) and tungsten(vi) compounds related to the keggin structure," *Inorganic Chemistry*, vol. 22, no. 2, pp. 207–216, 1983.

[351] E. N. Glass, J. Fielden, A. L. Kaledin, D. G. Musaev, T. Lian, and C. L. Hill, "Extending metal-to-polyoxometalate charge transfer lifetimes: The effect of heterometal location," *Chemistry–A European Journal*, vol. 20, no. 15, pp. 4297–4307, 2014.

[352] A. P. Sgouros, M. R. Neupane, M. Sigalas, N. Aravantinos-Zafiris, and R. K. Lake, "Nanoscale phononic interconnects in thz frequencies," *Physical Chemistry Chemical Physics*, vol. 16, no. 42, pp. 23355–23364, 2014.

[353] J. J. Makwana and D. D. K. Schroder, "A non-volatile memory overview," 2004.

[354] E. J. Kim, L. Wang, P. M. Asbeck, K. C. Saraswat, and P. C. McIntyre, "Border traps in al2o3/in0. 53ga0. 47as (100) gate stacks and their passivation by hydrogen anneals," *Applied Physics Letters*, vol. 96, no. 1, p. 2906, 2010.

[355] D. Fleetwood, "Fast and slow border traps in mos devices," in *Radiation and its Effects on Components and Systems, 1995. RADECS 95., Third European Conference on*, pp. 1–8, IEEE, 1995.

[356] N. Bhat and K. C. Saraswat, "Characterization of border trap generation in rapid thermally annealed oxides deposited using silane chemistry," *Journal of applied physics*, vol. 84, no. 5, pp. 2722–2726, 1998.

[357] M. Maldovan and E. L. Thomas, "Simultaneous localization of photons and phonons in two-dimensional periodic structures," *Applied Physics Letters*, vol. 88, no. 25, p. 251907, 2006.

[358] M. Fox, *Optical properties of solids*, vol. 3. Oxford university press, 2010.

[359] M. Burghard, H. Klauk, and K. Kern, "Carbon-based field-effect transistors for nanoelectronics," *Advanced materials*, vol. 21, no. 25-26, pp. 2586–2600, 2009.

[360] W. Auwärter, D. Écija, F. Klappenberger, and J. V. Barth, "Porphyrins at interfaces," *Nature Chemistry*, vol. 7, no. 2, pp. 105–120, 2015.

[361] F. Wang, M.-Y. Han, K. Y. Mya, Y. Wang, and Y.-H. Lai, "Aggregation-driven growth of size-tunable organic nanoparticles using electronically altered conjugated polymers," *Journal of the American Chemical Society*, vol. 127, no. 29, pp. 10350–10355, 2005.

[362] R. C. Naber, C. Tanase, P. W. Blom, G. H. Gelinck, A. W. Marsman, F. J. Touwslager, S. Setayesh, and D. M. De Leeuw, "High-performance solution-processed polymer ferroelectric field-effect transistors," *Nature Materials*, vol. 4, no. 3, pp. 243–248, 2005.

[363] J. Roncali, P. Leriche, and A. Cravino, "From one-to three-dimensional organic semiconductors: In search of the organic silicon?," *Advanced materials*, vol. 19, no. 16, pp. 2045–2060, 2007.

[364] H. Sirringhaus, R. Friend, X. Li, S. Moratti, A. Holmes, and N. Feeder, "Bis (dithienothiophene) organic field-effect transistors with a high on/off ratio," *Applied physics letters*, vol. 71, no. 26, pp. 3871–3873, 1997.

[365] F. Evangelista, R. Gotter, N. Mahne, S. Nannarone, A. Ruocco, and P. Rudolf, "Electronic properties and orbital-filling mechanism in rb-intercalated copper phthalocyanine," *The Journal of Physical Chemistry C*, vol. 112, no. 16, pp. 6509–6514, 2008.

[366] N. Sai, R. Gearba, A. Dolocan, J. R. Tritsch, W.-L. Chan, J. R. Chelikowsky, K. Leung, and X. Zhu, "Understanding the interface dipole of copper phthalocyanine (cupc)/c60: Theory and experiment," *The journal of physical chemistry letters*, vol. 3, no. 16, pp. 2173–2177, 2012.

[367] H.-l. Fan, S.-l. Lei, J. Huang, and Q.-x. Li, "First-principles study of single tin-phthalocyanine molecule on ag (111) surface," *Chinese Journal of Chemical Physics*, vol. 23, no. 5, pp. 565–569, 2010.

[368] R. Ramprasad and N. Shi, "Polarizability of phthalocyanine based molecular systems: A first-principles electronic structure study," *Applied physics letters*, vol. 88, no. 22, p. 222903, 2006.

[369] L. Silva, A. Neto, L. Gaffo, R. Borges, T. C. Ramalho, and N. Machado, "Molecular dynamics of film formation of metal tetrasulfonated phthalocyanine and poly amidoamine dendrimers," *Journal of Nanomaterials*, vol. 2013, 2013.

[370] L. Deng, K. Wang, C. X. Zhao, H. Yan, J. F. Britten, and G. Xu, "Phase and texture of solution-processed copper phthalocyanine thin films investigated by two-dimensional grazing incidence x-ray diffraction," *Crystals*, vol. 1, no. 3, pp. 112–119, 2011.

[371] A. L. Thomas, *Phthalocyanine research and applications*. CRC Press, 1990.

[372] H. Jiang, J. Ye, P. Hu, F. Wei, K. Du, N. Wang, T. Ba, S. Feng, and C. Kloc, "Fluorination of metal phthalocyanines: Single-crystal growth, efficient n-channel organic field-effect transistors, and structure-property relationships," *Scientific reports*, vol. 4, 2014.

[373] D. Prime, S. Paul, and P. Josephs-Franks, "Gold nanoparticle charge trapping and relation to organic polymer memory devices," *Philosophical Transactions of the Royal Society of London A: Mathematical, Physical and Engineering Sciences*, vol. 367, no. 1905, pp. 4215–4225, 2009.

[374] V. Rivera, E. Marega Jr, and F. Ferri, *Localized surface plasmon resonances: noble metal nanoparticle interaction with rare-earth ions*. INTECH Open Access Publisher, 2012.

[375] T. Springer, M. L. Ermini, B. Spackova, J. Jablonku, and J. Homola, "Enhancing sensitivity of surface plasmon resonance biosensors by functionalized gold nanoparticles: size matters," *Analytical chemistry*, vol. 86, no. 20, pp. 10350–10356, 2014.

[376] D. Gaspar, A. Pimentel, T. Mateus, J. Leitao, J. Soares, B. Falcao, A. Araújo, A. Vicente, S. Filonovich, H. Aguas, *et al.*, "Influence of the layer thickness in plasmonic gold nanoparticles produced by thermal evaporation," *Scientific reports*, vol. 3, 2013.

[377] L. Sun, Y. A. Diaz-Fernandez, T. A. Gschneidtner, F. Westerlund, S. Lara-Avila, and K. Moth-Poulsen, "Single-molecule electronics: from chemical design to functional devices," *Chemical Society Reviews*, vol. 43, no. 21, pp. 7378–7411, 2014.

[378] J.-W. Park and J. S. Shumaker-Parry, "Structural study of citrate layers on gold nanoparticles: role of intermolecular interactions in stabilizing nanoparticles," *Journal of the American Chemical Society*, vol. 136, no. 5, pp. 1907–1921, 2014.

[379] R. Lavieville, Y. Zhang, A. Casu, A. Genovese, L. Manna, E. Di Fabrizio, and R. Krahne, "Charge transport in nanoscale all-inorganic networks of semiconductor nanorods linked by metal domains," *ACS nano*, vol. 6, no. 4, pp. 2940–2947, 2012.

[380] M.-S. Hu, H.-L. Chen, C.-H. Shen, L.-S. Hong, B.-R. Huang, K.-H. Chen, and L.-C. Chen, "Photosensitive gold-nanoparticle-embedded dielectric nanowires," *Nature materials*, vol. 5, no. 2, pp. 102–106, 2006.

[381] J. H. Park, Y. T. Lim, O. O. Park, J. K. Kim, J.-W. Yu, and Y. C. Kim, "Polymer/gold nanoparticle nanocomposite light-emitting diodes: enhancement of electroluminescence stability and quantum efficiency of blue-light-emitting polymers," *Chemistry of materials*, vol. 16, no. 4, pp. 688–692, 2004.

[382] N. Krasteva, I. Besnard, B. Guse, R. E. Bauer, K. Müllen, A. Yasuda, and T. Vossmeyer, "Self-assembled gold nanoparticle/dendrimer composite films for vapor sensing applications," *Nano Letters*, vol. 2, no. 5, pp. 551–555, 2002.

[383] D. Schaadt, B. Feng, and E. Yu, "Enhanced semiconductor optical absorption via surface plasmon excitation in metal nanoparticles," *Applied Physics Letters*, vol. 86, no. 6, p. 063106, 2005.

[384] H. Häkkinen, "The gold-sulfur interface at the nanoscale," *Nature chemistry*, vol. 4, no. 6, pp. 443–455, 2012.

[385] J. B. Lee, K. Kang, and S. H. Lee, "Comparison of theoretical models of electron-phonon coupling in thin gold films irradiated by femtosecond pulse lasers," *Materials transactions*, vol. 52, no. 3, pp. 547–553, 2011.

[386] E. W. Plummer, *Frontiers in surface and interface science*, vol. 500. Gulf Professional Publishing, 2002.

[387] A. V. Kabashin and M. Meunier, "Synthesis of colloidal nanoparticles during femtosecond laser ablation of gold in water," *Journal of Applied Physics*, vol. 94, no. 12, pp. 7941–7943, 2003.

[388] D. M. Mattox, *Handbook of physical vapor deposition (PVD) processing*. William Andrew, 2010.

[389] D. J. Griffiths and R. College, *Introduction to electrodynamics*, vol. 3. prentice Hall Upper Saddle River, NJ, 1999.

[390] C. Lausser, D. Zahn, and H. Cölfen, "Barium titanate nanoparticle self-organization in an external electric field," *Journal of Materials Chemistry*, vol. 21, no. 42, pp. 16978–16982, 2011.

[391] K. E. Fong and L.-Y. L. Yung, "Localized surface plasmon resonance: a unique property of plasmonic nanoparticles for nucleic acid detection," *Nanoscale*, vol. 5, no. 24, pp. 12043–12071, 2013.

[392] S. Wang, S. Boussaad, and N. Tao, "Surface plasmon resonance enhanced optical absorption spectroscopy for studying molecular adsorbates," *Review of Scientific Instruments*, vol. 72, no. 7, pp. 3055–3060, 2001.

[393] D. B. Pedersen and E. Duncan, "Surface plasmon resonance spectroscopy of gold nanoparticle-coated substrates: Use as an indicator of exposure to chemical warfare simulants," tech. rep., DTIC Document, 2005.

[394] K. L. Kelly, E. Coronado, L. L. Zhao, and G. C. Schatz, "The optical properties of metal nanoparticles: the influence of size, shape, and dielectric environment," *The Journal of Physical Chemistry B*, vol. 107, no. 3, pp. 668–677, 2003.

[395] T. Ung, L. M. Liz-Marzan, and P. Mulvaney, "Optical properties of thin films of au@ sio2 particles," *The Journal of Physical Chemistry B*, vol. 105, no. 17, pp. 3441–3452, 2001.

[396] R. Polony, G. Reinert, G. Holzle, A. Pugin, and R. Vonderwahl, "Process for combating micro-organisms, and novel phthalocyanine compounds," Mar. 9 1982. US Patent 4,318,883.

[397] T.-W. Pi, G.-R. Lee, C.-H. Wei, W.-Y. Chen, and C.-P. Cheng, "Interfacial electronic structure of copper phthalocyanine on a gold surface studied by synchrotron radiation photoemission," *Journal of Applied Physics*, vol. 106, no. 11, p. 113716, 2009.

[398] J. C. Love, L. A. Estroff, J. K. Kriebel, R. G. Nuzzo, and G. M. Whitesides, "Self-assembled monolayers of thiolates on metals as a form of nanotechnology," *Chemical reviews*, vol. 105, no. 4, pp. 1103–1170, 2005.

[399] H. Peisert, M. Knupfer, T. Schwieger, J. Auerhammer, M. Golden, and J. Fink, "Full characterization of the interface between the organic semiconductor copper phthalocyanine and gold," *Journal of applied physics*, vol. 91, no. 8, pp. 4872–4878, 2002.

[400] F. Evangelista, A. Ruocco, R. Gotter, A. Cossaro, L. Floreano, A. Morgante, F. Crispoldi, M. Betti, and C. Mariani, "Electronic states of cupc chains on the au (110) surface," *The Journal of chemical physics*, vol. 131, no. 17, p. 174710, 2009.

[401] J.-P. Bourgoin, "Molecular electronics: a review of metal-molecule-metal junctions," in *Interacting electrons in nanostructures*, pp. 105–124, Springer, 2001.

[402] C. Dupas and M. Lahmani, *Nanoscience: Nanotechnologies and nanophysics*. Springer Science & Business Media, 2007.

[403] T.-W. Pi, G.-R. Lee, C.-H. Wei, W.-Y. Chen, and C.-P. Cheng, "Interfacial electronic structure of copper phthalocyanine on a gold surface studied by synchrotron radiation photoemission," *Journal of Applied Physics*, vol. 106, no. 11, p. 113716, 2009.

[404] M. Gorgoi and D. Zahn, "band bending in copper phthalocyanine on hydrogen-passivated si (111)," *Organic electronics*, vol. 6, no. 4, pp. 168–174, 2005.

[405] T. Tran, I. Beloborodov, J. Hu, X. Lin, T. Rosenbaum, and H. Jaeger, "Sequential tunneling and inelastic cotunneling in nanoparticle arrays," *Physical Review B*, vol. 78, no. 7, p. 075437, 2008.

[406] R. Waser, *Nanoelectronics and information technology*. John Wiley & Sons, 2012.

[407] A. A. Middleton and N. S. Wingreen, "Collective transport in arrays of small metallic dots," *Physical review letters*, vol. 71, no. 19, p. 3198, 1993.

[408] J. C. Love, L. A. Estroff, J. K. Kriebel, R. G. Nuzzo, and G. M. Whitesides, "Self-assembled monolayers of thiolates on metals as a form of nanotechnology," *Chemical reviews*, vol. 105, no. 4, pp. 1103–1170, 2005.

[409] R. Lavieville, Y. Zhang, E. Di Fabrizio, and R. Krahne, "Electrical contacts to nanorod networks at different length scales: From macroscale ensembles to single nanorod chains," *Microelectronic Engineering*, vol. 111, pp. 185–188, 2013.

[410] M. Gorgoi and D. Zahn, "band bending in copper phthalocyanine on hydrogen-passivated si (111)," *Organic electronics*, vol. 6, no. 4, pp. 168–174, 2005.

[411] J. J. Storhoff, A. A. Lazarides, R. C. Mucic, C. A. Mirkin, R. L. Letsinger, and G. C. Schatz, "What controls the optical properties of dna-linked gold nanoparticle assemblies?," *Journal of the American Chemical Society*, vol. 122, no. 19, pp. 4640–4650, 2000.

[412] C. S. Choi and H. Tachikawa, "Electrochemical behavior and characterization of polypyrrole-copper phthalocyanine tetrasulfonate thin film: cyclic voltammetry and in situ raman spectroscopic investigation," *Journal of the American Chemical Society*, vol. 112, no. 5, pp. 1757–1768, 1990.

[413] L. D. Rollmann and R. T. Iwamoto, "Electrochemistry, electron paramagnetic resonance, and visible spectra of cobalt, nickel, copper, and metal-free phthalocyanines in dimethyl sulfoxide," *Journal of the American Chemical Society*, vol. 90, no. 6, pp. 1455–1463, 1968.

[414] G. Kumar, G. Jose, V. Thomas, N. Unnikrishnan, and V. Nampoori, "Nir to uv absorption spectra and the optical constants of phthalocyanines in glassy medium," *Spectrochimica Acta Part A: Molecular and Biomolecular Spectroscopy*, vol. 59, no. 1, pp. 1–11, 2003.

[415] A. Lever, "Milaeva. er; speier, g," *Phthalocyanines: Properties and Applications; Leznoff, CC and Lever, AB R, Eds*, 1993.

[416] A. W. Snow and N. L. Jarvis, "Molecular association and monolayer formation of soluble phthalocyanine compounds," *Journal of the American Chemical Society*, vol. 106, no. 17, pp. 4706–4711, 1984.

[417] A. Davidson, "The effect of the metal atom on the absorption spectra of phthalocyanine films," *The Journal of chemical physics*, vol. 77, no. 1, pp. 168–172, 1982.

[418] Q. Chen, D. Gu, J. Shu, X. Tang, and F. Gan, "Optical and recording properties of copper phthalocyanine films," *Materials Science and Engineering: B*, vol. 25, no. 2-3, pp. 171–174, 1994.

[419] S. A. Maier, *Plasmonics: fundamentals and applications*. Springer Science & Business Media, 2007.

[420] K.-H. Su, Q.-H. Wei, X. Zhang, J. Mock, D. R. Smith, and S. Schultz, "Interparticle coupling effects on plasmon resonances of nanogold particles," *Nano Letters*, vol. 3, no. 8, pp. 1087–1090, 2003.

[421] Y.-C. Yeo, T.-J. King, and C. Hu, "Metal-dielectric band alignment and its implications for metal gate complementary metal-oxide-semiconductor technology," *Journal of Applied Physics*, vol. 92, no. 12, pp. 7266–7271, 2002.

[422] J. Hölzl and F. Schulte, "Work function of metals," in *Solid Surface Physics*, pp. 1–150, Springer, 1979.

[423] H. B. Michaelson, "The work function of the elements and its periodicity," *Journal of Applied Physics*, vol. 48, no. 11, pp. 4729–4733, 1977.

[424] M. T. Bernius, M. Inbasekaran, J. OBrien, W. Wu, *et al.*, "Progress with light-emitting polymers," *Advanced Materials*, vol. 12, no. 23, pp. 1737–1750, 2000.

[425] F.-C. Chen, L.-J. Kung, T.-H. Chen, and Y.-S. Lin, "Copper phthalocyanine buffer layer to enhance the charge injection in organic thin-film transistors," *Applied physics letters*, vol. 90, no. 7, p. 073504, 2007.

[426] X. Luo, Y. Li, W. Lv, F. Zhao, L. Sun, Y. Peng, Z. Wen, J. Zhong, and J. Zhang, "Position-dependent performance of copper phthalocyanine based field-effect transistors by gold nanoparticles modification," *Nanotechnology*, vol. 26, no. 3, p. 035201, 2014.

[427] Y. L. Huang, E. Wruss, D. A. Egger, S. Kera, N. Ueno, W. A. Saidi, T. Bucko, A. T. Wee, and E. Zojer, "Understanding the adsorption of cupc and znpc on noble metal surfaces by combining quantum-mechanical modelling and photoelectron spectroscopy," *Molecules*, vol. 19, no. 3, pp. 2969–2992, 2014.

[428] G. Mattioli, F. Filippone, P. Giannozzi, R. Caminiti, and A. A. Bonapasta, "Ab initio theoretical investigation of phthalocyanine- semiconductor hybrid systems," *Chemistry of Materials*, vol. 21, no. 19, pp. 4555–4567, 2009.

[429] E. Ukraintsev, A. Kromka, H. Kozak, Z. Remeš, and B. Rezek, "Artifacts in atomic force microscopy of biological samples, atomic force microscopy investigations into biology-from cell to protein, dr," *ISBN*, pp. 978–953, 2012.

[430] S. Varghese, M. Iype, E. Mathew, and C. Menon, "Determination of the energy band gap of thin films of cadmium sulphide, copper phthalocyanine and hybrid cadmium sulphide/copper phthalocyanine

from its optical studies," *Materials Letters*, vol. 56, no. 6, pp. 1078–1083, 2002.

[431] Y. Sadaoka, T. Jones, and W. Göpel, "Effect of heat pretreatment on the electrical conductance of lead phthalocyanine films for no 2 gas detection," *Journal of materials science letters*, vol. 8, no. 9, pp. 1095–1097, 1989.

[432] Z. Bao, A. J. Lovinger, and A. Dodabalapur, "Organic field-effect transistors with high mobility based on copper phthalocyanine," *Applied Physics Letters*, vol. 69, no. 20, pp. 3066–3068, 1996.

[433] S. Yadav, A. Sharma, and S. Ghosh, "Organic transistor and inverter based on assembly of organic nanowires achieved by optimizing surface morphology," *Applied Physics Letters*, vol. 102, no. 9, p. 093303, 2013.

[434] G. Chaidogiannos, F. Petraki, N. Glezos, S. Kennou, and S. Nespurek, "Soluble substituted phthalocyanines for ofet applications," *Materials Science and Engineering: B*, vol. 152, no. 1, pp. 105–108, 2008.

[435] E. Meijer, M. Matters, P. Herwig, D. de Leeuw, and T. Klapwijk, "The meyer–neldel rule in organic thin-film transistors," *Applied Physics Letters*, vol. 76, no. 23, pp. 3433–3435, 2000.

[436] K. Kadish, K. Smith, and R. Guilard, "The porphyrin handbook: Phthalocyanines: Spectroscopic and electrochemical characterization," 2006.

[437] Y. Kanemitsu, H. Funada, and Y. Masumoto, "Electric-field dependence of the hole drift mobility in molecularly doped polymers: Importance of the disorder of hopping sites," *Journal of applied physics*, vol. 71, no. 1, pp. 300–303, 1992.

[438] J.-F. Chang, H. Sirringhaus, M. Giles, M. Heeney, and I. McCulloch, "Relative importance of polaron activation and disorder on charge transport in high-mobility conjugated polymer field-effect transistors," *Physical Review B*, vol. 76, no. 20, p. 205204, 2007.

[439] H. Bässler, "Charge transport in disordered organic photoconductors a monte carlo simulation study," *physica status solidi (b)*, vol. 175, no. 1, pp. 15–56, 1993.

[440] Y. Cai, D. Wolfkuhler, A. Myalitsin, J. Perlich, A. Meyer, and C. Klinke, "Tunable electrical transport through annealed monolayers of monodisperse cobalt- platinum nanoparticles," *ACS nano*, vol. 5, no. 1, pp. 67–72, 2010.

[441] H. E. Romero and M. Drndic, "Coulomb blockade and hopping conduction in pbse quantum dots," *Physical review letters*, vol. 95, no. 15, p. 156801, 2005.

[442] R. Parthasarathy, X.-M. Lin, K. Elteto, T. Rosenbaum, and H. M. Jaeger, "Percolating through networks of random thresholds: Finite temperature electron tunneling in metal nanocrystal arrays," *Physical review letters*, vol. 92, no. 7, p. 076801, 2004.

[443] I. Beloborodov, A. Lopatin, V. Vinokur, and K. Efetov, "Granular electronic systems," *Reviews of Modern Physics*, vol. 79, no. 2, p. 469, 2007.

[444] A. Zabet-Khosousi and A.-A. Dhirani, "Charge transport in nanoparticle assemblies," *Chemical reviews*, vol. 108, no. 10, pp. 4072–4124, 2008.

[445] A. Zabet-Khosousi and A.-A. Dhirani, "Charge transport in nanoparticle assemblies," *Chemical reviews*, vol. 108, no. 10, pp. 4072–4124, 2008.

[446] A. A. Middleton and N. S. Wingreen, "Collective transport in arrays of small metallic dots," *Physical review letters*, vol. 71, no. 19, p. 3198, 1993.

[447] T. Tran, I. Beloborodov, J. Hu, X. Lin, T. Rosenbaum, and H. Jaeger, "Sequential tunneling and inelastic cotunneling in nanoparticle arrays," *Physical Review B*, vol. 78, no. 7, p. 075437, 2008.

[448] C. Shen, A. Kahn, and J. Schwartz, "Chemical and electrical properties of interfaces between magnesium and aluminum and tris-(8-hydroxy quinoline) aluminum," *Journal of Applied Physics*, vol. 89, no. 1, pp. 449–459, 2001.

[449] J. J. van Hapert, "Hopping conduction and chemical structure: a study on silicon suboxides," *Dissertation*, 2002.

[450] D. B. Pedersen and S. Wang, "Remarkably strong interparticle coupling in two-dimensional ensembles of naked silver quantum dots: the effect on optical and conduction characteristics," *The Journal of Physical Chemistry C*, vol. 113, no. 12, pp. 4797–4803, 2009.

[451] V. Ambegaokar, B. Halperin, and J. Langer, "Hopping conductivity in disordered systems," *Physical review B*, vol. 4, no. 8, p. 2612, 1971.

[452] A. Efros and B. Shklovskii, "Coulomb gap and low temperature conductivity of disordered systems," *Journal of Physics C: Solid State Physics*, vol. 8, no. 4, p. L49, 1975.

[453] E. Levin and V. Nguyen, "Bi shklovski i, and al éefros," coulomb gap and hopping electric conduction. computer simulation,"," *Sov. Phys. JETP*, vol. 65, p. 842, 1987.

[454] N. F. Mott, "The basis of the electron theory of metals, with special reference to the transition metals," *Proceedings of the Physical Society. Section A*, vol. 62, no. 7, p. 416, 1949.

[455] T. Tran, I. Beloborodov, X. Lin, T. Bigioni, V. Vinokur, and H. Jaeger, "Multiple cotunneling in large quantum dot arrays," *Physical review letters*, vol. 95, no. 7, p. 076806, 2005.

[456] S.-i. Taniguchi, M. Minamoto, M. M. Matsushita, T. Sugawara, Y. Kawada, and D. Bethell, "Electron transport in networks of gold nanoparticles connected by oligothiophene molecular wires," *Journal of Materials Chemistry*, vol. 16, no. 34, pp. 3459–3465, 2006.

[457] M. SeokáJang *et al.*, "Reliable doping and carrier concentration control in graphene by aerosol-derived metal nanoparticles," *Journal of Materials Chemistry C*, vol. 3, no. 32, pp. 8294–8299, 2015.

[458] M. Meyns, S. Willing, H. Lehmann, and C. Klinke, "Metal domain size dependent electrical transport in pt-cdse hybrid nanoparticle monolayers," *ACS nano*, vol. 9, no. 6, pp. 6077–6087, 2015.

[459] K. Hipps and U. Mazur, "Electron affinity states of metal supported phthalocyanines measured by tunneling spectroscopy," *Journal of Porphyrins and Phthalocyanines*, vol. 16, no. 03, pp. 273–281, 2012.

[460] G. Mattioli, F. Filippone, P. Giannozzi, R. Caminiti, and A. A. Bonapasta, "Ab initio theoretical investigation of phthalocyanine- semiconductor hybrid systems," *Chemistry of Materials*, vol. 21, no. 19, pp. 4555–4567, 2009.

[461] C. Shen, I. G. Hill, A. Kahn, and J. Schwartz, "Organometallic chemistry at the magnesium-tris (8-hydroxyquinolino) aluminum interface," *Journal of the American Chemical Society*, vol. 122, no. 22, pp. 5391–5392, 2000.

[462] A. Kronemeijer, E. Huisman, I. Katsouras, P. Van Hal, T. Geuns, P. Blom, S. Van Der Molen, and D. De Leeuw, "Universal scaling in highly doped conducting polymer films," *Physical review letters*, vol. 105, no. 15, p. 156604, 2010.

[463] M. P. Fisher and A. T. Dorsey, "Dissipative quantum tunneling in a biased double-well system at finite temperatures," *Physical review letters*, vol. 54, no. 15, p. 1609, 1985.

[464] M. Bockrath, D. Cobden, and J. Liu, "a. rinzler, r. smalley, l. balents, and p. mceuen," *Nature*, vol. 397, p. 598, 1999.

[465] J. D. Yuen, R. Menon, N. E. Coates, E. B. Namdas, S. Cho, S. T. Hannahs, D. Moses, and A. J. Heeger, "Nonlinear transport in semiconducting polymers at high carrier densities," *Nature materials*, vol. 8, no. 7, pp. 572–575, 2009.

[466] J.-F. Dayen, T. Wade, G. Rizza, D. Golubev, C.-S. Cojocaru, D. Pribat, X. Jehl, M. Sanquer, and J.-E. Wegrowe, "Conductance of disordered semiconducting nanowires and carbon nanotubes: a chain of quantum dots," *The European Physical Journal Applied Physics*, vol. 48, no. 01, p. 10604, 2009.

[467] L. Li, N. Lu, and M. Liu, "Physical origin of nonlinear transport in organic semiconductor at high carrier densities," *Journal of Applied Physics*, vol. 116, no. 16, p. 164504, 2014.

[468] M. Ghulinyan and L. Pavesi, *Light Localisation and Lasing: Random and Pseudo-random Photonic Structures*. Cambridge University Press, 2014.

[469] R. Parthasarathy, X.-M. Lin, and H. M. Jaeger, "Electronic transport in metal nanocrystal arrays: The effect of structural disorder on scaling behavior," *Physical Review Letters*, vol. 87, no. 18, p. 186807, 2001.

[470] U. Mishra and J. Singh, *Semiconductor device physics and design*. Springer Science & Business Media, 2007.

[471] M. Araidai and M. Tsukada, "Theoretical calculations of electron transport in molecular junctions: Inflection behavior in fowler-nordheim plot and its origin," *Physical Review B*, vol. 81, no. 23, p. 235114, 2010.

[472] E. B. Sonin, "Tunneling into 1d and quasi-1d conductors: Luttinger-liquid behavior and effects of environment," *Physica E: Low-dimensional Systems and Nanostructures*, vol. 18, no. 1, pp. 331–332, 2003.

[473] H. Grabert, G.-L. Ingold, M. H. Devoret, D. Estève, H. Pothier, and C. Urbina, "Single electron tunneling rates in multijunction circuits,"

*Zeitschrift für Physik B Condensed Matter*, vol. 84, no. 1, pp. 143–155, 1991.

[474] H. Grabert and M. H. Devoret, *Single charge tunneling: Coulomb blockade phenomena in nanostructures*, vol. 294. Springer Science & Business Media, 2013.

[475] G. Schmid, *Nanoparticles: from theory to application*. John Wiley & Sons, 2011.

[476] C.-Y. Lin and W.-M. Zhang, "Single-electron turnstile pumping with high frequencies," *Applied Physics Letters*, vol. 99, no. 7, p. 072105, 2011.

[477] M. W. Keller, J. M. Martinis, N. M. Zimmerman, and A. H. Steinbach, "Accuracy of electron counting using a 7-junction electron pump," *Applied Physics Letters*, vol. 69, no. 12, pp. 1804–1806, 1996.

[478] H.-O. Müller, D. A. Williams, H. Mizuta, and Z. A. Durrani, "Simulating si multiple tunnel junctions from pinch-off to ohmic conductance," *Materials Science and Engineering: B*, vol. 74, no. 1, pp. 36–39, 2000.

[479] P. Moetakef, C. A. Jackson, J. Hwang, L. Balents, S. J. Allen, and S. Stemmer, "Toward an artificial mott insulator: Correlations in confined high-density electron liquids in srtio 3," *Physical Review B*, vol. 86, no. 20, p. 201102, 2012.

[480] M. Tsutsui and M. Taniguchi, "Single molecule electronics and devices," *Sensors*, vol. 12, no. 6, pp. 7259–7298, 2012.

[481] N. Tao, "Electron transport in molecular junctions," *Nature nanotechnology*, vol. 1, no. 3, pp. 173–181, 2006.

[482] I. Nakada, K. Ariga, and A. Ichimiya, "The electrical conductivity of anthracene," *Journal of the Physical Society of Japan*, vol. 19, no. 9, pp. 1587–1591, 1964.

[483] C. Hamann and G. Lehmann, "A model of the electrical transport phenomena in imperfect crystals of copper phthalocyanine ii. surface states of phthalocyanine single crystals," *physica status solidi (b)*, vol. 60, no. 1, pp. 407–413, 1973.

[484] G. Lehmann and C. Hamann, "A model of the electrical transport phenomena in imperfect crystals of copper phthalocyanine. iii. the position of the fermi level in the $\delta$-model," *physica status solidi (b)*, vol. 63, no. 1, pp. 341–347, 1974.

[485] A. Sussman, "Electrical properties of copper phthalocyanine thin films as influenced by the ambient," *Journal of Applied Physics*, vol. 38, no. 7, pp. 2748–2752, 1967.

[486] T. Tran, I. Beloborodov, X. Lin, T. Bigioni, V. Vinokur, and H. Jaeger, "Multiple cotunneling in large quantum dot arrays," *Physical review letters*, vol. 95, no. 7, p. 076806, 2005.

[487] R. Parthasarathy, X.-M. Lin, and H. M. Jaeger, "Electronic transport in metal nanocrystal arrays: The effect of structural disorder on scaling behavior," *Physical Review Letters*, vol. 87, no. 18, p. 186807, 2001.

[488] M. D. Hartle, S. K. Sommer, S. R. Dietrich, and M. D. Pluth, "Chemically reversible reactions of hydrogen sulfide with metal phthalocyanines," *Inorganic chemistry*, vol. 53, no. 15, pp. 7800–7802, 2014.

[489] S. Dogo, J.-P. Germain, C. Maleysson, and A. Pauly, "Interaction of no 2 with copper phthalocyanine thin films i: Characterization of the copper phthalocyanine films," *Thin solid films*, vol. 219, no. 1, pp. 244–250, 1992.

[490] S. Kurosawa, N. Kamo, D. Matsui, and Y. Kobatake, "Gas sorption to plasma-polymerized copper phthalocyanine film formed on a piezoelectric crystal," *Analytical Chemistry*, vol. 62, no. 4, pp. 353–359, 1990.

[491] K. Andersen, S. Latini, and K. S. Thygesen, "Dielectric genome of van der waals heterostructures," *Nano letters*, vol. 15, no. 7, pp. 4616–4621, 2015.

[492] K. Agladze, D. Jackson, and T. Romeo, "Periodicity of cell attachment patterns during escherichia coli biofilm development," *Journal of bacteriology*, vol. 185, no. 18, pp. 5632–5638, 2003.

[493] A. Zabet-Khosousi and A.-A. Dhirani, "Charge transport in nanoparticle assemblies," *Chemical reviews*, vol. 108, no. 10, pp. 4072–4124, 2008.

[494] H. Grabert and M. H. Devoret, *Single charge tunneling: Coulomb blockade phenomena in nanostructures*, vol. 294. Springer Science & Business Media, 2013.

[495] K. Schouteden, N. Vandamme, E. Janssens, P. Lievens, and C. Van Haesendonck, "Single-electron tunneling phenomena on preformed gold clusters deposited on dithiol self-assembled monolayers," *Surface science*, vol. 602, no. 2, pp. 552–558, 2008.

[496] G. Schmid, *Nanoparticles: from theory to application*. John Wiley & Sons, 2011.

[497] C.-Y. Lin and W.-M. Zhang, "Single-electron turnstile pumping with high frequencies," *Applied Physics Letters*, vol. 99, no. 7, p. 072105, 2011.

[498] M. W. Keller, J. M. Martinis, N. M. Zimmerman, and A. H. Steinbach, "Accuracy of electron counting using a 7-junction electron pump," *Applied Physics Letters*, vol. 69, no. 12, pp. 1804–1806, 1996.

[499] L. Geerligs and J. Mooij, "Charging effects and turnstileclocking of single electrons in small tunnel junctions," in *Granular Nanoelectronics*, pp. 393–412, Springer, 1991.